Multiply Surface-Functionalized Nanoporous Carbon for Vehicular Hydrogen Storage

Final Technical Report

DOE Award: DE-FG36-08GO18142
Recipient Institution: University of Missouri, Columbia, MO
Project Title: Multiply Surface-Functionalized Nanoporous Carbon for Vehicular Hydrogen Storage
Project Director: Peter Pfeifer, Department of Physics, University of Missouri, Columbia, MO 65211
Phone: 573-882-2335; Email: pfeiferp@missouri.edu
Consortium Members: a) University of Missouri: M.F. Hawthorne, S. Jalisatgi, M.W. Lee, J.D. Robertson, G.J. Suppes, C. Wexler
b) Université Aix-Marseille, Marseille, France: B. Kuchta
c) Université Montpellier, Montpellier, France: L. Firlej
d) MRIGlobal, Kansas City, MO: P. Buckley, S. Chakraborti, J. Clement, P. Doynov
Partners/Collaborators: Advanced Photon Source, Argonne National Laboratory: J. Ilavsky
MeadWestvaco Corporation, Charleston, SC: B.P. Holbrook
Missouri U. Science & Technology, Rolla, MO: D. Waddill
National Renewable Energy Laboratory: T. Gennett, P. Parilla
NIST Center for Neutron Research: C. Brown, J.W. Burress, R. Paul, Y. Liu
Norwegian U. Science & Technology, Trondheim: S. Kjelstrup
Oak Ridge National Laboratory: J. Idrobo, R. Olsen, M. Stone
OsComp, Inc., Houston, TX: T.A. Rash, J. Romanos
Université Aix-Marseille, Marseille, France: P. Llewellyn
University of Missouri, Columbia, MO: J.W. Burress, M. Greenlief, T. Lam, H. Taub, T.A. White, P. Yu
University of Missouri, Kansas City, MO: P. Rulis
Washington University, St. Louis, MO: M. Conradi
Wroclaw U. Technology, Wroclaw, Poland: S. Roszak
Cost-Sharing Partners: University of Missouri, Columbia, MO
DOE Program Managers: Ned Stetson, Fuel Cells Technologies Office
U.S. Department of Energy, 1000 Independence Ave. SW
Washington, DC 20585
Phone: 202-586-9995; Email: ned.stetson@ee.doe.gov
Jesse Adams, Fuel Cells Technologies Office
U.S. Department of Energy, Golden Field Office
15013 Denver West Parkway, Golden, CO 80401
Phone: 720-356-1421; Email: jesse.adams@ee.doe.gov
Project Period: 9/1/2008 – 11/30/2014
Date of Report: 5/15/2015, 2/20/2017
Report Prepared by: Peter Pfeifer, Andrew Gillespie, David Stalla, Elmar Dohnke

Table of Contents

Executive Summary

The purpose of the project "Multiply Surface-Functionalized Nanoporous Carbon for Vehicular Hydrogen Storage" is the development of materials that store hydrogen (H_2) by adsorption in quantities and at conditions that outperform current compressed-gas H_2 storage systems for electric power generation from hydrogen fuel cells (HFCs). Prominent areas of interest for HFCs are light-duty vehicles ("hydrogen cars") and replacement of batteries with HFC systems in a wide spectrum of applications, ranging from forklifts to unmanned areal vehicles to portable power sources. State-of-the-art compressed H_2 tanks operate at pressures between 350 and 700 bar at ambient temperature and store 3-4 percent of H_2 by weight (wt%) and less than 25 grams of H_2 per liter (g/L) of tank volume. Thus, the purpose of the project is to engineer adsorbents that achieve storage capacities better than compressed H_2 at pressures less than 350 bar.

Adsorption holds H_2 molecules as a high-density film on the surface of a solid at low pressure, by virtue of attractive surface-gas interactions. At a given pressure, the density of the adsorbed film is the higher the stronger the binding of the molecules to the surface is (high binding energies). Thus, critical for high storage capacities are high surface areas, high binding energies, and low void fractions (high void fractions, such as in interstitial space between adsorbent particles, "waste" storage volume by holding hydrogen as non-adsorbed gas). Coexistence of high surface area and low void fraction makes the ideal adsorbent a nanoporous monolith, with pores wide enough to hold high-density hydrogen films, narrow enough to minimize storage as non-adsorbed gas, and thin walls between pores to minimize the volume occupied by solid instead of hydrogen. A monolith can be machined to fit into a rectangular tank (low pressure, conformable tank), cylindrical tank (high pressure), or other tank shape without any waste of volume.

The research covers four areas:

(1) Development of high-surface-area nanoporous carbon materials ("engineered nanospaces"), which serve as scaffold for insertion of boron atoms, B, into the carbon lattice as high-binding-energy sites (surface functionalization, boron doping).

(2) Conversion of the carbon into B_xC by adsorption and thermal decomposition of decaborane ($B_{10}H_{14}$) on the parent material, followed by annealing, ideally without loss of surface area and nanopores.

(3) Demonstration that a significant fraction of the boron in B_xC is present in the form of correctly coordinated boron in the carbon lattice (electron-deficient, sp^2-bonded B-C bonds), hosts high binding energies, and enhances hydrogen adsorption—in line with one of the final recommendations of the DOE Hydrogen Sorption Center of Excellence, which stated: "*... it became clear that only correctly coordinated boron substituted in graphitic carbon is a viable route to improved hydrogen storage for substituted carbon materials. ... The Center recommends that researchers should develop substituted/heterogeneous materials that can be used to enhance dihydogen isosteric heats of adsorption in the range of 10-25 kJ/mol. ... Development efforts should focus on creating materials with the appropriate chemical and electronic structure, sufficient composition, and high specific surface areas ...*" [L. Simpson, *DOE Hydrogen Sorption Center of Excellence, Final Report Executive Summary*, National Renewable Energy Laboratory (2010), p. 36-37].

(4) Fabrication of undoped and doped monoliths (carbon and B_xC) from parent materials, most of which are powders, using appropriate binders and binding procedures, without loss of surface area and high-binding-energy sites, and demonstration that monolithic materials exhibit expected superior volumetric storage capacities.

Notable achievements include:

(1) In undoped monoliths optimized for volumetric storage capacity, gravimetric and volumetric hydrogen storage capacities at liquid nitrogen temperature and 190 bar are nominally (excluding tank shell and cryogenic equipment) 180% and 130%, respectively, of the 2020 DOE targets for light-duty vehicles (Table 0).

(2) In undoped monoliths optimized for volumetric storage capacity, gravimetric and volumetric hydrogen storage capacities at room temperature and 190 bar are nominally (excluding tank shell and auxiliary equipment) 200% and 75%, respectively, of the 2015 DOE targets for portable power supplies (Table 0).

(3) In a 5.3-L stationary hydrogen tank, packed with 1.5 kg carbon powder (packing fraction 0.63) optimized for gravimetric storage capacity, gravimetric and volumetric storage capacities are 0.031 kg H_2/kg carbon and 0.0088 kg H_2/L internal tank volume, respectively, at room temperature and 100 bar.

(4) B_xC materials were produced with 0-10 wt% B, 0-30% loss of surface area, 0-8% loss of porosity (void fraction), and 0-1.7 wt% high-binding-energy sites (boron atoms sp^2-bonded to carbon; approximately 1 out of 7-8 boron atoms are sp^2-bonded). Associated high isosteric heats were 7.1-9.6 kJ/mol, in excellent agreement with electronic structure calculations performed during the early part of the project, for boron concentrations 0-10 wt%.

(5) High isosteric heats on B_xC were determined by high-precision isotherm analyses, based on experimental observation of Henry's law (linear adsorption isotherm at low pressure), free of uncertainties due to uncertain film volumes in traditional isosteric heat determinations.

(6) Discovery of exceptionally dense, liquid- or solid-like H_2 films at liquid nitrogen temperature. Saturated film densities are 100-120 g/L across all carbon samples investigated at the University of Missouri, at pressures as low as 35-70 bar. These densities are 4-5 times the density of compressed hydrogen at the same temperature and pressure, and 1.4-1.7 times the density of liquid hydrogen at its normal boiling point, 71 g/L. Experimental thicknesses of the saturated films are 0.30-0.32 nm. This is the first time the density and thickness of supercritically adsorbed films has been determined experimentally on carbon-based materials (C, B_xC). The films are monomolecular, and their densities suggest that exceptionally high volumetric storage capacities can be achieved in appropriately engineered nanoporous materials.

– How does the research add to the understanding of the area investigated?
Answer: Accomplishments (4)-(6)
– What is the technical effectiveness and economic feasibility of the methods or techniques investigated or demonstrated?
Answer: Accomplishments (1)-(3)
– How is the project is otherwise of benefit to the public?
Answer: Material costs for adsorbents are 10-20 times lower than DOE targets for storage system cost (Table 0).

Table 0. Progress towards meeting 2015 and 2020 DOE targets for hydrogen storage [Multi-Year Research, Development and Demonstration Plan, 2012-15, Updated May 2015], http://energy.gov/sites/prod/files/2015/05/f22/fcto_myrdd_storage.pdf. U. Missouri sorbent is BR-0311 (undoped carbon monolith, 0.4 kg); void fraction, ϕ, refers to a single monolith. Referenced targets for portable equipment are for rechargeable equipment. Performance of U. Missouri material at liquid-nitrogen temperature, 77 K, is compared with storage targets for vehicles, highlighted in yellow, because cryogenic tanks are under active consideration by the DOE for vehicles. Performance of U. Missouri material at room temperature, 296 K, is compared with storage targets for portable equipment, highlighted in yellow, because winning tank technology for portable power supplies will most likely operate at ambient temperature.

Storage Parameter	On-Board Storage for Light-Duty Vehicles, 2020	Storage Material Handling Equipment, 2015	U. Missouri 2014 Status (77 K, 190 bar; $\phi = 0.74$)
System Gravimetric Storage Capacity	0.055 kg H_2/kg system	N/A	0.099 kg H_2/kg sorbent
System Volumetric Storage Capacity	0.040 kg H_2/L system	0.030 kg H_2/L system	0.051 kg H_2/L sorbent
Storage System Cost	\$400/kg H_2 stored	\$667/kg H_2 stored	\$39/kg H_2 stored (storage material cost)

Storage Parameter	Storage for Low Power Portable Equipment, 2015	Storage for Medium Power Portable Equipment, 2015	U. Missouri 2014 Status (296 K, 190 bar; $\phi = 0.74$)
System Gravimetric Storage Capacity	0.015 kg H_2/kg system	0.015 kg H_2/kg system	0.030 kg H_2/kg sorbent
System Volumetric Storage Capacity	0.020 kg H_2/L system	0.020 kg H_2/L system	0.015 kg H_2/L sorbent
Storage System Cost	\$3/g H_2 stored	\$6.70/g H_2 stored	\$0.15/g H_2 stored (storage material cost)

1. Goals, Objectives, Accomplishments

1.1 Project Objectives and Scope

Project Objectives

The objective, as formulated in the Statement of Project Objectives (SOPO), 2/29/2009, and updated in SOPO modifications (2013, 2014), is to fabricate, optimize, and test monolithic nanoporous carbon-based materials made from corncob or other sources, suitably surface-engineered, for high-capacity reversible hydrogen storage. The materials will simultaneously host high surface areas, created in a multi-step process including neutron irradiation, and a large fraction of sites with high binding energy for hydrogen, created by surface functionalization with boron, iron, and possibly other metals. Expected outcomes are surface areas in excess of 4500 m^2/g and average binding energies in excess of 12 kJ/mol, manufactured reproducibly at the kg scale. Objectives at the system level are to determine, in test vessels that are surrogates of an on-board hydrogen tank, the monoliths' potential to meet: (i) what was the 2010 DOE volumetric storage capacity target at the time, 0.028 kg H_2/liter system (DOE Targets for On-Board Hydrogen Storage for Light-Duty Vehicles, Feb. 2009), at ambient temperature and a pressure of 50 bar, with charge/discharge purely by pressure swing; and (ii) what was the 2015 DOE volumetric storage capacity target at the time, 0.040 kg H_2/liter system, at near liquid-nitrogen temperature and 50 bar, with charge/discharge purely by pressure swing.

Project Scope

Under the DOE's National Hydrogen Storage Project, materials are sought for on-board hydrogen tanks, on hydrogen-powered vehicles, that have a sufficient storage capacity and meet consumer requirements without compromising passenger or cargo space. Ideally, the tank is lightweight and conformable, installed under the floor or in other unused space of the vehicle, has a driving range of more than three hundred miles, can be fueled in less than three minutes (for a 5-kg hydrogen charge), and requires a minimum of auxiliary on/off-board equipment and infrastructure.

This project is a systematic program to "surface-engineer" existing nanoporous carbons (activated carbon) made from corncob or other sources. These materials will be engineered with the objective of achieving, by reversible physical adsorption, what were the 2010 system targets (0.045 kg H_2/kg system, 0.028 kg H_2/liter system) at ambient temperature and low pressure (50 bar), and what were the 2015 targets (0.055 kg H_2/kg system, 0.040 kg H_2/liter system) at a temperature between cryogenic and ambient and low pressure. The project addresses the technical challenges identified by DOE: system volume and weight, system costs, efficiency, charging/discharging rates, and thermal management, as follows. Low pressure enables a conformable tank design, lightweight tank walls, and low hydrogen compression costs. Low pressure is made possible by strong surface-gas interactions (high binding energies), which adsorb hydrogen as a high-density film on the surface. Storage by adsorption provides a tank free of material regeneration requirements, with rapid charge/discharge by pressure control and minimum thermal management. Production of carbon from corncob uses low-cost, renewable raw materials and is fully scalable.

1.2 Project Tasks and Milestones—Proposed and Actually Achieved

The tables below list key accomplishments and progress towards milestones formulated in the Statement of Project Objectives (SOPO), 2/25/2009, for Phase 1; in the modified SOPO, 1/28/2013, for Phase 2; and in a further modfication of Phase 2 during the Site Visit at the University of Missouri, 1/29/2014.

Table 1.1. Tasks, milestones, and achievement of milestones for Phase 1. Color—Light green: milestone partly achieved; dark green: milestone achieved. Abbreviations:

- Σ: specific surface area measured by Brunauer-Emmett-Teller method ("BET surface area")
- ΔH: isosteric heat of adsorption
- n_{st}: gravimetric storage capacity in wt% material [= mass H_2/mass (sorbent + H_2)]
- v_{st}: volumetric storage capacity of material [= mass H_2/volume (sorbent + H_2)]
- LN: liquid nitrogen temperature (77 K)
- RT: room temperature (296 K)
- [B]: total boron concentration [= mass B/mass (B + C + O)]
- [$B_{B\text{-}C}$]: concentration of boron in B-C bonds [sp^2-bonded B; B completely substituted in C lattice; mass sp^2-bonded B/mass (B + C + O)]
- [$B_{B\text{-}B}$]: concentration of boron in B-B bonds
- [$B_{B\text{-}O}$]: concentration of boron in B-O bonds
- [O]: concentration of oxygen [= mass O/mass (B + C + O)]

Task	Milestones	Achieved	Comments
1.0 –Fabricate functionalized carbons (non-hybrid)	Granular + monoliths (boron-free) with Σ > 4500 m^2/g	Σ ~ 2700 m^2/g reproducibly	Σ ~ 6000 m^2/g with carbon possible. Simulations predict high performance at LN. But not necessarily better at RT
	Protocol to manufacture at kg scale	Produced 1.5 kg of high-performance carbon (powder), 3K-120C. Scale-up of 10^4 from lab	
	Boron/alkali functionalized materials	Boron-doped samples: [B] = 1-9 wt% Σ = 2200 m^2/g	Alkali functionalized materials discontinued in agreement with DOE
2.0 –Fabricate hybrid materials	Hybrid materials, Σ > 3500 m^2/g, 6% Pt with spillover	N/A	Pt hybrid materials discontinued in agreement with DOE
3.0—Characterize and optimize materials/H_2 performance	Validation of theoretical modeling predictions of ΔH	Observed, [B] = 9 wt%: ΔH = 10-17 kJ/mol Theoretical, [B] = 10 wt%: ΔH = 10-12 kJ/mol	Determined ΔH from absolute adsorption isotherms, with experimental estimates of film volume (thermodynamically consistent Clausius-Clapeyron) 2014: ΔH values may be inaccurate due to temperature instability during isotherm measurements.

	Structural & compositional characterization	N_2, SAXS, NMR, PGNAA, XPS, FTIR, IINS, TEM. Established B-C bonds (FTIR, XPS) and nanopore dimensions (SAXS, TEM)	
	Characterization of H_2 uptake/discharge, storage capacities, kinetics	– H_2 storage in 5.3-L tank, with1.5 kg of 3K-120C: n_{st} = 3.0 wt% (RT, 100 bar) – Fast kinetics in tank	– 1st H_2 sorption tank in U.S. (2 × 5.3 L). Uptake with flow meter = uptake with HTP1. – Tank 95% full in 3 min
	Test for $\Sigma > 4500$ m^2/g, $\Delta H > 12$ kJ/mol, $n_{st} > 4.5$ wt% at 50 bar & RT	In B-doped samples at RT: ΔH = 10-17 kJ/mol Σ = 2200 m^2/g	ΔH, Σ repeatable on remanufactured materials. 2014: ΔH values may be inaccurate due to temp. instability during isotherm measurements.
	Hybrid materials	N/A	Discontinued in agreement with DOE
	3.2—Completed design of test vessel	0.5-L H_2 test fixture at RT designed and built 10.6-liter tank, at RT and –78 ºC, designed and built	Construction of tank supported by DLA
	3.3—Compare different methods of B functionalization	• Decaborane deposition and thermolysis • Thermodynamics of decaborane adsorption • 3 methods developed for B-deposition (I, II, III). • 2 annealing temperatures (600 ºC, 1000 ºC) • 1-step and multi-step methods	• Samples with up to [B] = 9 wt% (PGNAA, XPS) • Small reduction in surface area (15-20%) • Fundamental: O_2-free conditions • Doubled ΔH: 7→17 kJ/mol (zero coverage), 6→10 kJ/mol (high coverage) • Increased excess adsorption by 40% at RT, 200 bar

Table 1.2. Tasks, milestones, and achievement of milestones for Phase 2, according to modified SOPO, 1/28/2013, and later modifications. Colors and abbreviations as in Table 1.1.

Task	Milestones	Achieved	Comments
4.0—Manufacture, characterize, and optimize B-doped monoliths	• Establish effective deoxygenation of materials before doping • Establish uniform [B] in doped materials • Establish [B_{B-C}] limit for complete substitution of B in carbon lattice	• Best result, T = 800 ºC: [O]: 8→4 at% (XPS) Σ: 2700→2500 m^2/g • TEM/EFTEM: [B] uniform over ≥200 nm laterally & ≥1 nm vertically • From [B] = 0–15 wt% (1-step stationary doping) and XPS: [B_{B-C}] = 0–1.7 wt% [B_{B-C}] ~ 0.13 [B]	• [O]↓ yields [B_{B-C}]↑; T↑ yields [O]↓ & Σ↓; but T = 1200 ºC: [B_{B-O}]/[B]: 60→10 at% (good) Σ: 2700→2300 m^2/g (too low) • Uniform [B] confirmed also by TEM-EELS • Observed maximum [B_{B-C}] = 1.7 wt% agrees with theoretical prediction that sp^2-bonded B forms only below solubility limit, 2.1 wt%, of B in C. [B_{B-C}]/[B] ~ 0.13: 1 in 7–8 B atoms are sp^2-bonded

	Establish ΔH at zero coverage & 77 K from Henry's law	From [B] = 0–10 wt%, observation of Henry's law at 77 K, 87 K, n_{st} = 0–0.002 wt% or higher: ΔH = 7.1–9.6 kJ/mol $\Delta H \sim (7.1 + 0.31\ [B]/wt\%)$ kJ/mol $\Delta H \sim (7.1 + 2.4\ [B_{B-C}]/wt\%)$ kJ/mol	– Added 1/29/2014, redirection by DOE – ΔH from Clausius-Clapeyron relation applied to observed Henry's law regime (low coverage) – ΔH vs. [B] and $[B_{B-C}]$ represents best fit to the experimental data
	Establish B-doped powders with ΔH > 12 kJ/mol, $[B_{B-C}]$ > 10 wt%	Best result, U. Missouri powder 5K-0215: ΔH = 9.6 kJ/mol at $[B_{B-C}]$ = 1.7 wt%	
	Establish uniform [B] in doped monoliths	In U. Missouri monoliths: – [B] = 5–15 wt% – Δ[B]/Δr = 1–4 wt%/cm – Uniform [B] up to 1 cm	– Discontinued 1/29/2014, redirection by DOE – Δ[B]/Δr = radial concentration gradient at periphery of monolith
	B-doped monoliths, $\Sigma \sim 2700\ m^2/g$, ΔH > 10 kJ/mol, • LN, 100 bar: n_{st} > 12 wt% v_{st} > 80 g/L • RT, 100 bar: n_{st} > 5.5 wt% v_{st} > 40 g/L	U. Missouri monolith BR-0311 (B:C = 0%): $\Sigma = 2300\ m^2/g$, ΔH = 5.6 kJ/mol (high coverage) • LN, 190 bar: n_{st} = 9.0 wt% v_{st} = 51 g/L Γ(max) = 20 µg/m^2 • RT, 190 bar: n_{st} = 2.9 wt% v_{st} = 15 g/L Γ(190 bar) = 4 µg/m^2	– Best-performing monolith (highest v_{st}) was undoped monolith BR-0311 – Highlighted in Table 0 – Surface excess concentration Γ (gravimetric excess adsorption/Σ) is figure of merit to predict/project n_{st}, v_{st} for monoliths with variable Σ

1.3 Accomplishments in Terms of Adsorption Metrics

1.3.1 How do gravimetric and volumetric storage capacity depend on surface area, binding energy, and void fraction?

A key instrument to develop and optimize materials for high gravimetric and volumetric storage capacity was to understand how different materials end up in different locations in the "universal storage performance graph," Fig. 1.1. Does a particular sorbent have a high gravimetric but low volumetric capacity because it has a high surface area and high binding, but too high a porosity? If so, by how much would volumetric capacity increase if we managed to reduce porosity at constant surface area and binding energy? By how much would gravimetric capacity decrease? By how much would volumetric capacity increase if we managed to reduce porosity, but would lose surface area in the process? In order to be able to answer such questions we performed the following analysis. The analysis culminates in a grid of "equipotential lines" in the universal storage performance graph, at fixed pressure and temperature, which locates every sorbent uniquely in terms its gravimetric excess adsorption and porosity (void fraction). In fact, the grid allows the user to reverse-engineer any sorbent in terms of excess adsorption and porosity, given the gravimetric and volumetric capacity of the material.

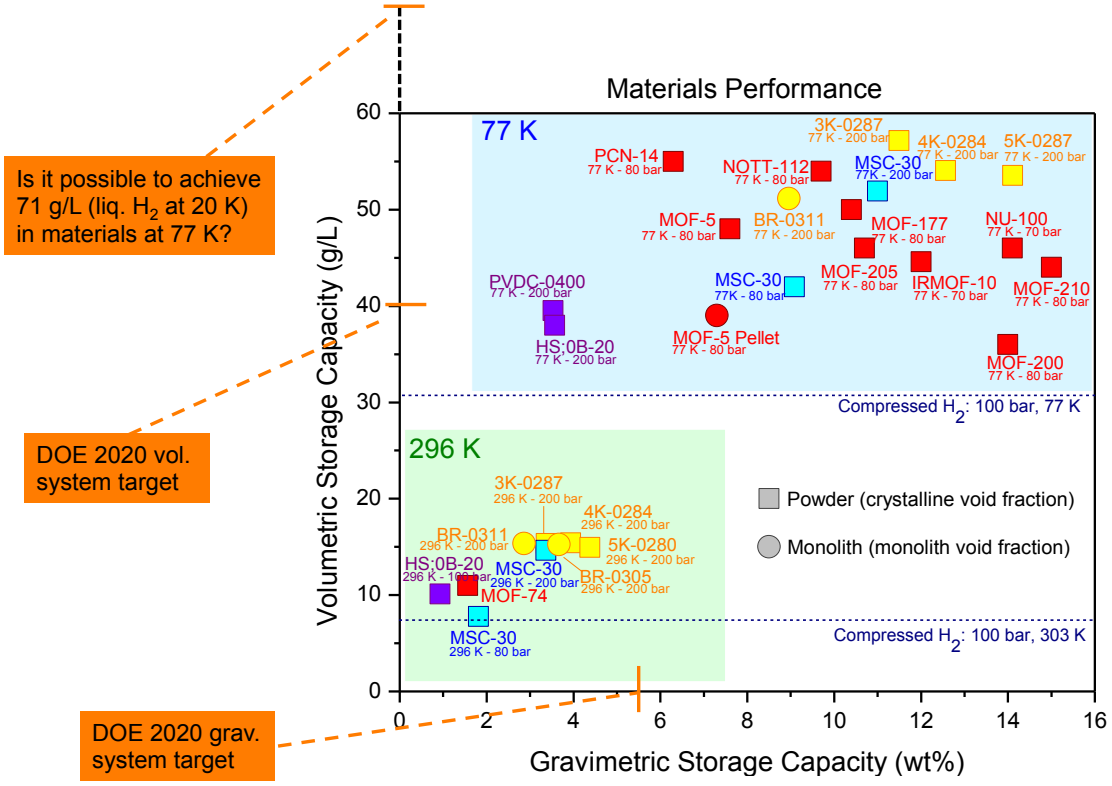

Figure 1.1. "Universal hydrogen storage performance graph:" plot of volumetric vs. gravimetric storage capacity of different materials, here adsorbents, at conditions of interest, here cryogenic temperature (upper right corner) and room temperature (lower left corner). Included are metal-organic frameworks (MOFs, red), select U. Missouri biocarbons (yellow), U. Missouri synthetic carbons (purple), and a commercial carbon (turquoise). Adsorbents are classified as to whether storage capacity refers to individual powder particles ("crystalline void fraction"), which cannot be packed into a tank without interstitial space between adsorbent particles, or to monoliths ("monolith void fraction"), which can be machined and packed into a tank of arbitrary shape without interstitial space. Note that the graph mixes some "apples and oranges" in the sense that not all storage capacities reported are at the same pressure.

Gravimetric storage capacity, G_{st} (total mass of hydrogen stored, adsorbed film and non-adsorbed gas in pores, per mass of solid), and volumetric storage capacity, V_{st} (total mass of hydrogen stored per volume of solid and pore space), were determined from gravimetric excess adsorption, G_{ex} (mass of excess adsorbed H_2 per mass of solid, Fig. 1.2) according to:[1]

$$G_{st}(p,T) = G_{ex}(p,T) + [\rho_{gas}(p,T)/\rho_{skel}]\phi/(1-\phi) \quad (1.1)$$

$$V_{st}(p,T) = G_{st}(p,T)(1-\phi)\rho_{skel} \quad (1.2a)$$

$$= G_{ex}(p,T)(1-\phi)\rho_{skel} + \phi\rho_{gas}(p,T) \quad (1.2b)$$

[1] In these and other formulas, gravimetric quantities (G_{ex}, G_{st}, G_{abs}) are per mass of the sorbent (e.g., kg H_2/kg monolith) for simple conversion to or from volumetric quantities (V_{st}, ...), which are per volume of the sorbent (e.g., kg H_2/L monolith). Formula (1.2a) is a case in point. However, we do report gravimetric quantities in weight % (e.g., kg H_2/(kg monolith + kg H_2)), as defined by the DOE. Tables 1.1-1.2 and Figure 1.1 are cases in point.

In these formulas, ϕ is the porosity or void fraction of the sample ($0 < \phi < 1$),

$$\phi = \frac{V_{\text{pore}}}{V_{\text{solid}} + V_{\text{pore}}} \tag{1.3}$$

with V_{pore} the pore volume or void volume, and V_{solid} the volume occupied by the solid (skeletal volume); ϱ_{skel} is the skeletal density of the adsorbent; ϱ_{gas} is the bulk density of H_2 gas; and p, T are pressure and temperature. Figure 1.2 illustrates the relation between gravimetric excess adsorption, the experimental quantity from which everything else follows, and the two storage capacities, G_{st} and V_{st}, as a function of pressure at constant temperature. Formulas (1.1-1.2) are straightforward consequences of the definitions of G_{ex}, G_{st}, V_{st} [P. Pfeifer *et al*., in: *DOE Hydrogen Program, FY 2009 Annual Progress Report*, ed. S. Satyapal (U.S. Department of Energy, Washington, DC, 2009), p. 646-651]. For example, in formula (1.1), the term

$$\left[\rho_{\text{gas}}/\rho_{\text{skel}}\right]\phi/(1-\phi) = \frac{\rho_{\text{gas}}\phi \times (1\ \text{cm}^3)}{\rho_{\text{skel}}(1-\phi) \times (1\ \text{cm}^3)} \tag{1.4}$$

adds $\rho_{\text{gas}}\,\phi \times (1\ \text{cm}^3)$ grams of H_2—the amount of H_2 gas that would be present in the pore space in the absence of adsorption—per $\rho_{\text{skel}}(1 - \phi) \times (1\ \text{cm}^3)$ grams of adsorbent, to excess adsorption, to account for all hydrogen in the sample. In formula (1.2a), the factor $(1 - \phi)\rho_{\text{skel}}$ is the mass of solid per volume of solid and pore space (bulk density), and thus correctly converts gravimetric storage capacity into volumetric storage capacity by multiplication with the bulk density.[2] Figure 1.2 also previews key adsorbent characteristics that can be deduced from the shape of the excess adsorption isotherm, $G_{\text{ex}}(p)$, including the significance of the pressure p_{max}, at which excess adsorption reaches a maximum.

The decomposition of gravimetric and volumetric storage capacity in terms of gravimetric excess adsorption G_{ex}, porosity ϕ, and skeletal density ρ_{skel} —Eqs. (1.1, 1.2b)—is unique and universal in three distinct ways:

[2] We point out that the pore volume V_{pore} in formula (1.4) is always the volume of the *empty* pore space (degassed or evacuated sample, test bed, tank, ...). This guarantees that the porosity ϕ correctly counts *all* H_2, adsorbed and non-adsorbed, in formulas (1.1-1.2). At variance, it has been suggested that V_{pore} should be the volume of pore space lined with a layer of bound hydrogen, so that V_{pore} counts volume available for free, non-adsorbed hydrogen. This alternate definition of pore volume shifts the Gibbs dividing surface for excess adsorption from the surface of the solid into the adsorption space, and is one of many possible choices of the dividing surface. But it transforms the task of determining the pore volume from a standard operational procedure into complicated questions about the nature and extent of the layer of bound hydrogen, without clear benefits. Our operational method to determine V_{poer}, both for a powder and monolithic adsorbent, is to measure the amount of N_2 adsorbed at 77 K and relative pressure $p/p_0 = 0.995$, at which pressure liquid N_2 fills essentially the entire pore space by capillary condensation. The volume of the solid in (1.3) is determined from $V_{\text{solid}} = m_{\text{solid}}/\rho_{\text{skel}}$, the mass of the solid, m_{solid}, and the skeletal density. If the sorbent is a powder, the void fraction is that in an individual sorbent particle, averaged over many particles, and the bulk density $(1 - \phi)\rho_{\text{skel}}$ equals the envelope density of the particle. For most carbon powders in this project, undoped and doped, $\rho_{\text{skel}} = 2.00 \pm 0.03$ g/cm^3 as determined from He pycnometry. Typical values for U. Missouri carbon monoliths are $\rho_{\text{skel}} = 2.03 \pm 0.03$ g/cm^3, also from He pycnometry.

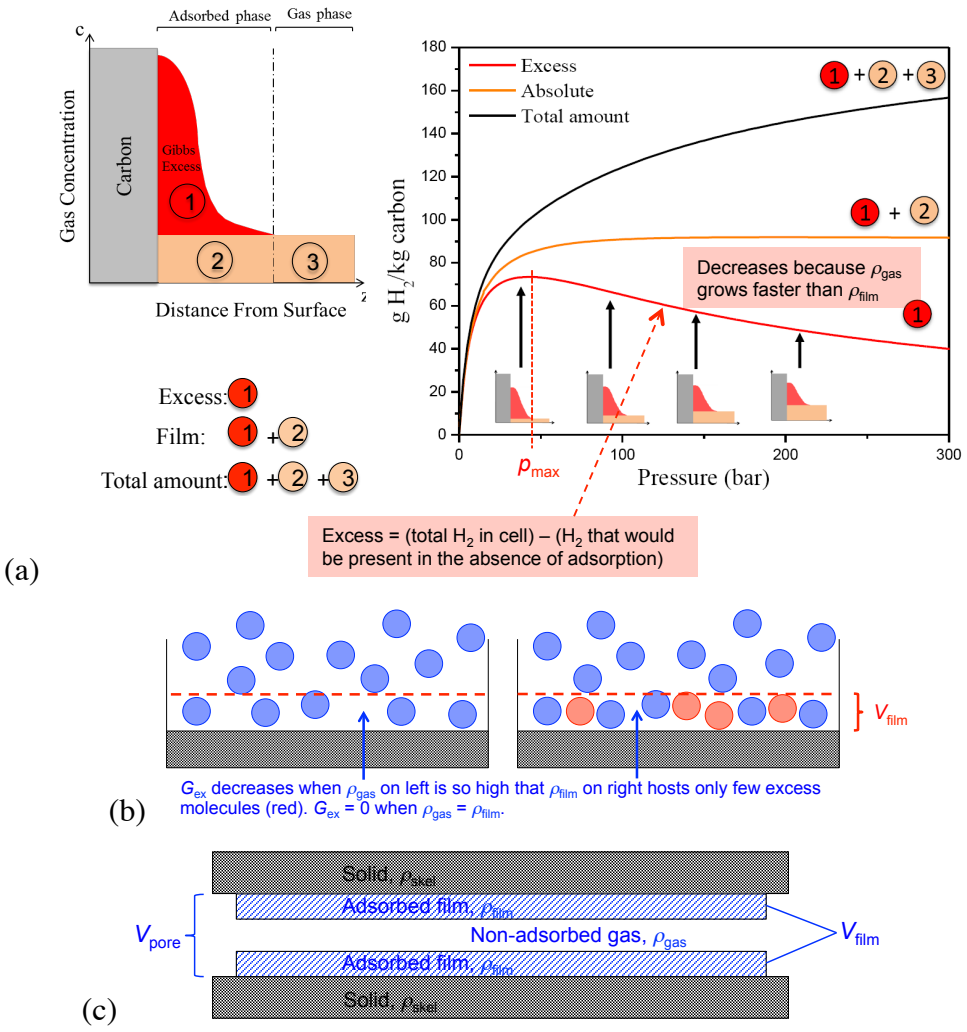

Figure 1.2. (a) Gravimetric excess adsorption, $G_{ex}(p)$, and gravimetric storage capacity, $G_{st}(p)$ ("total amount"), as a function of gas pressure p at $T = 77$ K, on a typical high-surface-area carbon (graph courtesy J. Romanos, 2012). Volumetric storage capacity $V_{st}(p)$ is proportional to $G_{st}(p)$ by Eq. (1.2a), since bulk density, $(1 - \phi)\rho_{skel}$, is independent of pressure and temperature for all practical purposes. Also shown is absolute adsorption, the mass of the adsorbed film, $m_{film} = m_{ex} + V_{film}\rho_{gas}$, per mass of adsorbent. It levels off at the mass of the saturated film per mass of sorbent as p grows without bound. (b) Illustration why G_{ex}, the difference between H_2 molecules on the right and on the left, increases at low p, goes through a maximum at p_{max}, and decreases at $p > p_{max}$. At $p = p_{max}$, the film density begins to grow more slowly than the gas density. So:

- G_{ex} rises fast/slow if binding energy E_b is high/low
- p_{max} is low/high if E_b is high/low
- $p = p_{max}$ signals the onset of saturation of the film
- Maximum $G_{ex}(p_{max})$ is low/high if specific surface Σ area is low/high
- At fixed Σ, G_{ex} drops fast/slow if saturated film density is low/high

(c) Two-fluid model in a pore of volume V_{pore}. The adsorbed film, with density ρ_{film}, occupies a volume of V_{film}. Non-adsorbed gas, with density ρ_{gas}, occupies the volume $V_{pore} - V_{film}$.

(i) The quantities G_{ex}, ϕ, ρ_{skel} are intrinsically independent, directly measurable variables. Gravimetric excess adsorption depends only on the surface area (Σ) and binding energies (E_b, "chemistry") of the adsorbent, but not on porosity, pore volume, or the nature and structure of the pore space (Fig. 1.2).[3] Porosity describes the fraction of void space surrounding the adsorbent (void space in pores and sample cell), regardless of the chemical and surface structure of adsorbent. The skeletal density controls the volume occupied by the adsorbent in the absence of adsorption.

(ii) If the volume surrounding the adsorbent, such as in a test bed or tank packed with adsorbent, is included in the void volume and ϕ is evaluated accordingly, Eqs. (1.1-1.3) automatically give the capacities of the bed. Thus Eqs. (1.1-1.3) are universal—not restricted to any particular geometry of the void space in or surrounding the sorbent. For a particulate sorbent (powder, granular, …), the two void fractions of principal interest were [P. Pfeifer *et al*., in: *DOE Hydrogen and Fuel Cells Program, 2012 Annual Progress Report*, ed. S. Satyapal (U.S. Department of Energy, Washington, DC, 2012), p. IV-(72-77)]:

- *Void fraction in individual sorbent particles*, ϕ_{cryst}, which we refer to as "crystalline" in analogy to the void fraction in MOFs, zeolites, and other porous solids; occasionally we also use the term "envelope," "intraparticle," or "intragranular" void fraction or porosity.
- *Void fraction after packing of sorbent particles in a bed or tank*, ϕ_{tank}, which depends on the packing fraction, f ($0 < f < 1$; fraction of tank volume that is occupied by particles), and on ϕ_{cryst} through

$$\phi_{tank} = (1 - f) + f \cdot \phi_{cryst}, \tag{1.5}$$

where $1 - f$ is the void fraction due to the interstitial volume between particles, and $f \cdot \phi_{cryst}$ is the void fraction hosted by the particles Formula (1.5) shows that $\phi_{tank} > \phi_{cryst}$ for all f, and that ϕ_{tank} approaches ϕ_{cryst} as f approaches 1 (monolith limit). The limit $f = 1$ amounts to a monolith made of particles packed with zero interstitial volume (e.g., binderless stack of cubic particles); alternatively, $f = 1$ may be interpreted as one large particle/monolith with void fraction ϕ_{cryst} filling the entire tank. In both cases, $\phi_{tank} = \phi_{cryst}$. An analysis of storage capacity with variable packing is reported in Section 5.

(iii) Formulas (1.1, 1.2) are universal structure-function relations for hydrogen storage, which predict gravimetric and volumetric storage capacity ("function") under variable design/control parameters—G_{ex}, ϕ, ρ_{skel}, ρ_{gas} ("structure").[4] For ease of analysis, we repeat them in the form

$$G_{st} = G_{ex} + (\rho_{gas}/\rho_{skel})(\phi^{-1} - 1)^{-1} \tag{1.6}$$
$$V_{st} = G_{ex} \cdot (1 - \phi)\rho_{skel} + \phi\rho_{gas} \tag{1.7}$$

They lead to the following "storage vs. porosity" upward or downward inequalities, as ϕ decreases and G_{ex}, ρ_{skel}, ρ_{gas} are held constant: Gravimetric storage capacity, G_{st}, universally

[3] The circumstance that binding energies may depend on pore structure, most prominently in narrow, sub-nm pores where overlapping van der Waals potentials from opposite pore walls create deep potential wells [1], is classified as a property of the adsorbent ("chemistry"), not of the pore space.

[4] Section 1.3.3 will report a structure-function relation for V_{st}, in which the structure variables G_{ex} and ϕ in formula (1.7) are deduced from microscopic input: pore-size distribution, thickness of the adsorbed film, and density of the adsorbed film.

decreases. This is because narrow pores store less non-adsorbed gas than wide pores between otherwise fixed pore walls (Fig. 1.2c). Volumetric storage capacity V_{st} increases if $G_{ex} > \rho_{gas}/\rho_{skel}$ ("good sorbent") and decreases if $G_{ex} < \rho_{gas}/\rho_{skel}$ ("poor sorbent"), at the conditions selected.[5] V_{st} increases when in narrow pores low-density non-adsorbed gas is traded for a high-density adsorbed film (Fig. 1.2c), and it decreases when a high-density film on a pore wall stores less than an equal volume (film + wall) of high-density gas without wall would store.

Early DOE-sponsored work in hydrogen storage placed a premium on high gravimetric storage capacity. The push for high volumetric capacity by reduction of porosity—at the price of lower gravimetric capacity—as stipulated in the preceding paragraph, came relatively late: "*What was less noticed [is that] the volumetric storage density is an important factor for mobile storage applications. ... The most efficient material candidates are the ones with the highest surface area per unit volume. ... Even with no loss of specific surface area and micropore volume [during densification, packing], the volumetric enhancement by packing is done at the cost of gravimetric capacity, system cost, and net delivery*" [R. Chahine, *DOE Hydrogen Storage Principal Investigator/Contractor Meeting*, Washington, DC, November 27-28, 2012]. So it is of interest to record that the U. Missouri had developed a framework, based on Eqs. (1.6, 1.7), to investigate competing targets—high volumetric capacity under low loss of gravimetric capacity—as early as in 2009 (Fig. 1.3), as follows.

The structure parameters to design and track materials via relations (1.6, 1.7) in the U. Missouri project were G_{ex} and ϕ. By eliminating one or the other of the two parameters between the two equations and solving the resulting single equation for V_{st}, one obtains two sets of curves—one for V_{st} vs. G_{st} at constant G_{ex} (elimination of ϕ), and the other for V_{st} vs. G_{st} at constant ϕ (elimination of G_{ex}). The curves are, written in analogy to conditional probabilities:[6]

$$V_{st}(G_{st}|G_{ex}) = \frac{\rho_{gas}}{1-(G_{ex}-\rho_{gas}/\rho_{skel})/G_{st}} \quad (G_{st} \geq G_{ex}) \tag{1.8}$$
$$= V_{st} \text{ vs. } G_{st} \text{ at constant } G_{ex}, \rho_{skel}, \rho_{gas}$$
$$= \text{equi/iso-}(G_{ex}, \rho_{skel}, \rho_{gas}) \text{ curves along which } \phi \text{ varies}$$

$$V_{st}(G_{st}|\phi) = (1-\phi)\rho_{skel}G_{st} \cdot \tag{1.9}$$
$$= V_{st} \text{ vs. } G_{st} \text{ at constant } \phi, \rho_{skel}, \rho_{gas}$$
$$= \text{equi/iso-}(\phi, \rho_{skel}, \rho_{gas}) \text{ curves along which } G_{ex} \text{ varies}$$

The curves are hyperbolas and straight lines, respectively (Figs. 1.3-1.5). For introductory purposes, we first consider the case of constant G_{ex} and variable ϕ. Figure 1.3 shows early U. Missouri (G_{st}, V_{st}) data plotted together with nearby lines of V_{st} vs. G_{st} at constant G_{ex}. The take-home message is: (i) As a result of the steep rise of V_{st} as G_{st} decreases from right to left,

[5] By this classification, every adsorbent is a good sorbent at sufficiently low pressure (low ρ_{gas}). Most U. Missouri sorbents are good sorbents up to pressures of 200 bar or higher and T = 77 K – 300 K (Figs. 1.4-1.5). The classification 'good'/'poor' is in 1-1-correspondence with the question whether storage by adsorption outperforms storage by compression. See Eq. (1.24), Fig. (1.7) below, including estimates of the pressure p^* above which the sorbent turns poor.

[6] $P(A|B)$ = probability of A under the condition B.

volumetric storage capacity increases strongly and gravimetric storage capacity decreases weakly, under reduction of porosity at a high value of G_{ex}. (ii) High values of G_{ex} in Fig. 1.3 come from high specific surface areas, Σ = 2500–3400 m^2/g, and/or high binding energies, E_b = 5–12 kJ/mol from boron doping. The principal ways of reducing porosity in the U. Missouri project were: nanopore engineering (Sect. 2); fabrication of monolith materials (Sect. 4); compaction of adsorbent in a 5.3-liter tank (Sect. 5); and fabrication of synthetic carbons (Sect. 8).

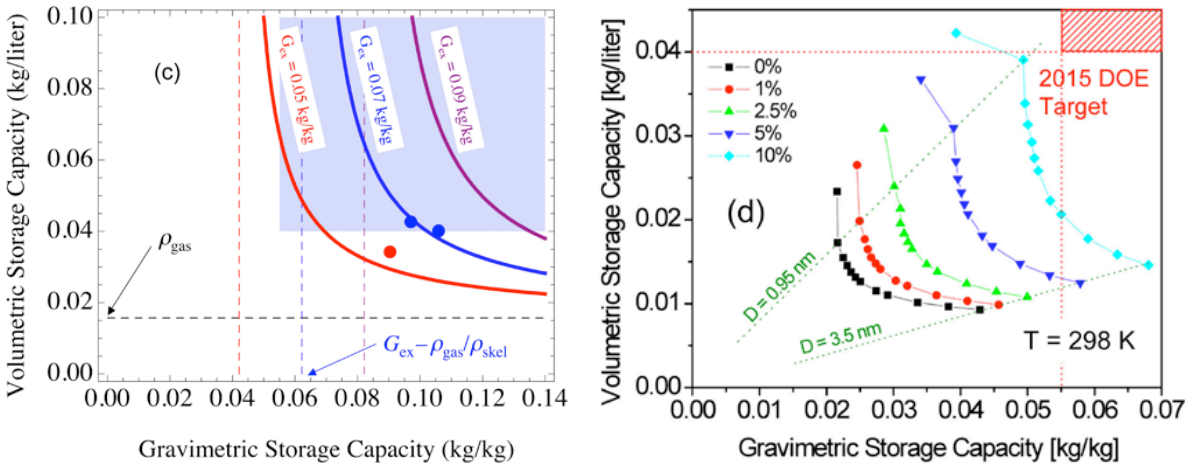

Figure 1.3. Figures reproduced from P. Pfeifer *et al.*, in: *DOE Hydrogen Program, FY 2009 Annual Progress Report*, ed. S. Satyapal (U.S. Department of Energy, Washington, DC, 2009), p. 646-651]. *Left*: Gravimetric and volumetric hydrogen storage capacity of commercial carbon MSC-30 (red dot) and U. Missouri carbons 3K and 4K (blue dots) at T = 80 K and p = 50 bar. The curves are plots of volumetric storage capacity vs. gravimetric storage capacity at constant gravimetric excess adsorption, $V_{st}(G_{st}|G_{ex})$, evaluated at 80 K, 50 bar [ρ_{gas} = 0.016 g/cm^3], and ρ_{skel} = 2.0 g/cm^3. Large/small values of G_{st} correspond to high/low porosity at fixed G_{ex}, Eq. (1.6). So V_{st} rises with decreasing G_{st} because decreasing porosity raises V_{st}, Eq. (1.7), for a good sorbent. Thus the hyperbolas $V_{st}(G_{st}|G_{ex})$, as we move from right to left, show how V_{st} and G_{st} vary with decreasing ϕ at fixed G_{ex}: G_{st} slowly decreases, and V_{st} rapidly increases. Each hyperbola ends when the porosity nominally reaches zero, i.e., at the abscissa $G_{st} = G_{ex}$.. But the porosity in the three samples was ϕ = 0.78–0.81, far from small. So the steep rise of the curves $V_{st}(G_{st}|G_{ex}$ = 0.07 kg/kg) and $V_{st}(G_{st}|G_{ex}$ = 0.05 kg/kg) to the left of the experimental data points shows that if the porosity can be reduced below 0.8, V_{st} increases strongly and G_{st} decreases weakly. In order for G_{ex} to remain constant, the specific surface area Σ must remain constant, or, if Σ drops, the binding energy E_b must increase. — *Right*: Increase in binding energy E_b by boron doping at constant Σ. The five curves show volumetric and gravimetric storage capacities of boron-substituted carbons at T = 298 K and p = 100 bar, as a function of pore width (variable ϕ), for five different boron concentrations. Increasing boron concentrations create $V_{st}(G_{st}|G_{ex})$ curves with increasing values for G_{ex} by increasing the binding energies on the surface, E_b ~ 5–12 kJ/mol, from left to right. Straight lines corresponding to $V_{st}(G_{st}|\phi)$, Eq. (1.9), are labeled by pore width, D. The data were from grand-canonical Monte Carlo simulations carried out on boron-doped carbons by collaborators of the U. Missouri team (L. Firlej *et al.*, *J. Chem. Phys.* **131**, 164702 (2009); B. Kuchta *et al.*, *Carbon* **48**, 223-231 (2010)).

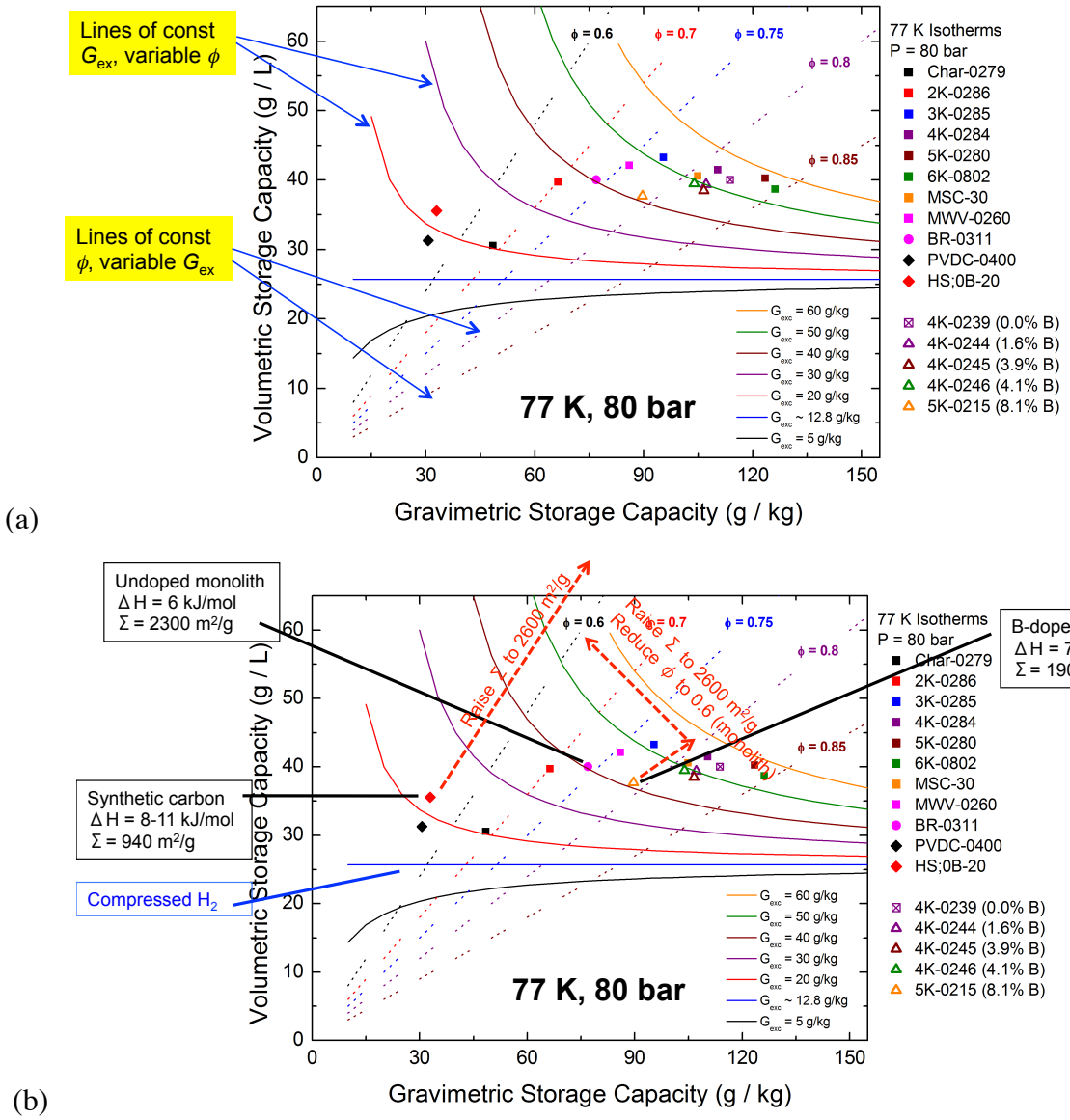

Figure 1.4. (a) Volumetric and gravimetric storage capacities of U. Missouri carbons at $T = 77$ K and $p = 80$ bar, located on the grid of lines $V_{st}(G_{st}|G_{ex})$ (hyperbolas, constant gravimetric excess adsorption) and $V_{st}(G_{st}|\phi)$ (straight lines, constant porosity) generated by Eqs. (1.8, 1.9), for ρ_{skel} = 2.0 g/cm^3 and ρ_{gas}(80 bar) = 26 g/L. Samples are powders, except BR-0311, which is a monolith. Porosities are intraparticle porosity, ϕ_{cryst}, but for the monolith it may also be interpreted as tank porosity, $\phi_{tank} = \phi_{cryst}$. Samples range from ($G_{ex}$, ϕ) = (23 g/kg, 0.46) at the left to (G_{ex}, ϕ) = (55 g/kg, 0.85) at the right. Samples from left to right progress from low to high specific surface area Σ, low to high G_{ex}, and low to high porosity. The U. Missouri boron-doped carbon 4K-0246 and commercial activated carbon MSC-30 perform nearly identically in terms of G_{ex}, ϕ, G_{st}, V_{st}, but have Σ = 2400 and 2700 m^2/g, respectively. This shows entirely in terms of adsorption metrics, without reference to binding energies, that boron doping enhances adsorption. The highest volumetric storage capacity in the graph is 43 g/L for 3K-0285, which nominally meets the 2020 DOE target at an unexpectedly low pressure. — (b) Pathways to convert two high-binding-energy carbons into low-ϕ, high-Σ materials with $V_{st} > 60$ g/L.

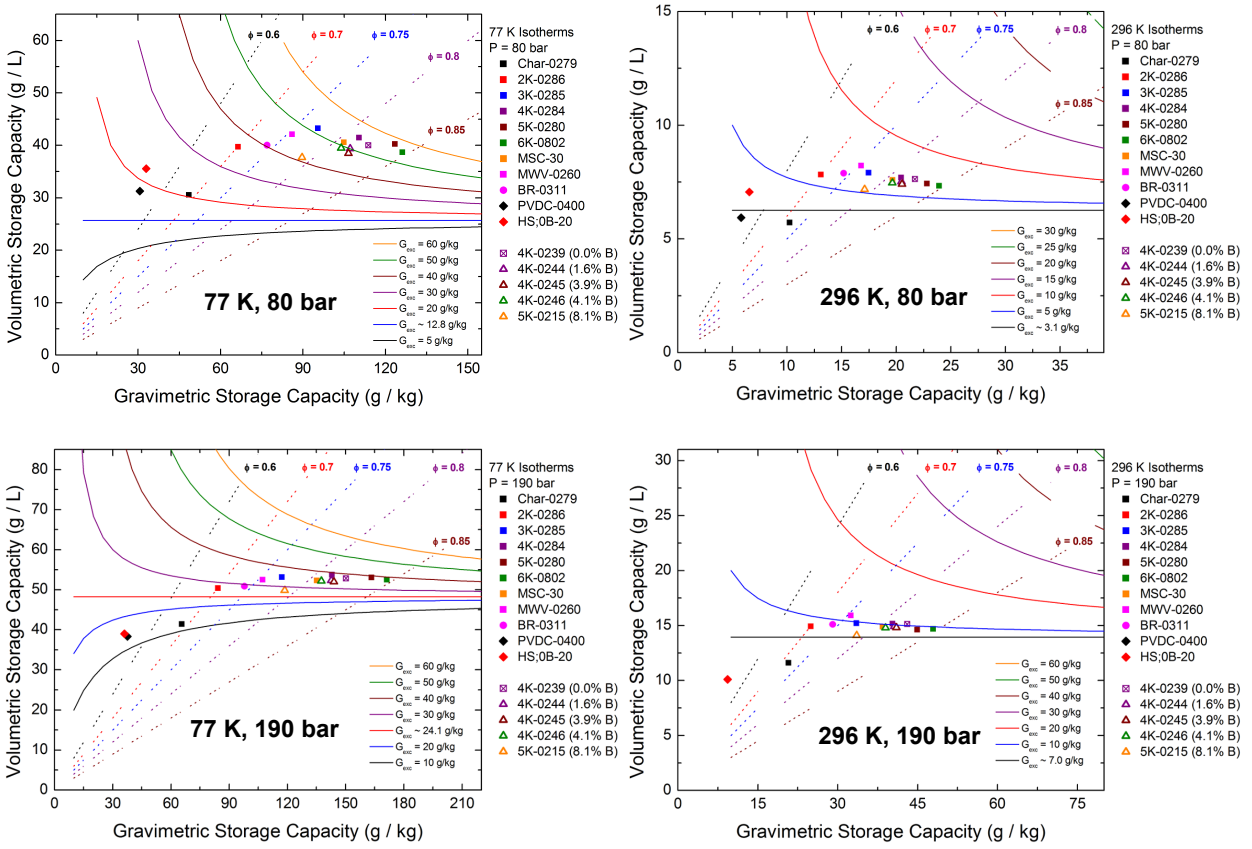

Figure 1.5. Storage performance of the materials in Fig. 1.4, in terms of the (G_{ex}, ϕ) coordinates, at cryogenic temperature and two different pressures (left), and at room temperature and same two pressures (right). Volumetric storage capacities increase with increasing pressure, but the difference between V_{st} and ρ_{gas} (horizontal line in each graph) decreases when the density of the adsorbed film grows more slowly than the gas density. (The onset of slow growth occurs at $p = p_{max}$ (Fig. 1.2), which is $p_{max} \sim 50$ bar for the high-G_{ex} samples and $p_{max} \sim 20$ bar for the low-G_{ex} samples at 77 K in the figure.) E.g., for 3K-0285 at 77 K ("winner at 77 K and 80 bar"), the ratio V_{st}/ρ_{gas} drops from 1.7 at 80 bar to 1.1 at 190 bar. For MWV-0260 at 296 K ("winner at 296 K and 80 bar"), the ratio V_{st}/ρ_{gas} drops from 1.3 to 1.1 between the two pressures. While each of the four G_{st}, V_{st} diagrams has its fixed set of equi-G_{ex} lines, $V_{st}(G_{st}|G_{ex})$, the experimental data points (G_{st}, V_{st}) "move all over the place" as pressure and temperature change because the G_{ex}-values of the samples depend on p, T. This is how the "winner at p, T" may no longer be the winner at p', T'. In contrast, the experimental data points remain on the same equi-ϕ lines, $V_{st}(G_{st}|\phi)$, because the porosity and skeletal density of a sample does not change with p, T.

The two sets of curves—hyperbolas $V_{st}(G_{st}|G_{ex})$ at constant G_{ex} and straight lines $V_{st}(G_{st}|\phi)$ at constant ϕ—are plotted in Figs. 1.4 and 1.5. Together, they generate the grid of "equipotential lines" or curvilinear coordinates in the universal storage performance graph, Fig. 1.1, that was advertised. They identify every sorbent uniquely in terms of the coordinate pair (G_{ex}, ϕ). The straight lines, Eq. (1.9) represent, of course, the proportionality between volumetric and gravimetric storage capacity, Eq. (1.2a), with the proportionality factor equal to bulk density,

$(1 - \phi)\rho_{skel}$. But here, in the storage performance graphs, when intersected with an equi-G_{ex} line $V_{st}(G_{st}|G_{ex})$, they show by how much porosity needs to be reduced in order to go from a low-V_{st} material to a high-V_{st} material. Or, a single straight line $V_{st}(G_{st}|\phi)$, when passing through several equi-G_{ex} lines, shows by how much the specific surface area Σ or the binding energy E_b needs to increase (so as to generate an increase in G_{ex}), in order to go from a low low-V_{st} material to a high-V_{st} material at constant ϕ.

Such pathways to high-V_{st} materials are indicated in Fig. 1.4b. In the case of the synthetic carbon HS;0B-20, with monodisperse pores of width 0.7-nm and binding energies E_b = 8–11 kJ/mol (Sect. 8),[7] the pathway from existing Σ = 940 m^2/g to a target of Σ = 2600 m^2/g is along constant ϕ.[8] In the case of boron-doped carbon 5K-0215, with Σ = 1900 m^2/g, E_b = 7–10 kJ/mol, ϕ = 0.79, the pathway to the target (Σ = 2600 m^2/g, ϕ = 0.6) is to first raise Σ along constant ϕ, and then reduce ϕ by monolith fabrication.

Figures 1.4, 1.5 also include volumetric storage curves $V_{st}(G_{st}|G_{ex})$ for poor sorbents, $G_{ex} < \rho_{gas}/\rho_{skel}$. These are hyperbolas that curve downward and lie below the horizontal line $V_{st} = \rho_{gas}$. Along a downward hyperbola, V_{st} decreases with decreasing ϕ as we move from right to left. Thus good/poor adsorbents lie on hyperbolas that curve upward/downward and lie above/below the horizontal line $V_{st} = \rho_{gas}$. The line $V_{st} = \rho_{gas}$ not only separates good and poor adsorbents, but the difference $V_{st}(G_{st}|G_{ex}) - \rho_{gas}$ is a direct measure by how much a good adsorbent outperforms storage by compression, or a poor adsorbent underperforms storage by compression. In fact, the storage pressure p = 80 bar at 77 K in Fig. 1.4 was selected to display "adsorptive storage at its best." At 80 bar and 77 K, the relative difference, density ratio, and values of V_{st}, G_{st},

$$[V_{st}(G_{st}|G_{ex}) - \rho_{gas}]/\rho_{gas} = 0.65 \quad (1.10)$$
$$V_{st}(G_{st}|G_{ex})/\rho_{gas} = 1.7 \text{ (close to "2×")} \quad (1.11)$$
$$V_{st}(G_{st}|G_{ex}) = 43 \text{ g/L (nominally meets the 2020 DOE target)} \quad (1.12)$$
$$G_{st} = 95 \text{ g/kg ("8.7 wt\%)} \quad (1.13)$$
$$V_{st}(G_{st}|G_{ex})/[\rho_{gas}(296 \text{ K}, 700 \text{ bar})] = 1.1 \text{ (competitive with room-temperature compressed } H_2 \text{ at 700 bar)} \quad (1.14)$$

respectively (evaluated for sample 3K-0285), are near optimum because on most U. Missouri adsorbents at 77 K the adsorbed film saturates around 70-80 bar. Higher pressures only serve to compress non-adsorbed gas, but do not increase the film density, so outperformance of adsorption over compression diminishes. Lower pressures would, of course, make the ratios (1.10, 1.11) even larger because adsorption outperforms compression most effectively at low pressure, but the lower storage capacities would not be competitive. For the hypothetical material targeted by the "boron-doped pathway in Fig. 1.4b," the enhancement over (1.10-1.14), also at 80 bar and 77 K, would be

$$[V_{st}(G_{st}|G_{ex}) - \rho_{gas}]/\rho_{gas} = 1.3 \quad (1.15)$$
$$V_{st}(G_{st}|G_{ex})/\rho_{gas} = 2.3 \quad (1.16)$$

[7] In this discussion, we equate measured isosteric heats, ΔH, to binding energies, E_b.
[8] An effort was undertaken to implement this pathway experimentally by controlled exfoliation and sonication of HS;0B-20. But the results were disappointing.

$V_{st}(G_{st}|G_{ex}) = 60$ g/L (1.17)
$G_{st} = 75$ g/kg ("7.0 wt%) (1.18)
$V_{st}(G_{st}|G_{ex})/[\rho_{gas}(296\text{ K}, 700\text{ bar})] = 1.5$ (1.19)

Take-home message from Fig. 1.4 and results (1.10-1.19): (i) Adsorbed H_2 on U. Missouri carbons at 80 bar and 77 K outperforms cryogenic compressed H_2 (same temperature and pressure) by nearly a factor two, and is competitive with room-temperature compressed H_2 at 700 bar by way of 10 times lower pressure, thinner vessel walls, and lower compression costs. (ii) Adsorbed H_2 on U. Missouri carbons at 80 bar and 77 K nominally meet the 2020 DOE volumetric storage target. (iii) Pathways have been identified to increase volumetric storage at 80 bar and 77 K by 50%, to 60 g/L.

Figure 1.5 reports and compares storage performance in the "pressure-temperature matrix," which samples low/high pressure and low/high temperature:

$$\begin{pmatrix} 77\text{ K}, 80\text{ bar} & 296\text{ K}, 80\text{ bar} \\ 77\text{ K}, 190\text{ bar} & 296\text{ K}, 190\text{ bar} \end{pmatrix} \quad (1.20)$$

It shows that a few low-Σ materials turn from good to poor sorbents at high pressure; that the V_{st} values of good sorbents get pushed close to the $V_{st} = \rho_{gas}$ line at high pressure, as expected; that the differences $V_{st} - \rho_{gas}$ (advantage of adsorption over compression) accordingly decrease at high pressure; and that the decrease is most pronounced when G_{ex} is low. However, storage capacities V_{st} do significantly increase (even by a factor two at room temperature), and density ratios V_{st}/ρ_{gas} remain respectable:

$$V_{st} = \begin{pmatrix} 43\text{ g/L} & 8.3\text{ g/L} \\ 53\text{ g/L} & 16\text{ g/L} \end{pmatrix} \quad (1,21)$$

$$V_{st}/\rho_{gas} = \begin{pmatrix} 1.7 & 1.3 \\ 1.1 & 1.1 \end{pmatrix} \quad (1.22)$$

We consider it remarkable that at room temperature, 296 K, where adsorption is much weaker than at 77 K, the density V_{st}/ρ_{gas} is as high as 1.3 at 80 bar. It suggests that 80 bar may be an attractive operating pressure for an adsorbed H_2 tank both at 77 K and 296 K.

We conclude this survey of adsorbents in terms of storage capacities with a table of best-performing U. Missouri carbons (Table 1.3), from which many of the materials in Figs. 1.4 and 1.5 were taken.

We turn to the question under what conditions H_2 storage by adsorption outperforms H_2 storage by compression, i.e., up to what pressure p^* will density ratios $V_{st}/\rho_{gas} > 1$, such as in Eq. (1.22), prevail, and when does compression win, $V_{st}/\rho_{gas} < 1$? An often-used approach to address the question is shown in Fig. 1.6. It requires that volumetric storage capacity isotherms have been measured to very high pressures, in Fig. 1.6 to 350 bar, and that the intersection of nearly parallel isotherms, $V_{st}(p)$ and $\rho_{gas}(p)$, can be determined accurately. Equality of the two, $V_{st}(p^*) = \rho_{gas}(p^*)$, gives p^*. The approach also begs the question whether p^* determined in this way depends on

Table 1.3. Best performing, reproducible U. Missouri carbons 2013-14 (undoped, doped, powders, and monoliths) at liquid-nitrogen temperature (77 K) and room temperature (296 K), high-lighted in yellow. Performance metrics are: gravimetric storage capacity, G_{st}; volumetric storage capacity, V_{st}; binding energy, E_B; and enthalpy of adsorption, ΔH. Specific surface areas, Σ, and void fractions, ϕ, are from N_2 adsorption at 77 K. Gravimetric and volumetric storage capacities are calculated from experimental gravimetric excess adsorption, G_{ex}, and void fraction according to Eqs. (1.6, 1.7). Void fraction is related to bulk density by $\rho_{bulk} = (1 - \phi)\, \rho_{skel}$, where the skeletal density is 2.0 g/cm^3 for University of Missouri carbons. The reported maximum values of gravimetric excess adsorption, Max. G_{ex}, are for the pressure interval 0-190 bar. The maximum occurs at 40-50 bar for 77 K, and at 190 bar for 296 K.

	Sample	Σ (m^2/g)	ϕ	Max. G_{ex} (wt%)	G_{st} (wt%)	V_{st} (g/L)	ΔH, E_b (kJ / mol)
Nanoporous Graphene-like Carbons	5K-0280 (77 K, 190 bar) (296 K, 190 bar)	2700	0.84	5.9 0.9	14 4.4	54 15	5.8, N/A
	4K-0284 (77 K, 190 bar) (296 K, 190 bar)	2600	0.81	5.6 1.0	13 3.9	54 15	4.7, N/A
B-Doped Graphene-like Carbons	4K-0246 (B=4%) (77 K, 190 bar) (296 K, 190 bar)	2400	0.81	5.1 0.9	12 3.8	52 15	5.5, 7.5
	5K-0215 (B=8%) (77 K, 190 bar) (296 K, 190 bar)	1900	0.79	4.3 0.7	11 3.3	50 14	6.2, 9.2
Synthetic Nanoporous Carbons	HS;0B-20 (77 K, 190 bar)	940	0.46	2.5	3.5	40	6.6, 9.4
	PVDC-0400 (77 K, 190 bar)	780	0.49	2.0	3.7	28	7.8, 10.8
Monoliths	4K Monolith (297 K, 100 bar)	2100		0.9	2.5	9.5	-
	BR-0311 (77 K, 190 bar) (296 K, 190 bar)	2300	0.74	4.3 0.9	9.0 2.9	51 15	5.6, N/A
Commercial Carbon	MSC-30 (77 K, 190 bar) (296 K, 190 bar)	2700	0.80	5.3 0.9	12 3.6	53 15	5.0, N/A

packing of the adsorbent in the tank, i.e., on the void fraction ϕ used to calculate $V_{st.}$. We determined p^* alternatively as follows. We start with the inequality $V_{st} > \rho_{gas}$ ("adsorption outperforms compression," "good adsorbent"), substitute Eq. (1.6) into the left-hand side, and solve for G_{ex}:

$$G_{ex}\cdot(1-\phi)\rho_{skel} + \phi\rho_{gas} > \rho_{gas} \quad (1.23)$$

$$G_{ex} > \rho_{gas}/\rho_{skel} \quad (1.24)$$

$$G_{ex}(p^*) = \rho_{gas}(p^*)/\rho_{ske} \quad (1.25)$$

Thus we intersect G_{ex} with ρ_{gas}/ρ_{skel}, which in a G_{ex} vs. ρ_{gas} plot amounts to intersecting two straight lines at nearly a right angle—Fig. 1.7. The result for 3K-0285 at 77 K is $p^* = 280$ bar. Since conditions (1.24, 1.25) do not depend on ϕ, neither does p^*. So, remarkably, all $V_{st}(p)$ curves with identical $G_{ex}(p)$ but different ϕ must intersect $\rho_{gas}(p)$ at the same pressure, p^*.

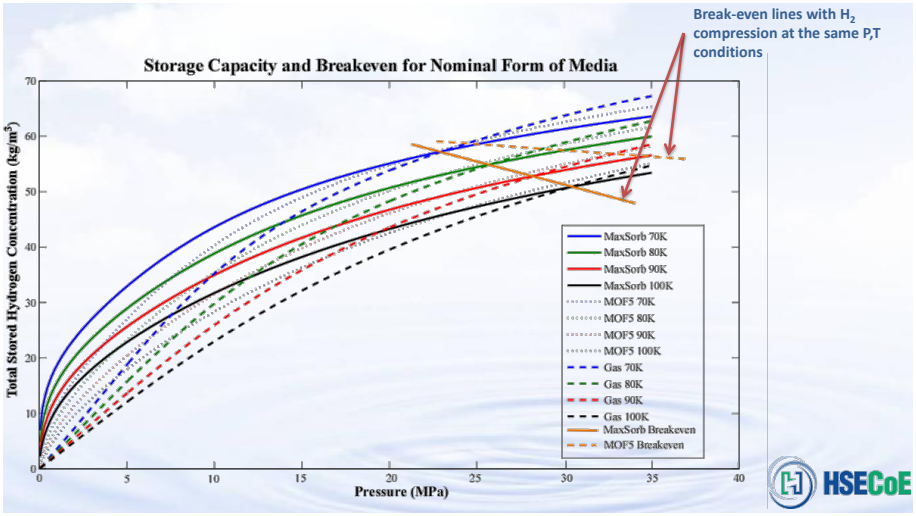

Figure 1.6. Intersection of volumetric storage capacity, $V_{st}(p)$, and gas density, $\rho_{gas}(p)$. The two intersect at pressure p^* (break-even point in figure), above which $\rho_{gas}(p) > V_{st}(p)$. For Maxsorb at $T = 80$ K, from figure: $p^* \sim 250$ bar. From: R. Chahine, *DOE Hydrogen Storage Principal Investigator/Contractor Meeting*, Washington, DC, November 27-28, 2012.

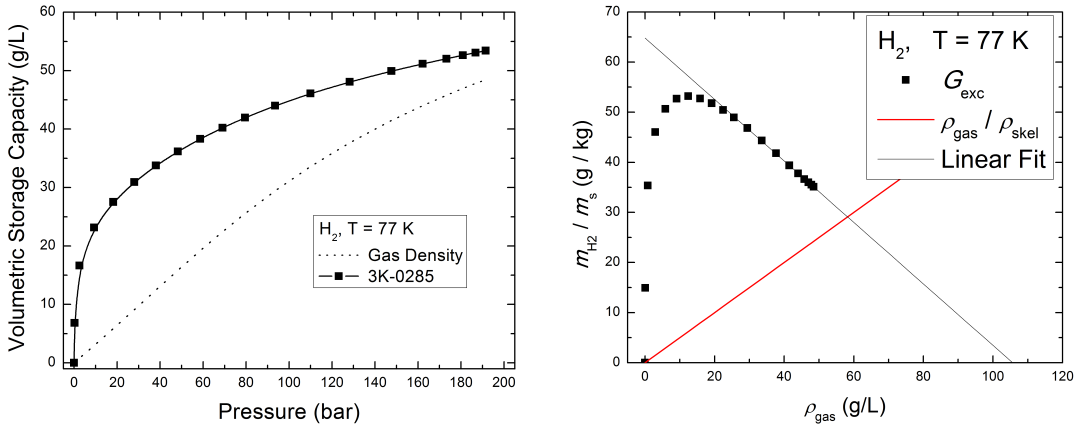

Figure 1.7. *Left:* $V_{st}(p)$ for U. Missouri sample 3K-0285 and $\rho_{gas}(p)$ at 77 K. The data does not go to high enough pressure to determine the intersection of the two curves. *Right:* Intersection of G_{ex} vs. ρ_{gas} with ρ_{gas}/ρ_{skel} gives $\rho_{gas}(p^*) = 58$ g/L, from which $p^* = 280$ bar.

1.3.2 How do possible uncertainties in skeletal density affect storage capacities?

Accurate determination of the skeletal density, ρ_{skel}, of a sample is a critical component for accurate determination of the adsorption metrics: gravimetric excess adsorption G_{ex}, gravimetric storage capacity G_{st}, and volumetric storage capacity V_{st}. We did perform a large number of skeletal density measurements using He pycnometry ("helium density"), resulting in $\rho_{skel} = 2.00 \pm 0.03$ g/cm^3 for a wide range of powdered, high-surface-area carbons, and $\rho_{skel} = 2.03 \pm 0.03$ g/cm^3 for carbon monoliths. However, we did also use a default value of $\rho_{skel} = 2.00$ g/cm^3 for many samples. We sometime preferred the default value over values from He pycnometry because high-surface-area carbons adsorb non-negligible amounts of He (just as they adsorb non-negligible amounts of H_2), which are not easy to correct for (P. Malbrunot *et al*., *Langmuir* **13**, 539-544 (1997)). When a sample adsorbs He, it appears to displace less He than it would in the absence of adsorption, and the skeletal volume appears to be smaller than it would in the absence of adsorption. An underestimate of the skeletal volume leads to an overestimate of the skeletal density, and in extreme case we have seen apparent densities higher than the density of single-crystal, nonporous graphite, 2.26 g/cm^3.

Our default density, $\rho_{skel} = 2.0$ g/cm^3, is the nominal density of amorphous carbon, is between ~1.7 g/cm^3 for a single sheet of graphene and ~2.2 g/cm^3 for graphite, and is likely to overestimate the actual skeletal density of U. Missouri carbons. (A measurement of the skeletal density of a U. Missouri test sample by Micromeritics in October 2011 gave a skeletal density of 1.5-1.6 g/cm^3. We think this was unrealistically low, but it served to make the point that, if anything, our value $\rho_{skel} = 2.0$ g/cm^3 is on the high side.)

Based on such potential uncertainty in ρ_{skel}, we performed a systematic analysis of how the uncertainty may affect G_{ex}, G_{st}, V_{st}. We made the analysis broadly applicable by asking, how would a quantity X based on skeletal density ρ_{skel} change to a new value X' if skeletal density were ρ_{skel}' instead of ρ_{skel}. Here are the answers.

Gravimetric excess adsorption G_{ex}' based on skeletal density ϱ_{skel}' is related to gravimetric excess adsorption G_{ex} based on skeletal density ϱ_{skel} by

$$G_{ex}'(p,T) = G_{ex}(p,T) + \rho_{gas}(p,T)\left[\frac{1}{\rho_{skel}'} - \frac{1}{\rho_{skel}}\right] \tag{1.26}$$

This shows that if the actual skeletal density, ϱ_{skel}', is less than the default density, $\varrho_{skel} = 2.0$ g/cm^3, then the actual excess adsorption G_{ex}' is larger than G_{ex} based on the default density. I.e., G_{ex} increases with decreasing ϱ_{skel} at constant experimental, manometric readings. (If the skeletal density decreases, the skeletal volume increases, the void volume in the sample cell decreases, and a smaller amount of non-adsorbed H_2 gas will be subtracted in the determination of G_{ex}. Whence the increase in G_{ex}.) So, to the extent that $\varrho_{skel} = 2.0$ g/cm^3 is likely to overestimate, rather than underestimate, skeletal densities of U. Missouri carbons, our values for G_{ex} will underestimate, rather than overestimate, gravimetric excess adsorption. As an illustration, if sample with G_{ex}(190 bar, 80 K) = 0.058 g/g had a skeletal density of 1.8 g/cm^3 instead of 2.0 g/cm^3, gravimetric excess adsorption would be G_{ex}'(190 bar, 80 K) = 0.061 g/g from Eq. (1.26). Thus a 10% decrease in skeletal density increases gravimetric excess adsorption by 5%.

For particulate sorbents, whose porosity is determined by pore volume from N_2 adsorption and solid volume from mass of the solid and skeletal density, an uncertainty in skeletal density entails also an uncertainty in porosity. Porosity ϕ' based on skeletal density ϱ_{skel}' is related to porosity ϕ based on skeletal density ϱ_{skel}, for fixed sorbent mass and pore volume, by

$$\phi' = \frac{1}{1 + (\phi^{-1} - 1)\rho_{skel}/\rho_{skel}'} \tag{1.27}$$

It quantifies by how much ϕ decreases if ϱ_{skel} decreases. If a sample had a porosity of 0.76 and a skeletal density of 1.8 g/cm^3 instead of 2.0 g/cm^3, its porosity would be 0.74 instead 0.76, from (1.27). Thus a 10% decrease in skeletal density decreases the porosity by 3%.

How do variations in skeletal density translate into variations of gravimetric and volumetric storage capacity? It follows from Eqs. (1.6) and (1.27) that

$$G_{st}' = G_{st} + (G_{ex}' - G_{ex}) \tag{1.28}$$

so that gravimetric storage capacity differs by exactly the same amount as gravimetric excess adsorption does, Eq. (1.26). The reason is simple: gravimetric storage capacity and gravimetric excess adsorption differ by the amount of H_2 gas that would be present in the pore space in the absence of adsorption per gram of adsorbent. But neither the pore space nor the mass of adsorbent varies if the skeletal density varies. Specifically, if a sample had G_{st}(190 bar, 80 K) = 0.132 g/g and a skeletal density of 1.8 g/cm^3 instead of 2.0 g/cm^3, the gravimetric storage capacity would be G_{st}'(190 bar, 80 K) = 0.135 g/g instead of 0.132 g/g, up by 2%.

The effect on volumetric storage capacity, $V_{st} = G_{st} \cdot (1 - \phi)\varrho_{skel}$, is that, if the skeletal density decreases, the factor G_{st} increases, as we have just seen, but the factor $(1 - \phi)\varrho_{skel}$ decreases by Eq. (1.27), and the two effects largely cancel each other. In the case of the sample with G_{st}(190 bar, 80 K) = 0.132 g/g, the net effect would be that the volumetric storage capacity would decrease from V_{st}(190 bar, 80 K) = 0.0635 g/cm^3 to V_{st}'(190 bar, 80 K) = 0.0632 g/cm^3, which is only 0.3%.

Altogether, these calculations—done on storage data at high pressure and low temperature, where the effects are largest—show that G_{ex}, ϕ, G_{st}, and V_{st} vary by less than 5%, 3%, 2%, and 0.3%, respectively, if the skeletal density varies by 10%.

1.3.3 Two-fluid model of hydrogen adsorption: exceptionally dense films at 77 K

In addition to G_{ex}, G_{st}, V_{st}, we considered three additional metrics of performance of hydrogen storage materials. They are specific to sorption-based storage and focus on the adsorbed phase ("film"), as opposed to the gas phase (non-adsorbed H_2) or carrier phase ("solid," sorbent). Sorption-based storage is a three-phase equilibrium, and of the three phases the film is where all the action is. The metrics are: absolute adsorption, G_{abs} (mass of adsorbed film per mass of solid; also referred to as coverage or coverage by mass[9]); film density, ρ_{film} (mass of adsorbed film per

[9] Coverage as a quantity between 0 and 1 is the fraction of surface sites occupied by an H_2 molecule.

volume of film); and intrapore density, ρ_{ip} (total mass of H_2 stored, i.e, mass of adsorbed film and non-adsorbed gas, per volume of pore space), all three illustrated in Fig. 1.2:

$$G_{abs}(p,T) = G_{ex}(p,T) + \rho_{gas}(p,T)\cdot V_{film}(T)/m_{solid} \quad (1.35)$$

$$\rho_{film}(p,T) = G_{abs}(p,T)\cdot m_{solid}/V_{film}(T) \quad (1.36a)$$

$$= G_{ex}(p,T)\cdot m_{solid}/V_{film}(T) + \rho_{gas}(p,T) \quad (1.36b)$$

$$\rho_{ip}(p,T) = V_{st}(p,T)/\phi \quad (1.37a)$$

$$= G_{ex}(p,T)(\phi^{-1} - 1)\rho_{skel} + \rho_{gas}(p,T) \quad (1.37b)$$

The relation (1.37a) between volumetric storage capacity and intrapore density follows from the observation that intrapore density assigns the hydrogen stored to the pore space only, while V_{st} assigns the hydrogen stored to the solid plus pore space. Hence the intrapore density is larger than V_{st} by a factor of $1/\phi$. Chahine advocated a similar concept under the term average storage density in micropores: "*... The average storage density of H_2 in micropores varies from 61 to 71 kg per m^3 which is the same as LH_2 @ 20 K*" [R. Chahine, *DOE Hydrogen Storage Principal Investigator/Contractor Meeting*, Washington, DC, November 27-28, 2012].

The three metrics are relevant as follows:

(i) Absolute adsorption is the source for accurate isosteric heats of adsorption, ΔH (enthalpy of adsorption at constant coverage, G_{abs}; Sects. 1.4, 8, 9).[10]

(ii) The film density is quantitative measure #1 to investigate the DOE "liquid H_2 question," Fig. 1.1: Is it possible to store 71 g/L, the density of liquid H_2 at its normal boiling point (p = 1 bar, T = 20 K), or higher, in a suitably engineered sorbent at 77 K? The unexpected answer is yes: A wide variety of U. Missouri carbons were found to exhibit saturated film densities $\rho_{film,sat}$ = 100–120 g/L at 77 K, which is 50-70% higher than the density of liquid H_2 at 20 K, and 20-40% higher than the density of solid H_2, 86 g/L, at 14 K. The finding is unexpected because the high film density occurs at a temperature more than twice the liquid-gas critical temperature of H_2, T_c = 33 K, above which no bulk liquid exists at any pressure. The existence of a high-density H_2 film above T_c, to which we refer as *supercritical condensation* (we leave undetermined whether the film is liquid-like or solid-like), is not in contradiction to the non-existence of bulk

[10] ΔH as a function of coverage G_{abs} maps out the distribution of binding energies, E_b, of H_2 on a sorbent: ΔH at low coverage displays high binding energies, and ΔH at high coverage displays low binding energies. Absolute adsorption is the sole source for ΔH because ΔH physically is the heat given off (> 0) or taken up (< 0) during addition to the *adsorbed film,* or removal from the *adsorbed film*, of one molecule of H_2, per molecule. Only the full mass of the film, G_{abs}, tracks added or subtracted H_2 correctly. A *partial mass* such as G_{ex}—if in formula (1.36) one approximates the film volume as zero, $V_{film} = 0$—would underestimate G_{abs}. Likewise, a mass of the film plus non-adsorbed gas such as G_{st}—if in (1.36) one equates the film volume to the pore volume, $V_{film} = V_{pore}$—would overestimate G_{abs}. Whence the lower and upper bounds for G_{abs} illustrated in Fig. 1.2a: $G_{ex}(p,T) < G_{abs}(p,T) < G_{st}(p,T)$ for $p > 0$. In the absence of experimental data for V_{film}, calculation of ΔH with these bounds, which we denote by ΔH^- [$G_{abs} \mapsto G_{ex}$] and ΔH^+ [$G_{abs} \mapsto G_{tt}$], has been the mainstay of determination of ΔH by other researchers ("poor man's isosteric heat"). Our results for ΔH show that these approximations of G_{abs} under/overestimate the actual isosteric heat: $\Delta H^+ < \Delta H < \Delta H^-$ (Sects. 1.4, 8, 9). At high pressure, $p > p_{max}$, the approximation ΔH^- becomes even ill-defined. The inequality $\Delta H^+ < \Delta H$ follows from the observation that, by virtue of $G_{abs} < G_{st}$, the replacement $G_{abs} \mapsto G_{st}$ makes ΔH^+ take the value of ΔH at an effectively higher coverage, at which ΔH is lower. Likewise for the inequality $\Delta H < \Delta H^-$.

liquid: the film is not a bulk, 3D phase, but a monomolecular 2D phase. Table 1.4 summarizes these exceptional film densities and illustrate pathways to $V_{st} \geq 71$ g/L from materials with $\rho_{film,sat}$ = 100-120 g/L and film thickness t_{film} = 0.30–0.32 nm at 77 K. The pathways in Table 1.4 are for the scenario that materials can be synthesized with an effective single pore width w_{pore} and single wall width w_{wall}. Table 1.5 locates such pathways in materials with ratio $w_{pore}/w_{wall} < 1$ ("narrow pores, thick walls"). When the adsorbent has a whole distribution of pore widths, the decomposition of storage into high-density film and low-density non-adsorbed gas, coexisting in the pore space, reads

$$V_{st}(p,T) = \phi\left[\left\{\frac{1}{V_{pore}}\int_0^\infty \frac{2}{w}\frac{dV_{pore}}{dw}dw\right\} t_{film}(T)\cdot\left[\rho_{film}(p,T) - \rho_{gas}(p,T)\right] + \rho_{gas}(p,T)\right] \tag{1.38}$$

where dV_{pore}/dw is the differential pore size distribution of the adsorbent (volume in pores of width between w and $w + dw$, per pore width increment dw) and V_{pore} is the total pore volume of the sample as before. The integral in (1.38) has units of area and, through the product with the film thickness, divided by the total pore volume, counts the volume fraction occupied by the dense film. The factor $2/w$ gives narrow pores a large weight, consistent with the fact that narrow/wide pores host a large/small fraction of their volume as dense film. Thus, the decomposition (1.38) reduces the search for materials with "narrow pores, thick walls" (Table 1.5) to a search for materials in which the integral {...} in (1.38) is large.

(iii) Intrapore density is like the volumetric storage capacity, V_{st}, but considers the volume of the pore space only, without skeletal volume of the sorbent. So the intrapore density is quantitative measure #2 to investigate the "liquid H_2 question." By including the film and gas, it is one step closer to V_{st} in the progression to low density, from the inside out:

$$\text{adsorbed film } (\rho_{film}) \rightarrow \text{adsorbed film + non-adsorbed gas } (\rho_{ip}) \tag{1.39a}$$
$$\rightarrow \text{adsorbed film + non-adsorbed gas + sorbent } (V_{st}) \tag{1.39b}$$

Table 1.3 illustrates a pathway to $V_{st} \geq 71$ g/L from a material with ρ_{ip} = 80 g/L at 77 K and 120 bar. The virtue of the intrapore density is that it can be evaluated entirely from gravimetric excess adsorption and porosity, Eq. (1.37b), without any additional information. This is important when the film volume needed to calculate the film density, Eq. (1.36), is not available, such as in H_2 adsorption at room temperature. In this case, ρ_{ip} is a lower bound for ρ_{film}. In the case that ρ_{film} can be determined from (1.36), the inequality between ρ_{ip} and ρ_{film} provides a consistency test between the two independently determined quantities. The inequalities and relations between the different densities read, in ascending order:

$$\rho_{gas}(p,T) \leq \rho_{ip}(p,T) \leq \rho_{film}(p,T) \tag{1.40}$$
$$V_{st}(p,T) < \rho_{ip}(p,T) \tag{1.41}$$
$$\rho_{ip}(p,T) = \frac{V_{film}(T)}{V_{pore}}\rho_{film}(p,T) + \frac{V_{pore} - V_{film}(T)}{V_{pore}}\rho_{gas}(p,T) \tag{1.42a}$$
$$= \frac{V_{film}(T)}{V_{pore}}\left[\rho_{film}(p,T) - \rho_{gas}(p,T)\right] + \rho_{gas}(p,T) \tag{1.42b}$$

valid and rigorous for any sorbent. [(1.41) follows from (1.37a) and $\phi < 1$.] For good sorbents, as introduced in Sect. 1.3.1, it is additionally true that $\rho_{gas}(p,T) < V_{st}(p,T)$.

Table 1.4. High observed film densities and intrapore densities in U. Missouri carbons and resulting pathways to $V_{st} \geq 71$ g/L at 77 K ("liquid H_2 question"). In the samples studied, the film volume occupies only ~25-50% of the total pore volume, and ~35-70% of the local pore space. So one pathway is to create narrower pores, so as to eliminate the pore space holding non-adsorbed gas ("wasted pore space"). The other pathway is to make walls between pores thinner. In the formulas, N_A is Avogadro's number, M is the molar mass of H_2, and Σ is the specific surface area. The formulas for film thickness (slab model of the adsorbed film), average pore width ("hydraulic pore width," ratio of total pore volume to total surface area), and average wall width (slab model of the adsorbent) are from Fig. 1.8 and Sect. 8.

	Saturated film density, $\rho_{film,sta}$	Intrapore density, ρ_{ip}
High observed values Source	100–120 g/L at $p \geq$ 35–75 bar Fig. 1.8, Sect. 8	80 g/L at p = 120 bar Sect. 8
Samples	Most U. Missouri carbons, MSC-30	U. Missouri carbon HS;0B-20
Pore structure	Sub-nm & supra-nm pores	Monodisperse 0.7 nm pores
Does the film globally fill pore space?	No: V_{film}/V_{pore} = 0.25–0.53	No: V_{film}/V_{pore} = 0.53
Film thickness, $t_{film} = (\rho_{film,sat} \cdot N_A/M)^{-1/3}$	0.30–0.32 nm	0.31 nm
Average pore width, $w_{pore,av} = 2/(\Sigma \cdot \rho_{skel})\ (\phi^{-1} - 1)^{-1}$	0.87–1.87 nm	0.87 nm
Average wall width, $w_{wall,av} = 2/(\Sigma \cdot \rho_{skel})$	0.36–1.28 nm	1.01 nm
Does the film locally fill pore space (Fig. 1.2.c)?	No: $2 \cdot t_{film}/w_{pore,av}$ = 0.34–0.71	No: $2 \cdot t_{film}/w_{pore,av}$ = 0.71
Pathway to $V_{st} \geq 71$ g/L	Given ρ_{film}, store film and gas in narrow pores between narrow walls (minimize $w_{pore,av}$ and $w_{wall,av}$)	Given ρ_{ip} and $w_{pore,av}$, store film and gas between narrow walls (minimize $w_{wall,av}$ without raising $w_{pore,av}$)

Table 1.5. Classification of materials into narrow vs. wide pores and thick vs. thin pore walls. Input: average pore width, $w_{pore,av}$, and average wall width, $w_{wall,av}$, from Table 1.4. Classifier: ratio $r := w_{pore,av}/w_{wall,av}$. Numerical values are from Sect. 8. Samples with a small pore-width-to-wall-width ratio, $r < 1$ ("narrow pores, thick walls"), or equivalently with porosity < 0.5, are carriers of high intrapore densities.

	Narrow pores, thick walls	Wide pores, thin walls
Illustration		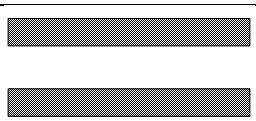
Pore width to wall width, $r := w_{pore,av}/w_{wall,av} = (\phi^{-1} - 1)^{-1} = V_{pore}/V_{solid}$ Observed values in U. Missouri samples	$r < 1$ r = 0.86, 0.96	$r > 1$ r = 1.3–4.6
Characterization in terms of porosity, ϕ Observed values in U. Missouri samples	$0 < \phi < 0.5$ ϕ = 0.46, 0.49	$0.5 < \phi < 1$ ϕ = 0.56–0.82
Characterization in terms of pore volume to skeletal volume, V_{pore}/V_{solid} Observed values in U. Missouri samples	$V_{pore}/V_{solid} < 1$ V_{pore}/V_{solid} = 0.86, 0.96	$V_{pore}/V_{solid} > 1$ V_{pore}/V_{solid} = 1.3-4.6

Equation (1.41) states that ρ_{ip} equals the weighted average of the density of the adsorbed film and the density of the non-adsorbed gas, with weights equal to the fraction of the pore volume that is occupied by the film and gas, respectively.[11]

Formulas (1.41) and (1.37a) can be combined to express the volumetric storage capacity entirely in terms of film volume and density,

$$V_{st}/\phi = \left(1 - \frac{V_{film}}{V_{pore}}\right)\rho_{gas} + \frac{V_{film}}{V_{pore}}\rho_{film} \tag{1.43}$$

$$= (1 - \lambda)\rho_{gas} + \lambda\rho_{film} \quad \text{(linear dependence on } \rho_{gas}\text{)} \tag{1.44}$$

$$\lambda := V_{film}/V_{pore} \quad \text{(ratio film volume to pore volume[12])} \tag{1.45}$$

$$= (S_{TF}/V_{pore})\cdot t_{film} \quad \text{(film volume from surface area } S_{TF} \text{ and } t_{film}\text{)} \tag{1.46}$$

$$S_{TF} := \int_0^\infty \frac{2}{w}\frac{dV_{pore}}{dw}dw \quad \text{(“two-fluid-weighted” surface area)} \tag{1.47}$$

Results (1.43-1.47) bring a number of remarkable relations together. In Table 1.4, the ratio λ was an experimental figure of merit, with V_{film} determined from the slope of G_{ex} vs. ρ_{gas} at high pressure (Fig. 1.8) and V_{pore} from N_2 adsorption, to address the question, does the film globally fill pore space? Here, in (1.44), the ratio λ determines the slope of V_{st}/ϕ vs. ρ_{gas} at high pressure when the film density approaches saturation and V_{st}/ϕ vs. ρ_{gas} becomes a straight line,

$$V_{st}/\phi = A\rho_{gas} + B \quad \text{(large-}p\text{ asymptote, } p > p_{max}\text{)} \tag{1.48}$$

$$A = 1 - \lambda \tag{1.49}$$

$$B = \lambda\rho_{film,sat} \tag{1.50}$$

Conversely, λ and $\rho_{film,sat}$ can be determined from a linear fit, (1.48), to high-pressure volumetric storage capacity (Fig. 1.9). Finally, Eqs. (1.46, 1.47) relate λ to the surface area alluded to in Eq. (1.38) and film thicknesses tabulated in Table 1.4. In fact, (1.46, 1.47) follow from comparing the right-hand sides of (1.44) and (1.38). The relation (1.46) decomposes λ into a purely pore-geometric factor, S_{TF}/V_{pore}, and a purely thermodynamic factor, t_{film}. We call the surface area (1.47) “two-fluid-weighted” surface area S_{TF} because it manifestly does not count area in narrow and wide pores equally, but counts area according to the fraction of pore volume the area supports, perpendicular to the surface (Fig. 1.2c), in a pore of width w. The weight $2/w$ gives area in narrow pores a large weight and discounts area in large pores. BET surface area, $\Sigma\cdot m_{solid}$, in contrast, counts surface area in narrow and wide pores equally. As a result, we expect, and indeed find (Sect. 8) that

$$S_{TF} < \Sigma\cdot m_{solid} \tag{1.51}$$

This concludes the analysis of, and results from, the two-fluid model of H_2 adsorption.

---

[11] If we take the weighted average, (1.42), as the conceptual definition of the intrapore density, the working formula (1.37) has the status of a “sum rule,” which says that ρ_{ip} can be determined without any knowledge of V_{film} and ρ_{film}. Similarly, the bounds (1.40) may be regarded as the result of evaluating (1.42) with the lower bound $0 \le V_{film}$ and upper bound $V_{film} \le V_{pore}$ for the film volume, respectively.

[12] Later sections will refer to the ratio λ as pore filling factor.

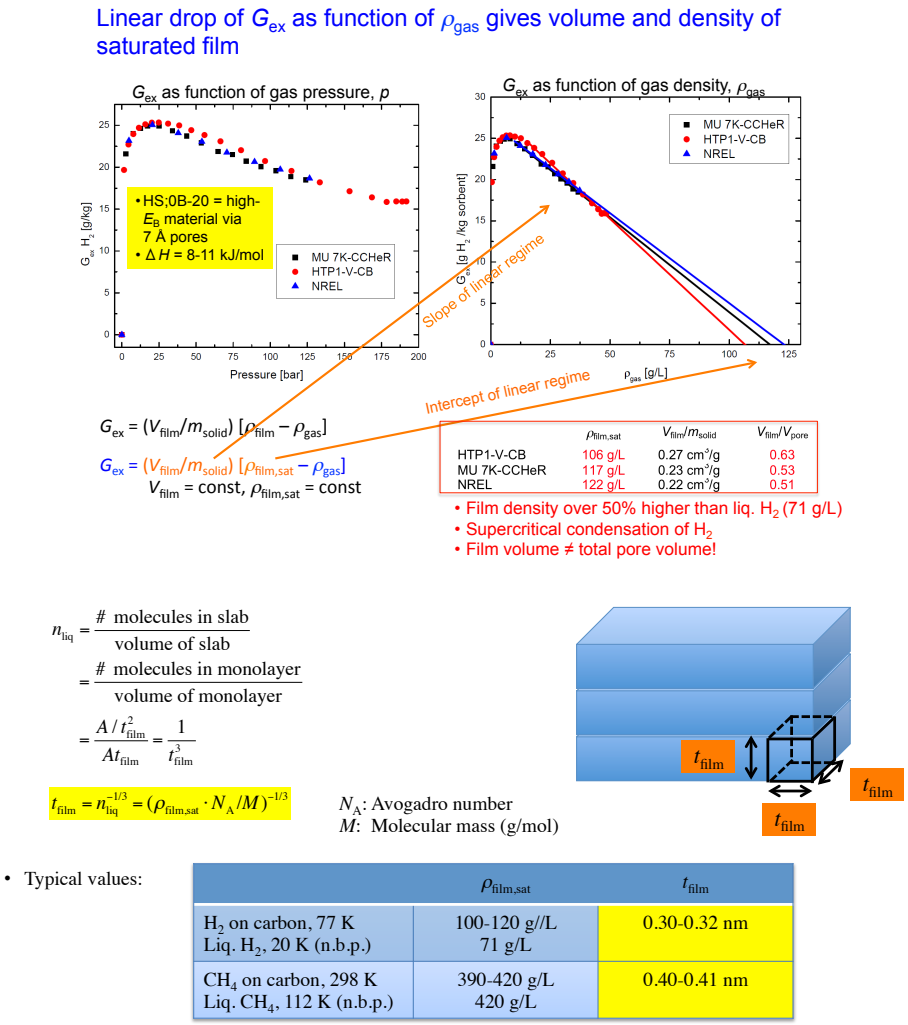

Figure 1.8. *Top:* Determination of film volume V_{film} and saturated film density $\rho_{film,sat}$ from high-pressure gravimetric excess isotherms, G_{ex}, vs. gas density, ρ_{gas} (from Section 8). *Bottom*: Determination of film thickness, t_{film}, from saturated film density, $\rho_{film,sat}$.

Figure 1.9. Asymptotic linear relation for volumetric storage capacity V_{st} as a function of gas density ρ_{gas}, at high pressure: $V_{st}/\phi = (1-\lambda)\rho_{gas} + \lambda\rho_{film,sat}$ for different values of film-to-pore-volume $\lambda = V_{film}/V_{pore}$ and saturated film density $\rho_{film,sat}$ = 100 g/L. Materials with low λ start out low and fill rapidly with gas. Materials with high λ start out high, with large fraction of pore volume filled with saturated film, and fill slowly with additional gas.

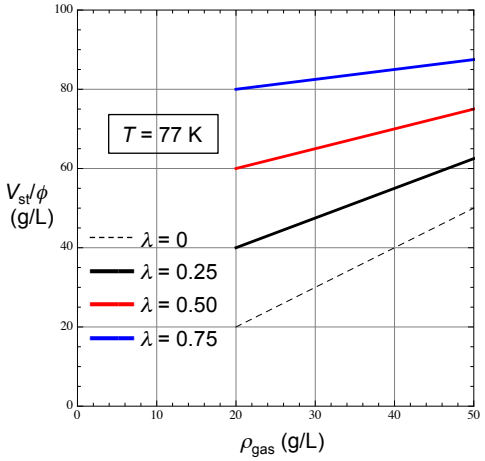

1.4 Accomplishments in Terms of Binding Energy Metrics (Binding Energies, E_b, Enthalpies of Adsorption, ΔH)

Isosteric heats of adsorption and binding energies of doped materials—methods

In the past, we determined isosteric heats of adsorption, ΔH, from Clausius-Clayperon analysis of two adsorption isotherms at nearby temperatures such as 77 K and 87 K, or 273 K and 303 K, and estimated the volume of the adsorbed hydrogen film, which is needed to convert experimental gravimetric excess adsorption into calculated gravimetric absolute adsorption, by methods we pioneered in Phase I of the U. Missouri Project (see, e.g., our 2010 and 2012 Annual Progress Reports). The relation between excess adsorption, absolute adsorption, and ΔH is:

$$\frac{m_{\text{film}}}{m_s} = \frac{m_{\text{exc}}}{m_s} + \rho_{\text{gas}}(p,T)\frac{V_{\text{film}}}{m_s} \tag{1.10}$$

$$\Delta H = -R\left(\frac{\partial(\ln p)}{\partial(1/T)}\right)_{m_{\text{film}}/m_s} \tag{1.11a}$$

$$\approx -R\left(\frac{\ln p_2 - \ln p_1}{1/T_2 - 1/T_1}\right)_{m_{\text{film}}/m_s} = \frac{RT_1T_2}{T_2 - T_1}\ln\left(\frac{p_2}{p_1}\right)_{m_{\text{film}}/m_s} \tag{1.11b}$$

where m_{film} and V_{film} are the mass and volume of the H_2 film (absolute adsorption), m_{exc} is the mass of excess adsorbed H_2, m_s is the mass of the solid or sorbent, R is the gas constant, and (1.11b) is the Clausius-Clapeyron evaluation of (1.11a) [finite-difference evaluation of the derivative in (1.11a)]. The conversion, (1.10), is critical because isosteric heat measures the heat of adsorption as a H_2 molecule is added to the film at constant coverage, m_{film}/m_s ("isosterically"), Eq. (1.11). (Evaluation of (1.11) at constant excess adsorption instead of constant coverage gives unphysical values, which increase instead of decrease with increasing coverage or are not well-defined [5]). The importance of proper execution of Eqs. (1.10, 1.11) and the sensitive dependence of ΔH on how (1.10, 1.11) are implemented was emphasized in a recent publication by Mason et al. [7]. While we agree with the generic recommendations of Mason et al.—(i) specify how V_{film} is estimated; (ii) specify the mathematical model that is used to interpolate between measured data points for m_{film}/m_s ("to determine the exact pressures that correspond to the same amount adsorbed at different temperatures")—we regard the specifics advocated in [7],

(i) V_{film}= total pore volume, V_{pore} (1.12)
(ii) Model isotherm for m_{film}/m_s: single-site or dual-site Langmuir model, (1.13)

as too simple and inaccurate in general. The approximation (1.12), when substituted into (1.11), approximates absolute adsorption as equal to gravimetric storage capacity (total mass, adsorbed and non-adsorbed H_2, per mass of sorbent), which overestimates m_{film}/m_s exactly by the amount of non-adsorbed H_2. The overestimate is the larger, the larger the fraction of supra-nm pores(width >1.0 nm) in the material is. But the overestimate persists even in materials in which most of the pore volume resides in sub-nm pores: In Fig. 1.7, we present a case study in which the volume of the adsorbed H2 film is only about 50-60% of the total pore volume, V_{pore}, even though the fraction of pore volume in pores <1.0 nm is 80-90% of the total pore volume. Approximation (1.12) is also unsatisfactory because it is silent on cases of interest such as

nonporous adsorbents or the presence of 2nd-layer adsorption [8]. Approach (1.13) is unsatisfactory because it allows for only one or two binding energies, E_b (unimodal or bimodal distribution of binding energies), instead of a whole distribution of binding energies as expected for B-doped carbons with E_b = 3.2 kJ/mol at edge sites of a single graphene sheet [9], E_b = 4.5 kJ/mol on single-sheet graphene sites [9], E_b = 5.0 kJ/mol on multi-sheet graphene sites [10], E_b = 7.8 kJ/mol on graphene sites with a carbon atom substituted by an isolated B– anion (Fig. 6), and E_b = 11-12 kJ/mol for B– concentration ~10 wt% [11].

Based on this background and to provide the DOE with best-practice estimates of experimental isosteric heats, ΔH, as a function of coverage, and best-practice estimates of experimental binding energies, E_b, at zero coverage - recommended at the DOE Site Visit, 1/29/14, as principal instrument to assess whether very low boron concentrations in doped materials could measurably raise the binding energy[13]- we revisited our procedures for determining ΔH and newly developed procedures for determining E_b at zero coverage as follows.

ΔH at low, intermediate, and high coverage: Instead of approximations (1.12) and (1.13) used by Mason et al., we use

(i) $V_{film} = \Sigma \cdot t_{film}$ (1.14)
(ii) Model isotherm for m_{film}/m_s: modified Redlich-Peterson isotherm (1.15)

where Σ is the specific surface area from N_2 BET analysis, and the film thickness is set at t_{film} = 0.40 nm for all isotherm pressures and temperatures. The film thickness of 0.40 nm was found to be appropriate at 77 K [5], where it ensured that ΔH as a function of coverage m_{film}/m_s (absolute adsorption) did not increase with increasing coverage; the maximum coverage for this test was m_{film}/m_s = 0.06 [5]. For H_2 adsorption at room temperature, in work through 2012, we used a film thickness of 0.60 nm, which ensured that ΔH did not increase up to m_{film}/m_s = 0.03 [6]. The recent discussion regarding the trustworthiness of isotherm data measured at that time [11], however, raised the question whether 0.60 nm came perhaps from flawed data. Independently, we found samples in which V_{film} from (1.14) and t_{film} = 0.60 nm was very close to V_{pore}, i.e., suffered from the same deficiency as approximation (1.12). This suggested that t_{film} = 0.60 nm was too high for a typical film thickness at room temperature, and it was abandoned in January 2014 in favor of t_{film} = 0.40 nm at all temperatures. All ΔH vs. m_{film}/m_s curves calculated since January 2014 decreased or remained constant with increasing coverage, which validates that film thicknesses are not too small.

An illustration of the excellent quality of fits of m_{film}/m_s vs. p (from Eqs. (1.10, 1.14)) with the modified Redlich-Peterson isotherm is given in Fig. 2a, specifically for low pressure, where

[13] The rationale for focus on low boron concentrations, 1-2 wt%, and binding energies at zero coverage is this: The best chances to create sp^2-bonded boron (sp^2 B-C bonds, high-binding-energy sites) in a high-surface-area material is to dope at low concentration, so as to avoid blocking of pores with elemental boron, to give surface-diffusing boron atoms ample opportunity to find defects in the carbon matrix and substitute for a missing carbon atom in the lattice, and by virtue of the low concentration to avoid being trapped by oxygen atoms in the matrix, which we have been able to remove only in part prior to doping. Low concentrations of sp^2 B-C bonds create only few high-binding-energy sites, and these will only be detected at zero coverage.

small differences in data, such as from different interpolation procedures, can lead to large differences in ΔH. Table 1gives a comprehensive account of the quality of fits over all pressures and for a whole series of samples. To improve the accuracy of ΔH values, ΔH was no longer calculated from two-temperature Clausius-Clapeyron analyses, but from plots of

$$(\ln p)_{m_{film}/m_s} \text{ vs. } 1/T \qquad (1.16)$$

from pressures at four different temperatures, Fig. 1.8a (isosteres). If the data points for (1.16) fall on a straight line, the slope equals $-\Delta H/R$ by Eq. (1.11a) and states that ΔH is independent of temperature in that temperature interval. The resulting ΔH values are more accurate than from Clausius-Clapeyron because they result from straight lines through four data points instead of only two. Each isostere, i.e., set of data points ($\ln p$, $1/T$) at constant coverage gives rise to a ΔH value at that particular coverage, and the collection of ΔH values at different coverages gives the isosteric heat curves in Fig 1.8b, which are for four B-doped materials. None of the curves shows an increase in ΔH with increasing coverage, as advertised.

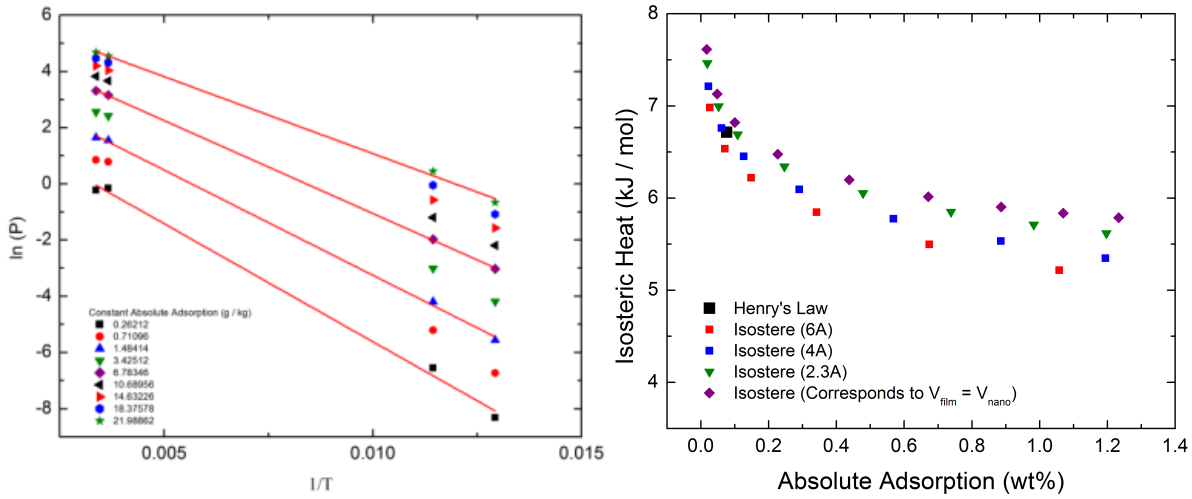

Figure 1.8. *Left*: Nine isoteres for coverage from $m_{film}/m_s = 0.26$ g/kg (*bottom*) to $m_{film}/m_s = 22$ g/kg (*top*) for one B-doped material. The four temperatures for each isostere are $T = 77$ K, 87 K, 273 K, 303 K, from right to left. Decreasing slopes from bottom to top show decreasing isosteric heats from low to high coverage. *Right*: Isosteric heat curves for four different B-doped materials. Their ΔH values and dependence on boron concentration will be discussed in Sect. 9.

The high end of the coverage range for the doped materials, $m_{film}/m_s = 1.2$ wt% H_2 (Fig. 1.8b), is lower than the high end for undoped materials, $m_{film}/m_s = 1.5$ wt% H_2 (Fig. 1.8, right), because doped materials have lower surface area, which leads to a lower maximum coverage at 303 K for doped materials.

E_b at zero coverage: By measuring H_2 isotherms at pressures $p = 0.001$-0.15 mbar at 77 K and 87 K, we were able to observe Henry's law regime and deduce values for the binding energy, E_b (defined as depth of the adsorption potential), from the Langmuir isotherm as follows. We equate excess adsorption to absolute adsorption, valid at low pressure because the gas density in Eq. (1.10) is negligible, and calculate absolute adsorption m_{film}/m_s from the Langmuir model for mobile adsorption [1],

$$\frac{m_{exc}(p,T)}{m_s} = \frac{m\Sigma}{\alpha(T)}\frac{\chi(T)p}{1+\chi(T)p} \tag{1.17}$$

$$\chi(T) = \frac{\alpha(T)\exp(E_b/(N_A k_B T))}{\sinh(h\nu_\perp/(2k_B T))}\sqrt{\frac{h^2}{8\pi m(k_B T)^3}} \tag{1.18}$$

In these expressions, m is the mass of the hydrogen molecule; Σ is the specific surface area; $\alpha(T)$ is the footprint area of a hydrogen molecule (surface area occupied by a hydrogen molecule at full coverage of the surface), at temperature T; E_b is the binding energy per mole H_2; N_A is Avogadro's constant; k_B is Boltzmann's constant; h is Planck's constant; and $\nu_\perp$ is the frequency of vibration of the hydrogen molecule (center of mass) to and from the surface. For low p and high T, eqs. (1.17, 1.18) simplify to

$$\frac{m_{exc}(p,T)}{m_s} = \Sigma p \exp(E_b/(N_A k_B T))\sqrt{\frac{m}{2\pi k_B T \nu_\perp^2}} \tag{1.19}$$

In Eq. (1.19), the footprint area $\alpha(T)$ has dropped out (at low pressure gas molecules find empty adsorption sites regardless of their footprint area), Planck's constant has dropped out (quantum effects are negligible at high temperature), and gravimetric excess adsorption is proportional to pressure. This linear relation between excess adsorption and pressure is Henry's law, and the proportionality factor is Henry's law constant, for which (1.19) gives an explicit expression in terms of the constants involved in the Langmuir model. Taking the ratio of (1.19) at temperatures T_1 and T_2 gives

$$\frac{m_{exc}(p,T_1)}{m_{exc}(p,T_2)} = \sqrt{\frac{T_2}{T_1}}\exp\left(\frac{E_b}{R}\left(\frac{1}{T_1}-\frac{1}{T_2}\right)\right) \tag{1.20}$$

$$E_b = R\frac{T_1 T_2}{T_2 - T_1}\ln\left(\sqrt{\frac{T_1}{T_2}}\frac{m_{exc}(p,T_1)}{m_{exc}(p,T_2)}\right) \tag{1.21}$$

Eq. (1.21) gives an explicit expression for the determination of the binding energy, E_b, from the linear regime for excess adsorption. Figure 1.9 shows the case of B-doped sample 5K-0215 (8.0 wt% B), with the highest binding energy obtained so far, E_b = 9.2 kJ/mol, and finds excellent agreement with the binding energy from quantum-chemical calculations for B^- substituted into a graphene-like carbon matrix.

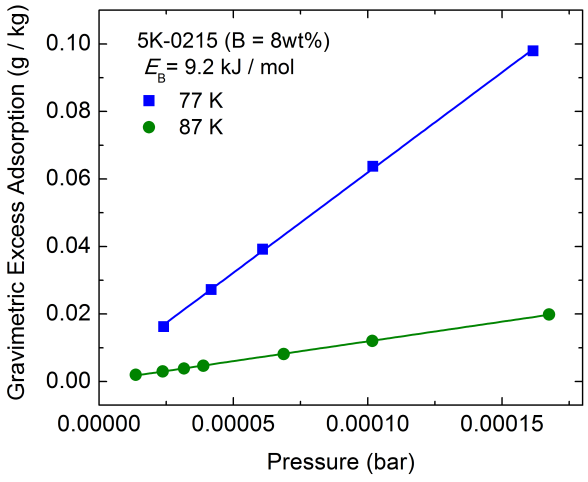

Figure 1.9. Gravimetric excess adsorption increases linearly with increasing pressure at sufficiently low pressure (Henry's law), here for sample 5K-0215 and p = 0.001–0.15 mbar. The slope of the isotherm grows exponentially with the binding energy E_b, Eq. (1.19). For fixed binding energy, the ratio of the slopes at two different temperatures gives E_b, Eq. (1.21), here E_b = 9.2.kJ/mol. The linear behavior of isotherm and the value of the slope were highly repeatable for all samples, also on different instruments.

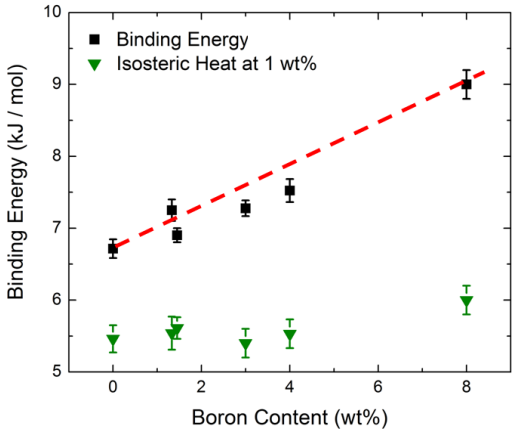

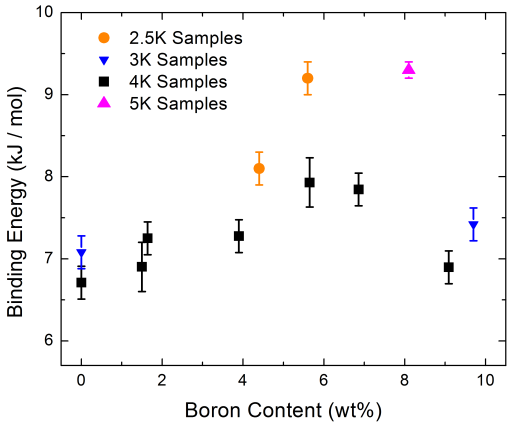

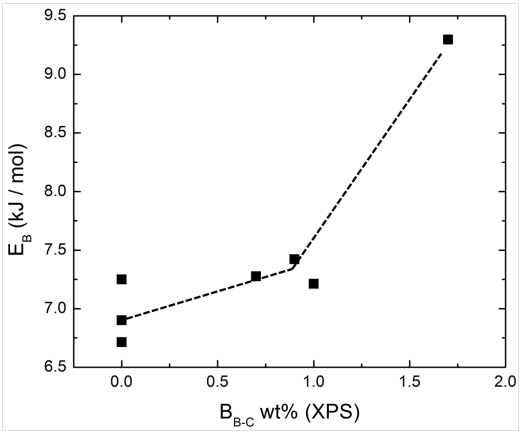

Figure 1.10. Binding energies obtained from Henry's Law and Langmuir isotherm as function of boron content (*above left, above right*) and as a function sp^2-bonded B-C bonds (*right*, from Section 1.5). A nonlinear growth of binding energy with increasing B-C concentration, suggested in the right frame, has been predicted by electronic structure calculations as a result of changes in the electronic structure beyond nearest neighbor carbon atoms [11].

We will show in Section 9.4 that the fraction of surface sites with high binding energy E_b can be estimated from the range of pressures over which the adsorption isotherm grows linearly with pressure (Henry's law). The result for the sample analyzed, 2.5K-0754, is that approximately 0.5% of all surface sites carry a binding energy of E_b = 8.1 kJ/mol, which compares well with Fig. 1.10, (*right*), which would predict a binding energy of 7.2 kJ/mol at $B_{B\text{-}C}$ = 0.5%.

[1] J. Burress, M. Kraus, M. Beckner, R. Cepel, G. Suppes, C. Wexler, P. Pfeifer, Nanotechnology **20**, 204026 (2009).
[2] G.L. Aranovich and M.D. Donohue, Carbon **33**, 1369 (1995).
[3] J. Romanos, M. Beckner, T Rash, L. Firlej, B. Kuchta, P Yu, G. Suppes, C. Wexler, P Pfeifer, Nanotechnology **23**, 015401 (2012).
[4] M. Beckner, A. Dailly, Am. J. Anal. Chem. **4**, 8 (2013).
[5] P. Pfeifer et al., 2010 Annual Progress Report.
[6] P. Pfeifer et al., 2012 Annual Progress Report.
[7] J.A. Mason, M. Veenstra, J.R. Long, Chem. Sci. **5**, 32 (2014).
[8] B. Kuchta, L. Firlej, P. Pfeifer, C. Wexler, Carbon **48**, 223 (2010).
[9] L. Firlej, M. Beckner, J. Romanos, P. Pfeifer, B. Kuchta, J. Phys. Chem. C **118**, 955 (2014).
[10] L. Mattera, F. Rosatelli, C. Salvo, F. Tommasini, U. Valbusa, G. Vidali, Surf. Sci. **93**, 515 (1980).
[11] L. Firlej, S. Roszak, B. Kuchta, P. Pfeifer, C. Wexler, J. Chem. Phys. **131**, 164702 (2009).

1.5 Accomplishments in Terms of Functionalization Metrics (B-C, C-N Bonds)

Functionalization I: Replace Carbon with Boron

Table 1.4. Colors—Yellow: quantities of interest—concentration of sp^2-bonded B-C (carrier of high binding energies) and binding energies; light green: B_xC sample with the highest binding energy (5K-0215); white: samples annealed at 800 ºC for 3 hours; orange hatched: samples annealed at 1000 ºC for 3 hours; blue hatched: samples first annealed at 1000 ºC for 3 hours and subsequently annealed at 1200 ºC for 15 hours.

Sample	B_{tot} (wt%, XPS)	$B_{B\text{-}C}$ (wt%)	$B_{B\text{-}C}/B_{tot}$ (%)	O (wt%)	E_b (kJ/mol)
Liquid-phase deposition					
4K-0240	1.2	0.0	0.0	6.2	6.9
4K-0244	1.7	0.0	0.0	7.8	7.2
4K-0245	4.1	0.7	18	10	7.3
4K-0748	5.2	1.0	19	7.9	7.2
3K-0205	7.5	0.9	13	9.0	7.4
3K-0211	7.6	0.6	8.5	11	N/A
5K-0215	8.4	1.7	21	8.7	9.2
3K-0208	15	1.7	12	9.7	N/A
Vapor-phase deposition					
3K-0230	2.2	0.1	3.1	5.7	N/A
3K-1035	3.9	0.4	9.9	8.9	N/A
3K-0231	6.1	0.8	13	11	N/A
3K-1036	3.8	1.1	23	7.7	N/A
3K-0234	4.8	0.6	13	8.5	N/A
3K-0235	24	1.3	5.4	14	N/A
3K-1038	19	1.4	7.5	12	N/A

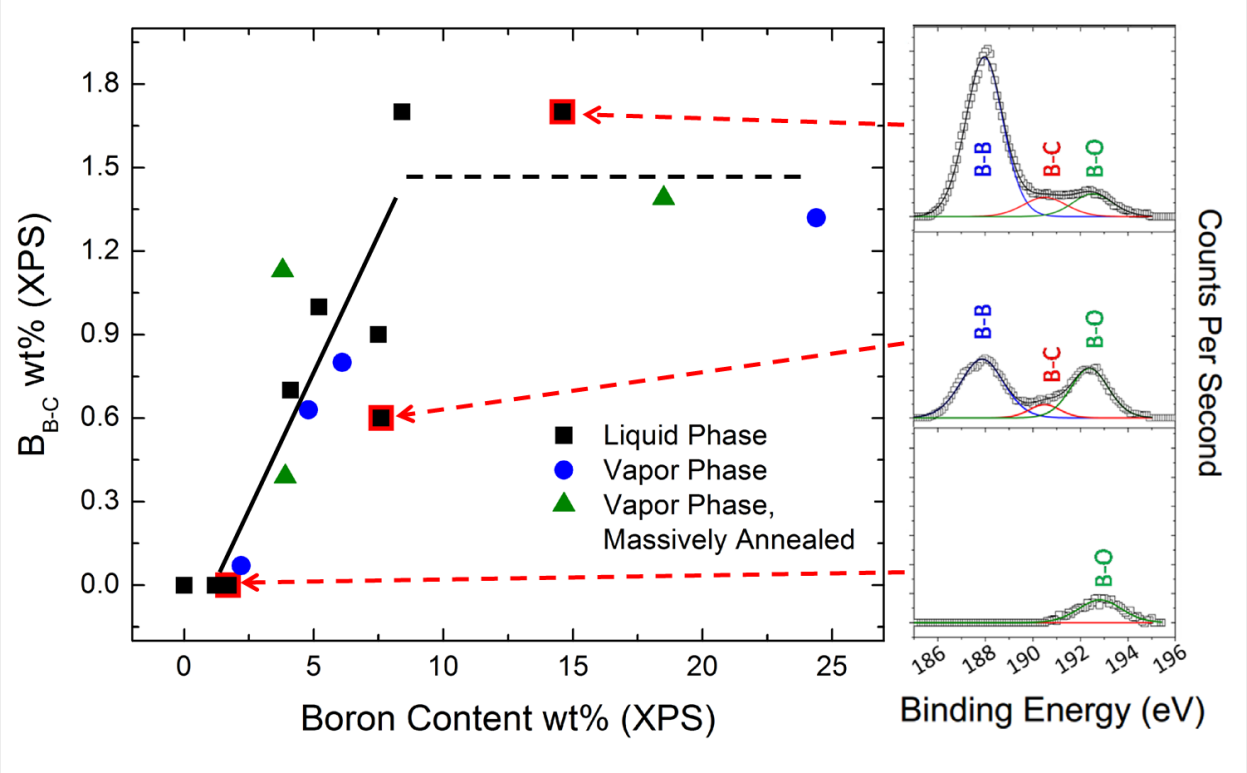

Figure 1.10. *Left*: Concentration of sp^2-bonded boron (B-C bonds, high-binding-energy sites) in different samples as a function of total boron concentration in the samples. XPS spectra for boron, carbon and oxygen were simultaneously fit (methodology described in Sec. 7.3) to determine amounts of sp^2-bonded boron in doped carbon samples. sp^2-bonded boron increases with increasing total boron content. *Bottom Right*: Boron spectra for sample 4K-0244. This spectra is representative of all samples with boron contents < 2 wt%. In this range, the decomposition of $B_{10}H_{14}$ readily forms B-O bonds. No B-C bonds are observed. *Middle Right*: Boron spectra for sample 3K-0211. This spectrum is representative of samples with 2 < B wt% < 7. In this range, peak splitting is observed as B-B and B-C bonds emerge in addition to the formation of B-O bonds. *Top Right*: Boron spectra for sample 3K-0208. This spectrum is representative of samples with B wt% > 7. The B-B peak is most prominent in this spectrum due to the larger quantity of total boron in the sample. Further, the area under the B-C peak increased to be approximately equal to that under the B-O peak, indicating a larger amount of sp^2 bonded boron in the sample.

Functionalization II: Replace Carbon with Nitrogen

Graphitic carbon nitride (g-C_3N_4) is an attractive candidate for H_2 adsorption because it has a layered structure like graphene, but also regular patterns of voids which upon exfoliation host high edge-to surface ratios and correspondingly higher surface areas, estimated as high as 4000-6000 m^2/g. Alternating N and C atoms lead to negative and positive partial charges on N and C atoms, respectively, expected to result in strong dipole interactions with adsorbed H_2 molecules.

To resolve in-plane features, supplemental techniques are required. The XRD spectrum of MU-created g-CN is dominated by a large peak at 27.3° (d = 3.26Å) and contains several smaller features at 2θ < 25°, similar to what is seen for graphite. The large peak corresponds to the interplanar spacing of the sheets and agrees well with the measurements from HRTEM, while those at smaller angles refer to the larger, in-plane features. These features are resolved well assuming a combination of two distinct structures (Fig. 1.11): s-triazine g-C_3N_4 (80%) and a polymeric chain of heptazine units (20%), commonly referred to as a melon.

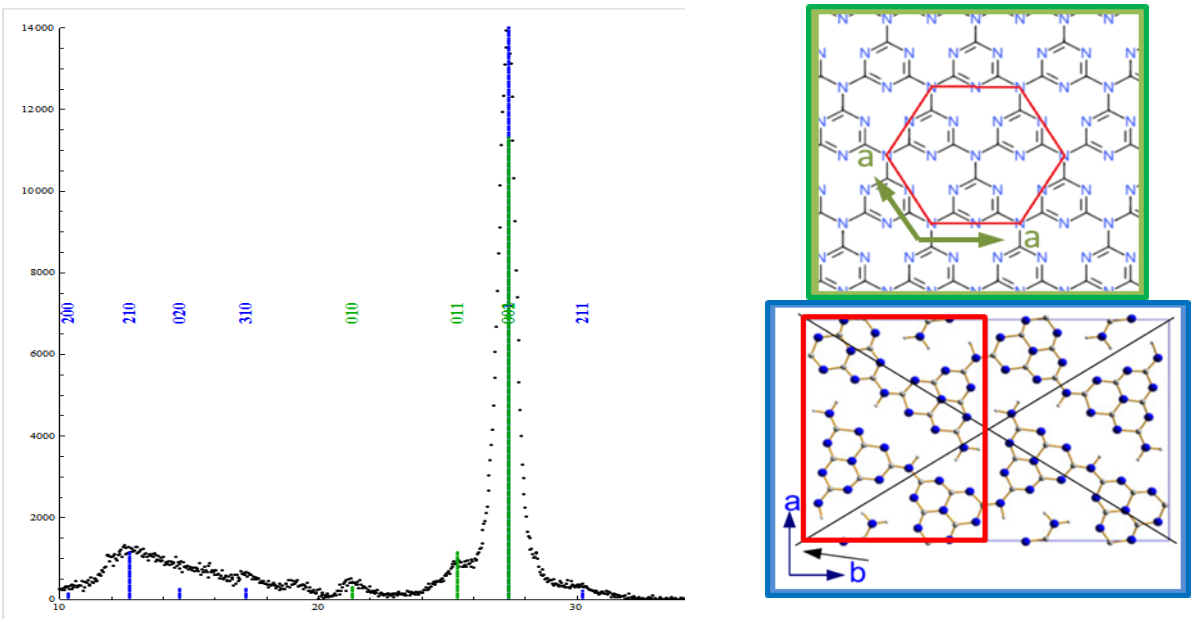

Figure 1.11.*Left*: XRD spectrum of MU-created g-C_3N_4, fitted to a combination of two structures. *Top right*: s-triazine based g-CN. *Bottom right*: heptazine based polymeric carbon nitride chains, figure and peak assignments from (Tyborski et al., *Journal of Physics: Condensed Matter*, **25**(2013), 395-402). Both models agree to an inter-planar distance of 3.26Å. Tyborski et al. explain that the broadening of the low-angle peaks is due to a temperature-induced shearing of the plane, driving the chains apart; this ultimately results in a split of previously superpositioned, symmetric reflections.

1.6 Accomplishments in Terms of Improved "Understanding of Hydrogen Physisorption and Chemisorption" (Film Thicknesses, Film Densities, Beyond Chahine Rule)

High binding energies without boron doping: synthetic carbon HS;0B-20

Synthetic carbon HS;0B-20, from Sect. 8, gave unusually high binding energy (isosteric heat ΔH = 8-11 kJ/mol), which was attributed to the presence of a highly monodisperse distribution of pores of width ~0.7 nm. In such narrow pores, adsorption potentials from neighboring pore walls overlap and produce potential wells with depth up to 2 × 5 kJ/mol (two times the well depth of a single-wall potential). The material gave also gave exceptionally high saturated film density of 100-120 g/L at 77 K, over 50% higher than that of liquid H_2 (71 g/L). The film volume V_{film} and saturated film density $\rho_{film,sat}$ was determined by fitting the form $G_{ex} = (V_{film}/m_s)[\rho_{film,sat} - \rho_{gas}]$ to the experimental excess isotherm (Fig. 1.12). The film volumes and densities were validated by three independent isotherm measurements (Fig. 1.12, Table 1.5).

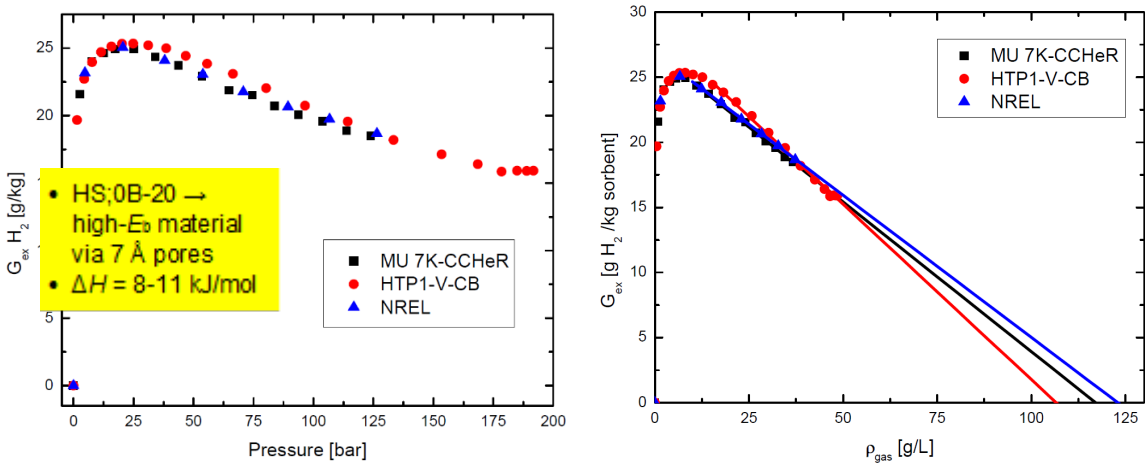

Figure 1.12. Independent gravimetric excess adsorption of sample HS;0B-20, as measured at MU on the HTP1-V-CB ("Hiden HTP") and 7K-CCHeR ("7K Sievert"), and NREL, show excellent agreement. Isotherms at high ρ_{gas} are linearly fitted (parameters in Table 1.5).

Table 1.5. High density linear fit parameters for sample HS;0B-20 as shown in Fig 1.12. HS;0B-20, a high-ΔH material by virtue of consisting almost entirely of 7 Å pores (Fig 8.3), reproducibly demonstrates a film density over 50% higher than that of liquid H_2 (71 g/L).

Instrument	$\varrho_{film,sat}$	V_{film}/m_{solid}	V_{film}/V_{pore}	Max. Film Cap.
HTP1-V-CB	106 g/L	0.27 cm^3/g	0.63	28.6 g H_2/kg sorbent
MU 7K-CCHeR	117 g/L	0.23 cm^3/g	0.53	26.9 g H_2/kg sorbent
NREL	122 g/L	0.22 cm^3/g	0.51	26.8 g H_2/kg sorbent

Are saturated film densities ~100 g/L at 77 K universal?

We expected HS;0B-20 and other U. Missouri synthetic carbons with a sub-nm monodisperse pore size distribution to be rare materials with high values $\varrho_{film,sat}$ ~ 100 g/L, related or caused by the high binding energies. But we found that nearly all carbon samples, regardless of binding energies, gave similarly high film densities (Fig. 1.13, left). This includes high-surface-area "MSC-30"-type carbons, which have predominantly pore sizes >1nm and peak around the normal value of p_{max} ~ 50 bar, rather than the low value of p_{max} ~ 20 bar of HS;0B-20. So the

answer is yes, carbons and even a metal-organic framework exhibit values for $\varrho_{film,sat}$, nominally 98-120 g/L, that are in good approximation universal. For comparison, Poirier and Dailly (2009) similarly report a "universal value", albeit at significantly lower value, of 51-69 g/L at 50 K.

Universal film thickness

Following suggestions in the literature (G. Aranovich and M. Donohue, J. Colloid Interface Sci. **194**, 392-397 (1997)) that the monolayer volume V_{film} can be used to estimate surface areas, if the film thickness is known, or estimate film thicknesses if the surface area is known, we calculated H_2 film thicknesses by dividing film volumes by BET surface area, $V_{film}/(\Sigma \cdot m_s)$. The resulting values, all less than 0.3 nm (Table 1.6), are much too low. Monte Carlo simulations of adsorbed films on carbon at 77 K show that H_2 molecules cannot approach each other closer than 0.3 nm, whence film thicknesses cannot be less than 0.3 nm. The alternative method of calculating film thickness from $\varrho_{film,sat}$ (Sect. 1.3.3, Table 1.4, Fig. 1.8), without film volumes or surface areas, gives values, t_{film} = 0.30–0.32 nm, which are in perfect agreement with Monte Carlo simulations.

We consider it a significant achievement of the "two-fluid model" in Sect. 1.3.3 that: (i) It gives, for the first time, accurate experimental values for the thickness of H_2 films at 77 K; (ii) It explains, in terms of coexistence of high-density film and low-density gas in pores, why the "surface area" determined from V_{film}/t_{film} is systematically lower than the BET area; (iii) It identifies pathways to volumetric storage capacities "better than liquid H_2."

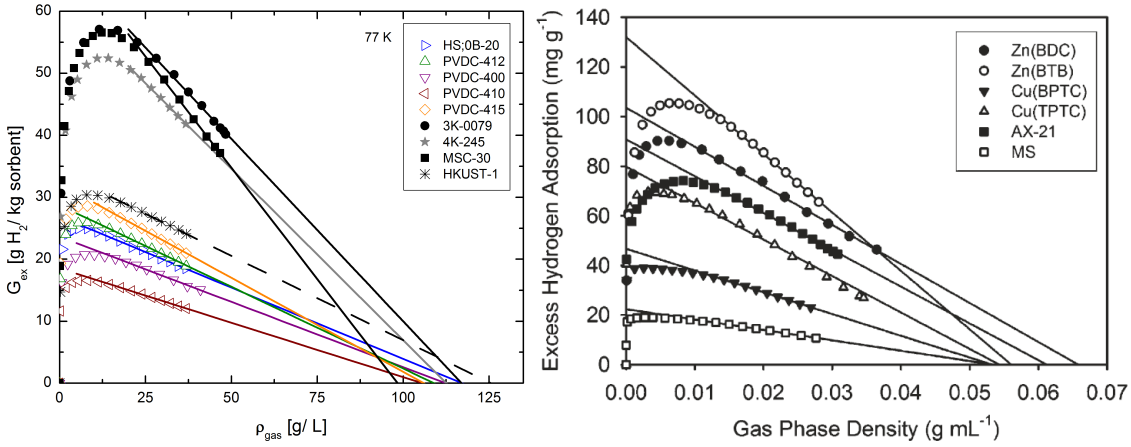

Figure 1.13. Determination of saturated film densities at 77 K at U. Missouri (*left*) and at 50 K by Poirier and Dailly (2009) (*right*).

Table 1.6. Film thicknesses calculated from $V_{film}/(\Sigma \cdot m_s)$ and pore filling factors.

Sample	d_{film} **(nm)**	**Pore-filling Factor**
HS;0B-20	0.24 ± 0.02	53%
PVDC-412	0.25 ± 0.03	40%
PVDC-400	0.27 ± 0.03	44%
PVDC-410	0.26 ± 0.03	28%
PVDC-415	0.25 ± 0.04	44%
MSC-30	0.26 ± 0.02	34%
3K-0079	0.23 ± 0.03	34%
4K-245 (3.8 wt% boron)	0.23 ± 0.04	25%
HKUST-1	0.14 ± 0.03	26%

Chahine rule

Chahine's rule, in a somewhat recent formulation [R. Chahine, *DOE Hydrogen Storage Principal Investigator/Contractor Meeting*, Washington, DC, November 27-28, 2012], states:

1) Excess adsorption of H_2 (at $T = 77$ K and $p = p_{max}$) is 2 wt% per 1000 m^2/g of BET surface area;
2) Excess adsorption of H_2 in micropores is 50 kg per m^3;
3) The average storage density of H_2 in micropores varies from 61 to 71 kg per m^3 which is the same as LH_2 @ 20 K.

(It is mostly Rule 1 that goes by name Chahine's rule, originally put forth in 1996.) The U. Missouri version of Chahine's rule has been that excess adsorption per BET surface area, often referred to as areal excess adsorption in this report or surface excess concentration, is about the same for most adsorbents,

$$G_{ex}(p_{max}(T), T)/\Sigma \sim 20\ \mu g/m^2 \text{ at } T = 77\ K$$

and we have taken departures from this value as indicator of higher (or lower) binding energy from the normal value of 5 kJ/mol for carbon and related materials. A particularly striking departure from Chahine's rule was, in fact, observed for HS;0B-20, where areal excess adsorption was ~30% and ~60% higher, at 77 K and 296 K, respectively, than on the commercial reference carbon MSC-30 (Fig. 1.14). This was attributed to the high binding energy, 8-11 kJ/mol. The alternative, that high areal excess adsorption on HS;0B-20 might be due to the high saturated film density can be ruled out because both materials have $\varrho_{film,sat} \sim 100$ g/L. The departure of HS;0B-20 from Chahine's rule also highlights that most interesting differences between materials may not occur at $p = p_{max}$ for each material, but at a fixed pressure $p < p_{max}$.

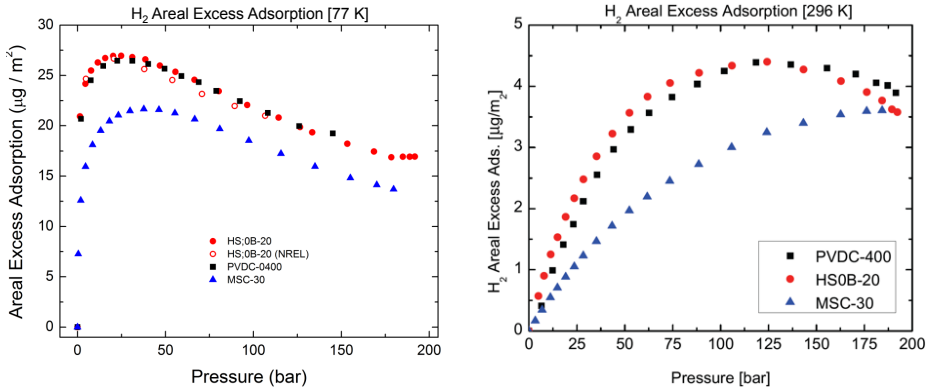

Figure 1.14. Areal excess adsorption on HS;0B-20 is ~30% and ~60% higher than on MSC-30, at 77 K and 296 K, respectively.

Departures from Chaine's rule may also occur for reasons other than high or low binding energy. In the light of the result (1.51) in Sect. 1.3.3 that the "two-fluid-weighted" surface area is systematically lower than the BET surface area, departures from the Chahine rule may come from using the "wrong surface area."

2. Adsorbent Engineering I: Undoped Nanoporous Carbon (Phase 1)

2.1 Material Structure Characterization

A systematic study was carried out to investigate the effect of KOH:C (mass ratio) and activation temperature on the activated carbon structure and hydrogen adsorption characteristics. Surface area and porosity data for these samples are given in Table 2.1 below. Increasing the activated temperature reduced the micropore volume (pores < 10 Å) and increased the mesopore volume (pores > 10 Å) (Figures 2.1 and 2.3). Increasing the KOH:C resulted in an increase in mesopore volume but had a negligible effect on the micropore volume (Figure 2.2). Ultra-small angle x-ray scattering (USAXS) and small angle x-ray scattering (SAXS) corroborated the nitrogen data. As the activation temperature is increased for sample 3K, there was a decreasing presence of a "knee" in the scattering curves at approximately 2 $Å^{-1}$ which indicates and increase in the contributions to the scattering intensity from mesopores (Figure 2.3).

Table 2.1. List of surface areas and porosities for KOH activated carbons.

Sample	Surface Area (m^2/g)	Porosity
2.5 K 800 °C	1900	0.69
3K 700 °C	2200	0.65
3K 790 °C	2600	0.78
3K 800 °C	2600	0.78
3K 900 °C	2500	0.78
3K 1000 °C	2000	0.78
3.5K 700 °C	2000	0.70
3.5K 800 °C	2500	0.75
3.5K 900 °C	2500	0.78
4K 790 °C	2600	0.81
5K 790 °C	3200	0.81
6K 790 °C	2700	0.80

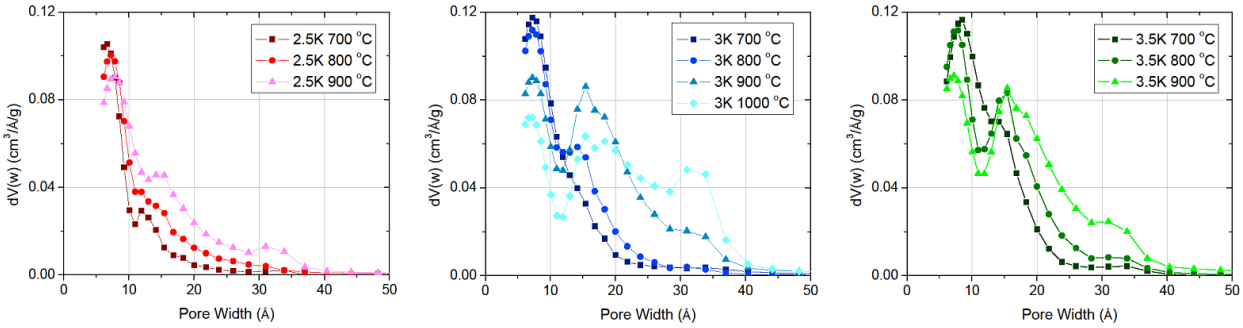

Figure 2.1. Pore size distributions for 2.5K activated at 700, 800, and 900 °C (*left*), 3K activated at 700, 800, 900, and 1000 °C (*center*), and 3.5 K activated at 700, 800, and 900 °C (*right*). In all cases, increasing the activated temperature reduced the micropore volume (pores <10 Å) and increased the mesopore volume (pores > 10 Å). [J. Romanos *et al*., Nanotechnology **23**, 015401 (2012)]

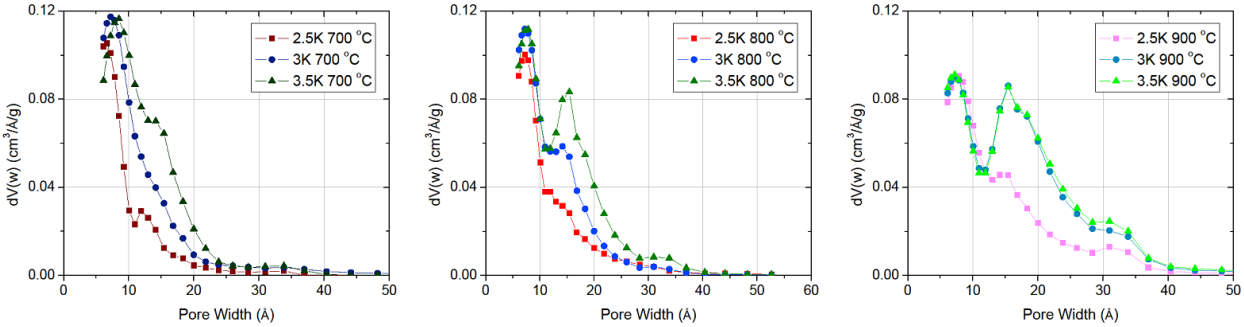

Figure 2.2. Pore size distributions for 2.5K, 3K, and 3.5K activated at 700 °C (*left*), 2.5K, 3K, and 3.5K activated at 800 °C (*center*), and 2.5K, 3K, and 3.5K activated at 900 °C (*right*). In all cases, increasing the KOH:C resulted in an increase in mesopore volume (pores > 10 Å) but had a negligible effect on the micropore volume (pores < 10 Å). [J. Romanos *et al.*, Nanotechnology **23**, 015401 (2012)]

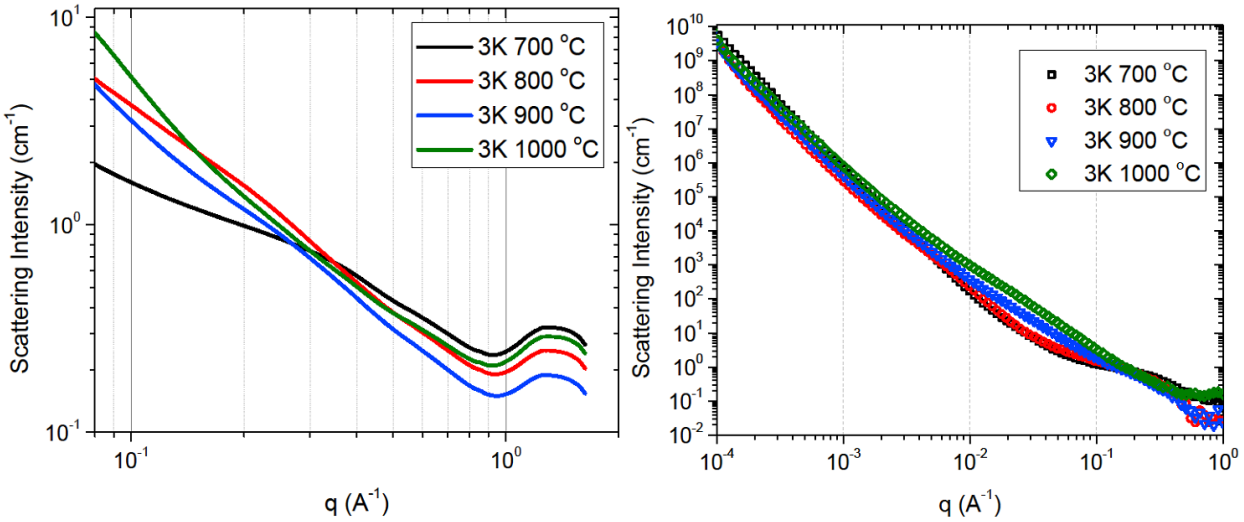

Figure 2.3. Small Angle X-ray Scattering (*left*) and Ultra-Small Angle X-ray Scattering (*right*) data for 3K activated at different temperatures. The diminishing presence of a "knee" in the scattering curve at indicates an increasing contribution to the scattering from mesopores (pores > 10 Å), i.e. an increase in the total volume of mesopores.

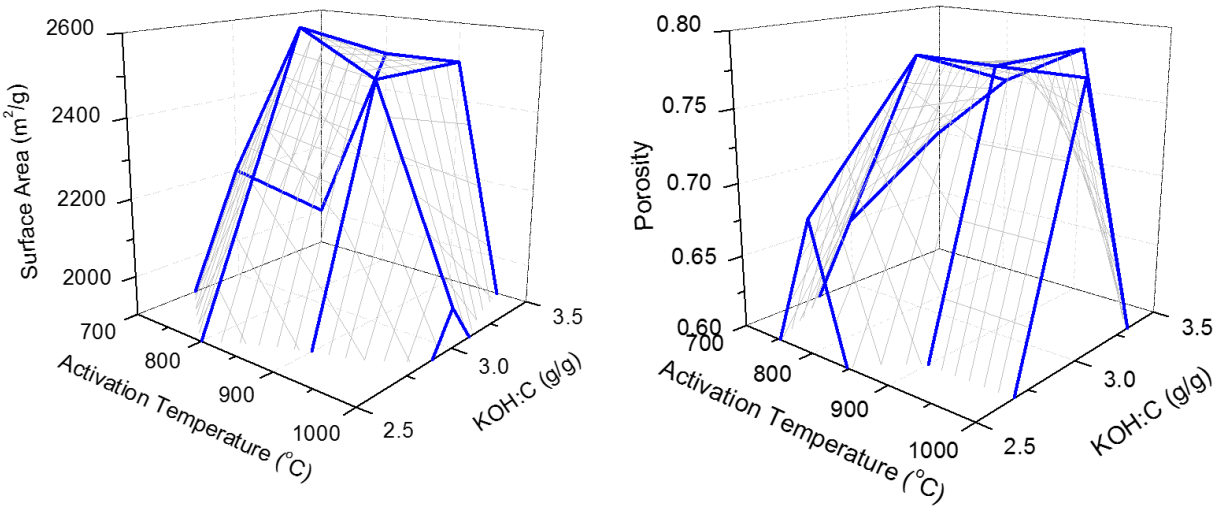

Figure 2.4. 3D plots of surface area (left) and porosity (right) as a function of activation temperature and KOH:C. From these graphs, it is clear that a KOH:C ratio of 3 gives the maximal surface area and porosity.

2.2 Hydrogen Measurement Validation

Excess adsorption on the standard carbon reference sample, AX-21 MSC-30, was measured at 77 K and compared with published data on samples from the same commercial product line ("Maxsorb", "MSC30", manufactured by Kansai Coke and Chemical Co., Ltd., Japan), measured by other groups. The agreement between our data and such published data is excellent (Figure 2.5). From these comparisons, we concluded that our instrument and operational procedures are functioning properly.

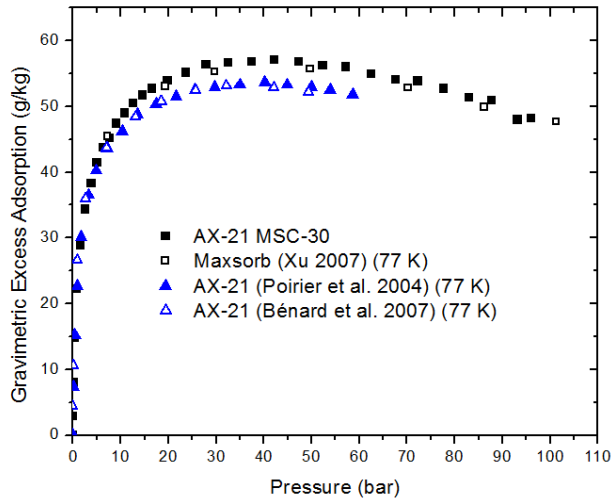

Figure 2.5. Comparison of MU data on AX-21 MSC-30 [black full squares] with data on "Maxsorb" measured by W. Z. Xu et al., Int. J. Hydrogen Energy 32, 2504-2512 (2007) [black open squares].

2.3 Surface Area, Porosity and Hydrogen Adsorption Data

Room Temperature (303 K) Data

Gravimetric excess adsorption, gravimetric storage capacity, and volumetric storage capacity of 2K, 2.5K, 3K, 3.5K, 4K, 5K, and 6K at various KOH:C ratios and activation temperatures were measured at dry-ice and room temperature with the Hiden HTP-1 Volumetric Analyzer.

Table 2.2. Summary of gravimetric excess adsorption, gravimetric storage capacity, and volumetric storage capacity at room temperature (303 K), all measured on the Hiden instrument. For briquettes, a small piece of the monolith was analyzed.

Sample	Surface Area (m^2/g)	Porosity	Room Temp. Grav. Excess Adsorption (100 bar) (g/kg)	Room Temp. Grav. Storage Capacity (100 bar) (g/kg)	Room Temp. Vol. Storage (100 bar) (g/L)	Number of Room Temp. Isotherms Averaged
2K-0286	1900	0.70	6.6	15.6	9.3	2
2.5 K 800 °C	1900	0.69	5.3	13.2	8.2	1
2.5K-0807	2400	0.74	7.8	18.9	9.8	2
3K-0285	2600	0.77	7.7	20.9	9.5	2
3K 700 °C	2200	0.65	6.7	13.3	9.3	1
3K 790 °C	2600	0.78	9.3	21.8	9.6	3
3K 800 °C	2600	0.78	7.5	19.4	8.5	1
3K 900 °C	2500	0.78	8.3	20.9	9.2	1
3K 1000 °C	2000	0.78	6.0	18.5	8.1	1
3.5K 700 °C	2000	0.70	6.3	14.6	8.8	1
3.5K 800 °C	2500	0.75	8.5	19.6	9.8	1
3.5K 900 °C	2500	0.78	7.5	20.7	9.1	1
4K 790 °C	2600	0.81	5.6	20.6	7.8	5
4K-0284	2600	0.81	7.9	24.6	9.3	2
5K-0280	2700	0.84	7.5	27.4	8.9	2
5K 790 °C	3200	0.81	6.5	21.5	8.2	1
6K-0802	2600	0.85	7.4	28.9	8.8	1
6K 790 °C	2700	0.80	7.7	21.8	8.7	2

Fig. 2.6, 2.7, and 2.8 (below) show the room-temperature isotherms for the 3K series (KOH:C = 3.0), 3.5K series (KOH:C = 3.5), and top performers from all series, respectively. The isotherms in the 3.5K series are for the first time in the pressure range 0-200 bar, taking advantage of the upgrade of the Hiden instrument described in the Quarter 8 report.

In the 3K series, Fig. 2.6, sample 3K 790 °C is the best overall powder performer at room temperature. Sample 3K 800 °C is underperforming by all measures, possibly due to the change in the type of KOH used for activation. In some sample preparations, a KOH solution was used instead of KOH flakes to activate the carbons. The change caused a significant change in the

physical characteristics of the samples. Activation with KOH solution gave lower surface area and hydrogen uptake.

In the 3.5K series, Fig. 2.7, sample 3.5K 800 °C is the best performer in terms of gravimetric excess adsorption and volumetric storage capacity. Sample 3.5K 900 °C is the best performer in terms of gravimetric storage capacity.

From Fig. 2.7 and 2.8, we conclude that the optimal activation temperature is near 800 °C since those samples perform best in terms of gravimetric excess adsorption and volumetric storage capacity. (Excluded in this assessment is 3K 800 °C, which is believed to be atypical because of activation with KOH solution as mentioned above.)

Altogther (Fig. 2.8), 3K at 790 °C is the best performer at room temperature by all criteria—gravimetric excess adsorption, gravimetric storage capacity, and volumetric storage capacity.

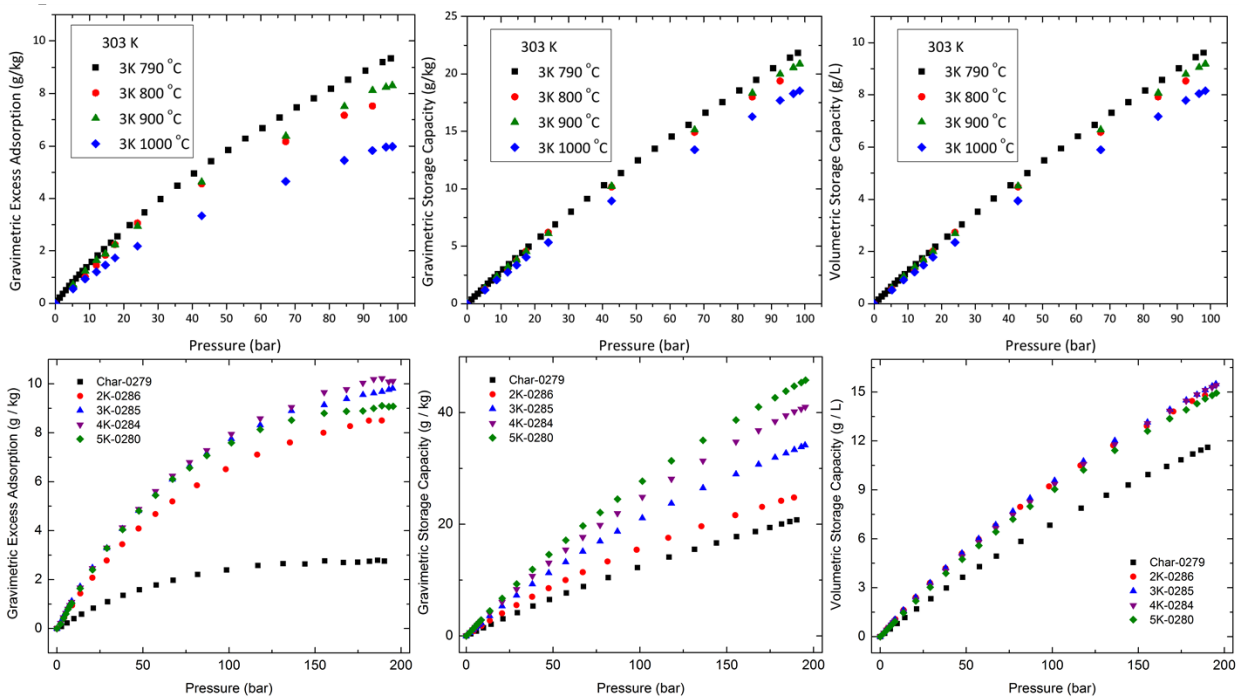

Figure 2.6. Room-temperature data: gravimetric excess adsorption (*left*), gravimetric storage capacity (*center*), and volumetric storage capacity (*right*). *Top*: 3K activated at 790, 800, 900, and 1000 °C. *Bottom*: Carbon samples activated at 790 °C with various KOH:C ratios.

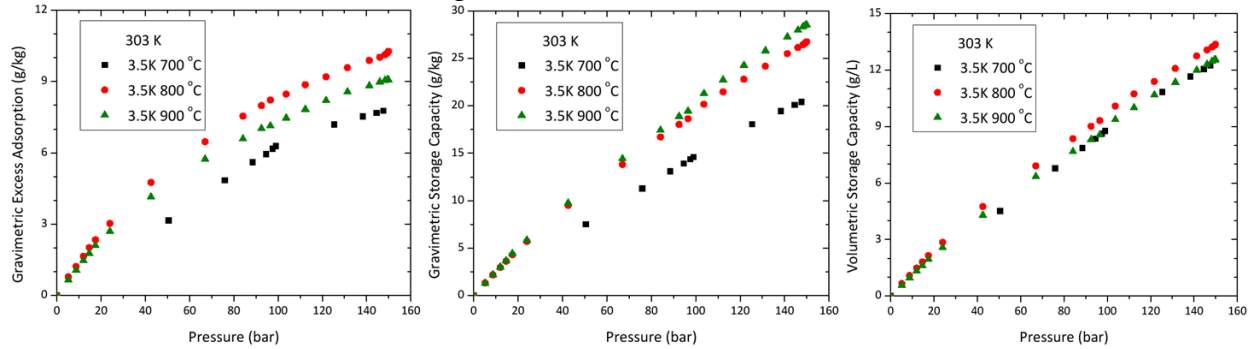

Figure 2.7. 3.5K room-temperature data: gravimetric excess adsorption (*left*), gravimetric storage capacity (*center*) and volumetric storage capacity (*right*), all at 303 K, of sample 3.5K activated at 700, 800, 900 °C.

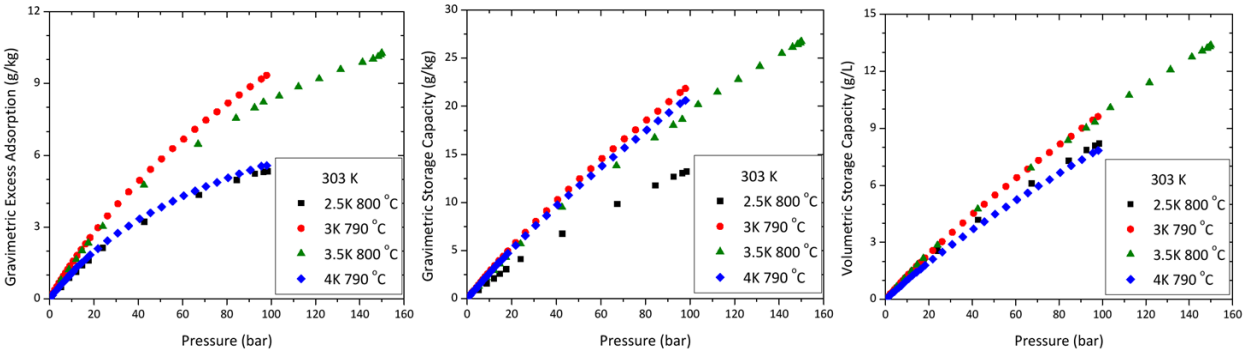

Figure 2.8. Optimized room-temperature data: comparison of gravimetric excess adsorption (*left*), gravimetric storage capacity (*center*), and volumetric storage capacity (*right*) of the best performing carbons at 303 K.

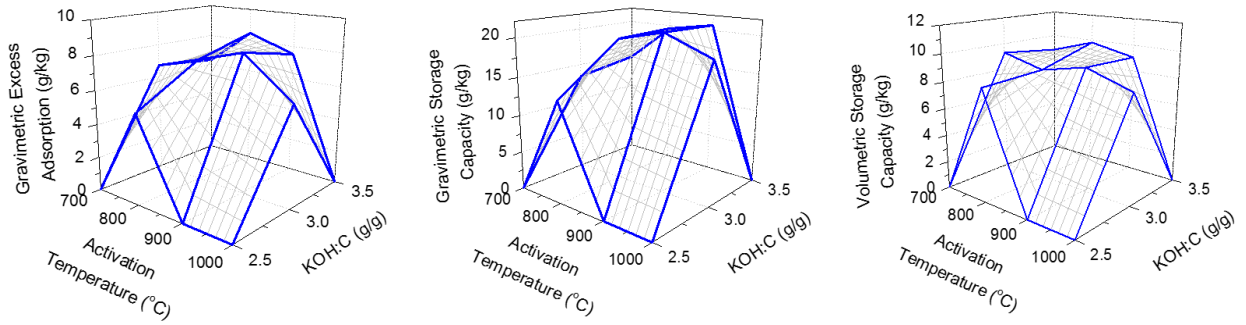

Figure 2.9. 3D plots of gravimetric excess adsorption (*left*), gravimetric storage capacity (*center*) and volumetric storage capacity (*right*) as a function of activation temperature and KOH:C. Using these data and the data in Figure 2.8, we conclude that 3K activated at 790 °C represents the best balance between gravimetric and volumetric storage.

Dry-Ice Temperature (194 K) Data

Table 2.3.Summary of gravimetric excess adsorption, gravimetric storage capacity, and volumetric storage capacity at dry-ice temperature (194 K). N/A: not available.

Sample	Surface Area (m^2/g)	Porosity	Dry Ice Temp. Grav. Excess Adsorption (100 bar) (g/kg)	Dry Ice Temp. Grav. Storage Capacity (100 bar) (g/kg)	Dry Ice Temp Vol. Storage (100 bar) (g/L)	Number of Dry Ice Temp Isotherms Averaged
2.5 K 800 °C	1900	0.69	16.4	29.0	18.0	1
3K 700 °C	2200	0.65	20.5	31.0	13.6	1
3K 790 °C	2600	0.78	N/A	N/A	N/A	N/A
3K 800 °C	2600	0.78	21.7	40.4	17.8	1
3K 900 °C	2500	0.78	23.2	43.3	19.0	1
3K 1000 °C	2000	0.78	18.3	38.2	16.8	1
3.5K 700 °C	2000	0.70	18.8	32.0	19.2	1
3.5K 800 °C	2500	0.75	22.3	38.9	19.4	1
3.5K 900 °C	2500	0.78	22.7	43.6	19.2	1
4K 790 °C	2600	0.81	N/A	N/A	N/A	N/A
5K 790 °C	3200	0.81	N/A	N/A	N/A	N/A
6K 790 °C	2700	0.80	N/A	N/A	N/A	N/A

Fig. 2.10 shows the isotherms of the best dry-ice performers in the 3K series that have been measured. Performance of samples 3K 800 °C and 900 °C at dry-ice temperature is virtually indistinguishable, similar to the indistinguishable performance of the two samples at room temperature (Fig. 2.6). At dry-ice temperature, sample 3.5K 900°C at this time appears to be the best performer in terms of gravimetric storage capacity (Fig. 2.10, center).

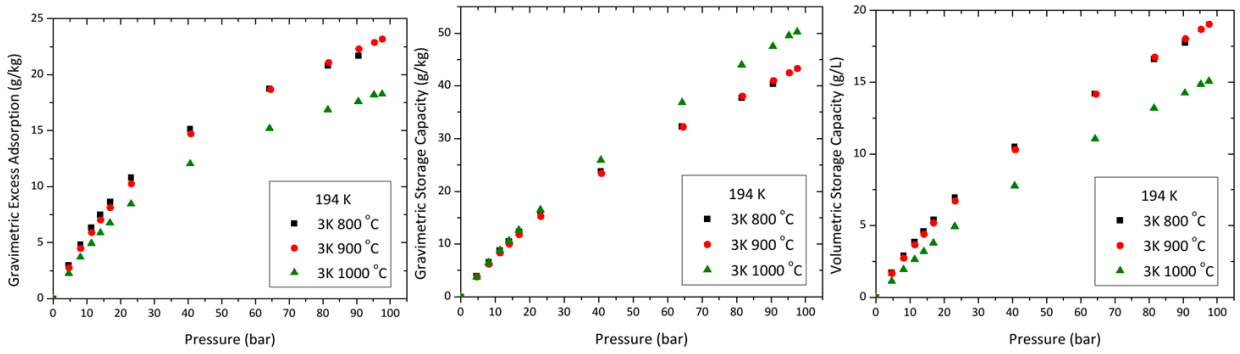

Figure 2.10. Gravimetric excess adsorption (*left*), gravimetric storage capacity (*center*) and volumetric storage capacity (*right*) of sample 3K activated at 800, 900, and 1000 °C and tested at dry-ice temperature (194 K).

Cryogenic (77 - 80 K) Storage

Table 2.4. Summary of gravimetric excess adsorption, gravimetric storage capacity, and volumetric storage capacity at cryogenic temperatures (77 K), all measured on the Hiden instrument.

Sample	Surface Area (m^2/g)	Porosity	Cryogenic Grav. Excess Adsorption (100 bar) (g/kg)	Cryogenic Grav. Storage Capacity (100 bar) (g/kg)	Cryogenic Vol. Storage (100 bar) (g/L)	Number of Isotherms Averaged
2K-0286	1900	0.70	34.3	70.3	42.3	1
2.5K-0807	2400	0.74	42.8	87.1	45.3	2
3K-0285	2600	0.77	47.9	100.9	45.8	3
4K-0284	2600	0.81	51.3	118.4	44.5	2
5K-0280	2700	0.84	53.7	133.5	43.5	3
6K-0802	2600	0.85	51.2	137.4	42.1	1

Below are 77 K isotherms for undoped and boron-doped carbons, averaged from multiple measurements. All carbon samples here were activated at 790 °C. All repeated measurements agree within better than 5% in the range 1-200 bar. Often, the agreement between repeat measurements is within 1%.

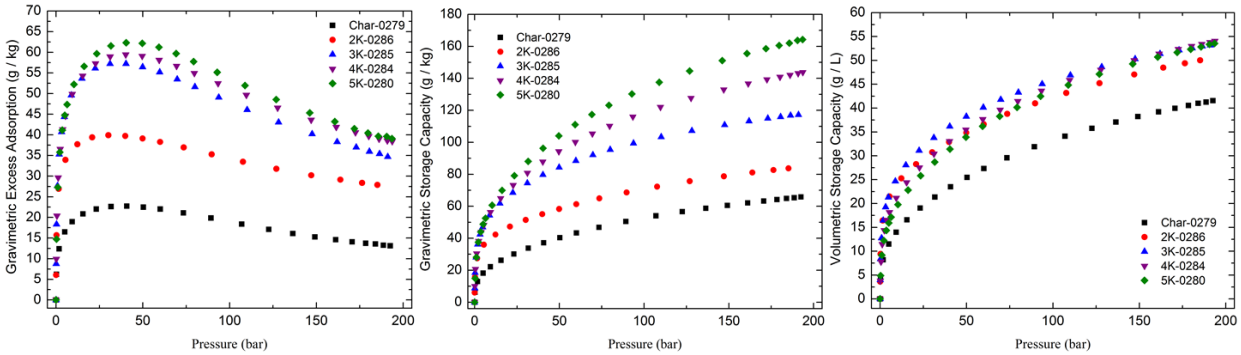

Figure 2.11. Gravimetric excess adsorption (*left*), gravimetric storage capacity (*center*) and volumetric storage capacity (*right*) of samples activated using various KOH:C ratios and tested at cryogenic temperatures (77 K). Isotherms here are averages of repeated measurements. All repeated measurements agree within better than 5% in the range 1-200 bar.

Below are 80 K isotherms for undoped and boron-doped carbons, averaged from multiple measurements. All carbon samples here were activated at 790 °C. All repeated measurements agree within better than 5% in the range 1-40 bar, and within 5-7% in the range 40-100 bar. Often, the agreement is within better than 1%. E.g., the individual isotherms for "3K" are indistinguishable from the average shown in the graph. "HS;0B," and "HS:2B" were samples prepared for another project made from carbonization of polyvinylidene chloride and contain only micropores. Samples "3K," "4K (6/09)," "4K (12/09)", "AX-21 MSC-30," and "HS;0B"

are boron-free carbons. All other samples are boron-doped carbons. Samples "4K (6/09)" and "4K (12/09)" are from the same batch, but were measured in March and June 2009, and in December 2009, respectively. The large drop in adsorption from June 2009 to December 2009 is attributed to a loss of high binding energies due to slow oxidation by air. Other large differences in adsorption seen in the isotherms are due to differences in surface areas and/or binding energies (Table 2.3). Of special interest in this and the next section is the question whether the irradiated sample "3K-H6 (II, A) Irr 1min" [open purple squares] exhibits a hydrogen isotherm that is significantly different from that of the unirradiated parent material, "3K-H6 (II, A)" [full purple squares], because of a difference in surface area, difference in binding energies, or both. The pressures pmax ~ 23 bar and pmax ~ 40 bar for the two samples show that the irradiated sample hosts higher binding energies (Quarter 6 report; Section 2.5).

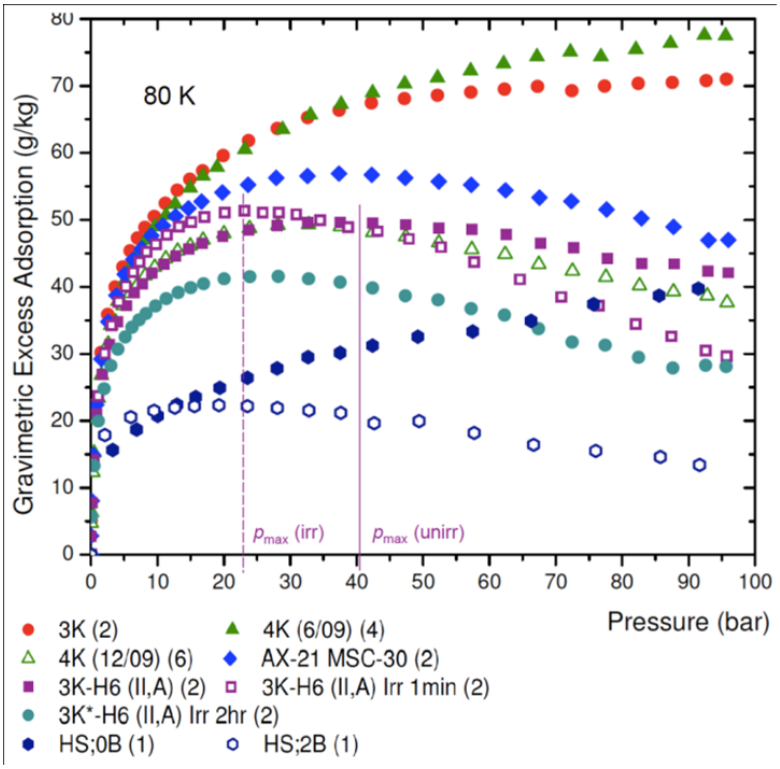

Figure 2.12. Isotherms here are averages of repeated measurements; the number in parenthesis shows how many individual isotherms were averaged. All repeated measurements agree within better than 5% in the range 1-40 bar, and within 5-7% in the range 40-100 bar.

From the data presented in this section, we concluded that 3K 790°C is the best candidate for use in the 5.3-liter test fixture and the best starting point for boron-doping experiments.

3. Adsorbent Engineering II: High-Surface-Area B_xC Materials (Phase 1)

3.1 Theoretical Modeling of Hydrogen Adsorption on Boron-Doped Graphene

Adsorption potentials for boron-substituted graphene were computed from first principles and showed binding energies (potential well depths) of 12 kJ/molfor 10 wt% boron. Grand Canonical Monte Carlo (GCMC) simulations in this potential predict gravimetric and volumetric storage capacities of 0.050 kg H_2/kg carbon and 0.032 kg H_2/liter carbon, respectively, at 298 K and 100 bar, which will deliver the 2010 DOE targets at room temperature. To generate systematic models of H2 storage on boron-substituted carbons as a function of boron concentration and distribution of boron at the surface and to be able to analyze experimental isotherms accordingly, we computed adsorption potentials for boron-substituted graphene from first principles and performed GCMC simulations of H_2 adsorption in these potentials. Results are shown in the figures below. Boron substitution creates potential wells with binding energy (potential well depth) of ~5, 8, 9, and 12 kJ/mol for 0, 1, 5, and 10 wt% boron, respectively. The simulations predict gravimetric and volumetric storage capacities of 0.050 kg H_2/kg carbon and 0.032 kg H_2/liter carbon for 10 wt% boron, 298 K, and 100 bar (Fig. 3.1a).

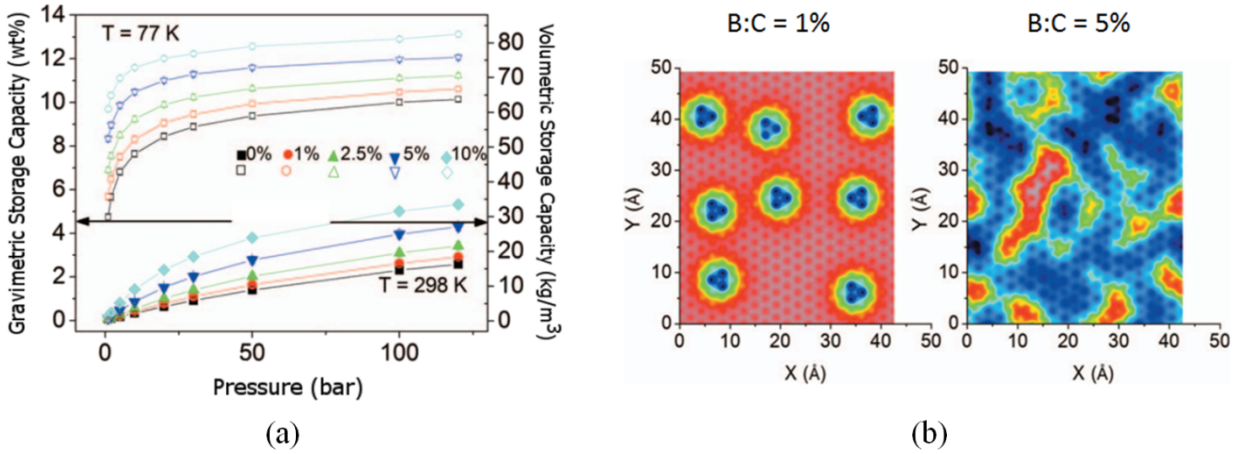

Figure 3.1. (a) Gravimetric (left axis) and volumetric (right axis) storage capacity of hydrogen in graphene slit shaped pores of width d = 1.2 nm as a function of pressure and the percentage of boron content in the pore wall, for T = 77 and 298 K. For reference, the arrows indicate both gravimetric and volumetric U.S. DOE targets required to be reached by 2010 by the storing system. (b) Energy landscape of graphite surface containing 1% (left) and 5% (right) of substitutional boron atoms. Substitution is assumed to be random. Isoenergetic lines are separated by $\Delta E/k_B$ = 10 K; the color code on both graphs is identical: from -580 K (pink gray) to -1100 K (dark navy).

3.2 Fabrication and Analysis of B_xC Materials

Twenty-four samples were made using deposition of decaborane and 20 samples were produced using impregnation with boron compounds under Task 1 (Quarters 1-3) and tested under Task 2 (Quarters 1-3). Notable samples from those produced during this time are listed in Table 3.1. Initial hydrogen measurements showed a decrease in gravimetric excess adsorption and storage capacity upon boron doping (Quarter 4 and 5 reports) and a decrease in surface area. It was

determined that samples doped with decaborane or by impregnation of boron containing compounds were very sensitive to oxygen due to the vacant p_z orbital present after doping. Because sample created using an impregnation of boron containing compounds could not be created in the absence of oxygen or moisture, future production and characterization of these material was discontinued (Quarter 4). Production of new samples using deposition of decaborane was suspended until equipment could be purchased and implemented to fabricate and measure samples without exposing them to oxygen or moisture. However, irradiated samples were still studied under Task 3 (see Section 2.3.)

Table 3.1. List of notable boron doped samples prepared.

Sample	Fabrication Method	B:C	Surface Area (m^2/g)
3K-H5 (III, A)	DB deposition method III	0.008	3200
3K-H6 (II, A)	DB deposition method II	0.014	2400
3K-H7 (I, A)	DB deposition method I	0.060	2300
3K*-H6 (II,A)	DB deposition method II using carbon activated in alumina crucible	0.019	2900
3K*-H7 (I,A)	DB deposition method II using carbon activated in alumina crucible	0.069	2000

Four samples were manufactured and measured under oxygen free conditions and are listed in Table 3.2 below. A reduction in surface area and pore volume was observed for all samples (Fig. 3.2). In the case of 3K-H60 (I,A), the gravimetric excess adsorption was higher at pressures greater than 100 bar despite the reduction in surface area (Fig. 3.3) indicating an increase in the concentration of hydrogen on the surface. The increase in gravimetric excess adsorption at high pressures indicates an increase in binding energy of the largest pores.

Table 3.2. List of boron-doped samples manufactured and measured under oxygen free conditions.

Sample	Precursor	B:C (mass ratio)	Surface Area (m^2/g)	Total Pore Volume (cm^3/g)	Porosity	Date Fabricated
3K 3/3/10 B	N/A	N/A	2700	1.682	0.77	3/3/10
3K-H30 (I,A)	3K 3/3/10 B	0.084	2300	1.536	0.75	7/10
3K-H31 (III,A)	3K 3/3/10 B	0.100	2000	1.329	0.73	7/10
3K 3/3/10 B (outgassed at 600 °C)	N/A	0.003	2600	1.587	0.76	11/10
3K-H60 (I,A)	3K 3/3/10 B (outgassed at 600 °C)	0.082, 0.089	2100	1.387	0.74	11/10
3K-H60 (I,B)	3K 3/3/10 B (outgassed at 600 °C)	0.065, 0.069	2100	1.290	0.72	12/10

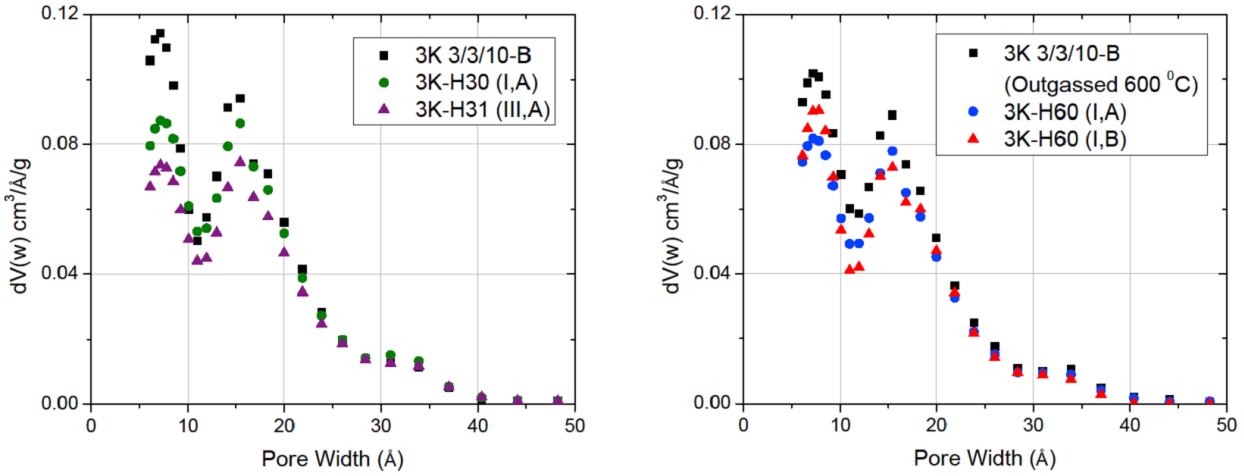

(a) (b)

Figure 3.2. (a) Pore size distribution for samples "3K 3/3/10-B", "3K-H30 (I,A)" and "3K-H31 (III,A)." Before boron doping, sample 3K3/3/10-B was outgassed at 200-250°C for 72 hours to remove oxygen. (b) Pore size distribution for samples "3K 3/3/10-B (Outgassed at 600 °C)", "3K-H60 (I,A)", and "3K-H60 (I,B)." Before boron doping, sample 3K 3/3/10-B was outgassed at 600 °C for 63 hours.

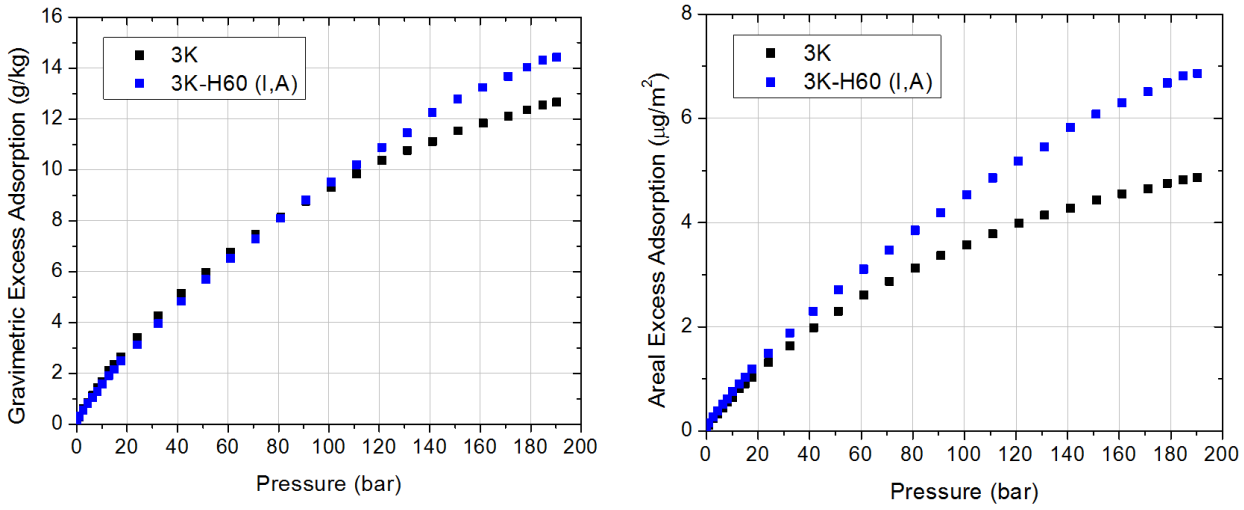

(a) (b)

Figure 3.3. (a) Gravimetric excess adsorption for samples 3K 3/3/10 (Outgassed at 600 °C) and 3K-H60 (I,A). The increase in excess adsorption at higher pressures indicates an increase in binding energy of the lowest binding energy sites (the larger pores). (b) Areal excess adsorption for samples 3K 3/3/10 (Outgassed at 600 °C) and 3K-H60 (I,A). The areal excess adsorption tim' To avoid liquid $B_{10}H_{14}$ condensation in the pores, which can occur when it is allowed to melt in close proximity to the carbon, an effort to perfom deposition facilitated via Ar flow (pure vapor deposition) was undertaken. It is theorized that Ar will help overcome the strong $B_{10}H_{14}$-C binding energy (70-80 kJ/mol) in diffusion inward through the pore space. The results shown in Table 3.3 below.

Table 3.3. List of boron doped carbons manufactured under oxygen-free conditions with deposition facilitated by Ar flow.

Sample	g_{DB}/g_C	Ar Flow Rate [cm^3/s]	Deposition Cell Press. [bar(g)]	B:C [wt%]	Doping Efficiency (PGAA/stoich)	Σ [m^2/g]	ϕ
0224-3K-600C	N/A	N/A	N/A	N/A	N/A	2700	0.79
0230-3K-DB2 (V,C)	0.125/1	22.5	1.5	1.6	0.16	2300	0.78
0231-3K-DB2 (V,C)	0.125/1	5.63	1.5	3.0	0.30	2200	0.75
0234-3K-DB2 (V,C)	0.125/1	5.63	0.2	5.2	0.52	1900	0.72
0235-3K-DB2 (V,C)	0.5/1	5.63	1.5	11	0.35	1700	0.72

Samples were produced under a variety of environments to determine the optimal deposition conditions (flow rate and cell pressure). The greatest final boron content was determined from low flow (5.6 cm^3/s) and low pressure (0.2 bar(g)), a result which was reproducible upon using a larger initial concentration of $B_{10}H_{14}$ to C. All of the manufactured samples yielded boron contents far in excess than what was observed in the absence of a carrier gas (Fig 3.4).

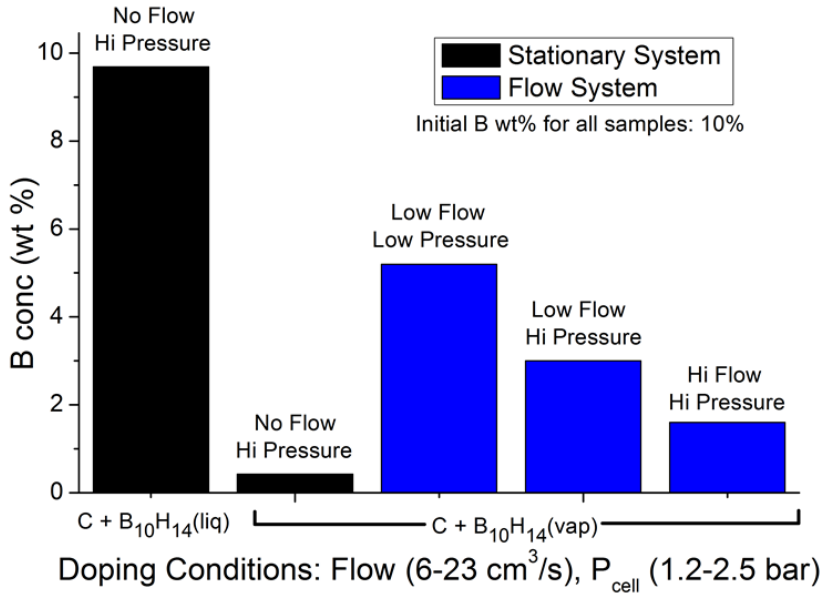

Figure 3.4. Boron concentrations of samples produced with and without the presence of an Ar carrier gas. All samples used a quantity of $B_{10}H_{14}$ equivalent to 10 weight percent B:C. For the first time, MU has demonstrated a significant quantity of B deposited on C entirely in the vapor phase.

For future experiments, a phase diagram for decaborane was constructed using various literature sources (Fig. 3.5). During the entire doping process, all of the decaborane must be in the gas phase before decomposition to ensure an even coating of boron on the surface and to prevent blocking of pores. A condition was developed relating the mass ratio of decaborane used χ_{DB}, density of the starting carbon material ρ_{bulk}, the initial pressure p_i at room temperature, and the initial and final temperatures T_i (room temperature) and $T_f$to the vapor pressure at a given final temperature and is given by

$$p_{vapor}(T_f) > \frac{\chi_{DB}}{M_{DB}} \frac{\rho_{bulk}\rho_s}{\rho_s - \rho_{bulk}} RT_f + \frac{p_i T_f}{T_i} \quad (3.1)$$

Here M_{DB} is the molar mass of decaborane, ρ_s is the skeletal density of the carbon, and R is the gas constant. If the condition given by equation 3.1 is satisfied, then all of the decaborane will be in the gas phase for any temperature greater than T_f. For measured bulk densities (Quarter 9 report) and the vapor pressure obtained from literature sources, it is necessary to use multiple dopings in order to achieve 10 wt% B:C and ensure that the decaborane is entirely in the gas phase before decomposition.

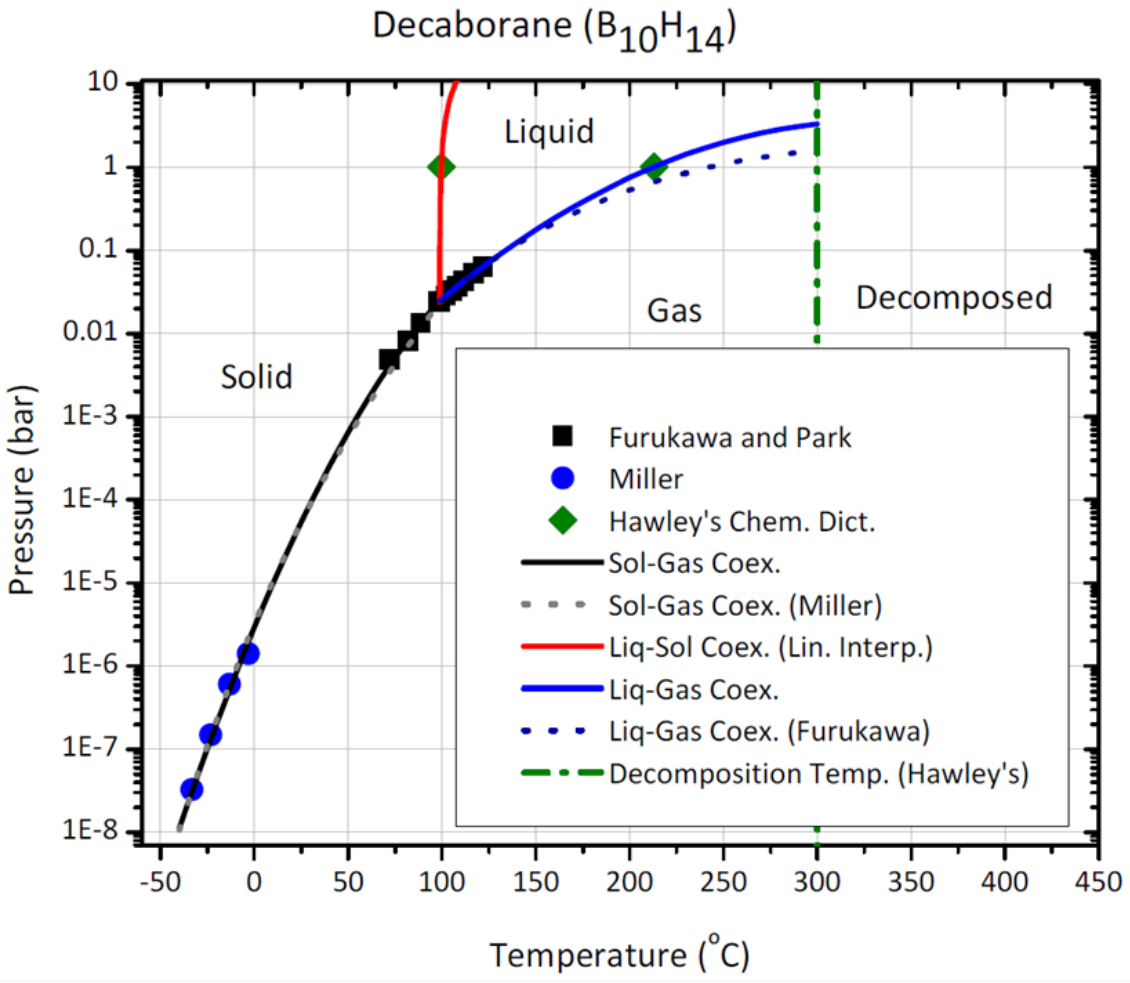

Figure 3.5. Phase diagram for decaborane constructed from various literature sources.

3.3 Estimates of Binding Energies, E_b

Binding energies were evaluated by measuring the isosteric heat of adsorption (Quarter 3, 4, and 6 reports) and by using a single hydrogen adsorption isotherm (Quarter 6 report). The customary method of determining isosteric heats of adsorption, in which the Clausius-Claperyon equation

$$\Delta H = R\frac{T_1 T_2}{T_2 - T_1}\ln\left(\frac{p_2}{p_1}\right) \tag{3.2}$$

is evaluated with pressures p_1 and p_2 from the T_1 = 80 K and T_2 = 90 K isotherms, respectively, at constant excess adsorption leads to unphysical results—such as a rise in isosteric heats at high coverage (instead of a decrease), and a jump to negative isosteric heats at pressures above pmax. The thermodynamically correct way is to evaluate the Clausius-Clapeyron equation at constant absolute adsorption instead of excess adsorption. We implemented this corrected procedure and calculated revised, definitive isosteric heats of adsorption. An illustration of the difference between incorrect and correct evaluation of the Clausius-Clapeyron equation is shown in Fig. 3.6 for sample "AX-21 MSC-30."

Figure 3.7 shows the results for the incorrect (left) and correct (right) isosteric heat of adsorption as a function of excess adsorption (left) and absolute adsorption (right). The curves on the right no longer exhibit the earlier unphysical rise at high pressure/coverage. The data includes the boron-doped unirradiated and irradiated samples "3K-H6 (II, A)" and "3K-H6 (II, A) Irr 1 min" and includes an unusually wide range of coverage, up to absolute adsorption of 5 wt%. Isosteric heats at low/high coverage are high/low and unrepresentative/representative of the average binding energy because adsorbate molecules always go down on sites with high binding energy first (low coverage), and on sites with low binding energy last (high coverage). The isosteric heat for boron-doped samples here, which have all been exposed to oxygen, do not show a significant difference from the undoped precursor, 3K.

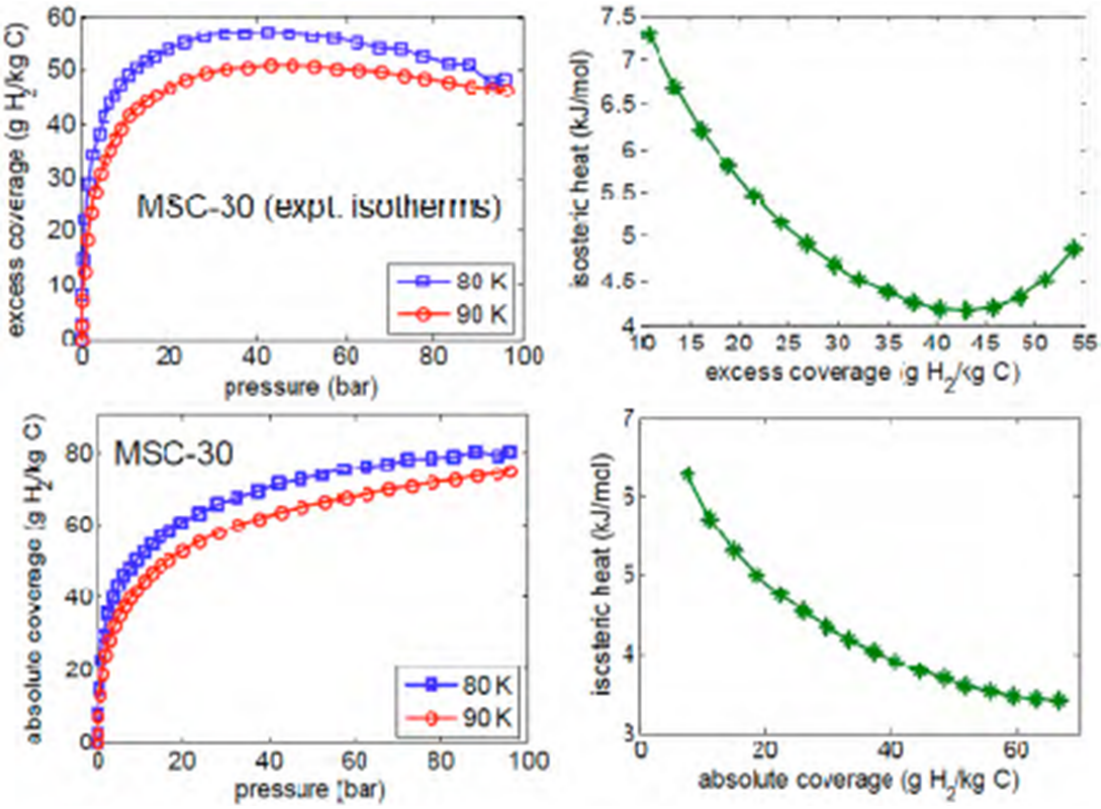

Figure 3.6. Evaluation of Clausius-Clapeyron equation at constant excess adsorption (*top*) and constant absolute adsorption (*bottom*), on reference sample "AX-21 MSC-30". Note the unphysical rise of the isosteric heat at high coverage when excess adsorption is used (*top right*).

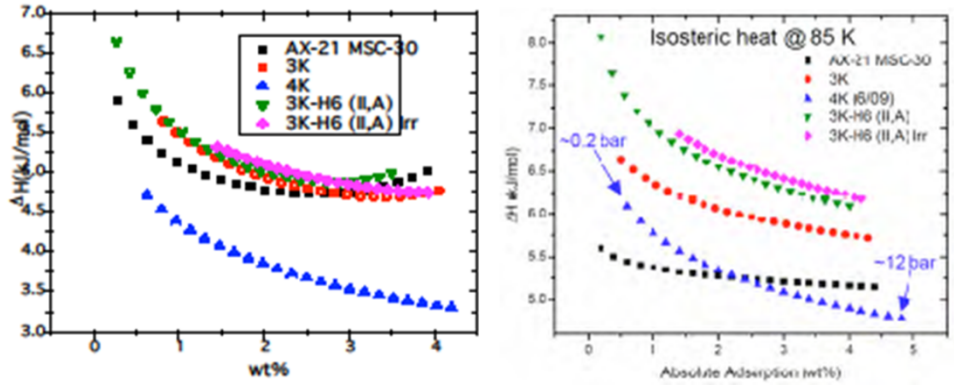

Figure 3.7. Isosteric heats of adsorption, calculated from Eq. (3.2) and excess adsorption (*left*, incorrect, Report 4) and absolute adsorption (*right*, correct).

The second method for estimating binding energies comes from observing the slope of the excess adsorption isotherm at high pressures. The linear drop in excess adsorption in the saturation regime can be used to determine the surface area of samples, as seen by H_2, as follows (G. Aranovich and M. Donohue, J. Colloid Interface Sci.**194**, 392-397 (1997)):

$$G_{ex}(p,T) = \frac{V_{film}(p,T)}{m_s}\left[\rho_{film}(p,T) - \rho_{gas}(p,T)\right] \tag{3.3}$$

$$\overset{p\to\infty}{\sim} \frac{V_{\text{film}}(\infty,T)}{m_{\text{s}}}\left[\rho_{\text{film},\infty}(T) - \frac{pm_{\text{H2}}}{kT}\right] \tag{3.4}$$

$$= G_{abs}(\infty,T) - \frac{\Sigma t(T) p m_{H_2}}{kT} \tag{3.5}$$

Here G_{ex} is gravimetric excess adsorption (mass of excess adsorbed H2 per mass of sample); m_{s} and m_{H2} are the mass of the sample and of an H_2 molecule; V_{film} and ϱ_{film} are the volume and density of the adsorbed film; $\varrho_{\text{gas}} = pm_{H2}/(kT)$ is the density of the non-adsorbed gas; k is Boltzmann's constant; G_{abs} is gravimetric absolute adsorption; Σ is the surface area of the sample per mass of sample; and t is the thickness of the adsorbed film ($V_{\text{film}}/m_{\text{s}} = \Sigma \cdot t$)—with all relevant pressure (p) and temperature (T) dependence displayed. Equation (3.3) is the definition of excess adsorption for general p, T; Eqs. (3.4, 3.5) show the behavior in the saturation regime; and Eq. (3.5) relates the linear behavior to surface area. Thus, if t is known, the slope of the straight line, G_{ex} vs. p, allows us to determine the surface area, Σ, as seen by adsorbed hydrogen.

Finally, as excess adsorption decreases linearly with increasing p, excess adsorption crosses zero at some pressure p_0 ($G_{\text{ex}}(p_0,T) = 0$; $p_0 >> p_{\text{max}}$) and is negative at $p > p_0$. At p_0, the gas density equals the film density, Eq. (3.3). This leads to the remarkable result that, from Eq. (3.3) and the experimental value of p_0, we can determine the film density at saturation,

$$\rho_{film,\infty}(T) = \frac{p_0(T) m_{H_2}}{kT} \tag{3.6}$$

A purely experimental value for the film thickness, free of assumptions about packing of molecules on the surface, is available from the film density at saturation, $t_{\text{film},\infty}$, as determined by the pressure p_0, Eq. (3.6). The film density divided by the mass of an H_2 molecule gives the number density, which counts the number of molecules per volume; the reciprocal of the number density is the volume occupied by one molecule in the saturated film; and the cube root of this volume gives the side length of the molecule, which—for the sake of a well-defined geometric picture—may be modeled as a small cube. When the molecules form a continuous structureless film, as they do, the cubic molecule model drops out, and the film thickness is (number density)$^{-1/3}$. This gives:

$$t(T) = \left[\frac{kt}{p_0(T)}\right]^{1/3} \tag{3.7}$$

$$\Sigma_{H_2} = \left(-\frac{\partial G_{ex}}{\partial p}\right)_{p \gg p_{max}} \frac{\left[(kT)^2 p_0(T)\right]^{-1/3}}{m_{H_2}} \tag{3.8}$$

$$E_{B,ave} = (N_A kT)\ln\left(p_0(T) - \frac{2p_{max}(T)}{p_{max}^2}\left[\sinh\left(\frac{h\nu}{2kT}\right)^3 \sqrt{\frac{\left(8\pi m_{H_2}\right)^3 (kT)^5}{h^6}}\right.\right. \tag{3.9}$$

The factor $(-\partial G_{\text{ex}}/\partial p)$ in Eq. (3.8) is the slope of the excess adsorption isotherm in the linear regime. Equation (3.9) presents an expression for the average binding energy, $E_{\text{b,ave}}$, from the pressure at maximum excess adsorption, p_{max}, and the pressure at which excess adsorption

crosses zero, p_0. It is a quantitative version of the relation between p_{max} and E_b developed above. It was obtained by entering the Langmuir model for localized adsorption into Eq. (3.3).

The results from Eqs. (3.7-3.9) are shown in Table 3.4. The first striking feature is that film thicknesses, t, vary considerably from one material to another and are systematically larger than the thickness of 2.3 Å that gave $\Sigma_{H2} = \Sigma_{N2}$ for "AX-21 MSC-30," and Σ_{H2}= 5500 m^2/g for"3K-H6 (II, A) Irr 1min". In fact, the experimental thicknesses agree well with the simulated thicknesses, 3.1-4.3 Å. The second striking result is that the H_2 and N_2 surface areas do not differ significantly from each other for most samples, if we allow for an experimental uncertainty of ±300 m^2/g in light of the fact that the slope of the excess adsorption isotherm in the linear regime and the intercept with the p axis have uncertainties due to limited precision in extrapolation to high pressures. In particular, $\Sigma_{H2} \sim \Sigma_{N2}$ for the irradiated samples, "3K-H6 (II, A) Irr 1min" and "3K*-H6 (II, A) Irr 2hr."

From this it was concluded that hydrogen and nitrogen do see the same surface after all, on each of "3K-H6 (II, A)," "3K-H6 (II, A) Irr 1min," and "3K*-H6 (II, A) Irr 2hr;" and that fission tracks did not create additional surface area visible only to hydrogen—against all expectations and evidence to the contrary presented in Reports 4 and 5.

Table 3.4. Thickness of H_2 film from Eq. (3.7), saturated film density from Eq. (3.6), surface area from H_2 adsorption from Eq. (3.8), and average binding energy from Eq. (3.9), from hydrogen excess adsorption isotherms. Pressures p_0 are rounded to nearest 10 bar; ϱ_{film}rounded to nearest 0.01 g/cm^3; $-\partial G_{ex}/\partial p$ rounded to nearest 10^{-5} bar^{-1}; $E_{b,ave}$ rounded to nearest 0.1 kJ/mol. The results for samples subjected to boron neutron capture are highlighted in yellow. Also included is the gas density for non-adsorbed H_2 gas at 80 K and 50 bar (last row), for comparison with the saturated film densities, $\varrho_{film,\infty}$.

Sample	p_0 (bar)	p_{max} (bar)	t (Å)	$\rho_{film,\infty}$ (g/cm^3)	$-\partial G_{ex}/\partial p$ (bar^{-1})	Σ_{H2} (m^2/g), Σ_{N2} (m^2/g)	$E_{B,av}$ (kJ/mol) [a]
AX-21 MSC-30	360	~40	3.1	0.11	$2.2 \cdot 10^{-4}$	2300, 2600	6.4
4K (12/09)	270	33	3.4	0.08	$2.2 \cdot 10^{-4}$	2100, 2700 [a]	6.4
3K-H6 (II, A)	300	~40	3.3	0.09	$1.6 \cdot 10^{-4}$	2200[b],3300	6.2 [10.9]
3K-H6 (II, A) Irr 1min	160	23	4.1	0.05	$3.8 \cdot 10^{-4}$	3100, 3000	6.5 [11.2]
3K*-H6 (II, A) Irr 2hr	190	24	3.9	0.06	$2.7 \cdot 10^{-4}$	2300, 2900	6.6 [11.3]
HS:2B	190	21	3.9	0.06	$1.4 \cdot 10^{-4}$	1200, 600	6.9 [11.5]
H_2 gas, 80 K & 50 bar	–	–	–	0.016	–	–	–

[a]) With ν for H_2-graphite potential. In bracket: with ν estimated for H_2-B/C potential
[b]) Uncertain due to uncertainty in extrapolation to high pressure

4. Adsorbent Engineering III: Monolith Materials (Phase 1)

4.1 Monolith Fabrication and Characterization

The 0.5-liter hydrogen test fixture (HTF) (Fig. 4.1) was designed by the Midwest Research Institute (MRI), in collaboration and consultation with the University of Missouri (MU). The HTF operates in the pressure range of 1-300 bar at room temperature under an inert atmosphere. MU personnel received training from MRI staff member after MU received the fixture.

To outgas samples to be tested in the chamber, a transfer vessel was constructed. Each sample was outgassed for 24 hrs at 200 ºC prior to analysis. After the first run, the sample was left in the test tank for 2nd, 3rd, 4th and 5th runs (first isotherm set). After the 5th run, the sample was removed from the test tank and outgassed for 24 hrs at 200 ºC again. The sample was reloaded into the test tank for a second set of isotherms to verify data repeatability.

To test samples in the form of a powder rather than as a monolith, a special cell was constructed with the same shape as a monolith (3.5" diameter, 0.75" height), but designed to hold carbon powder ("powder monolith").

Blank isotherms (isotherms in the absence of adsorbent in the sample chamber) were run on the HTF to determine potential error sources. Since the instrument contained no adsorbent, the results represent instrument fluctuations and show that every data point may have an uncertainty of 0.03 g of hydrogen.

Figure 4.1. 0.5-liter Hydrogen Test Fixture

Activated carbons were pressed into monoliths at 15000 psi using PVDC as a chemical binder and were characterized as shown in Fig. 4.2 before being tested on the 0.5-liter test fixture. Table 4.1 compares the BET surface areas and porosities of the briquettes and reference carbon MSC-30.

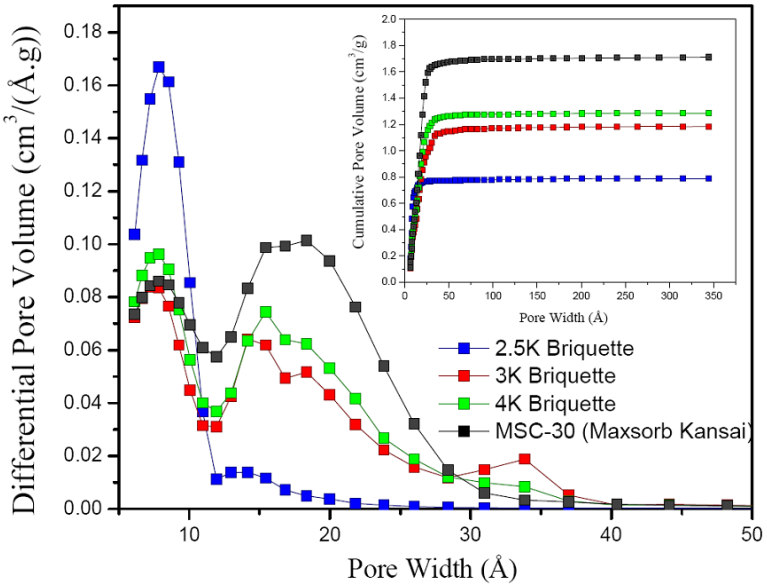

Figure 4.2. Comparison of pore size distribution as a function of KOH:C ratio of 2.5K, 3K, 4K briquettes and MSC-30 powder (a reference carbon).

These results show that the cumulative pore volume/mass of briquettes is proportional to the KOH:C weight ratio. Moreover, pores less than 1 nm decreased, and pores larger than 1nm increased by increasing the KOH:C weight ratio. In fact, a fraction of pores in the microporous region will be transformed to the mesoporous region.

Table 4.1. BET surface area and porosity of monolithic briquettes and MSC-30

	From nitrogen isotherms		Macroscopic measurements		
Sample	**Intragranular density (g/cm^3)**	**Intragranular porosity**	**Bulk density (g/cm^3)**	**Bulk porosity**	**BET surface area (m^2/g)**
MSC-30	0.42	0.79	NA	NA	2600
2.5K Briquette (30% binder)	0.74	0.63	0.70	0.65	2000
3K Briquette (25% binder)	0.56	0.72	0.47	0.77	1900
4K Briquette (25% binder)	0.53	0.74	0.37	0.81	2100

4.2 Hydrogen Isotherms from 0.5-Liter Test Fixture

Hydrogen isotherms measured with the 0.5 liter test fixture were used to calculate gravimetric storage capacity and volumetric storage using bulk porosity for briquettes. Averages of multiple runs are shown in the following graphs, Fig. 4.3.

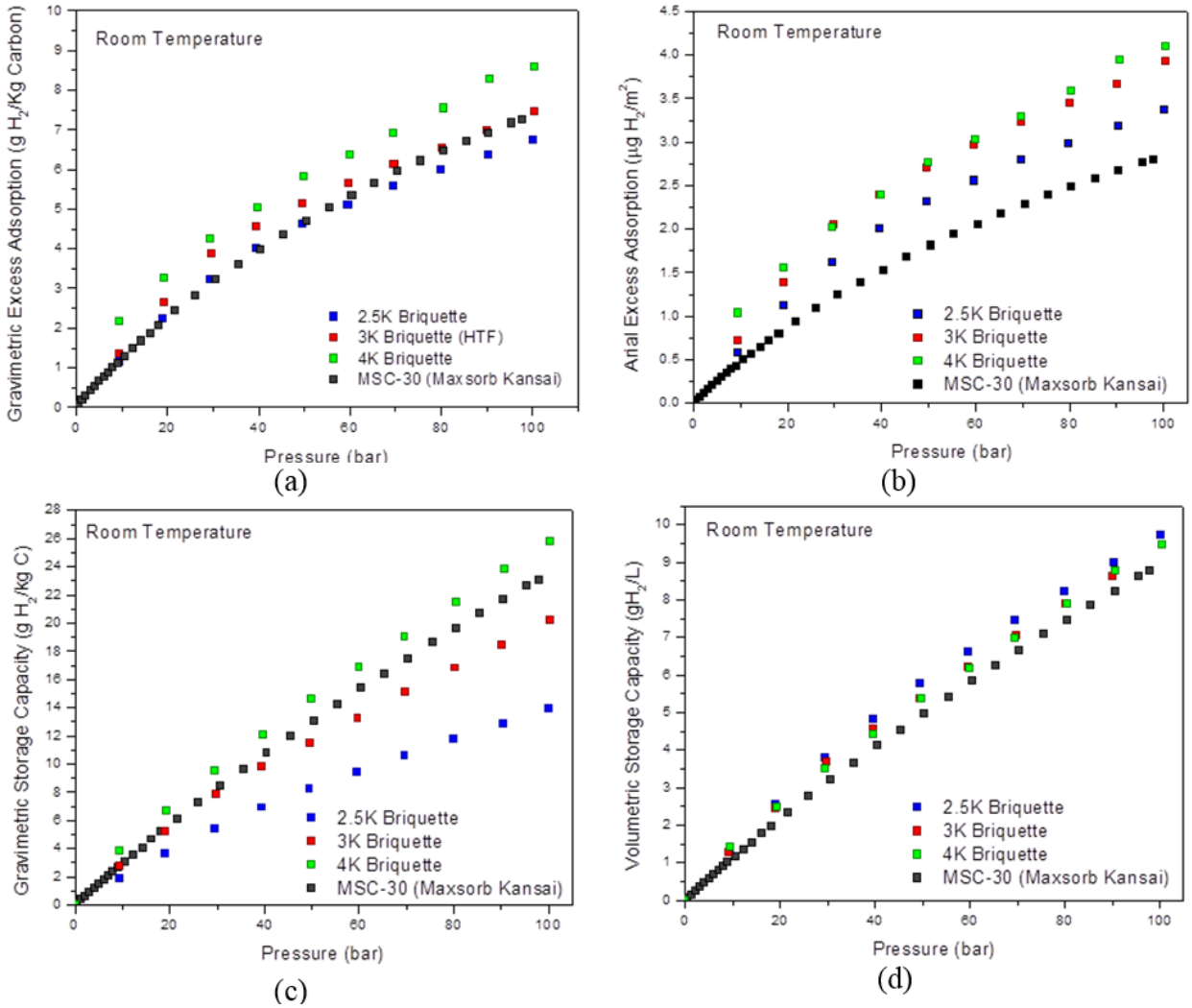

Figure 4.3.Hydrogen adsorption performance of briquettes and MSC-30 powder (reference sample).

These results confirm that All-Craft briquettes outperform MSC-30 at room temperature in terms of areal excess adsorption and volumetric storage capacity. 3K and 4K briquettes outperform MSC-30 in terms of gravimetric excess adsorption. 4K briquette outperforms MSC-30 in terms of gravimetric storage capacity. In fact, carbon made from PVDC improved hydrogen uptake at room temperature.

4.3 Boron Doping of Monoliths

Monoliths of different sizes were boron-doped, following the temperature protocol in Figure 6.1, under different orientations relative to the liquid-gas $B_{10}H_{14}$ reservoir 2013 APR, under different orientations relative to the liquid-gas $B_{10}H_{14}$ reservoir and in presence of a carried gas (Ar). See Fig. 4.4.

Figure 4.4. Cartoon depicting 'dispersion' (*left*) and 'flow-through' (*right*) deposition methods. The dispersion briquette was 33.0 mm tall and cut to a diameter of 38.3 mm, and the flow through briquette was 20.5 mm tall and cut to a diameter of 43.4 mm.

Results are promising: boron concentrations at well-exposed monolith peripheries were 5-15 wt%, and radial concentration gradients at well-exposed peripheries were 1-4 wt%/cm (Fig. 4.5). This implies that $B_{10}H_{14}$ molecules can easily diffuse across macroscopic distances, of the order of 1 cm, through networks of pores, a majority of which are less than 2 nm wide, before sticking to a pore wall irreversibly and decomposing. This is remarkable because the large binding energy of $B_{10}H_{14}$ on carbon, 70-80 kJ/mol, suggests that adsorption of $B_{10}H_{14}$ is strongly diffusion-limited, with short diffusion distances before deposition on a pore wall, unless temperatures are sufficiently high. It is likely that the carrier gas (Ar) present in the current doping protocol facilitates long diffusion distances and can be optimized to reduce deposition gradients even further.

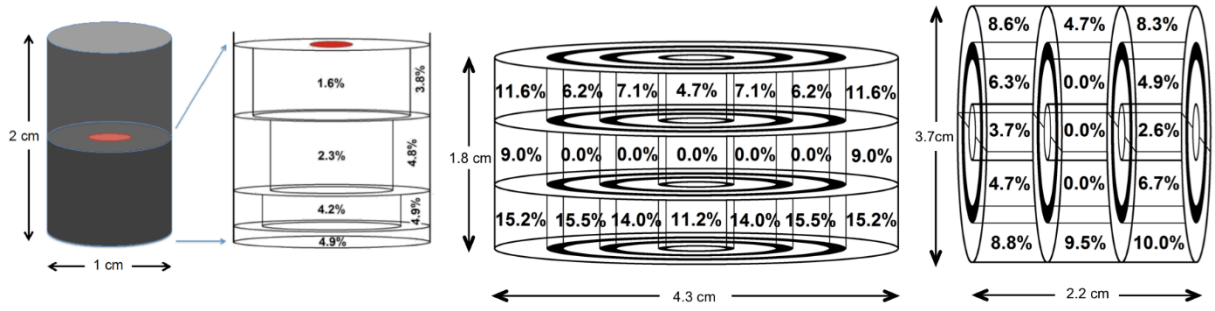

Figure 4.5. Boron concentration maps in monoliths doped with $B_{10}H_{14}$ from gas phase (mixture of Ar and $B_{10}H_{14}$) maintained at a constant pressure of 2 bar as the temperature was raised and the $B_{10}H_{14}$ partial pressure rose. The source was a $B_{10}H_{14}$ liquid-gas interface parallel to the horizontal direction in the figure. Nearby vertical walls creating uneven thermal gradients and $B_{10}H_{14}$ concentration gradients may have caused uneven concentrations in radially and axially symmetric monolith locations. Boron concentrations in monolith sections were determined by PGAA.

4.4 High-Performance Monoliths from CEC Project

Table 4.2. Summary of gravimetric excess adsorption, gravimetric storage capacity, and volumetric storage capacity at room temperature (303 K) and cryogenic temperatures (77 K), all measured on the Hiden instrument. For briquettes, a small piece of the monolith was analyzed. One briquette from the Cabot Corporation has been analyzed and included for comparison.

			Grav. Excess Adsorption (100 bar) (g/kg)		Grav. Storage Capacity (100 bar) (g/kg)		Vol. Storage Capacity (100 bar) (g/kg)		
Sample	Σ (m^2/g)	ϕ	77K	296K	77K	296K	77K	296K	No. of Isotherms averaged
BR-0122	1800	0.66	N/A	5.7	N/A	13.2	N/A	8.9	2
BR-0134	2000	0.70	34.8	6.4	70.5	15.3	42.8	9.3	1
BR-0311	2300	0.74	37.8	7.1	82.1	18.1	42.7	9.4	2
Cabot-14008	1100	0.54	20.1	4.3	38.1	8.8	35.4	8.2	2

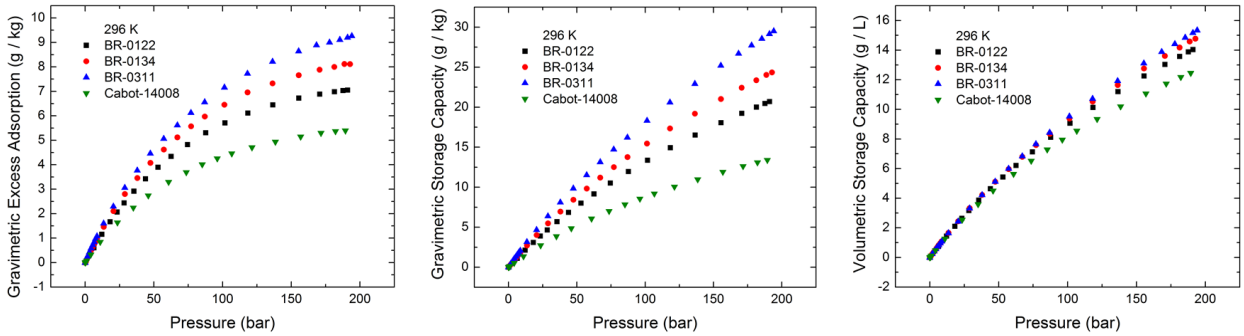

Figure 4.6. Room-temperature data: gravimetric excess adsorption (*left*), gravimetric storage capacity (*center*) and volumetric storage capacity (*right*), all at 296 K for high performing briquettes compared to Cabot-14008.

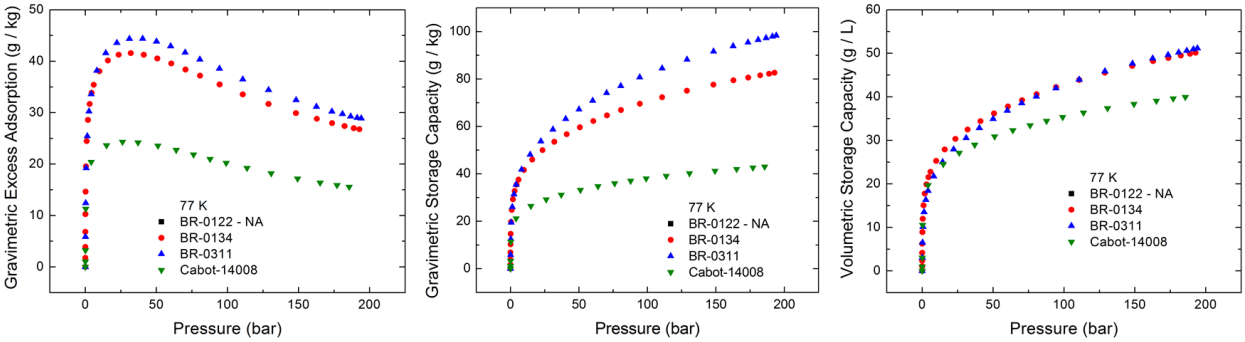

Figure 4.7. Cryogenic-temperature (77 K) data: gravimetric excess adsorption (left), gravimetric storage capacity (center) and volumetric storage capacity (right), all at 296 K for high performing briquettes compared to Cabot-14008.

5. Demonstration of 5.3-Liter Prototype Tank, Room-Temperature Storage

5.1 Design and Operation of Tank

The 5.3-liter tank system was designed to test carbon performance against the DOE 2015hydrogen targets which means testing for outflow (deliverable hydrogen) and total storagecharacteristics. The specifications of the tank system are as follows:

- 10 liter capacity total in 2 tanks of 5 liters each
- Pressure to 100 bar, 200 bar option
- Temperature ambient, option to -80 °C
- 5-9's pure hydrogen input (DOE specification: 4-9's)
- 0.02 g/s/kW capacity
- 30 kW maximum fuel cell simulation
- 36 g/min delivery
- Mass flow meter and controller based design
- Optional cold jacket for -80 °C

The schematic of the final design is shown below.

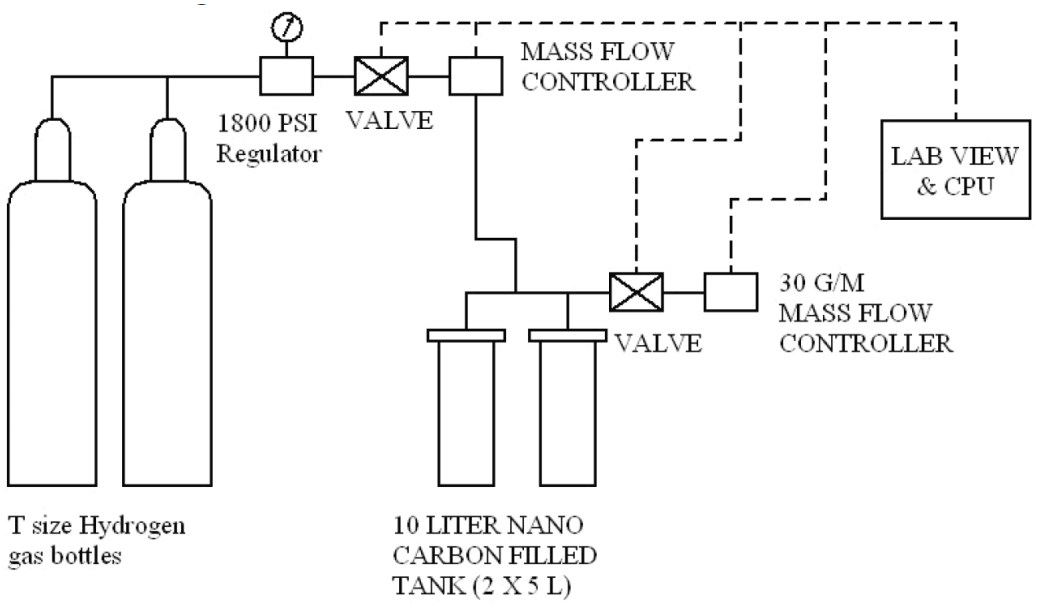

Figure 5.1.Illustration of the final design of the 10-liter tank. The tank comprises two 5-liter cylinders so tank tests can be run with minimal hydrogen and in multiple configurations to 2 μmevaluate alternate adsorbents if desired. A mass flow controller controls delivery flow at 0.6 grams per second hydrogen which is appropriate for a 30 kW forklift. A minimum of two "T" size tanks of 99.999% hydrogen feed the two 5-liter tanks to 100 bar at ambient temperature, and potentially at a low temperature of –78 °C which is the temperature of an ethanol/dry-ice bath.

As shown in the tank specifications the capability for dry-ice testing was included in the design. The design of the tank system is shown below. The external container is sheet metal with 2" insulation, with a plastic outer liner to keep the insulation dry. The base and lid have 2" insulation, with feet extending to the floor and drip lip extending to the OD. A drain pipe is available for condensate or use in event of use of antifreeze. Hydrogen flows to the base cap through dry ice to aid in cooling, while a thermistor in the top cap measures temperature.

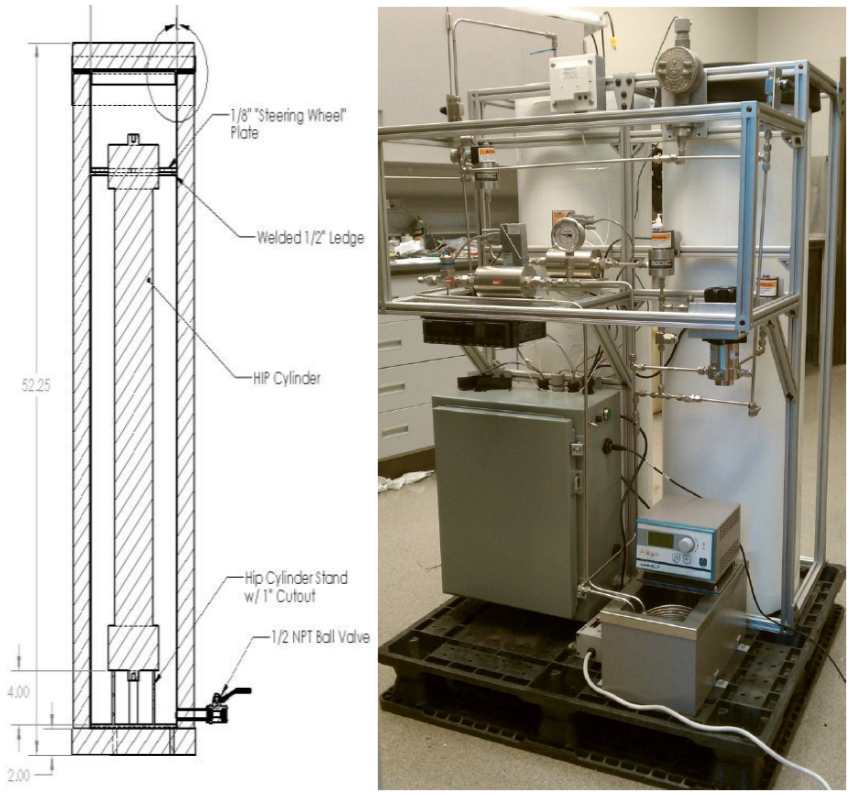

Figure 5.2. (*left)* Individual tank construction schematic for dry-ice temperature testing. (*right*) Completed 10-liter tank system.

At the rear are two 12 in. diameter cold containers in which the reactors are installed. Each reactor has an inside diameter of 3.5-in. and a 6 in. diameter cap that permits testing either carbon powder or monoliths. The approximate 3 in. annulus around the reactor will be filled with dry ice allowing the fixture to achieve dry ice temperatures, a function which has been tested in the lab. The configuration allowed for introduction of ethylene glycol which did not appear to measurably decrease the internal temperature of the reactor. The exterior of the cold tank has 2 in. of insulation with full coverage on the top, bottom and sides. The cold boxes are contained within the framework for stability. Electrical controls are installed in a NEMA four electrical box at the lower left of the fixture. The box to the right of the NEMA electrical control is the heating bath that uses a 25 ft. (7.6 m) stainless steel coil in an oil bath, which will be controlled to heat cold gas to a minimum of 0° C. Gas flow to the reactors is through the bottom port and the gas delivery and exhaust is through the ice bath in order to pre-cool the gas.

5.2 Mechanical Treatment of Carbon

Several methods of mechanically treating carbon were tested for increasing the density and presumably the hydrogen adsorption of several carbons for the purpose of improving the operation of the 10-liter tank. The first method tried was compaction of sample 3K-3/3/10B using a machined metal cylinder and piston in conjunction with a shop press. Sample mass was determined using a balance accurate to 0.0001 g. Samples were placed in the fixture and initially compacted by inserting the piston and pressing it manually. Samples were then compressed repeatedly up to ~7000 psig until the density limit was reached as determined by the position of the piston. Density increased from approximately 0.14 g/cm^3 to 0.49 ± 0.01 g/cm^3, under 7600 psig. The decompressed density from the two runs was 0.34 ± 0.01 g/cm^3. Density after a cycle of compression and stirring was 0.34 g/cm^3. In subsequent tests maximum densities of 0.62 g/cm^3 for sample 3K were achieved after compression at 17,000 psig, and 0.75 ± 0.02 g/cm^3 at 34,400 psig. The density of that sample after decompression was 0.38 ± 0.01 g/cm^3. However, there is little difference in the final density of samples compressed to 17,000 psig compared to those compressed to 7,200 psig. Compressing, stirring, and then recompressing the sample continuously also had little impact on carbon density.

After compression at 7600 psi, BET surface areas, intra-granular porosities, and pore-size distributions of "3K-3/3/10 B" were determined from N_2 adsorption at 77 K. No significant differences were found between the compressed and uncompressed sample. This was expected since most surface area and porosity resides in pores of width ≤50 Å, which are not expected to be affected by bringing carbon grains closer together and minor mechanical fragmentation of grains.

Table 5.1.Effect of sample compaction on BET surface area and porosity. Porosity here is intra-granular porosity, as measured by N_2 adsorption at 77 K and relative pressure 0.995 (filling of pores with liquid nitrogen).

Sample	Σ_{BET} (m^2/g)	ϕ	Description
3K-3/3/10 B	2600	0.78	KOH activated carbon. KOH:C ratio of 3.
3K-3/3/10 B compressed, ρ_{bulk} = 0.47 g/cm^3	2800	0.78	Compressed at 7600 psi to raise bulk density from 0.14 g/cm^3 to 0.47 g/cm^3

Clearly, compaction does affect the inter-granular porosity: increasing compaction leads to decreasing inter-granular porosity, and in turn to decreasing hydrogen gravimetric storage capacity (less pore space for non-adsorbed hydrogen gas) and increasing hydrogen volumetric storage capacity (more adsorbed hydrogen per unit volume). For our best-performing, well-validated sample at room temperature, "3K (6/08)" and best-performing, well-validated sample at dry-ice temperature, "3K-900 °C" (below), compaction predicts the storage capacities shown in Fig. 5.3. Compaction comparable to what was demonstrated for sample "3K-3/3/10 B" leads to an approximately 30% increase of the volumetric storage capacity at dry-ice temperature, relative to uncompressed powder.

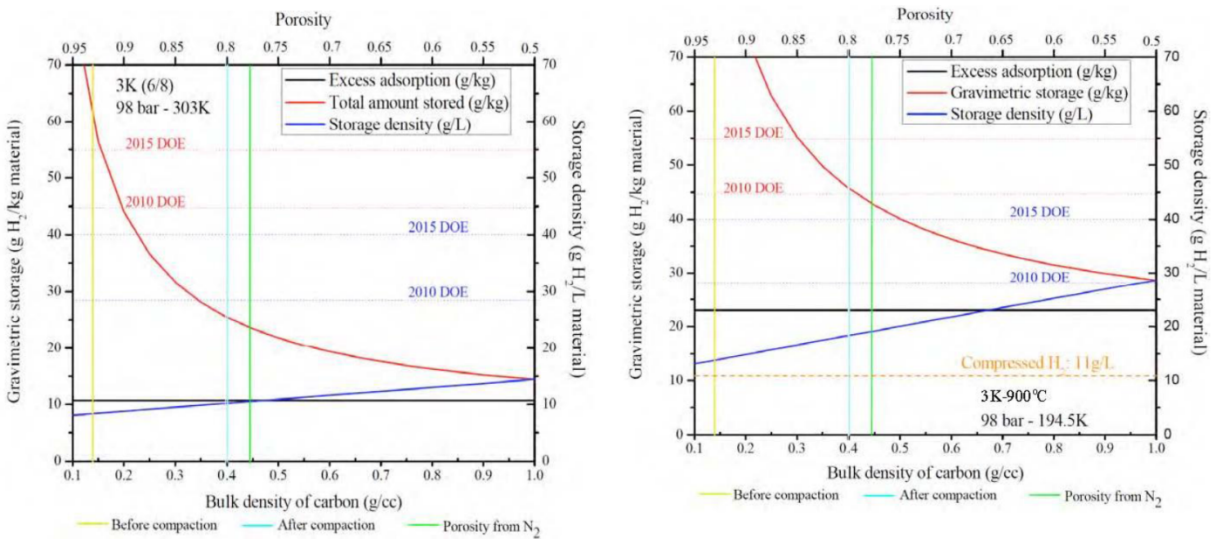

Figure 5.3. Effect of compaction on hydrogen gravimetric and volumetric storage capacity of sample "3K (6/08)" at room temperature (303 K, left), and sample "3K-900 °C" at dry-ice temperature (195 K, right). The volumetric capacities are realistic; the gravimetric capacities need to be revisited because the values here assume negligible weight of the vessel holding the adsorbent.

Packing Carbon Under Mechanical Pressure in the Tank

One possible option for improving H_2 adsorption in the 10-liter tank is packing the carbon under mechanical pressure. However, analysis of the tank stresses showed that mechanical pressure and pneumatic stresses are additive, and increasing mechanical pressure reduced the amount of gas pressure that could be applied to the tank. Rather than holding the carbon in the tank under mechanical pressure, pre-compacted carbon powder is poured into the tank and densified by vibrating the powder with an air chisel. The expected increase in density is shown in Table 5.2.

Table 5.2.Expected apparent carbon density, ρ_{app}, and corresponding volumetric storage capacity, V_{st}, of sample 3K 790 ºC at 100 bar and 303 K, as a function of various pressure applications.The density of regular carbon was measured by simply pouring carbon into a graduated cylinder and measuring the volume. The density of packed carbon was measured by placing carbon into the compression fixture and pressing on the piston manually. The compressed carbon density is for that of carbon that has been compressed and then transferred to another container. The compressed in tank density is the density of the carbon that has been compressed and remains in the same container in which it was compressed.

Carbon treatment	**Carbon density (g/cm^3)**	**Vol. storage capacity (g H_2/L)**	**% increase from uncompacted**
Uncompacted	0.14	8.12	0
Packed carbon	0.24	8.69	7.0
Compressed carbon	0.34	9.19	13.2
Comp. & packed carbon (in tank)	0.37	9.41	15.9

Microscopic Assessment of the Effect of Compaction on 3K 790 °C

To further investigate the potential effect of mechanical treatment on carbon density, samples were investigated using scanning electron microscopy (SEM). The uncompacted carbon had a bulk density of 0.24 g/cm^3. Contrary to the results mentioned above, microscopic examination showed that density of samples increased to 0.28 and 0.33 g/cm^3 after ball milling and subsequent compaction, respectively. Nitrogen adsorption tests revealed that compaction has no appreciable effect on pores <5 nm (nitrogen adsorption). **Figs. 5.3.1 (b) and 5.3.2 (b)** show the complete destruction of grains >20 μm. This supports the conclusion that the increase in bulk density results from elimination of large pores (>400 nm) and intergranular space.

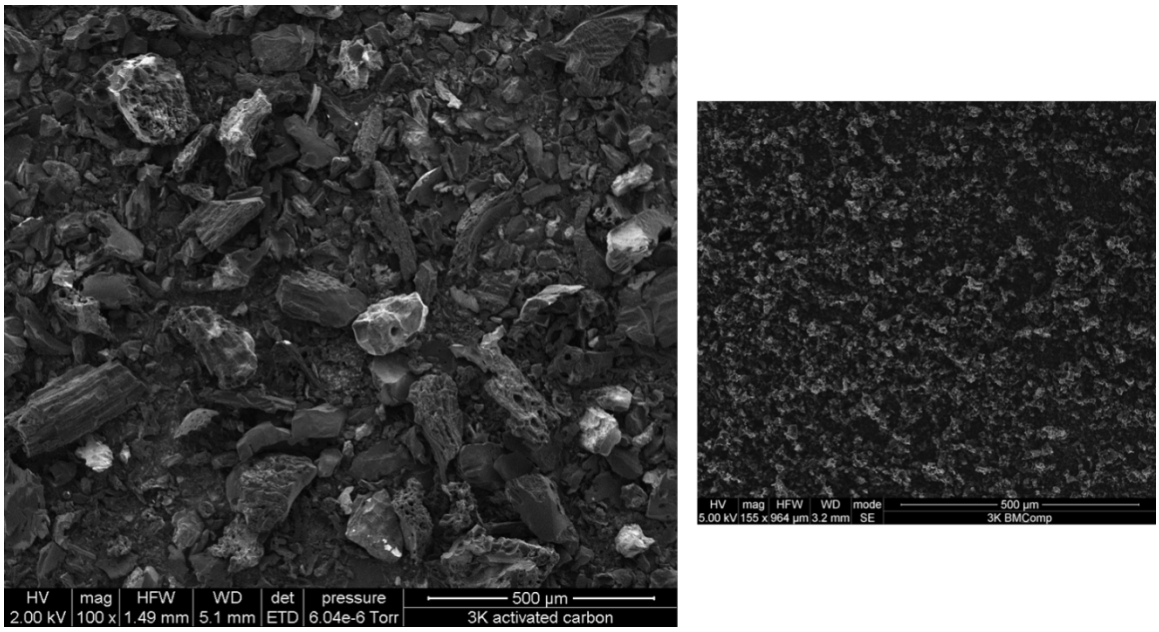

Figure 5.4.Comparison at 500 μm of uncompacted 3K 790 °C (*left*) and ball-milled/compacted 3K 790 °C (*right*). Figures have been adjusted to display the same length scales.

Compaction with this efficiency isn't without its drawbacks. Fig 5.6 (*right*) below is a close-up of one of the larger particles in the compressed sample. It is apparent that there are numerous grains that are smaller than 2 μm from all orientations, as well as several that are in two dimensions. Particles with a diameter less that 2 μm will bypass any standard, commercially available filters. From an engineer's perspective, while removing the intergranular porosity will inherently improve the volumetric storage capacity of the material, it is notpractical to implement such a material if it may not be easily contained within the storage tank.It can be seen in images of the uncompacted carbon that allof the large grains are larger than 2 μm, and will not pass through a sufficiently small filter.

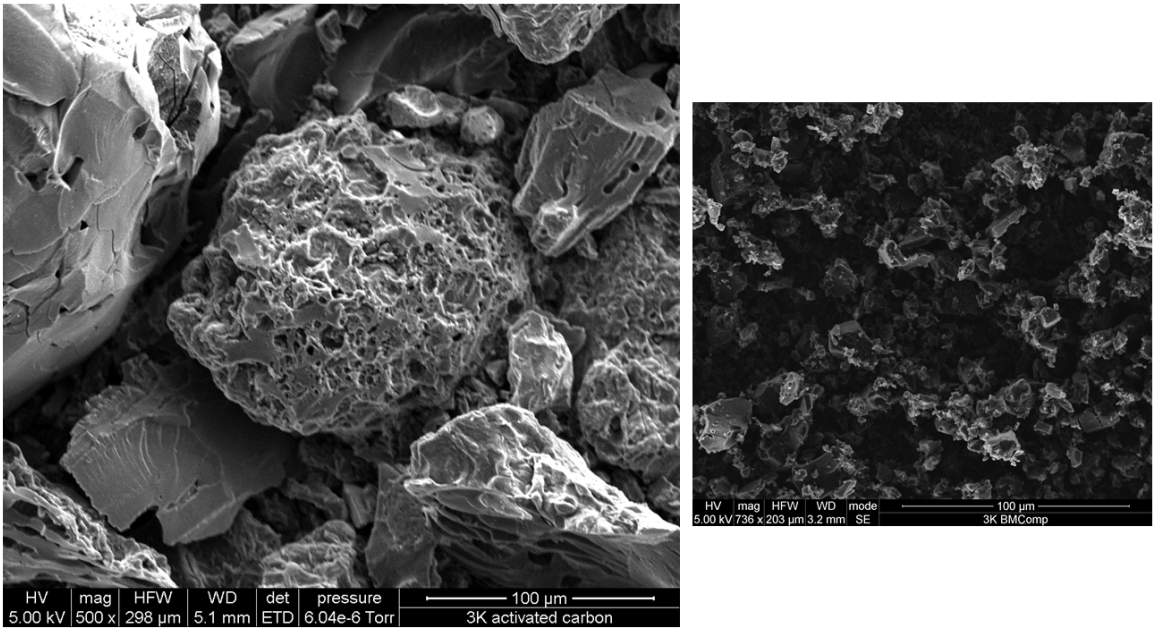

Figure 5.5.Microscopic-level comparison of uncompacted 3K (*left*) and 3K that has been ball milled and compacted (*right*). Figures have been adjusted to portray the same length scales. At this length scale, the efficiency of the compaction process is evident. While the uncompacted sample shows several structures larger than 100 µm, the largest grains after compaction are much lessthan 50 µm.

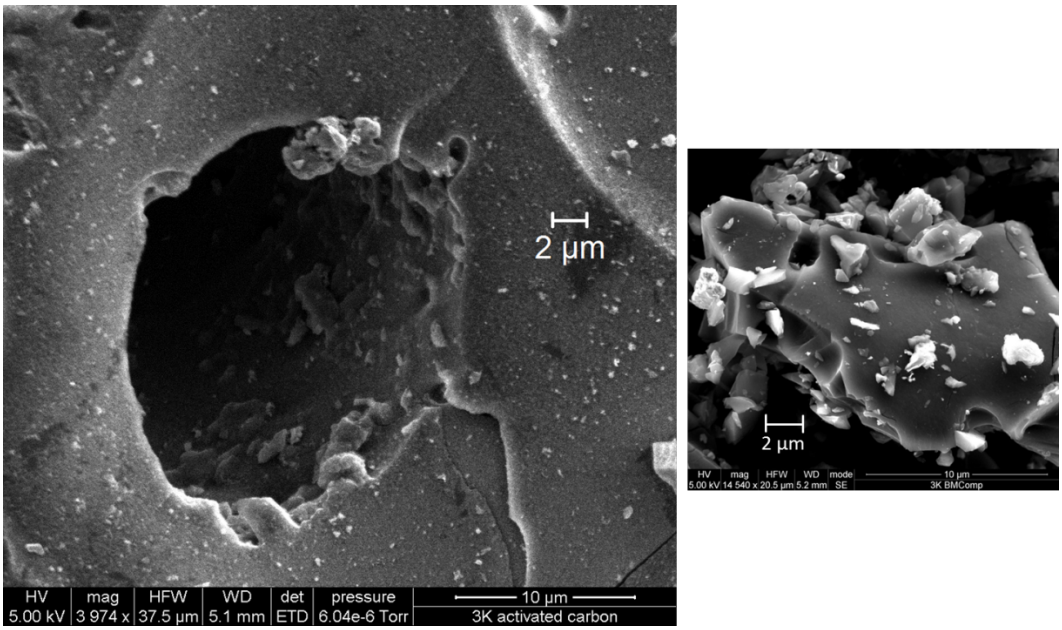

Figure 5.6.Features of the compacted (*left*) and uncompacted (*right*) 3K samples at the µm length scale. Many particles less than 2 µm are visible in the compacted sample, but not in the uncompacted.

5.3 Performance of Tank

Gravimetric and Volumetric Storage

The gravimetric and volumetric storage capacity at room temperature can be determined by integrating the H_2 flow rate that is measured with the mass flow meters and subtracting the gas that remains in ancillary tubing downstream from the mass flow meter. The volume of the ancillary tubing was determined by subtracting the volume of each empty tank from the empty system volume. The volume of each 5.3-L tank was given by the tank manufacture and was verified using a micrometer and tape measure.

The gravimetric and volumetric storage capacity of one of the 5.3-L tanks is compared against those measured using the commercially available Hiden HTP1-V volumetric gas analyzer in Fig 5.7. The HTP1-V measures the adsorption on 300 mg of powdered activated carbon while a single tank on the 5.3-L system holds 1.5 kg. The gravimetric storage in the 5.3-L system is 32.8 g/kg at 104 bar.

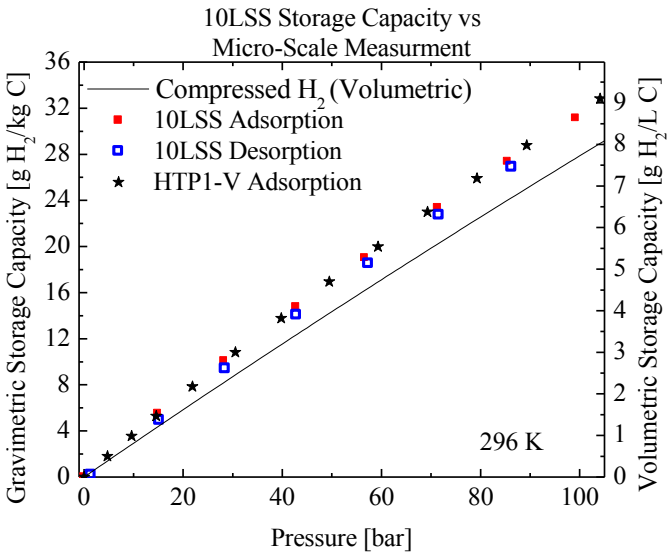

Figure 5.7. The Hiden HTP1-V data in this figure agrees within 1%across all pressures with the 5.3-L system gravimetric and volumetric storage capacity data. Gravimetric storage capacity is shown on the left axis while volumetric storage is shown on the right axis.
Gravimetric and volumetric storage capacities on the HTP1-V were determined by using the excess adsorption (measured by the HTP1-V) and the measured bulk density of the powdered activated carbon inside the 5.3 L system (0.28 kg/L). This bulk density (which was measured) corresponds to a packing fraction of 0.63 which is equivalent to that of random close packing of spheres.

These experiments demonstrate that the 5.3-L system can accurately measure the total amount of stored hydrogen using its mass flow meters. Since this measurement is the result of integrating the flow rates measured by the flow meters, the 5.3-L system has also demonstrated that it can accurately measure the charging and discharging rates of the system.

Charging, Discharging, and Time Dependent Measurements

Charging and discharging of the system for each data point in Fig. 5.6 and 5.7 is completed within a few minutes (see Fig. 5.8). However, the equilibration of the system for each data point is much longer (see Fig. 5.9). For the small scale measurements performed by the HTP1-V, thermal equilibrium is reached quickly. In Fig. 5.9 we also see that the temperature decreases upon desorption because it is endothermic.

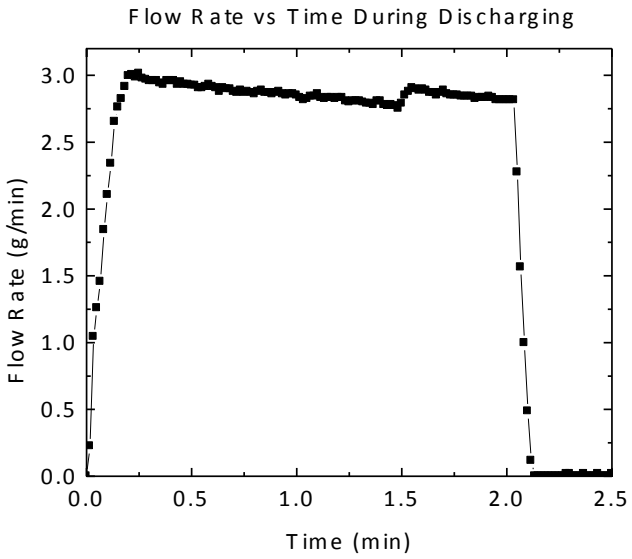

Figure 5.8. The flow rate that was measured between the 100 bar and the 84 bar desorption data points in Fig 5.6 and 5.7 is shown.

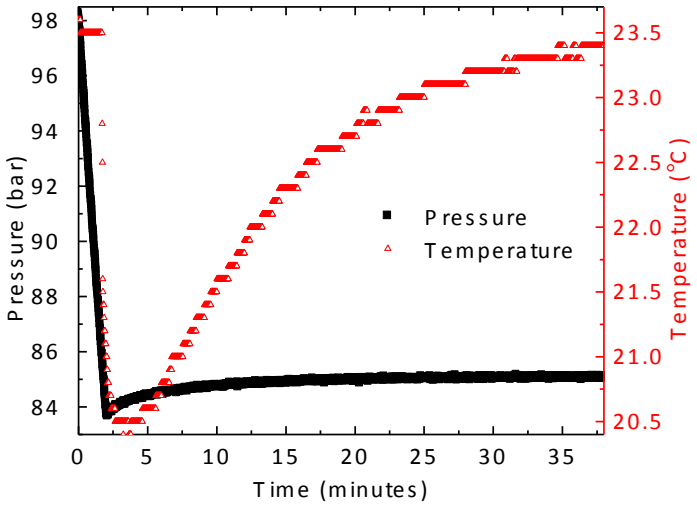

Figure 5.9. The temperature and pressure profiles are shown for the transition between the 100 bar and 84 bar desorption data points in Fig. 5.6 and 5.7 is shown.

Fast Fill

During a fast fill experiment, the 5.3-L system was filled for 3.3 minutes. During this process, 95% of the ultimate gravimetric storage capacity (32.8 g/kg) was achieved. Despite the inclusion of the 28 cm tubes to facilitate flow, the temperature at the center of the tank trailed the application of pressure to the system by 32 s (see Fig. 5.10). The 28 cm internal flow tubes were installed during this experiment to provide a free flow path. Because of this, the hydrogen only had to diffuse through ~13 cm of powdered activated carbon to reach the center of the tank.

The cusp and increase in the slope of the temperature vs time data about 2 minutes into the experiment is due to a reduction in gas flow into the system. The gas flowing into the system has a cooling effect which has lead others to explore flow-through cooling to aid in removing heat from hydrogen adsorbent systems during charging. A second, more subtle, discontinuity in the temperature data corresponding to when flow into the system was permanently stopped can be observed at 3.3 minutes.

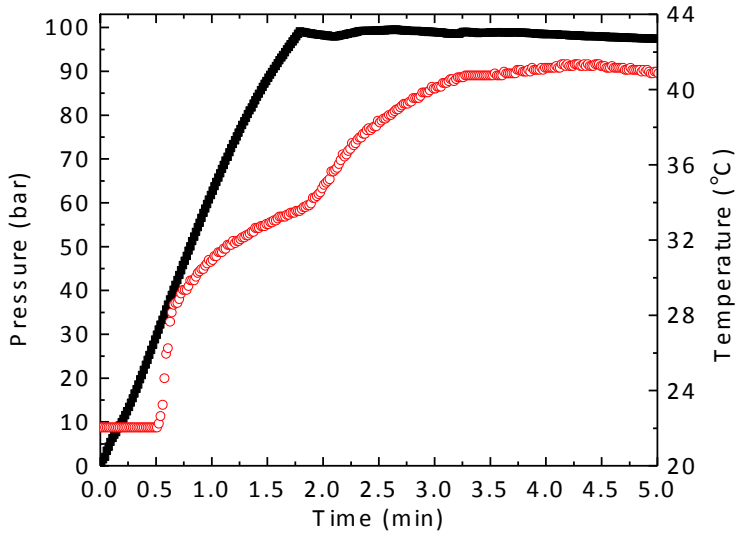

Figure 5.10. The pressure and temperature inside of the 5.3-L system during a fast fill.

6. Optimize Boron Doping and Incorporation in Carbon Lattice (Phase 2)

6.1 Stoichiometric and Nonstoichiometric B_xC Compounds

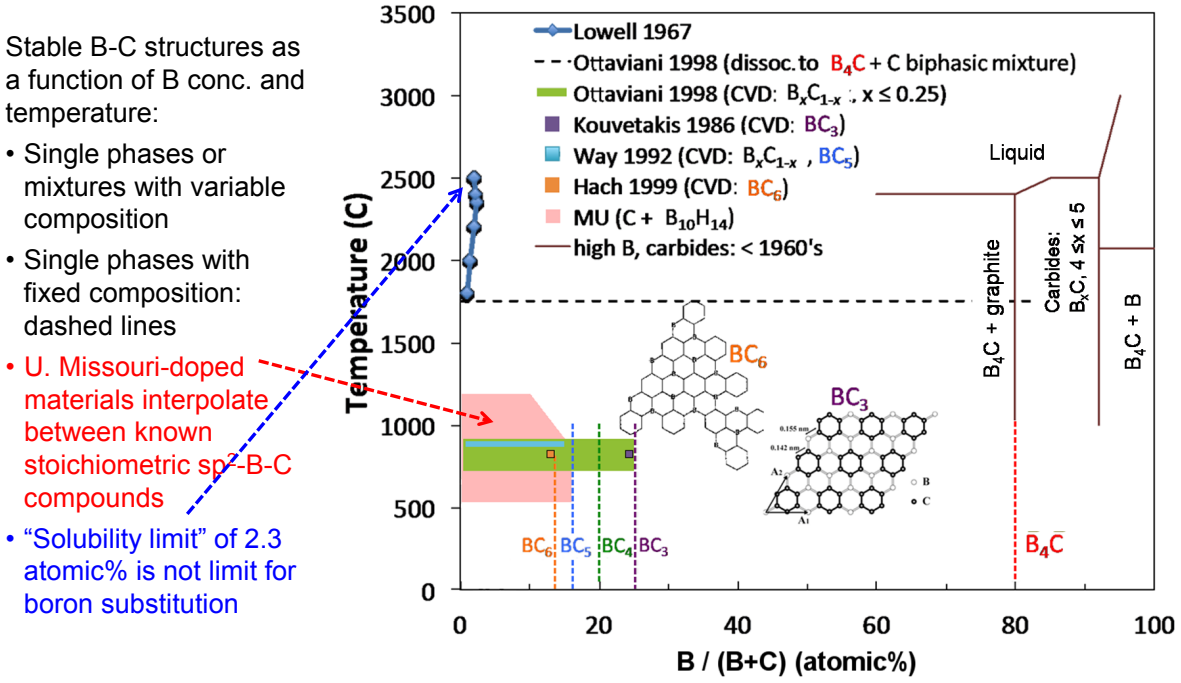

Figure 6.1. Boron-carbon phase diagram. Vertical dashed lines show phases with fixed stoichiometric composition. The targeted composition range and expected stability range are shown in red. It had been suggested that uniform boron concentration might be possible, as equilibrium structures, only for B concentrations less than the "solubility limit" of 2.3 atomic%. But concentrations above that limit were expected exist as non-equilibrium structures.

6.2 Thermodynamics of Deposition of $B_{10}H_{14}$ on Carbon Materials

Not executed

6.3 Chemistry of Decomposition of $B_{10}H_{14}$ (Case Study)

Not executed

6.4 Deoxygenation of Undoped Carbon

We recall the following conclusions from the 2013 AMR and 2013 APR:

(i) In samples heat-treated up to 600°C 90% of B-C bonds are sp^2 bonds, which enhance binding of H_2; 10% are B_4C bonds, which do not enhance binding of H_2; and the two types of B-C bonds coexist with B-O bonds, inert up to 600°C, presumed to originate from pre-existing oxygen in the carbon.

(ii) Upon heat treatment up to 1,000°C, samples lose 20-30% boron (PGAA) in the form of B_2H_6 (TGA-MS), but it remains to be determined whether the lost boron is sp^2 boron, B_4C boron, B-O boron, or yet other boron.

(iii) Throughout the decomposition process monitored by XPS, 20-600 ºC, the B-O peak remained unchanged, and the origin of the B-O bonds was attributed to surface-bound oxygen preexisting in the undoped carbon.

Boron atoms bonded to oxygen atoms are not expected to enhance binding of H_2. Therefore, a systematic effort was undertaken to remove oxygen from undoped carbon, prior to doping, while maintaining high surface areas (~2,700 m^2/g). Typical surface-bound oxygen groups are shown in Fig 7.6. Three different deoxygenation methods were used: (a) heat treatment up to 1,200 ºC; (b) microwave treatment; (c) treatment with hydrazine (reducing agent). The oxygen content was monitored with XPS. Surface areas and pore-size distributions were monitored with N_2 adsorption. Results are shown in Fig 7-9. Heat treatment and microwave treatment both gave a reduction of oxygen concentration from 8 to 1 atomic %, accompanied by a drop in surface area from 2700 to 2300 m^2/g or lower. The microwave treatment gave results that varied considerably upon repeat experiments (inhomogeneous microwave field in the oven), and was determined not to be suitable for "mass fabrication." The comparison of the three methods, in terms of oxygen concentration and surface area, is shown in Fig 10. From the data, hydrazine treatment gives the least loss of surface area (only 100 m^2/g) while reducing the oxygen concentration by 50%. Heat treatment at 800-1000 ºC gave comparable results.

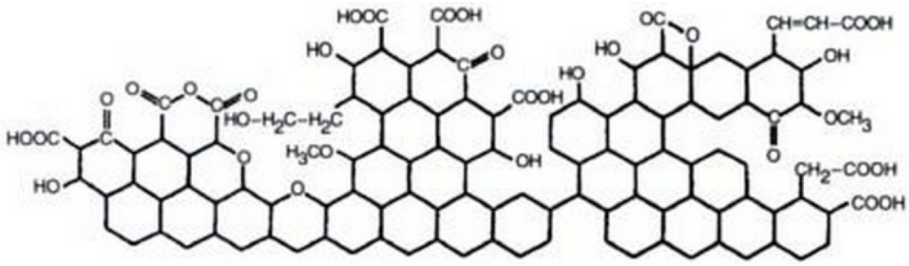

Figure 6.6. Surface-bound oxygen groups in graphitic/graphene-like carbon, representative of undoped 3K-type carbons manufactured at U. Missouri.

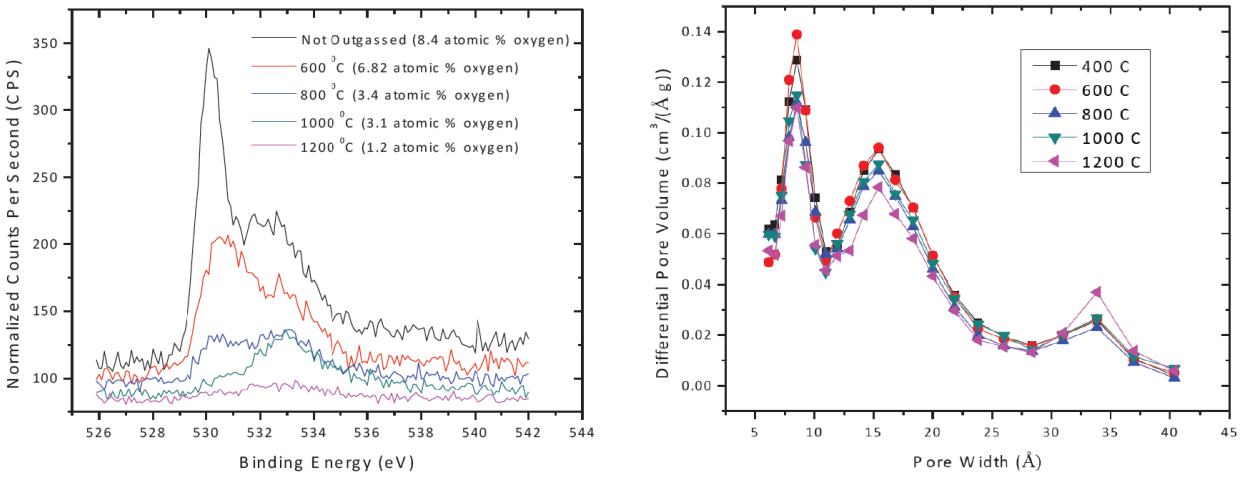

Figure 6.7. Oxygen XPS spectra (*left*) and pore-size distributions (*right*) of undoped 3K carbon deoxygenated by heattreatment at 400, 600, 800, 1000, and 1200 ºC. The respective oxygen content was 8.4, 6.8, 3.4, 3.1, and 1.2 atomic% oxygen (integrated intensity above background, 528-538 eV). The respective BET surface areas were 2700, 2700,2500, 2500, and 2300 m^2/g.

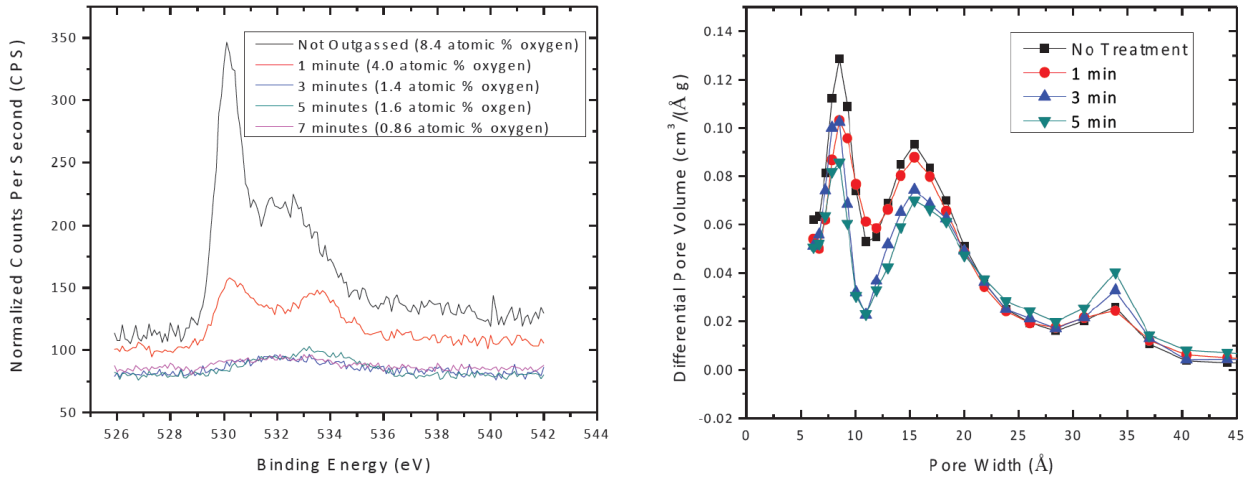

Figure 6.8. Oxygen XPS spectra (*left*) and pore-size distributions (*right*) of undoped 3K carbon deoxygenated bymicrowave treatment at varying duration. The respective oxygen content was 8.4, 4.0, 1.4, 1.6, and 0.9 atomic %oxygen (integrated intensity above background, 528-538 eV). The BET surface areas were 2700, 2600, 2400, 2200,and 2000 m^2/g. Repeat experiments gave surface areas that were lower by 100-300 m^2/g for the same procedure.

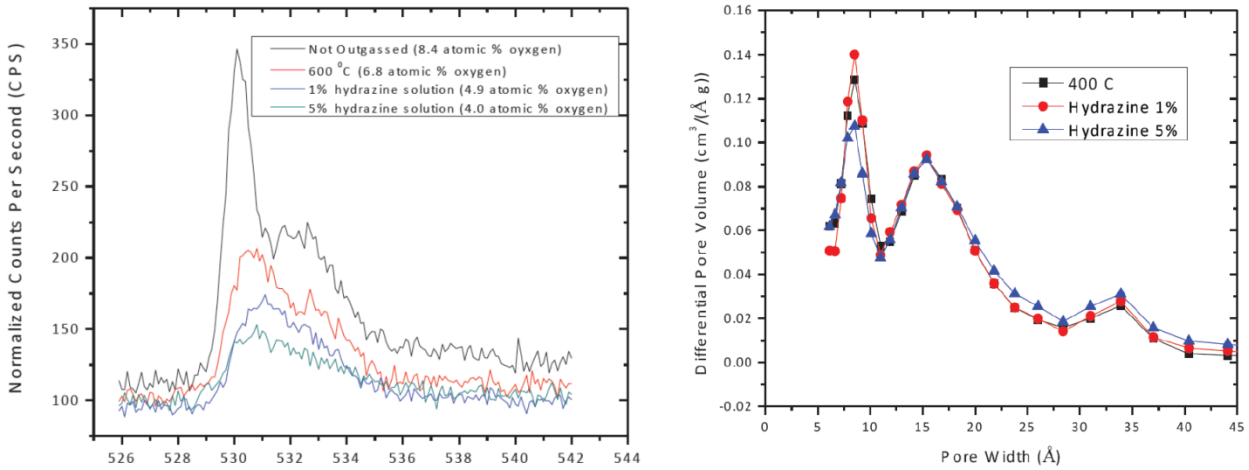

Figure 6.9. Oxygen XPS spectra (*left*) and pore-size distributions (*right*) of undoped 3K carbon deoxygenated by treatment with 1% and 5% hydrazine solution. The respective oxygen content was 8.4, 6.8, 4.9, and 4.0 atomic % oxygen (integrated intensity above background, 528-538 eV). The respective BET surface areas were 2700, 2700, 2700, and 2600 m^2/g.

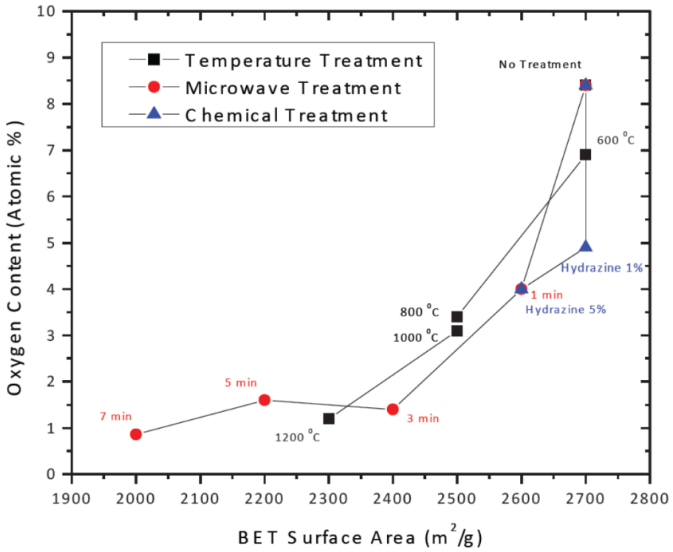

Figure 6.10. Oxygen concentration plotted as a function of surface area for the three deoxygenation methods. Inevitably, reduction of oxygen concentration (desirable) leads to loss of surface area (undesirable, "graphitization"). The loss of surface area also entails a loss of defects, which offer easy entry point for boron and host high binding energies (> 5 kJ/mol). Thus, a compromise between the two must be made.

6.5 Liquid-Phase Deposition of $B_{10}H_{14}$ (Stationary Doping)

Not executed

6.6 Vapor-Phase Deposition of $B_{10}H_{14}$ (Flow Doping)

Samples produced using the 1-step stationary doping, and previously Method I, inevitably are exposed to liquid decaborane deposition prior to (or instead of) gaseous deposition. It is believed that this is the cause of the relatively low percentage of boron atoms bound to carbons in a sp^2 configuration, as the melted decaborane condenses within the pores and forms B-B boron clusters. To prevent this, the 2-step flow doping (Fig 6.11) instrument deposits decaborane exclusively from the vapor phase.

The deposition occurs within a single long, narrow quartz tube and is facilitated by a flow of argon, controlled upstream via a supply pressure regulator and flow meter. The deposition cell pressure is controlled by a back-pressure regulator located downstream. The decaborane is held in a quartz boat at position (7) controlled by a separate heating element from the quartz boat containing the carbon at (8). This allows for the carbon to be preheated prior to deposition to prevent condensation at a thermal gradient.

The 2-step flow doping instrument features a heat bath that requires the sample to be removed and annealed for decomposition separately. A recent upgrade, headlined by the purchase of a split tube furnace, allows for temperatures of up to 1100 °C (Fig below). This allows for decomposition to immediately follow deposition, prohibiting condensation of decaborane in the pores that may occur when allowing the sample to cool.

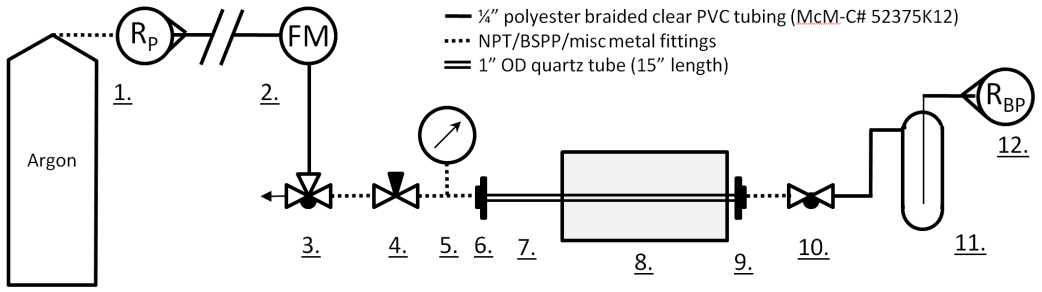

Figure 6.11. Decaborane deposition flow system schematic. The 2-step instrument has a heat plate and bath at (8), while the 1-step has a 1100 °C split tube furnace.

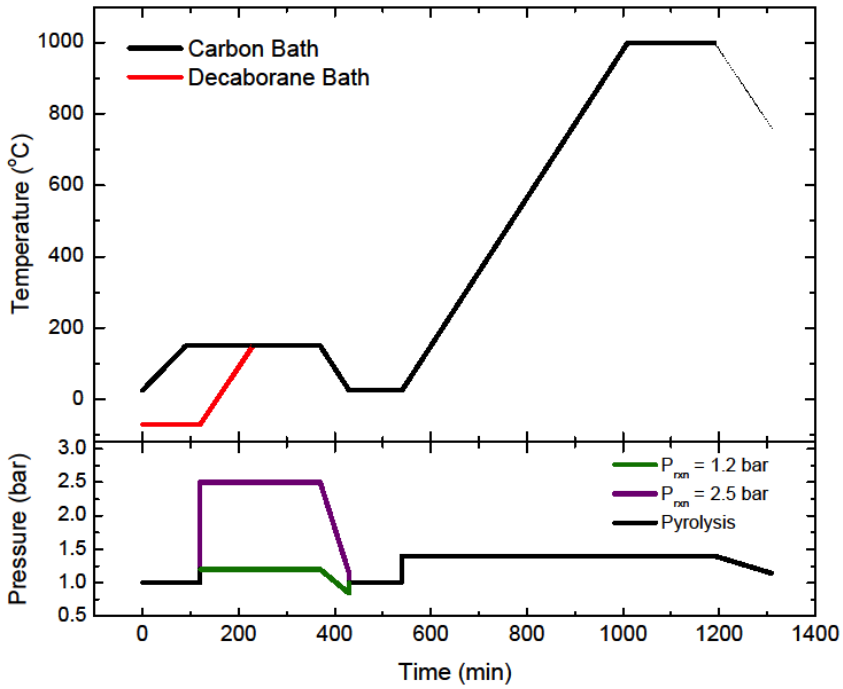

Figure 6.12. Heating and pressure profile for 2-step flow doping instrument. The 1-step instrument allows for annealing to begin immediately after deposition, negating the drop to room temperature.

Figure 6.13. Upgraded flow doping instrument, which allows decomposition of decaborane and annealing of samples at temperatures up to 1100 °C.

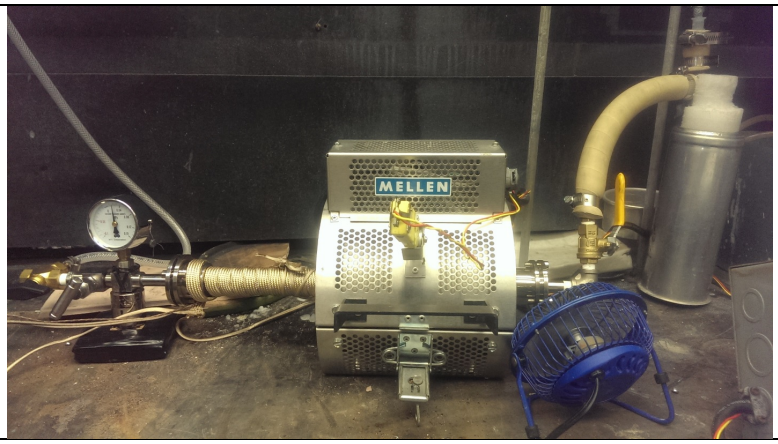

7. Structural and Spectroscopic Characterization of Phase-2 B_xC Materials

7.1 Surface Areas and Pore Structure of B_xC Materials

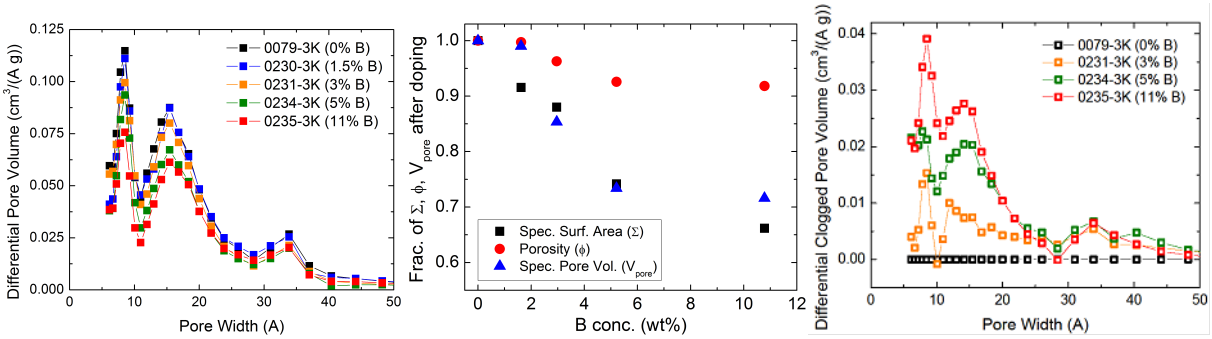

Figure 7.1. Geometric changes in pore volumes with varied boron concentrations. *Left*: Differential pore volume shows a fairly uniform reduction in pore space with increasing boron content. *Middle*: Fraction of specific surface area, crystal porosity, and pore volume change as a function of boron concentration. Surface areas and pore volumes decrease by up to ~30% at the highest boron contents, while porosities stayed within 90% of their undoped value.*Right*: Differential clogged pore volume for samples doped using vapor phase deposition, the differential pore volume of each doped sample subtracted from that of the undoped precursor. This represents the pore space that was lost upon doping. It's seen that the smallest pores are removed to a greater extent with increasing boron content, while those larger than 25 Å are removed to a similar extent, regardless of boron content.

Increase in boron concentration reduces pore volume and surface area, and porosity to a lesser extent. The decrease in surface area occurs approximately linearly. Subtracting the pore size distribution of the doped samples from the undoped precursor gives an idea as to the preference of each pore size to be clogged, with pores <15 Å being removed with increasing extent with boron content. 33 Å pore population reduction appears independent of boron content, indicative of some likely process-based threshold.This reduction in surface area corresponds to a decrease in H_2 gravimetric excess adsorption (Fig 7.2) in accordance with Chahine's rule, while an identical surface excess concentration (G_{exc}/Σ) points towards an identical average H_2 binding energy in doped and undoped samples.

Figure 7.2. Gravimetric Excess adsorption and surface excess concentration for flow-doped sample, 3K-0234, and its precursor, 3K-0079. The reduction in surface area upon doping to 5% B corresponds to a decrease in excess adsorption in accordance with Chahine's rule. However, the samples are identical upon normalizing to surface area, indicative of no appreciable change to the binding energy.

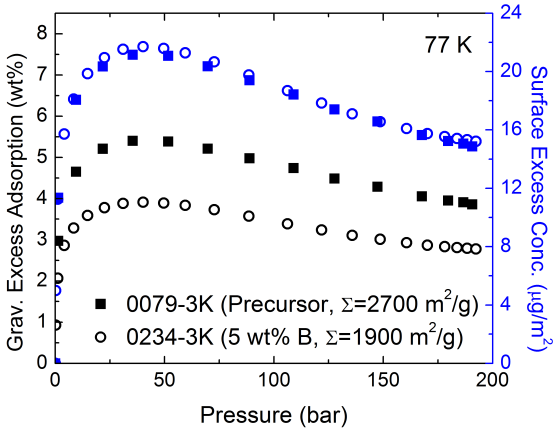

7.2 Fourier Transform Infrared Spectroscopy (FTIR)

Most work was completed attempting to measure the chemical environment of the boron after doping. Proton and carbon NMR proved to be ineffective because the carbon samples were not soluable in any known solvent and because they exhibited a paramagnetic behavior. Fourier Transform Infrared Microscopy (FT-IR) was a much more useful tool to quantify the nature of the boron-carbon bonds. Conventional FT-IR could not reveal the B-C bond due to the broadening of bands between 1000 cm^{-1} and 1100 cm^{-1}. This is due to the variation of micro-environment in the nanoporous carbon material. A controlled experiment showed that the B-C bond can be recognized in boron carbide sample in FT-IR microscopic spectrum with an aperture size of 20 μm. FT-IR microscopic spectra show no B-C bond in 3K sample. FT-IR microscopic spectra clearly showed B-C bonds in sample 3K-H31 (III,A) (Fig. 7.3).

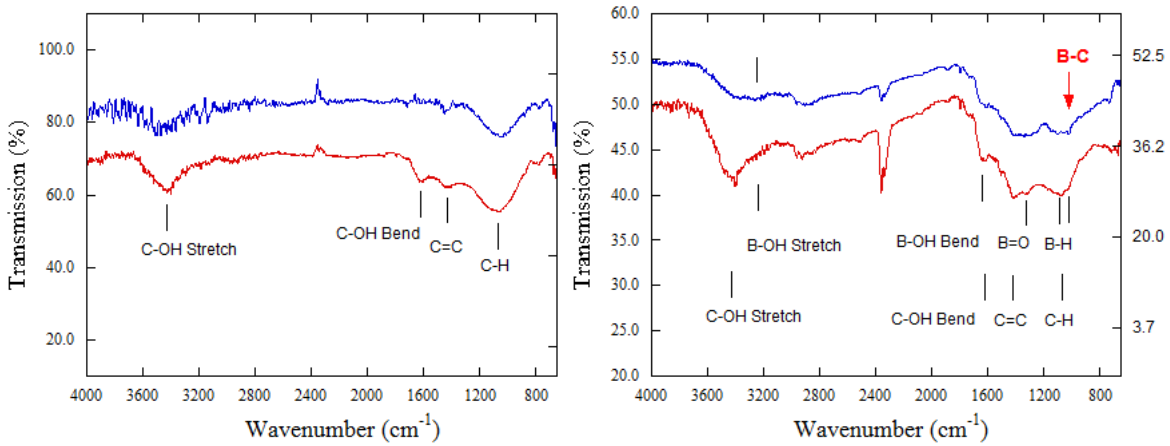

Figure 7.3. (*left*) FT-IR transmission spectra for 3K using the FT-IR microscope with a larger aperture (100 μm – red) and small aperture (20 μm – blue). The broadband around 1068 cm^{-1} is due to the in-plane C-H deformation bending modes in benzene. The micro-environment of porous carbon causes a broadening of C-H related bands, but B-C band is definitely absent in the spectra. (*right*) FT-IR transmission spectra for 3K-H31 (III,A) using the FT-IR microscope with a larger aperture (100 μm – red) and small aperture (20 μm – blue). In addition to carbon related peaks, this spectrum shows boron related bands. The narrow band associated with the B-C bond is clearer in the FT-IR spectrum using the small aperture while intensities of –OH related bands decrease and shift.

7.3 X-Ray Photoelectron Spectroscopy (XPS)

Development of Methodology

To better understand the chemistry of $B_{10}H_{14}$ decomposition and the resulting environment of boron in the carbon matrix, the process was monitored by X-ray photon spectroscopy (XPS), thermogravimetric analysis with mass spectroscopy (TGA-MS), prompt gamma neutron activation analysis (PGAA), and microscopic Fourier transform infrared spectroscopy.

XPS spectra can be notoriously hard to fit because of the number of deconvolutions that one can make. Any number of quantizations can be achieved for a given set of peaks depending on the

initial fitting conditions, especially for those that are so similar in 1s binding energy. Therefore, we have developed a method where XPS spectra are analyzed by quantitatively requiring consistency in multiple elemental spectra for a particular sample. Six equations have been developed to aid in the quantitative analysis of XPS spectra. These equations seek to improve consistency in the identification of chemical environments. Consistency is improved by requiring that if a compound of elements is observed in one high resolution elemental spectra, then that same compound must be observed in the complementary elemental spectra. For example, if we believe we observe the compound BC_3 in the high resolution boron spectrum, then we require an equal amount of BC_3 to show up in the high resolution carbon spectrum. Because saying with complete certainty what the exact oxygen surface groups are is difficult, we have modeled all surface oxides to be of the form B-O or C-O.

We fit our spectra assuming an environment comprised of 6 unique bonds (resulting in 9 peaks across three elemental ranges): C-C, B-C_3, B-B, C-O, B-O, and C-H. The comprehensive features for deconvolution are shown in Table 7.1.

Table 7.1. Peak deconvolution assignments for our boron doped carbon systems, including initial fitting peak positions and FWHM's reported in the literature.

Parameter	Description		
A_y^z	Raw area for each fitted peak of bond *z* in the spectra of element *y*		
A_y	Raw area of the element *y* feature of the spectra, generated from the sum of the individual components A_y^z		
σ_y	Relative sensitivity factor (RSF) of element y.		
x_y^z	Fraction of bond *z* in the element *y* feature. Calculated from A_y^z / A_y.		
X_y	Fraction (concentration) of element *y* in the sample. Calculated from applying the RSF corrections to the peak heights: $(A_y/\sigma_y)/\sum_1^\infty(A_n/\sigma_n)$		
Parameter	Description	Peak Pos. (eV)	FWHM (eV)
x_B^{BB}	Fraction of B1s spectrum with atoms in a BB bonding env.	188.5	2.0
x_B^{BC3}	Fraction of B1s spectrum with atoms in a BC_3 bonding env.	191.0	2.5
x_B^{BO}	Fraction of B1s spectrum with atoms in a BO bonding env.	193.0	1.9
x_C^{BC3}	Fraction of C1s spectrum with atoms in a BC_3 bonding env.	283.5	1.0
x_C^{CC}	Fraction of C1s spectrum with atoms in a CC bonding env.	284.4	0.8
x_C^{CH}	Fraction of C1s spectrum with atoms in a CH bonding env.	285.0	1.5
x_C^{CO}	Fraction of C1s spectrum with atoms in a CO bonding env.	286.5	1.5
x_O^{BO}	Fraction of O1s spectrum with atoms in a BO bonding env.	531.8	1.8
x_O^{CO}	Fraction of O1s spectrum with atoms in a CO bonding env.	532.8	1.8

The first three equations have been named the consistency equations. They require that the total concentration of each element be accounted for. For the concentration of a single element, the accounting takes place over all the different elemental spectra. The equations are:

$$\frac{1}{3}x_C^{BC3}X_C + x_O^{BO}X_O + x_B^{BB}X_B = X_B \quad (7.1)$$

$$3x_B^{BC3}X_B + x_O^{CO}X_O + x_C^{CC}X_C + x_C^{CH}X_C = X_C \quad (7.2)$$

$$x_B^{BO}X_B + x_C^{CO}X_C = X_O \quad (7.3)$$

The second three equations have been named the reciprocal equations. They require that, for a compound composed of two elements, that compound must be observed in equal parts in the compound's two separate elemental spectra. The equations are:

$$3\frac{A_B}{\sigma_B}x_B^{BC3} = \frac{A_C}{\sigma_C}x_C^{BC3} \tag{7.4}$$

$$\frac{A_B}{\sigma_B}x_C^{BO} = \frac{A_O}{\sigma_O}x_O^{BO} \tag{7.5}$$

$$\frac{A_C}{\sigma_C}x_C^{CO} = \frac{A_O}{\sigma_O}x_O^{CO} \tag{7.6}$$

Every value in these equations is either a constant or is a value determined from the spectral fit; there is nothing that is explicitly solved for in these equations. As there are 9 unknown values from the fit and only six equations,an explicit solution isn't possible. Instead, an individual sample's three spectra are initially fit using the values reported in Table 7.1. The parameters from that fit are plugged into theabove equations. How well the two sides of the equations agree guides what subsequent changes will be made to the fitting of the three spectra. i.e., if the left sides of eq.'s 7.3 and 7.6 are notably higher than their right sides, then x_C^{CO} is constrained to comprise a lower area; if 7.1 displays the greatest inequality on its own, thenx_B^{BB} is adjusted accordingly. The process is iterated until the difference between the two sides of each equation is minimized; typically agreement can be achieved to within 1%. This process is shown in Fig 7.4.

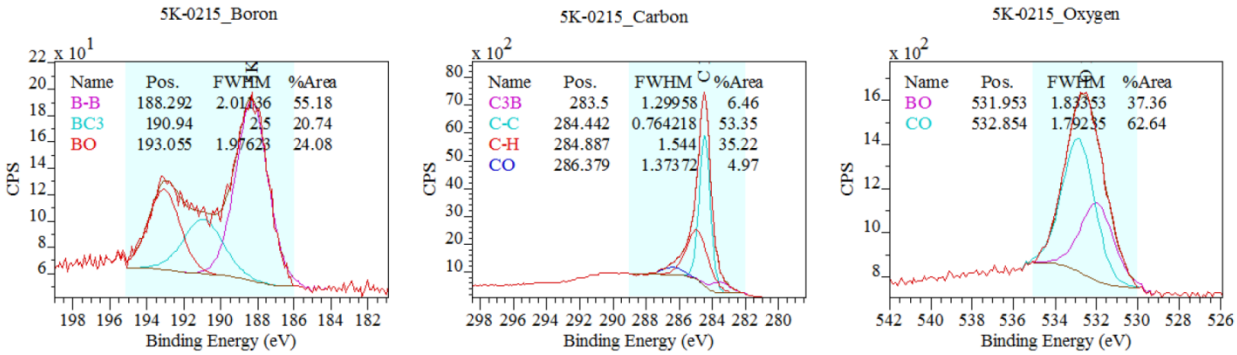

Figure 7.4. XPS deconvolution process/ protocol. The spectra is fit to the initial parameters outlined in Table 7.1 and the areas entered into a specially designed spreadsheet. These areas are converted into atomic fractions x_y^z and equations 7.1-6 are evaluated. Based on the results, the spreadsheet suggests which parameters to modify according to a user-defined threshold.

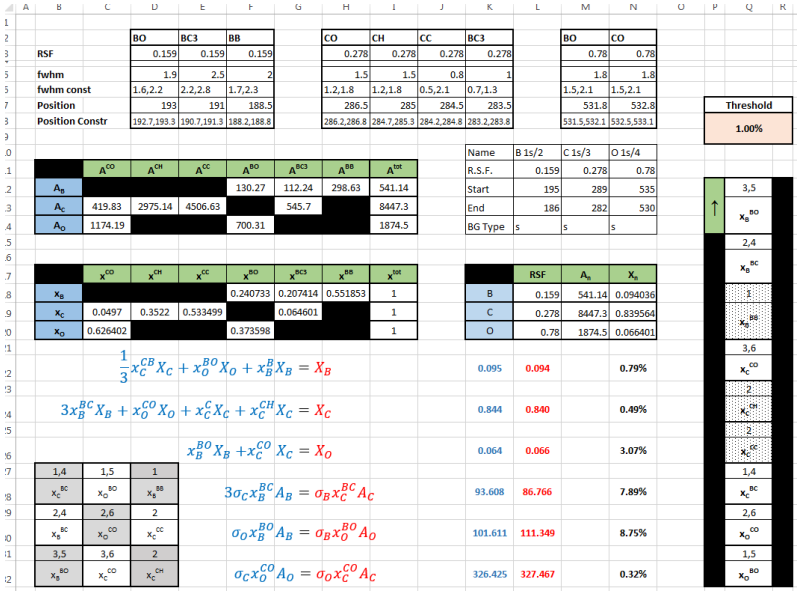

sp^2-bonded B via XPS

Table 7.2.Colors—Yellow: quantities of interest—concentration of sp2-bonded B-C (carrier of high binding energies) and binding energies; light green: B_xC sample with the highest binding energy (5K-0215); white: samples annealed at 800 ºC for 3 hours; orange hatched: samples annealed at 1000 ºC for 3 hours; blue hatched: samples first annealed at 1000 ºC for 3 hours and subsequently annealed at 1200 ºC for 15 hours.

Sample	B_{tot} (wt%)	B_{B-C} (wt%)	B_{B-C}/B_{tot} (%)	O (wt%)	E_b (kJ/mol)
Liquid-phase deposition					
4K-0240	1.2	0.0	0.0	6.2	6.9
4K-0244	1.7	0.0	0.0	7.8	7.2
4K-0245	4.1	0.7	18	10	7.3
4K-0748	5.2	1.0	19	7.9	7.2
3K-0205	7.5	0.9	13	9.0	7.4
3K-0211	7.6	0.6	8.5	11	N/A
5K-0215	8.4	1.7	21	8.7	9.2
3K-0208	15	1.7	12	9.7	N/A
Vapor-phase deposition					
3K-0230	2.2	0.1	3.1	5.7	N/A
3K-1035	3.9	0.4	9.9	8.9	N/A
3K-0231	6.1	0.8	13	11	N/A
3K-1036	3.8	1.1	23	7.7	N/A
3K-0234	4.8	0.6	13	8.5	N/A
3K-0235	24	1.3	5.4	14	N/A
3K-1038	19	1.4	7.5	12	N/A

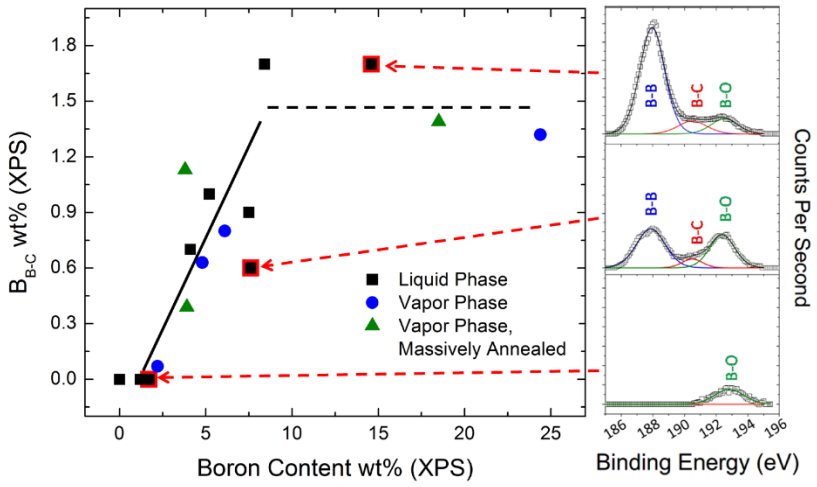

Figure 7.5.*Left*: Concentration of sp^2-bonded boron (B-C bonds, high-binding-energy sites) in different samples as a function of total boron concentration in the samples. XPS spectra for boron, carbon and oxygen were simultaneously fit to determine amounts of sp^2-bonded boron in doped carbon samples. sp^2-bonded boron increases with increasing total boron content. *Bottom Right*: Boron spectra for sample 4K-0244. This spectra is representative of all samples with

boron contents < 2 wt%. In this range, the decomposition of $B_{10}H_{14}$ readily forms B-O bonds. No B-C bonds are observed. *Middle Right*: Boron spectra for sample 3K-0211. This spectrum is representative of samples with 2 < B wt% < 7. In this range, peak splitting is observed as B-B and B-C bonds emerge in addition to the formation of B-O bonds. *Top Right*: Boron spectra for sample 3K-0208. This spectrum is representative of samples with B wt% > 7. The B-B peak is most prominent in this spectrum due to the larger quantity of total boron in the sample. Further, the area under the B-C peak increased to be approximately equal to that under the B-O peak, indicating a larger amount of sp^2 bonded boron in the sample.

7.4 High-Resolution Transmission Electron Microscopy (HRTEM) andEnergy-Filtered Transmission Electron Microscopy (EFTEM)

Exploring the distribution of deposited boron on a nanoporous carbon via TEM is made difficult by the amorphous structure of the material. Therefore, to explore the nature of the doping mechanism, a precursor with a well-defined ordered carbon structure is desired.
PVDC-based carbons are of interest because PVDC thermally decomposes stoichiometrically into pure carbon and gaseous HCl (pyrolysis at 700 ºC). The result[1] is a carbon, often monolithic, with a large micropore volume, a pore-size distribution narrowly peaked around 0.6 nm, and a BET surface area, Σ_{BET}, of about 600-900 m^2/g. The narrow pores are created by escaping HCl gas. PVDC-0736 was produced as described in Section 8.1 and subsequently doped following the 1-SSD procedure, resulting in a graphite-like boron-containing material suitable for study with TEM. The TEM of the carbon before doping is shown in Fig. 8.1.

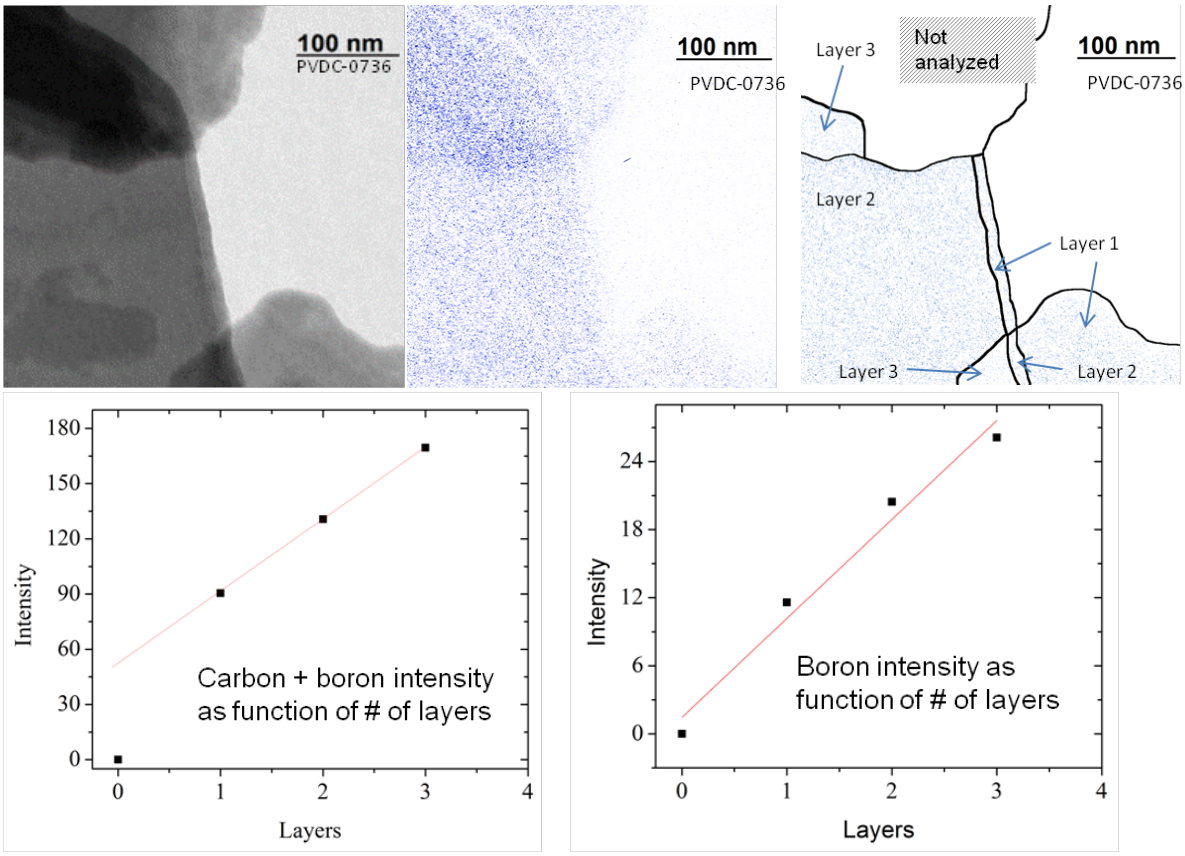

Figure 7.11. Top-left: EFTEM (carbon and boron) image of section comprised of less than three flat, parallel layers. Top-center: EFTEM boron map of the same region, showing uniform boron content throughout carbon sections. Top-right: Proposed model of the layout of structures based on the measured boron intensity and the assumption that boron is uniformly distributed. Bottom left and right: Plots of intensity vs identified number of layers. Linear nature of the fits confirms that the boron is distributed uniformly over >200 nm laterally and ≥3 graphene layers vertically.

[1]Early work:
(a) R.E. Franklin, "The interpretation of diffuse x-ray diagrams of carbon." *Acta Cryst*.**3**, 107-121 (1950).
(b) R.E. Franklin, "Crystallite growth in graphitizing and nongraphitizing carbon." *Proc. Roy. Soc. Lond*. A **209**, 196-218 (1951).
(c) J.J. Kipling and R.B. Wilson, "Adsorptive properties of polymer carbons. Part I—Comparative data." *Trans. Faraday Soc*. **56**, 557-561 (1960).
(d) J.J. Kipling and R.B. Wilson, "Adsorptive properties of polymer carbons. Part II—Determination of pore sizes." *Trans. Faraday Soc*. **56**, 562-569 (1960).

7.5 Electron Energy Loss Spectroscopy (EELS)

Determining the distribution of boron in real, discrete space has been a challenge, insurmountable by the standard techniques (i.e. FTIR, XPS, etc), due to the similar, low atomic weights of the organic (B/C/O/H) compounds comprising our systems. Transmission electron microscopy (TEM) electron energy loss spectroscopy (EELS) and energy filtered TEM (EFTEM) are spatial characterization techniques that are capable of overcoming these limitations. However, these are highly dependent on the thickness of the sample, as excessive thicknesses introduce multiple-scattering artifacts. As a rule, quality TEM-EELS and EFTEM require sample thicknesses less than one mean free path (< 200 nm at 300 kV for carbon based materials).

Scanning electron microscopy (SEM) has shown that our materials feature grain sizes on the microscale, necessitating some form of a thinning method. Standard microtoming isn't possible for powders. A common workaround is to embed them within an amorphous epoxy and microtome cross-sections of the appropriate thickness. However, this technique is not ideal for TEM analysis when encapsulating an amorphous material with similar high-carbon chemistries. Therefore, a novel technique must be developed.

Boron-doped carbons are notoriously oxygen sensitive and thus may not be separated via centrifugation as in a common workaround. Previously, samples were prepared for FTIR via isolation within a pressed KBr "pill". This technique was revisited as embedding an amorphous powder within a crystalline matrix also avoids many of the difficulties present when using an amorphous epoxy substrate. The pill was made using a 1:3000 mass ratio of 5K-0215 (PGAA: 8 wt% B) to KBr; a very low ratio is required to successfully induce crystalline formation upon compaction. Dual beam focused ion beam (DB-FIB) electron microscopy was then used to then select site specific thin samples for TEM.

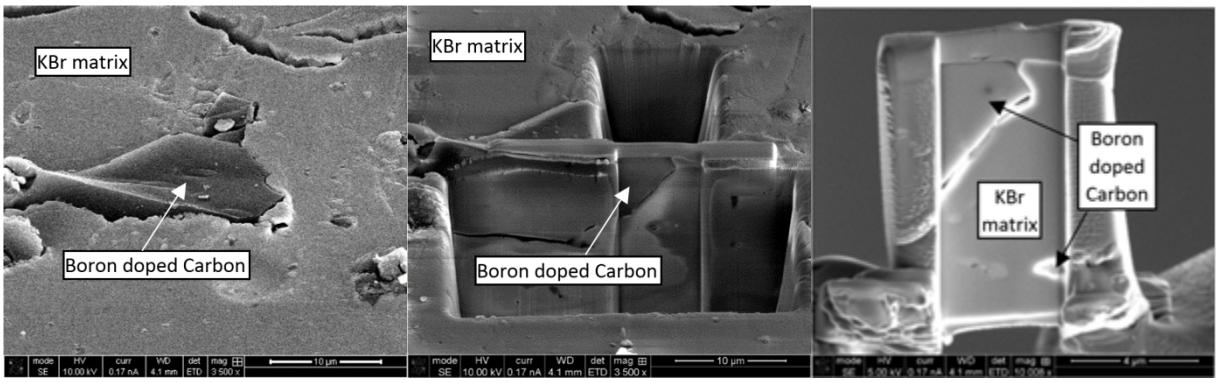

Figure 7.12 (*left to right*) SEM images of the boron doped carbon particle embedded within the KBr matrix, the region of interest for study being extracted by DB-FIB, and the successful TEM cross-section supported within a KBr substrate.

In the literature, KBr has been documented as being highly reactive. During transfer of the TEM sample from DB-FIB to the TEM, the thinned regions of the KBr matrix sublimed leaving only carbon sections attached to a thicker KBr frame (>1 micron in thickness) which did not react, an ideal result for TEM analysis. Figure 2 (left) shows the bright-field image of the DB-FIB sample.

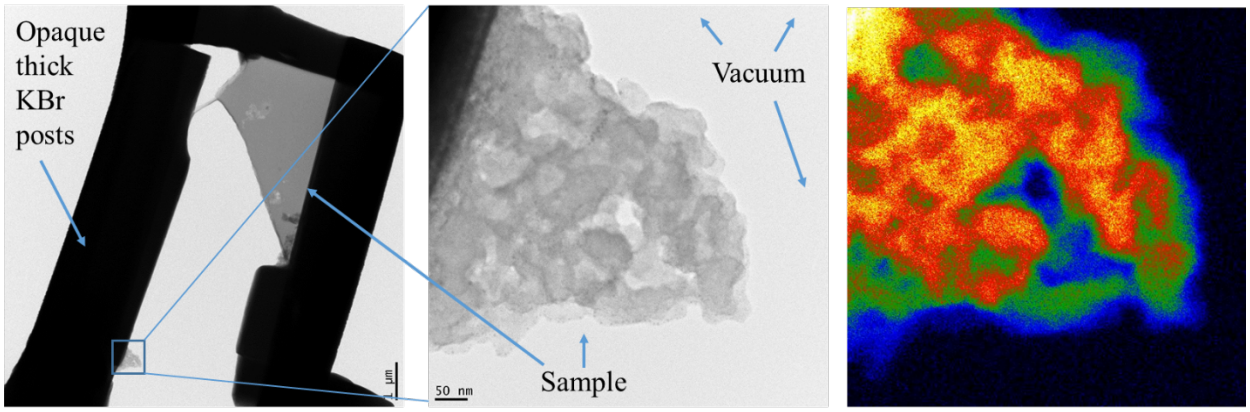

Figure 7.13. (*left, middle*) Bright-field image of carbon sample lifted out and suspended in vacuum via KBr posts after the milled KBr body has sublimated. This is viewed from the opposite side of the sample as seen in the previous figure. (*right*) Thickness analysis of suspended sample from EFTEM.All of the regions within this particular particle have a mean free path under one (brighter refers to increasing thickness).

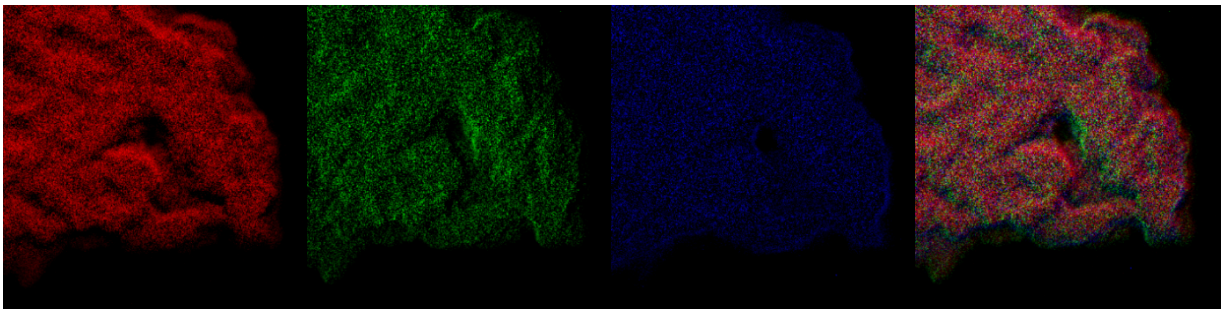

Figure 7.14.EFTEM chemical map of (*left to right*) carbon, boron, oxygen and composite map of the assigned mixed colors in RGB. The system is mainly carbon as the composite still shows mostly red with a minor purple hue. However, the boron (green) appears to largely aggregate at pore "pockets", a possible consequence of doping via deposition.

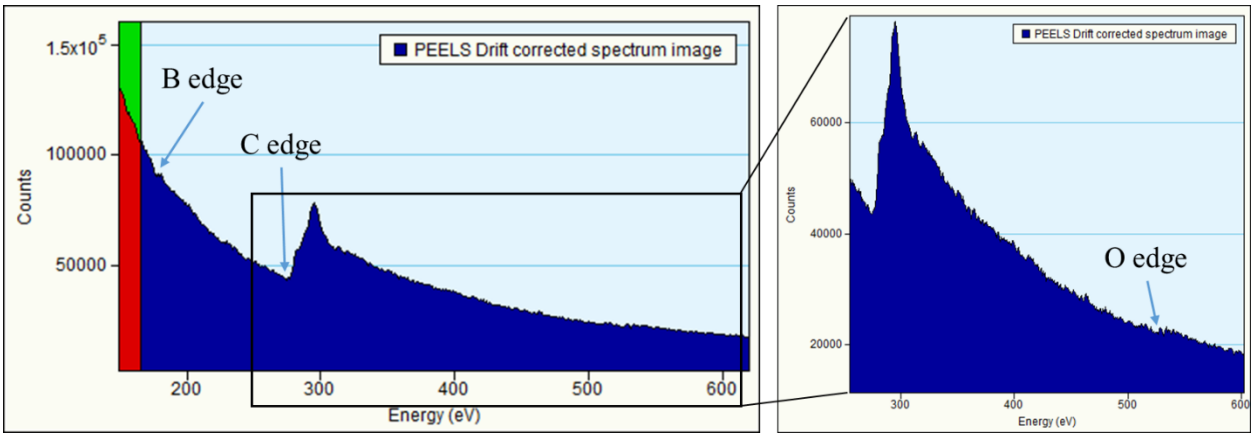

Figure 7.15.EELS spectra showing a minor boron K-edge, carbon K-edge, and the magnified region of a very minor oxygen edge indicating low oxygen content in this particle. Analysis of fine structure within the EELS edges can yield bonding and chemical environment information of the material system. However, the EELS capabilities accessible at the University of Missouri Electron Microscopy Core (EMC), where this work was performed, are chemical environment limited because the equipped gatan imaging filter features a prohibitively low energy resolution (~1 eV).

7.6 Nuclear Magnetic Resonance Spectroscopy (NMR)

Boron doped amorphous carbon was studied by solid state MAS NMR (magic angle spinning nuclear magnetic resonance) for the identification of chemical environment of ^{13}C and ^{11}B nucleus.^{11}B NMR spectra were obtained on a Bruker AVIII 500 and AVIII 400 spectrometers. CPMASS NMR spectra were obtained on a Bruker AMX 300 spectrometer. Chemical shifts are reported in parts per million (ppm) and referenced to the externally to neat Et_2O BF_3 (^{11}BNMR) and $NaBH_4$ (CPMASS NMR). ^{13}C and ^{11}B NMR were performed at room temperature with single pulse excitation and cross polarization of each nucleus. Magic angle spinning rate was reached at 7 kHz with a 5 mm CP MAS probe. The NMR was performed using a single pulse experiment on nuclei we are observing. Direct polarization (DP) of the ^{13}C and^{11}B nucleus by single pulse excitement enabled us to obtain reliable resonance peaks (Emmerich et al. and

Lannin et al.). Due to paramagnetic property of the carbon, the carbon was diluted with an inert material, such as aluminum oxide (Al_2O_3) for appropriate probe tuning and matching making it possible to obtain resonance peaks. Cross polarization (CP) was also attempted to get ^{11}B and ^{13}C NMR spectra. Qualitative ^{11}B nucleus resonance peaks were resolved in cross polarization (CP) spectra, but the determination of the ^{13}C spectrum was not successful. The ^{11}B nucleus spectrum of cross polarization (CP) was compared with that of direct polarization (DP). These studies were carried out on non-doped carbon sample (3K*) and boron doped carbon samples, including boron doped carbon samples with different heat treatment temperatures.

The non-doped carbon, 3K* was analyzed by MAS ^{13}C NMR using direct polarization (DP) of single pulse excitement of ^{13}C nucleus. The single broad resonance peak was observed at around 123.0 ppm in ^{13}C NMR spectrum (Fig7.16, left). This characteristic chemical shift indicated that the material consist of aromatic sp^2 carbon frameworks. The peak broadness was due to not only its paramagnetic property of carbons but also similarly magnetized many carbon atoms in the carbon frameworks. Boron doped carbon sample 3K*-H7 shows a peak at 122.0ppm with no identical chemical shift ranges (Fig7.16, right). This high chemical shift anisotropy associated with the aromaticity of carbon frameworks was observed without respect to the boron doping process.

Boron doped carbon samples were analyzed by DP MAS ^{11}B NMR. Distinctive ^{11}B resonance peaks were seen at the range of 1.20 ~ 1.44 ppm with a broad background boron peak at around -45 ppm (Fig7.17). The background peak at -45 ppm was related to the boron elementsof stators of the probe coming from MAS NMR probe system. After subtracting the background peak, one peak was resolved at the range of 1.66 ppm. CP MAS ^{11}B NMR spectrum also gave a single peak analogously shown at around 1.13 ppm (Fig7.18). The boron doped carbon samples prepared by different annealed temperature (600 °C and 1000 °C) were also analyzed by DP MAS ^{11}B NMR. An identical boron peak was resolved from the boron doped carbon samples with different boron ratios (2 ~ 50 wt %), heat treatment temperatures (120 °C ~ 250 °C) or varied annealed temperature (600 °C and 1000 °C) in DP MAS ^{11}B NMR. The ^{11}B resonance peak was resolved in the range of 1.47 ~ 1.68 ppm and for all samples a very analogous patterned spectrum is observed. The chemical shift ranges observed was believed to indicate the presence of boron on an environment of sp^2 carbon surfaces (Q2 report). However, a similar chemical shift was identified in thermal decomposed boranes, which has the empirical formula of$(BH_{0.6\sim0.9})_x$ from decaboranes ($B_{10}H_{14}$): with peaks resolved at 1.45 ppm of chemical shift in CPMAS ^{11}B NMR (Fig7.19). It is not possible to entirely exclude the possibility of 'BH_x' ($x < 1$). Table4 shows chemical shift assignments of ^{11}B and ^{13}C MAS NMR spectra.

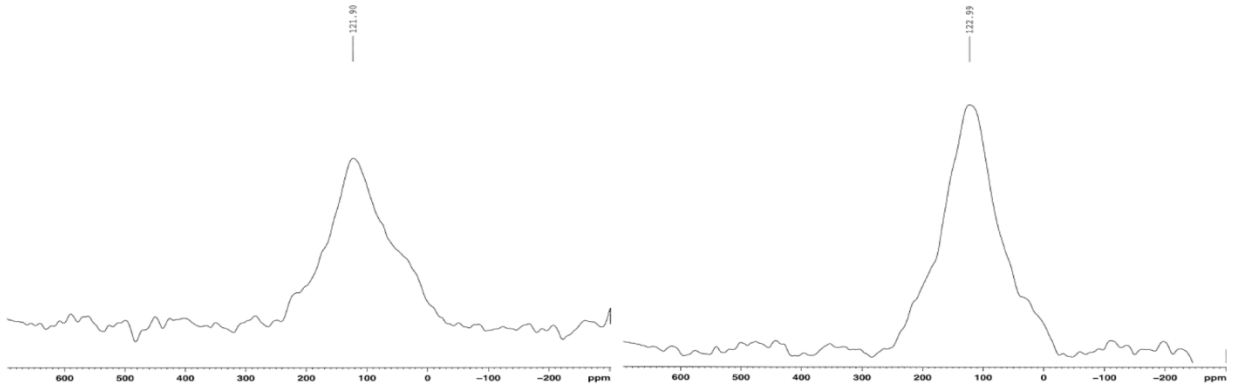

Figure 7.16.[13]C NMR spectrum of amorphous carbon 3K* (*left*) and boron doped carbon 3K*-H7 (*right*).

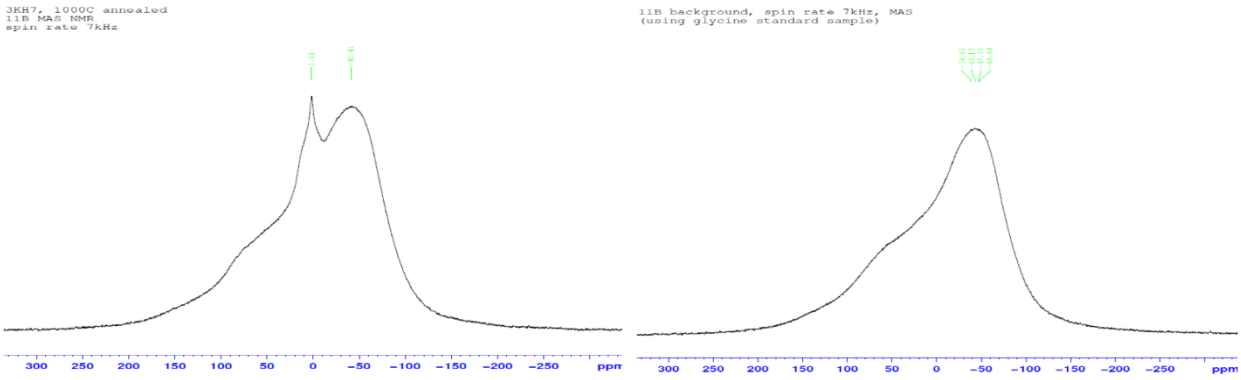

Figure 7.17. DP MAS [11]B NMRof 3K*-H7 annealed at 1000 °C(with background)(*left*),and background(*right*).

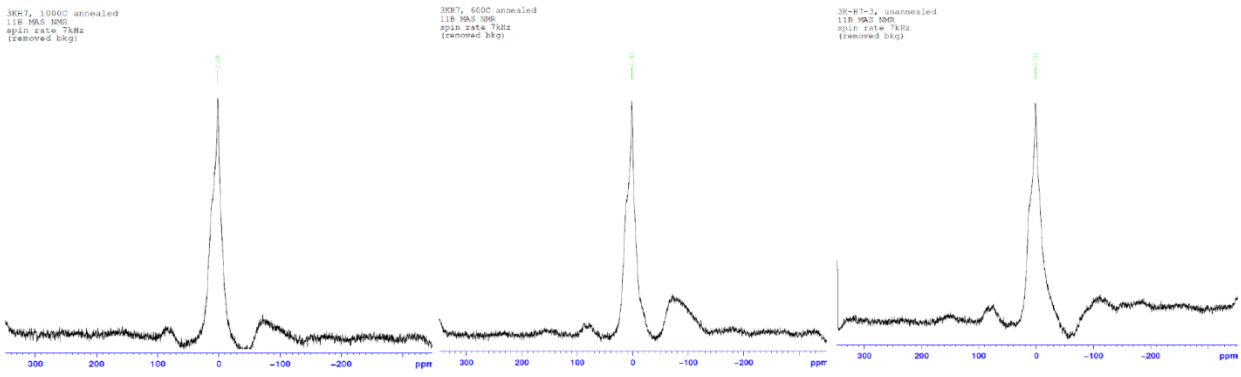

Fig 7.18. DP MAS [11]B NMR (background removed) of 3K*-H7 annealed at 1000 °C (*left*), 600 °C (*center*), and not annealed (*right*).

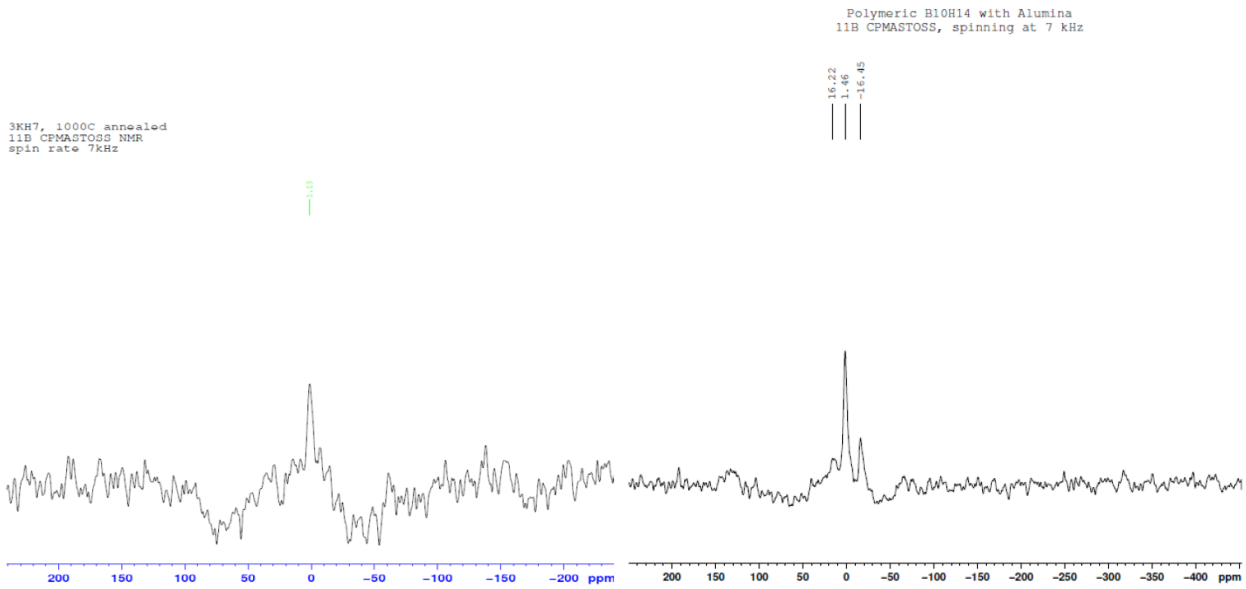

Figure 7.19.CP MAS ^{11}B NMR of 3K*-H7 annealed at 1000 °C (left) and decomposed decaboranes ($B_{10}H_{14}$).

Table 7.3.Chemical shift assignment of ^{11}B and ^{13}C MAS NMR spectra. ([a]) indicates major peak. ([b]) indicates sample annealed via solution NMR, all others used solid NMR

Samples	B conc	Doping Method /Temp.	Anneal. Temp.	Chemical Shift (ppm) from:		
				DP MAS ^{11}B NMR	CP MAS ^{11}B NMR	DP MAS ^{13}C NMR
3K*	0%	N/A	N/A	N/A	N/A	121.90
3K*-H1	10%	I/150 °C	N/A	N/A	N/A	122.99
3K*-H7	10%	I/120 °C	N/A	1.51	N/A	N/A
3K*-H7	10%	I/120 °C	600 °C	1.47	N/A	N/A
3K*-H7	10%	I/120 °C	1000 °C	1.68	1.13	N/A
Probe Bkgd	N/A	N/A	N/A	-45 (broad pk at -20~-60)	N/A	N/A
$B_{10}H_{14}$ (pyrolized)	100%	N/A	250 °C	16.22, 1.46[a], -16.46	N/A	N/A
$B_{10}H_{14}$ (solution)[b]	100%	N/A	N/A	12.05, 10.48, 0.57, -35.97	N/A	N/A

8. Adsorbent Engineering IV: Synthetic Carbons (Phase 2)

8.1 Monomodal Pore-Size Distributions

PVDC-based carbons are of interest because PVDC thermally decomposes stoichiometrically into pure carbon and gaseous HCl (pyrolysis at 700 ºC). The result is a carbon, often monolithic, with a large micropore volume, a pore-size distribution narrowly peaked around 0.6 nm, and a BET (Brunauer-Emmett-Teller) surface area, Σ_{BET}, of about 600-900 m^2/g. The narrow pores are created by escaping HCl gas. We compared hydrogen adsorption on such PVDC-based carbons with hydrogen adsorption on graphene-like activated carbons, with surface areas around 2600 m^2/g, derived from lignocelluluose. Unexpectedly, we found that PVDC-based carbons reproducibly adsorb significantly more hydrogen than would be expected from their surface area. This is consistent with that, in narrow pores, overlapping adsorption potentials from opposite carbon walls produce binding energies as high as 8-10 kJ/mol, if the single-wall binding energy is 4-5 kJ/mol.

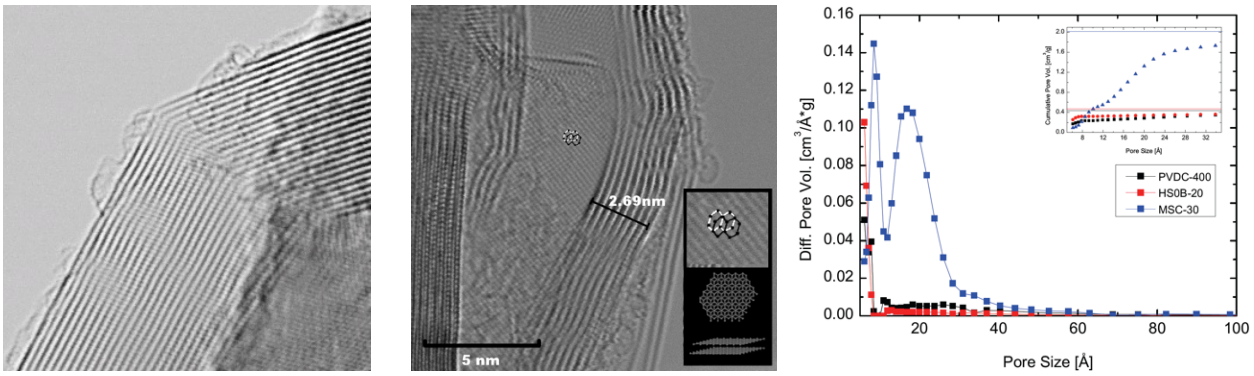

Figure 8.1 *Left* and *center*: High resolution transmission electron micrographs (Nion UltraSTEM, Oak Ridge National Laboratory) of U. Missouri PVDC-based carbon HS;0B-20. The center image shows a bilayer of graphene flanked by stacks of 8 graphene layers, perpendicular to the image plane, spanning a distance of 2.69 nm. The resulting interlayer spacing of 0.33-0.34 nm agrees perfectly with the interplanar spacing of graphene. *Right*: comparison of the pore size distribution of HS:0B-20 with that of commercial activated carbon MSC-30, with pore-size distribution peaked at 0.9 and 1.8 nm. HS;0B-20 has a very narrow, monodisperse distribution centered around 0.7 nm. Surface areas, Σ_{BET}, and porosities, ϕ: HS;0B-20: Σ_{BET} = 940 m^2/g, porosity ϕ = 0.46; MSC-30: Σ_{BET} = 2700 m^2/g, ϕ = 0.80.

Table 8.1. Comparison of BET surface areas (Σ_{BET}) and crystalline void fractions (ϕ) of synthetic carbons HS;0B-20 and PVDC-0400 as measured from N_2 and Ar isotherms

	HS;0B-20	**PVDC-0400**
BET surface area, Σ_{BET} (N_2)	940 m^2/g	780 m^2/g
BET surface area, Σ_{BET} (Ar)	980 m^2/g	660 m^2/g
Void fraction (cryst., total), ϕ (N_2)	0.46	0.49
Void fraction (cryst., total), ϕ (Ar)	0.45	0.45

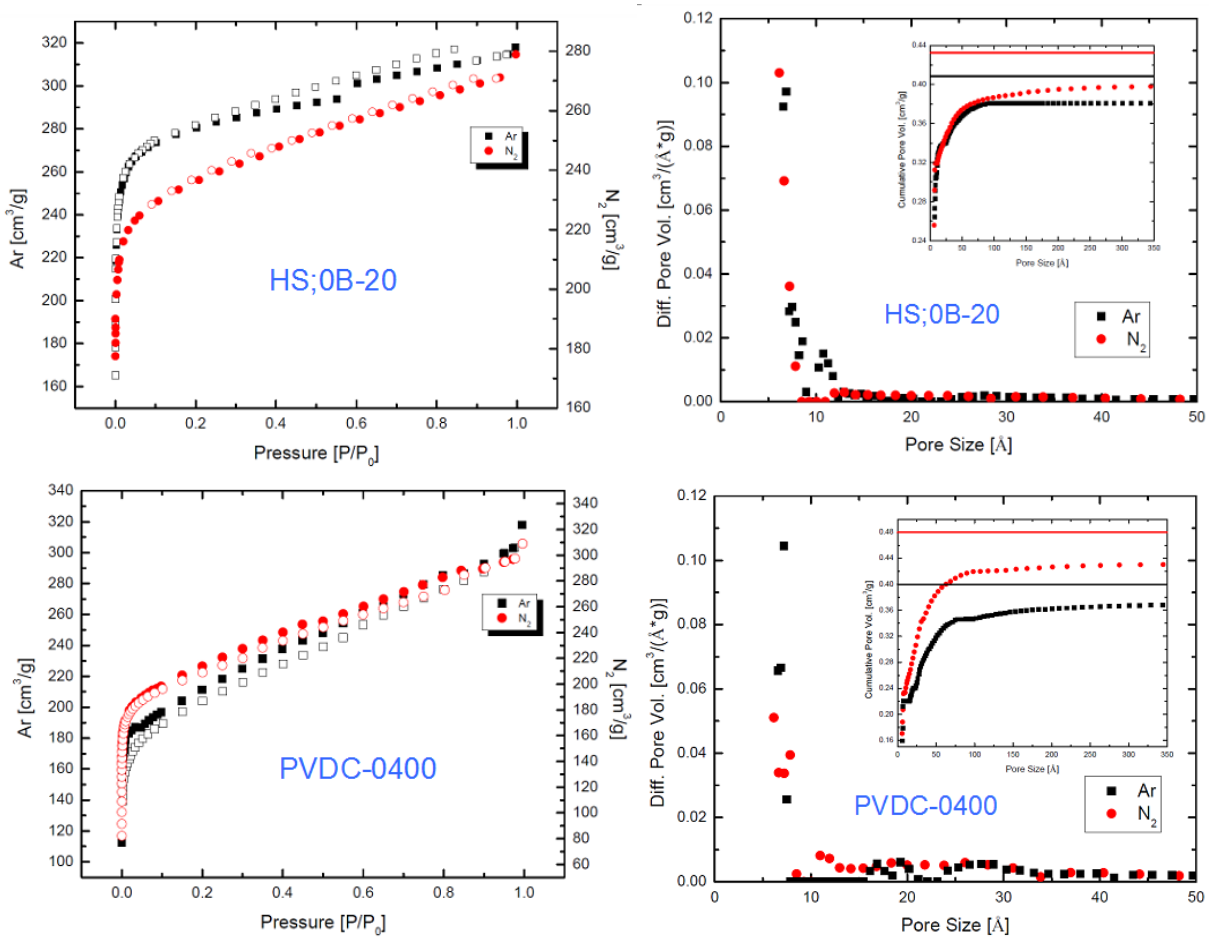

Figure 8.3. N_2/Ar sorption isotherms (*left*) and pore size distributions/cumulative pore volumes from N_2 and Ar (*right*) for samples synthetic carbons HS;0B-20 (*top*) and PVDC-0400.

8.2 High Binding Energies in Sub-nm Pores

Due to their significantly reduced surface areas, synthetic carbons predictably demonstrate reduced H_2 storage. However, the isotherms feature a few notable characteristics (Fig. 8.4). For one, the local maximum of G_{ex}, representative of a nearly saturated film, occurs at a much lower pressure than conventional activated carbons (MSC-30). At 77 K (296 K), the maximum occurs at approximately 20 bar (120 bar) for synthetic carbons, compared to approximately 50 bar (> 200 bar) for nanoporous activated carbon (Fig. 8.4). They are the only sorbents to demonstrate a local G_{ex} maximum at pressures less than 200 bar at room temperature. Further, the areal excess adsorption (excess adsorption per unit area) is up to 60% higher on synthetic carbon, a strong departure from Chahine's rule.

At high pressure, gravimetric excess adsorption as a function of gas density approaches a well-defined linear regime with negative slope (Fig. 8.5), so that the excess isotherm

$$G_{ex} = (V_{film}/m_s)[\rho_{film} - \rho_{gas}] \quad (8.1)$$

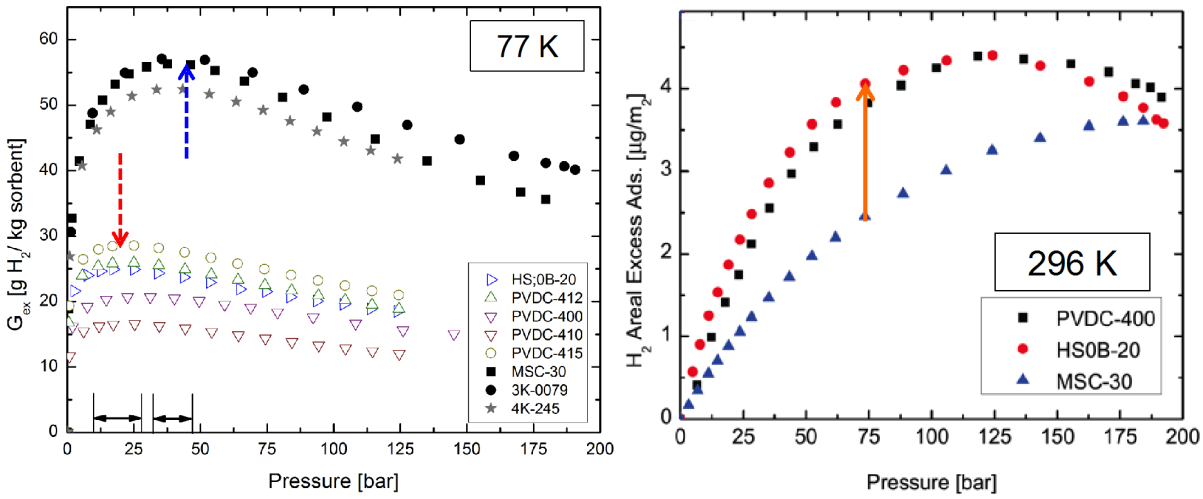

Figure 8.4. Gravimetric (*left*) and areal (per unit area) (*right*) excess adsorption isotherms of synthetic carbons compared to nanoporous activated carbons. The peak, representative of the pressure at which the saturated film is at a maximum density, occurs at a significantly lower pressure than MSC-30. Synthetic carbons also feature a dramatically increased areal excess adsorption (strong departure from Chahine's rule).

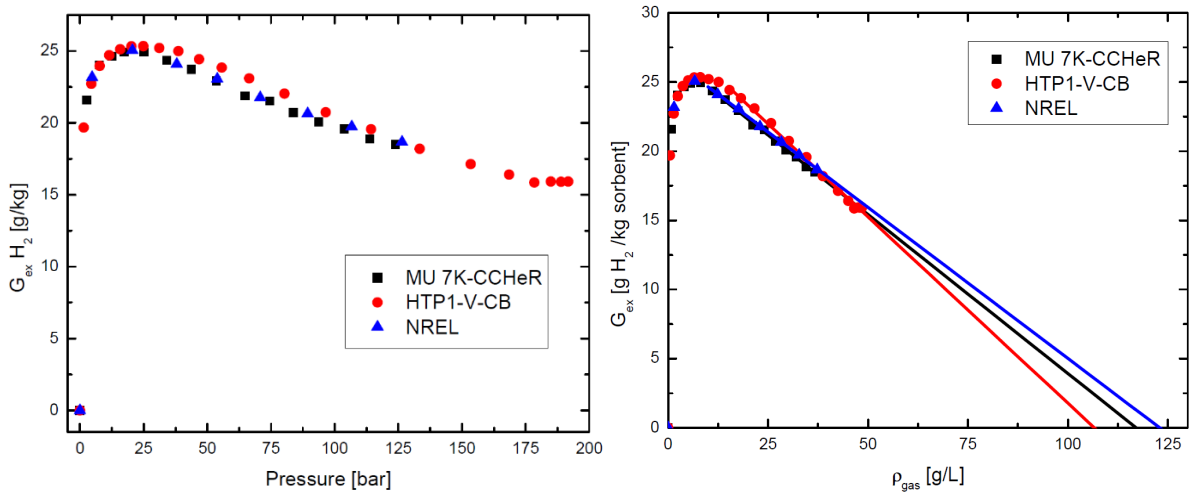

Figure 8.5. Independent gravimetric excess adsorption of sample HS;0B-20, as measured at MU on the HTP1-V-CB ("Hiden HTP") and 7K-CCHeR ("7K Sievert"), and NREL, show excellent agreement. Isotherms at high densities are linearly fitted (parameters in Table 8.2), resulting in calculated film densities greater than that of liquid H_2.

can be analyzed with constant V_{film} and ρ_{film}. Film saturation occurs near $p \sim p_{max}$ and the density of the saturated film can be read off by extrapolation of the linear form G_{ex} vs. ρ_{gas} to the point $G_{ex} = 0$, at which point the density of the film is equal to that of the nonadsorbed gas by Eq. (8.1). Therefore, V_{film} and the saturated film density $\rho_{film,sat}$ can be determined by fitting the form

$$G_{ex} = (V_{film}/m_s)[\rho_{film,sat} - \rho_{gas}] \qquad (8.2)$$

with constants V_{film} and $\rho_{film,sat}$, to the experimental excess isotherm. The graphical procedure is in Figure 8.2. The results from the fits are collected in Table 8.2.

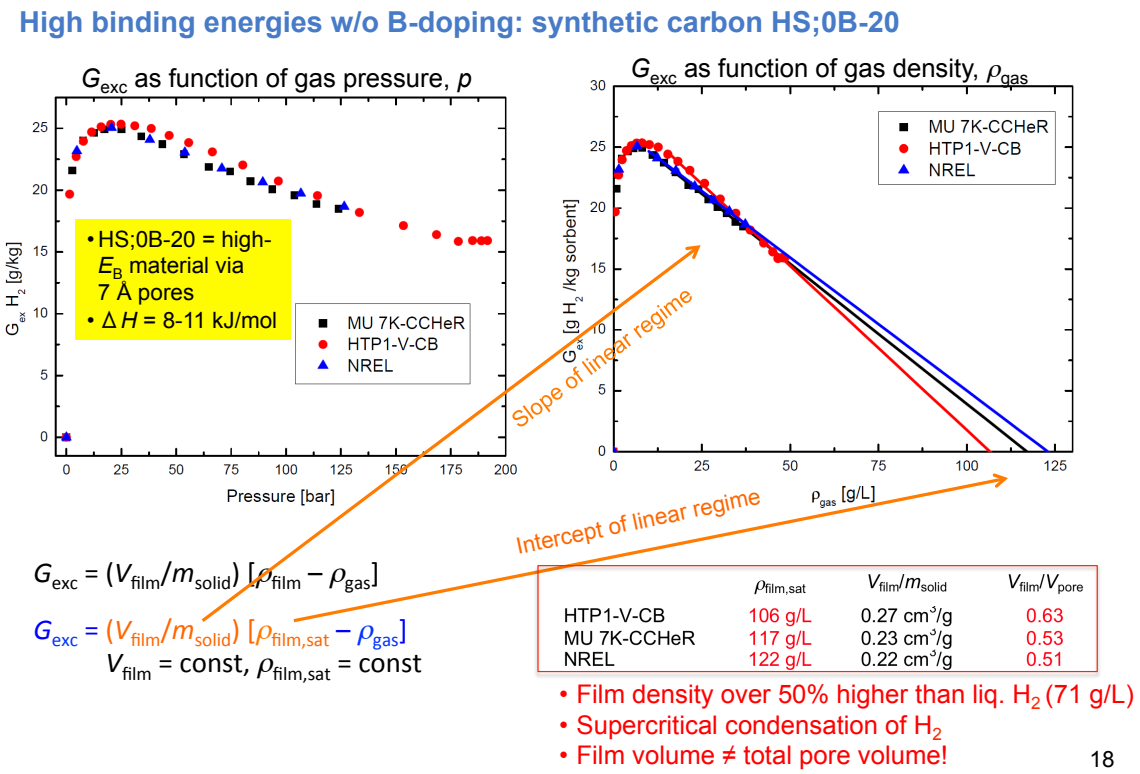

Figure 8.2. Determination of the film volume V_{film} and saturated film density $\rho_{film,sat}$ from fitting Eq. (8.2) to experimental G_{ex} vs. ρ_{gas} data.

Table 8.2. High density linear fit parameters for sample HS;0B-20 as shown in Fig 8.5. HS;0B-20, a high E_b (ΔH = 8-11 kJ/mol) material by virtue of consisting almost entirely of 7 Å pores (Fig 8.3), reproducibly yields a film density over 50% higher than that of liquid H_2 (71 g/L).

Instrument	$\rho_{film,sat}$	V_{film}/m_{solid}	V_{film}/V_{pore}	Max. Film Cap.
HTP1-V-CB	106 g/L	0.27 cm^3/g	0.63	28.6 g H_2/kg sorbent
MU 7K-CCHeR	117 g/L	0.23 cm^3/g	0.53	26.9 g H_2/kg sorbent
NREL	122 g/L	0.22 cm^3/g	0.51	26.8 g H_2/kg sorbent

8.3 High Saturated Film Densities

Saturated film density estimation

Cryogenic hydrogen isotherms at 77 K were collected for different adsorption materials and their saturated film density evaluated according to the method described earlier. For each sample multiple sets of experimental points are used for the linear fit, and the error was estimated by taking the difference between the obtained maximum and minimum value of all fits of one sample.

With the exception of MSC-30 (chemically activated carbon) all samples intersect the abscissa above 100 g/L despite their different PSD and surface areas. This density is remarkably high and even surpasses the liquid (20 K) density of hydrogen (71 g/L). Sample HS;0B-20 was sent to the

National Renewable Energy Laboratory (NREL) for validation, and the isotherm reproduced results shown here. All of the samples in this study were measured on two different instruments: HTP-1-V-CB, a modified version of the commercially available HTP-1 from Hiden Analytical, and the MU-7K instrument mentioned below, with the same result. Thus it is reasonable to assume systematic instrumental errors are insignificant.

Most adsorbent surfaces in this study are mainly composed of carbon hexagons, meaning that the adsorption potential is influenced by the carbon hydrogen interaction (van der Waals interaction) and the confinement due to the porous structure as mentioned earlier. One could therefore conclude that samples with mainly narrow pores should have high saturated film densities as they have a deeper adsorption potential. However, the data shown here do not show a direct correlation between saturated film density and the pore structure. Adsorbents with mainly sub-

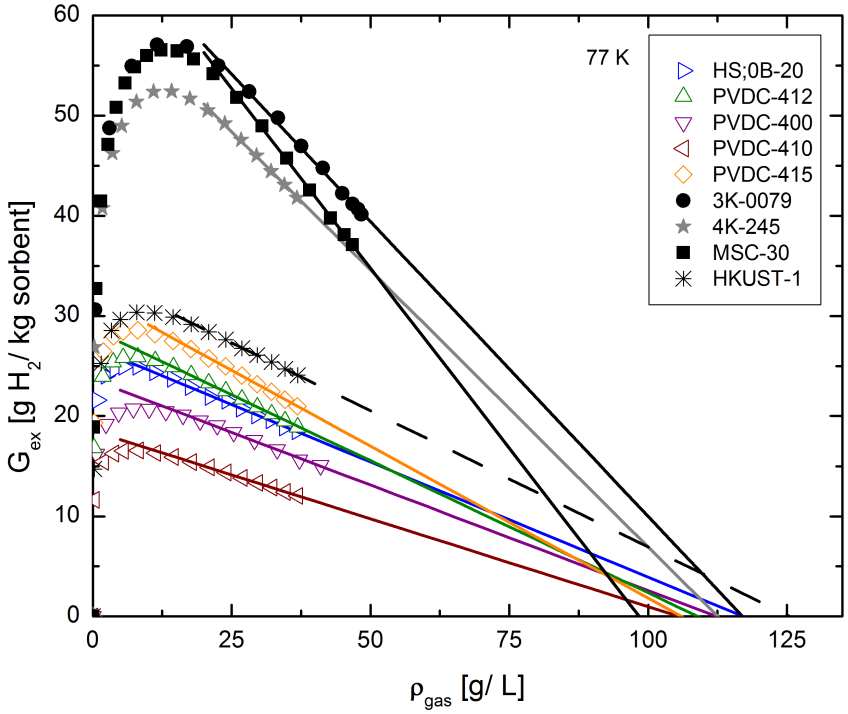

Figure 8.6. Linear fitting for samples shown in Fig. 8.4 (left) in addition to the metal organic framework (MOF) HKUST-1. Extrapolated saturated film densities are listed in Table 8.3.

Table 8.3. Saturated film densities calculated from the linear regime shown in Fig. 8.6.

Sample	$\rho_{film,sat}$ **(g/L)**
HS;0B-20	117 ± 7
PVDC-412	106 ± 6
PVDC-400	112 ± 3
PVDC-410	104 ± 5
PVDC-415	106 ± 6
MSC-30	99 ± 5
3K-0079	114 ± 7
4K-245 (3.8 wt% boron)	110 ± 3
HKUST-1	125 ± 7

nanometer pores (synthetic carbons, colored graphs) lead to the same film density as adsorbents with a variety of pores sizes (chemical activated carbons, black). The data suggest a universal density value for hydrogen (~109 g/L) adsorbed on a carbon surface. The only outlier for the carbon-based samples is the commercial activated carbon MSC-30. It has a slightly lower value compared to the rest, possibly due to problems with the data fitting. MSC-30 has a slight convex bend in the linear regime which makes it more difficult to fit.

Sample 4K-245 was boron-doped after chemical activation to increase its hydrogen binding energy by altering the surface chemisty. However, the film density is similar to undoped carbon samples, indicating surface deposition of boron does not influence the saturated film density. This is possibly due to the low ratio of boron to carbon atoms on the surface. According to prompt gamma neutron activation analysis (PGAA), this sample has 4 wt% boron, meaning the majority of the surface is composed of carbon atoms, similar to chemically activated carbon. The amount of boron deposited on the surface could be too low to sufficiently alter the film density to be detectable.

Metal organic frameworks (MOFs), such as HKUST-1, are porous materials made of metal sites connected by organic linkers resulting in a different surface chemistry compared to carbon based samples, and therefore give an indication if there is a dependency between film density and surface chemistry. The MOF HKUST-1 (Sigma-Aldrich, $Cu_3(BTC)_2$) used in this study has copper metal sites and benzene-1,3,5-tricarboxylate as an organic linker. It consists mainly of 7 nm wide pores. The linear interpolation of HKUST-1 gives rise to a saturated film density of 126 g/L, which is 7% higher compared to the highest carbon-based sample.

This sample has a comparably monodisperse PSD to synthetic carbons (mainly 7 nm wide pores) and therefore a difference in saturated film density is an indication if surface chemistry affects the adsorbed film. HKUST-1 has a 15% higher density compared to the average of synthetic carbons (109 g/L) which suggests surface chemistry can influence the saturated film density.

Film thickness from saturated film density

The film thickness can be directly calculated from the saturated film density, without the knowledge of the film volume or surface area. The model and requisite formula was introduced in Sect. 1.3.3 (Fig. 1.8). We reproduce it here for convenience (Fig. 8.6'). The only assumption in the model is that the saturated film is a monolayer. The results for the adsorbents in Table 8.3 are collected in Table 8.3'. We denote the film thicknesses so determined by t_{film} throughout. Error bars in t_{film} reflect exclusively error bars in $\rho_{film,sat}$ (Table 8.3). Table 8.3' also reports t_{film} values obtained from $\rho_{film,sat}$ at $T = 50$ K , from isotherms at 50 K not reported here, for readers who may be curious to see how t_{film} depends on temperature.

Just as saturated film densities are remarkably universal, $\rho_{film,sat}$ ~ 100–120 g/L at 77 K (Table 8.3), film thicknesses are equally universal, t_{film} = 0.30–0.32 nm at 77 K (Table 8.3'). Also remarkably, the values 0.30-0.32 nm agree very well with film thicknesses from high-pressure/ high-density grand-canonical Monte Carlo simulations of H_2 adsorbed in pores of variable width (L. Firlej, B. Kuchta, 2016). To the best of our knowledge, this is the first time that accurate experimental values for the thickness of H_2 films at 77 K have been obtained.

$$n_{liq} = \frac{\#\ \text{molecules in slab}}{\text{volume of slab}} = \frac{\#\ \text{molecules in monolayer}}{\text{volume of monolayer}} = \frac{A / t_{film}^2}{A t_{film}} = \frac{1}{t_{film}^3}$$

$$t_{film} = n_{liq}^{-1/3} = (\rho_{film,sat} \cdot N_A / M)^{-1/3}$$

N_A: Avogadro number
M: Molecular mass (g/mol)

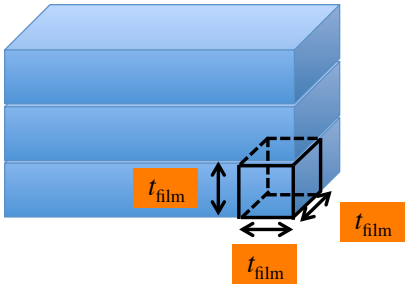

- Typical values:

	$\rho_{film,sat}$	t_{film}
H_2 on carbon, 77 K Liq. H_2, 20 K (n.b.p.)	100-120 g//L 71 g/L	0.30-0.32 nm
CH_4 on carbon, 298 K Liq. CH_4, 112 K (n.b.p.)	390-420 g/L 420 g/L	0.40-0.41 nm

Figure 8.6'. Determination of the film thickness, t_{film}, from the saturated film density, $\rho_{film,sat}$.

Table 8.6. Film thickness, t_{film}, calculated from saturated H_2 film density, $t_{film} = (\rho_{film,sat} \cdot N_A/M)^{-1/3}$

	Film thickness calculated from $\boldsymbol{\rho_{sat.\ film}}$ [nm]			
	77 K		50 K	
		Average of linear regime	1st	2nd
HS;0B-20	0.306 ± 0.006			
PVDC-412	0.317 ± 0.011	0.317 ± 0.015	0.334 ± 0.002	0.314 ± 0.007
PVDC-400	0.310 ± 0.009			
PVDC-410	0.317 ± 0.008	0.328 ± 0.005	0.331 ± 0.003	0.327 ± 0.003
PVDC-415	0.315 ± 0.009	0.345 ± 0.015	0.363 ± 0.001	0.34 ± 0.006
MSC-30	0.323 ± 0.018			
3K-0079	0.310 ± 0.007			
4K-245 (3.8 wt% boron)	0.310 ± 0.012	0.328 ± 0.13	0.34 ± 0.004	0.324 ± 0.006
HKUST-1	0.3 ± 0.008			

Film thickness estimation from surface areas

The film thickness may be estimated, from the linear regime of G_{ex} vs. ρ_{gas}, in a different way. The absolute value of the slope represents the volume of the adsorbed film. The thickness of the adsorbed layer is then estimated by taking the average film volume from each individual fit

divided by the material's surface area (Table 8.4):

$$d_{film} = \frac{volume\ of\ ads.\ film\ per\ g\ sorbent}{surface\ area\ of\ ads.\ film\ per\ g\ sorbent} = \frac{|slope|}{\Sigma} \quad (8.3)$$

The errors are represented by the spread of the obtained slopes. The surface area was determined from subcritical nitrogen isotherms according to the method described by Brunauer, Emmett, and Teller (BET) using an automated gas-adsorption instrument from Quantachrome (Autosorb-1). With the exception of HKUST-1, each sample's specific surface area was determined in the same pressure range (0.008–0.03 p/p_0) of the nitrogen isotherm. For HKUST-1 a higher pressure range (0.02-0.1 p/p_0) was used to get an accurate BET fit.

The amount of pore filling can also be estimated from the film volume, by taking the ratio of adsorbed film volume and the total pore volume measured with nitrogen at a pressure of 0.995 p/p_0.

Table 8.4.Saturated film thicknesses from Eq. (8.3) and pore filling factors.

Sample	d_{film} (nm)	Pore-filling Factor
HS;0B-20	0.24 ± 0.02	53%
PVDC-412	0.25 ± 0.03	40%
PVDC-400	0.27 ± 0.03	44%
PVDC-410	0.26 ± 0.03	28%
PVDC-415	0.25 ± 0.04	44%
MSC-30	0.26 ± 0.02	34%
3K-0079	0.23 ± 0.03	34%
4K-245 (3.8 wt% boron)	0.23 ± 0.04	25%
HKUST-1	0.14 ± 0.03	26%

Despite the fact that some of the materials have vastly different PSDs and isosteric heats of adsorption, their adsorbed films have very similar thicknesses. The adsorbed film thickness for all carbon based samples is approximately 0.25 nm and does not show much variation between different sample types. The only exception is the MOF HKUST-1, with a film thickness almost half that of the carbon based samples.

The hydrogen molecule size can be estimated by using the second viral coefficient, which leads to a diameter of 0.29 nm (at 273 K and 1 bar). In reality the size should be somewhat smaller because the measurement was performed at 77 K and pressures well above 1 bar. Given the film thickness of 0.25 nm for most of the materials, this corresponds to monolayer adsorption. However, HKUST-1 has a calculated film thickness of approximately half a hydrogen molecule, too small to be physically feasible. This is potentially due to the method used to calculate film thickness. The calculation method assumes that the hydrogen adsorbs onto the same surface area calculated from a subcritical nitrogen isotherm (Σ_{BET}). To estimate a correct surface area, the BET theory assumes adsorption happens on an energetically homogeneous surface. Infrared spectroscopy and powder neutron diffraction measurements of HKUST-1 reveal at least three distinct binding sites. First hydrogen adsorbs at the Cu sites, then fills the small cage structure near the metal sites, before filling the larger pores.

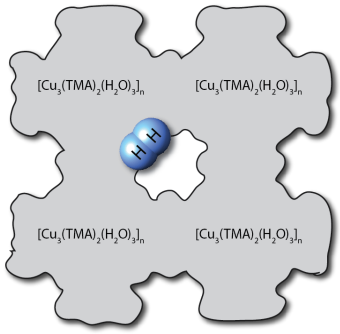

Figure 8.7.Position of hydrogen after adsorption in HKUST-1.

Raman spectroscopy also shows some chemical interaction between Cu and hydrogen (electron donation). In this case using the BET surface area as a surface reference on which hydrogen adsorbs is not the best choice and most likely leads to misleading results. Thus the monolayer thickness for HKUST-1 calculated with this method should be taken with caution.

In most porous systems the adsorbed film occupies only a quarter of the pore volume indicated by the pore filling factor of 25%. Only for some synthetic carbons does it reach a filling of 50%. These values represent the average pore filling because the calculation takes the film volume divided by the total pore volume measured by subcritical nitrogen adsorption close to the saturation pressure (0.995 p/p_0). Most samples do not have a monodisperse PSD, meaning they have several pore sizes. Thus, the calculated filling factors do not represent the actual filling of each individual pore.

The results presented here do not show signs of capillary condensation in sub-nanometer pores. This can be best seen with sample PVDC-400, which mainly made of pores in the sub-nanometer range (PSD shown in introduction). The pore volume is only 40% filled. If capillary condensation were to occur, then the filling factor should be close to 90%.
Most materials have filling factors of 25%, meaning three fourths of the pore volume is filled with unwanted low density bulk gas. This is especially true for chemically activated adsorption materials.

8.4 High Intrapore Hydrogen Densities in Sub-nm Pores

The previous section demonstrated how to estimate saturated film densities by using the linear regime at high pressures isotherms. For most samples such a behavior is only observed at cryogenic temperatures and high pressures, and therefore this method fails at room temperature. Another problem arises from the fit itself. In most cases it is not exactly clear where the linear regime starts.

One method to obtain information about the gas density inside the porous structure is by evaluating the intrapore density (ρ_{ip}). It is defined as the total amount of gas inside the porous network divided by pore volume and is therefore an average of film density and non-adsorbed gas over the entire sample pore space. The intrapore density's lower limit is that of the bulk gas, which occurs in systems where no adsorption takes place. On the other hand, ρ_{ip} reaches its upper limit if the pores are completely filled with adsorbate and an increase of pressure does not introduce more molecules in the pores.

Figure 8.8.Intrapore density is calculated by taking volumetric storage capacity and dividing by the sample porosity. Intrapore density ρ_{ip} of the adsorbent includes both the adsorbed film (blue) on the sorbent surface (black) plus non-adsorbed gas (tan) in the pore space.

The majority of synthetic carbon samples (Fig. 8.9) have high ρ_{ip}, with some even exceeding the liquid density of hydrogen at 20 K (71 g/L). This indicates that the actual film density must be even higher since $\rho_{gas}(p,T) \leq \rho_{ip}(p,T) \leq \rho_{film}(p,T)$, and therefore justifies the high saturated film densities governed by the linear extrapolation described earlier. This technique does not require any assumptions about the film thickness or curve fitting, which makes it very robust.

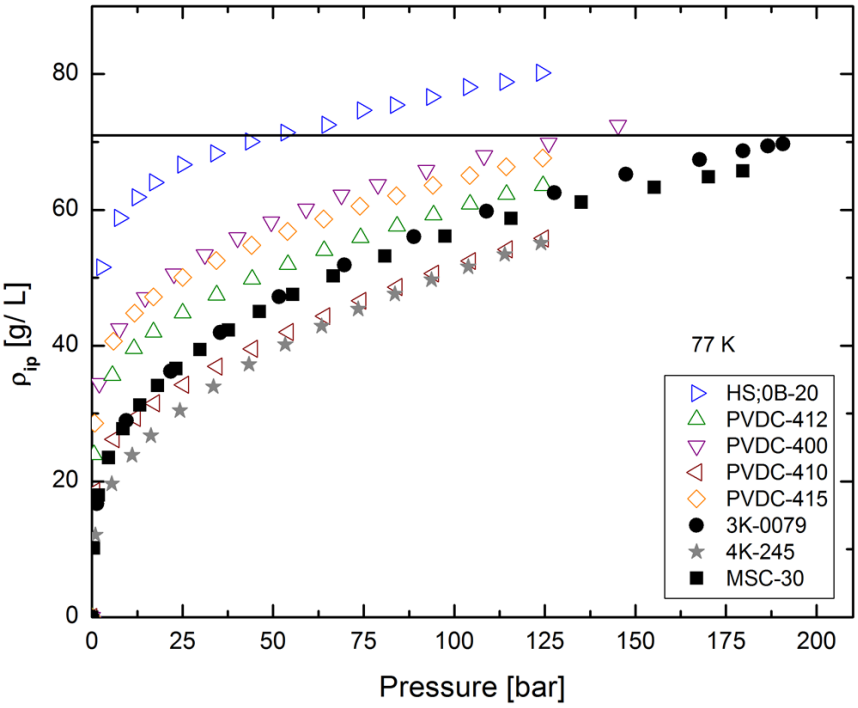

Figure 8.9. Intrapore densities (total mass H_2 stored, adsorbed and non-adsorbed, per volume of pore space – $\rho_{ip} = V_{st}/\phi$) of samples compared with the liquid (20 K) density of H_2, 71 g/L. At 77 K, ρ_{ip} on HS;0B-20 is ~60% higher than MSC-30-type carbons, crossing liq. H_2 density at 35 bar and approaching 90 g/L at 180 bar. This supports the conlusion that $\rho_{film,sat}$ = 106-122 g/L at 77K (Table 8.3). This gives an estimate of ρ_{film} without assumptions about film thickness or pore space: $\rho_{gas}(p,T) \leq \rho_{ip}(p,T) \leq \rho_{film}(p,T)$.

8.5 High Storage Capacity in Sub-nm Pores from Soft Spring Constants
Not executed

9. Hydrogen Adsorption on Phase-2 B_xC Materials and Synthetic Carbons

9.1 Experimental Observation of Henry's Law on B_xC Materials

> "At a constant temperature, the amount of a given gas that dissolves in a given type and volume of liquid is directly proportional to the partial pressure of that gas in equilibrium with that liquid."
> - William Henry,1803

In the figures below are displayed the seven best linear regimes in which we apply our binding energy analyses.

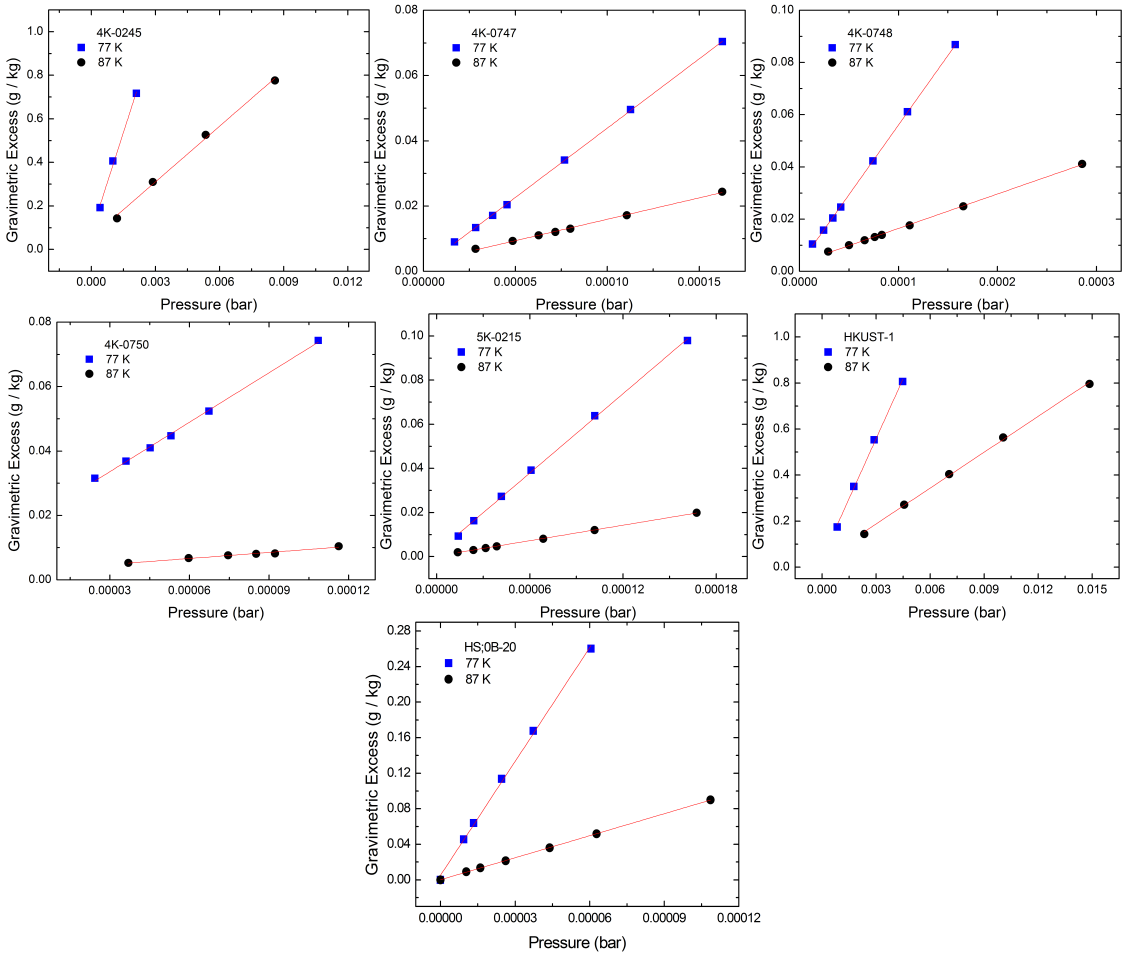

Figure 9.1: Gravimetric excess adsorption versus pressure for various adsorbent solids. These low pressure isotherms serve as a visual figure merit for the applicability of a linear isothermal model in the ultra-low pressure regime. Slopes and analyses can be found in the following table.

Table 9.1: Isosteric heats (*ΔH* determined via linear fitting in the Henry's Law regime as in Fig. 9.1) vs binding energies ($E_{b,mobile}$, determined via model-dependent fitting as in Sec. 1.4). Binding energy from localized adsorption, determined from $E_{b,localized} = E_{b,mobile} + 0.3416$ kJ/mol, is shown to be in remarkable agreement (≤~1%) to *ΔH*.

Sample Name	Applicable Coverage Range (g/kg)	Slope (77K)	Slope (88K)	ΔH (kJ/mol)	$E_{b,mobile}$ (kJ/mol)	$E_{b,localized.}$ (kJ/mol)	$\lvert\Delta H - E_{b,loc}\rvert / \Delta H$ (%)
4K-0245	0 – 0.4	467.7	119.8	7.618	7.280	7.622	0.05
4K-0747	0 – 0.02	421.6	119.1	7.070	6.730	7.072	0.03
4K-0748	0 – 0.03	524.4	118.4	8.322	7.933	8.275	0.56
4K-0750	0 – 0.02	511.7	118.2	8.195	7.757	8.098	1.18
5K-0215	0 – 0.02	638.5	114.6	9.607	9.297	9.638	0.32
HKUST-1	0 – 0.5	199.3	59.5	6.757	6.405	6.746	0.16
HS;0B-20	0 – 0.1	4451	773.4	9.787	9.446	9.787	0.00

9.2 ΔH at Low Coverage from Henry's Law and Clausius-Clapeyron

Starting from the Langmuir isotherm model:

$$\frac{m_{film}(p,T)}{m_s} = \frac{m\Sigma}{\alpha(T)}\theta(\mathrm{p,T}) = \frac{m\Sigma}{\alpha(T)}\frac{\chi(\mathrm{T})\mathrm{p}}{1+\chi(\mathrm{T})\mathrm{p}} \tag{9.1}$$

where χ (T) is the Langmuir constant (differs for local and mobile adsorption), θ (p,T) is H_2 surface coverage ($0 \le \theta \le 1$), and α (T) is the footprint per H_2 molecule (6.4 Å^2 at 77K, from J. Burress et al, Nanotechnology **20**, 204026 (2009)). In the low pressure regime, this simplifies to a linear form:

$$\frac{m_{film}(p,T)}{m_s} = \frac{m\Sigma}{\alpha(T)}\chi(\mathrm{T})\mathrm{p} \tag{9.2a}$$

$$= k_H(T) * p \tag{9.2b}$$

where k_H(T) is the experimentally determined slope of the Henry's Law regime. Therefore, at constant coverage, the isotherms are related by

$$\left(\frac{m_{film}(p,T)}{m_s}\right)^* = k_H(T_1)p_1 = k_H(T_2)p_2 \tag{9.3}$$

allowing the ratio of the pressures in 1.11b to be replaced by the ratio of the slopes, k_H:

$$\Delta H = R\frac{T_1T_2}{T_2-T_1}\ln\left(\frac{k_H(T_1)}{k_H(T_2)}\right) \tag{9.4}$$

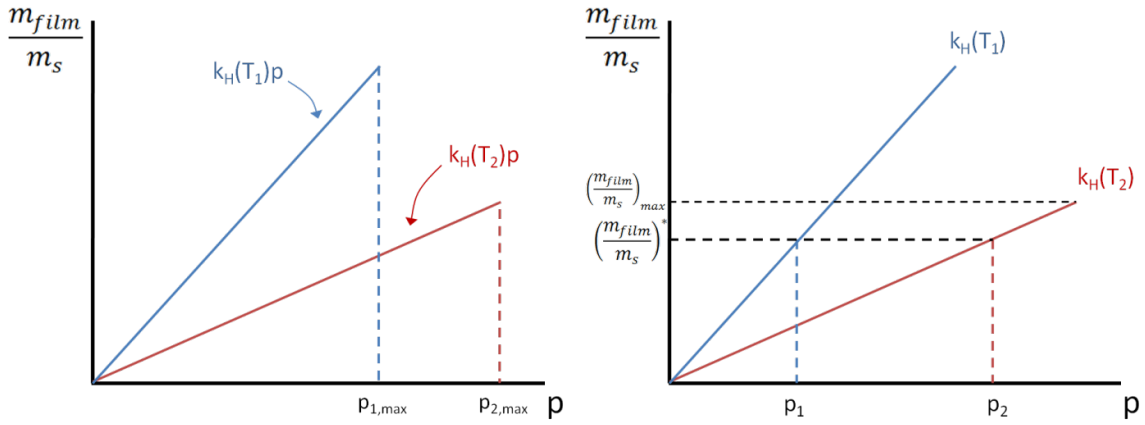

Figure 9.2. Clausius-Clapeyron applied to Henry's law. The slopes give the isosteric heat from Eq. (9.4). The range of coverages over which (9.4) is valid is given by $0 \le (m_{film}/m_s) \le (m_{film}/m_s)_{max}$.

Figure 9.3. Henry's Law (*pink*), where adsorption is proportional to the gas pressure, is valid only at low pressure. At higher pressure, the uptake is no longer linear and may be described by a Langmuir model with one binding energy (purple), or more than one binding energy (green).

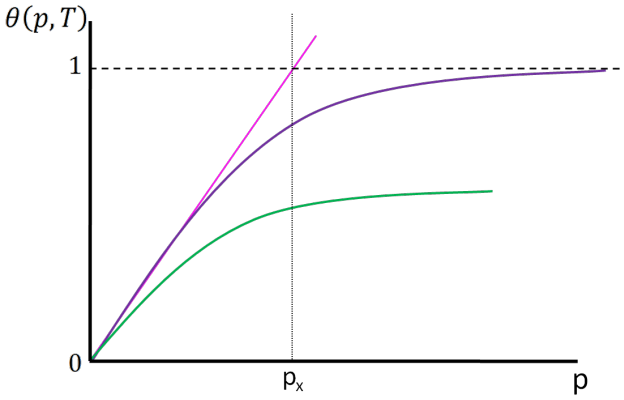

9.3 ΔH and Eb at Low Coverage from Henry's Law and Langmuir Model

The binding energies for mobile and localized adsorption via the Langmuir model, and using the slopes $k_H(T)$ of the linear isotherms described in the previous section, are given by:

$$e^{\frac{E_{b,mobile}}{R}\left(\frac{T_2-T_1}{T_1T_2}\right)} = \frac{k_H(T_1)}{k_H(T_2)}\sqrt{\frac{T_1}{T_2}} \tag{9.5a}$$

$$E_{b,mobile} = R\left(\frac{T_1T_2}{T_2-T_1}\right)\ln\left(\frac{k_H(T_1)}{k_H(T_2)}\sqrt{\frac{T_1}{T_2}}\right) \tag{9.5b}$$

$$e^{\frac{E_{b,localized}}{R}\left(\frac{T_2-T_1}{T_1T_2}\right)} = \frac{k_H(T_1)}{k_H(T_2)}\sqrt{\frac{T_2}{T_1}} \tag{9.6a}$$

$$E_{b,localized} = R\left(\frac{T_1T_2}{T_2-T_1}\right)\ln\left(\frac{k_H(T_1)}{k_H(T_2)}\sqrt{\frac{T_2}{T_1}}\right) \tag{9.6b}$$

$$= E_{b,mobile} + R\left(\frac{T_1T_2}{T_2-T_1}\right)\ln\left(\frac{T_2}{T_1}\right) \tag{9.6c}$$

$$= E_{b,mobile} + 0.3416\ kJ/mol \quad (T_1 = 77K,\ T_2 = 87K) \tag{9.6d}$$

Table 9.1 reports the values for ΔH from Clausius-Clapeyron at "zero coverage: (eq. 9.4) and E_b's from Langmuir and mobile/localized adsorption (eq. 9.5b & 9.6d). To compare ΔH with E_b, one needs to relate the enthalpy difference ΔH to the difference internal energy between the unadsorbed hydrogen gas and the adsorbed state at 77 K:

$$\Delta H_{mob.} = H_{gas} - H_{ads,mob.} = \left(\frac{3}{2}RT + RT\right) - \left(-E_b + \frac{2}{2}RT + RT\right) = E_b + \frac{1}{2}RT \quad (9.7)$$

$$\Delta H_{loc.} = H_{gas} - H_{ads,loc} = \left(\frac{3}{2}RT + RT\right) - (-E_b + 3RT) = E_b - \frac{1}{2}RT \quad (9.8)$$

Using a temperature T = (77 K + 87 K)/2 yields a modification of $\frac{1}{2}RT$ = 0.3409 kJ/mol to the binding energy E_b in determination of the isosteric heat ΔH. Table 9.2 reports all zero coverage values for E_b from Langmuir and mobile adsorption ("E_b at $\theta \approx$ 0wt%"), ΔH from mobile binding energy as in eq. 9.7 ("ΔH from E_b"), and ΔH from the Clausius-Clapeyron relation as in eq 1.11b ("ΔH from C-C") determined from Henry's Law low-pressure isotherms at 77 K and 87 K. ΔH values determined from the binding energy and Clausius-Clapeyron agree to within 1%. This demonstrates the appropriateness of the Langmuir model with mobile adsorption, advertised in Table 1.1, in a most remarkable way. The last column in Table 9.2 ("E_b at $\theta \approx$ 1wt%") reports the enthalpies of adsorption at non-zero coverage, obtained from the method of isosteres detailed in the Report for Quarter 21, which are a measure of the average binding energy, $E_{b,av}$, on the samples. XPS deconvolution confirms the statement, in Table 1.2, that a majority of boron atoms are present in the form of B-B bonds (column 6 in Table 9.2).

Table 9.2. Boron contents determined from prompt-gamma neutron activation analysis (PGAA, U. Missouri Research Reactor) and X-ray photoelectric spectroscopy (XPS, Missouri U. Science & Technology), as well as deconvolution of the B peak to quantitatively define the chemical environment, and binding energies and isosteric heats determined using a variety of methods. Specifically, isosteric heat values calculated from the binding energy and Clausius-Clapeyron agree exceptionally well.

Sample	B (wt%) PGAA	B (wt%) XPS	B_{B-C} (wt%) XPS	B_{B-C} /B (%)	B_{B-B} /B (%)	B_{B-O} /B (%)	O (wt%) XPS	E_b (kJ/mol) θ ≈ 0wt%	ΔH (kJ/mol) From E_b	ΔH (kJ/mol) From C-C	ΔH (kJ/mol) θ ≈ 1wt%
2.5K-0754	4.4	-	-	-	-	-	-	8.1	8.45	8.50	6.0
2.5K-0755	5.6	-	-	-	-	-	-	9.2	9.59	9.58	5.8
3K-0079	0	-	-	-	-	-	-	7.08	7.43	7.43	5.5
3K-0205	9.7	7.5	0.9	12.5	59.9	27.7	9.0	7.42	7.76	7.77	5.5
3K-0208	13.7	14.6	1.7	11.7	76.9	11.4	9.7	-	-	-	5.4
3K-0211	6.2	7.6	0.6	8.5	52.5	39.0	10.9	-	-	-	5.6
4K-0239	0	-	-	-	-	-	-	6.71	7.06	7.07	5.4
4K-0240	1.5	1.2	0.0	0.0	0.0	100.0	6.2	6.90	7.24	7.32	5.5
4K-0244	1.65	1.7	0.0	0.0	0.0	100.0	7.8	7.25	7.59	7.61	5.4
4K-0245	3.9	4.1	0.7	17.6	39.5	42.9	10.0	7.28	7.62	7.62	5.2
4K-0748	5.65	5.2	1.0	18.6	55.4	26.0	7.9	7.93	8.27	8.27	5.4
4K-0750	6.86	-	-	-	-	-	-	7.85	8.18	8.19	5.5
4K-0752	9.09	-	-	-	-	-	-	6.90	7.24	7.24	5.5
5K-0215	8.1	8.4	1.7	20.7	55.3	24.1	8.7	9.30	9.63	9.64	6.2

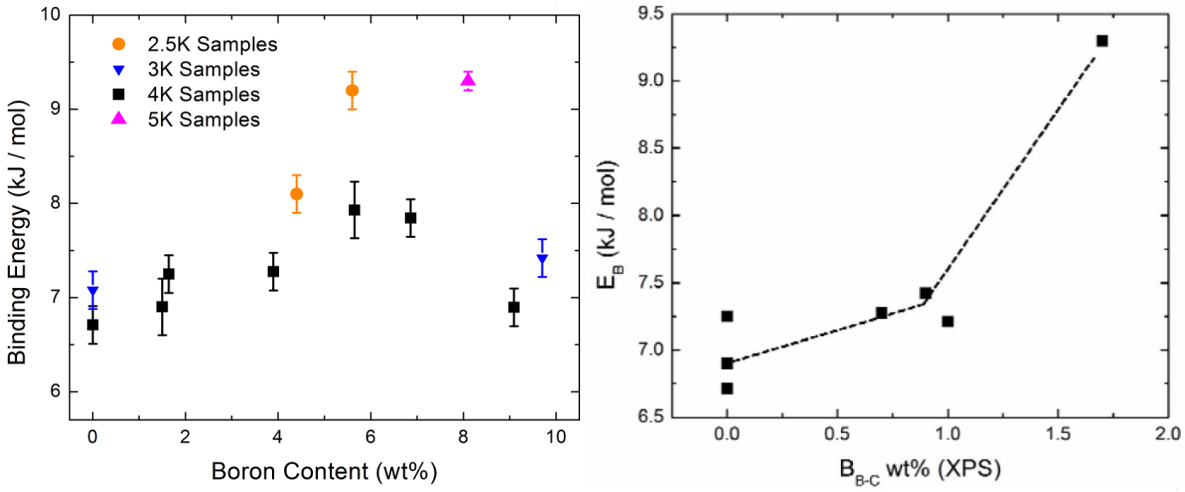

Figure 9.4. (*left*) An updated version of the data underlying Eq. (9.5b), reported in the Report for Quarter 21, Figure 8. It represents all E_b values at zero coverage determined to date. (*right*)The data underlying Eq. (9.5b), first reported in the 2014 Annual Progress Report.

9.4 Fraction of High-E_b Sites from Henry's Law

The wider the range of pressures over which Henry's law is observed, the larger is the fraction of sites with high binding energy E_b (Fig. 9.2). This observation can be used to estimate the fraction of high binding energy sites as follows. One sample, 2.5K-0754 has been analyzed as an example.

Figure 9.5. A maximum film capacity of approximately 49.9g/kg was determined by fitting the linear regime of the 77 K isotherm. The slope of the linear regime corresponds to the maximum film volume. The point at which the linear fit intercepts the abscissa corresponds to the saturated film density. The point at which the linear fit intercepts the ordinate axis corresponds to the maximum capacity of the adsorbed film.

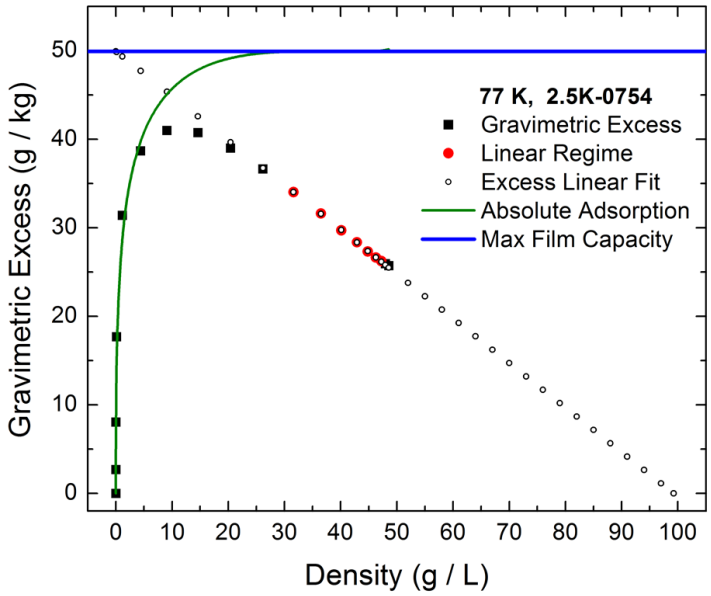

Surface coverage is defined as the number of adsorbed molecules per adsorption site available, which is equivalent to the fraction of the maximum film capacity reached at a given pressure:

$$\theta = \frac{G_{abs} N_A \alpha}{m_{H_2} \Sigma} = \frac{G_{abs}}{m_{film}(max)} \quad (9.9)$$

For any pressure, one calculate the absolute adsorption from the gravimetric excess and divide by the maximum film capacity to obtain the fraction of available adsorption sites occupied at that pressure. Looking at Henry Law regime of 77 K and 87 K isotherms for sample 2.5K-0754:

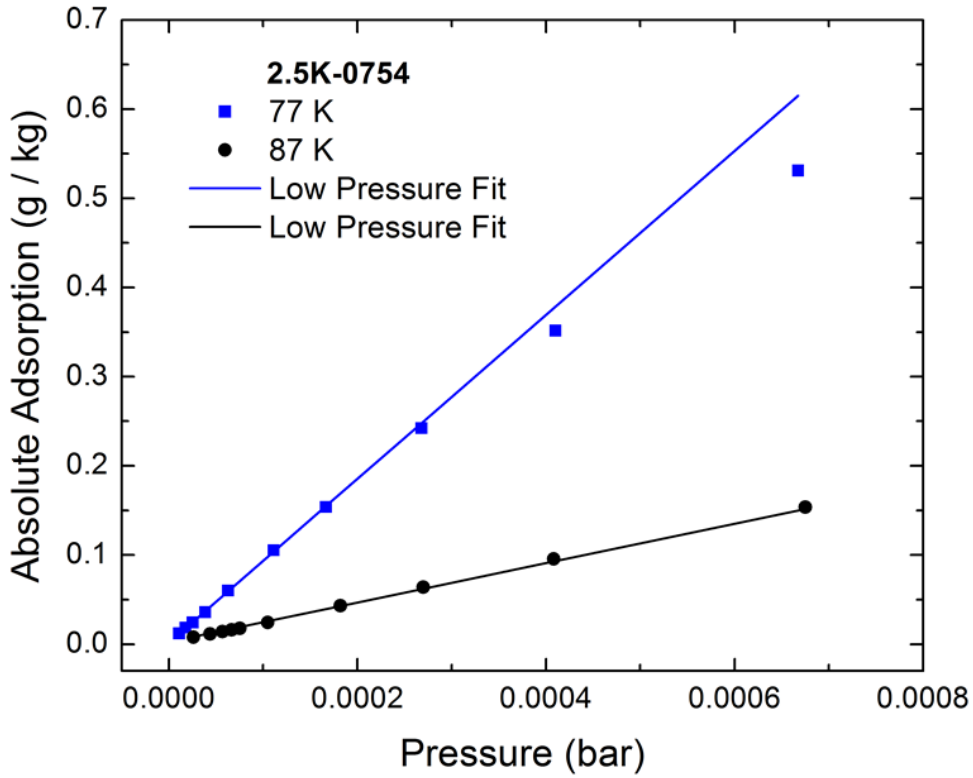

Figure 9.6.Henry's Law analysis using the Langmuir model on these two isotherms yielded a binding energy of 8.1 kJ/mol.

The 77 K isotherm is reasonably linear up to a pressure of $2.7 \cdot 10^{-4}$ bar, corresponding to an adsorption of approximately 0.248g/kg. We assume that this is a sufficiently low pressure such that absolute adsorption is equal to gravimetric excess adsorption. Using this value of absolute adsorption in eq.9.9 yields a surface coverage of $\theta = 0.0049$, which is 0.49% of all available adsorption sites.

9.5 ΔH at High Coverage on Phase-2 B_xC Materials

Note executed

9.6 ΔH at High Coverage on Synthetic Carbons

Not executed

10. Adsorbent Engineering V: Graphitic Carbon Nitride, C_3N_4 (Phase 2)

10.1 Theoretical Modeling of Hydrogen Adsorption on C_3N_4

Activated carbons as a competitive hydrogen storage medium are largely dependent on their large surface areas (>2000 m^2/g), a value which theoretically has a maximum (Σ = 2630 m^2/g for defect-free graphene). Further improvements to storage must subsequently come from surface functionalization and/or refinement of pore space engineering.

Graphitic carbon nitride (g- C_3N_4) is an attractive candidate for H2 adsorption because it has a layered structure like graphene, but also regular patterns of voids which upon exfoliation host high edge-to surface ratios and correspondingly higher surface areas, estimated as high as 4000-6000 m^2/g. Alternating N and C atoms lead to negative and positive partial charges on N and C atoms, respectively, expected to result in strong dipole interactions with adsorbed H2 molecules.

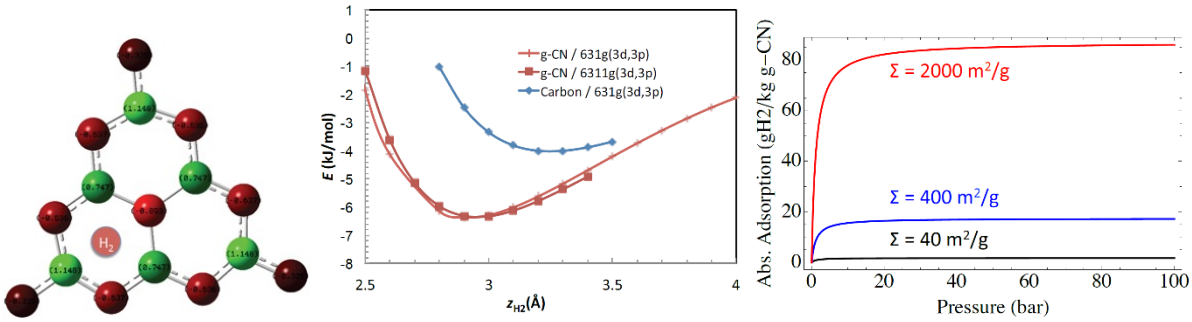

Figure 10.1.Model calculations for the electronic structure of g-C_3N_4 (*center*); resulting adsorption potential for H_2 (*center*); and resulting H_2 adsorption at 77 K (absolute adsorption, Langmuir model with localized adsorption (J. Romanos et al., Carbon **54**, 208 (2013))) for several hypothetical surface areas (*right*).*Left*: Mulliken charges in MP2/631g(3d,3p) basis; carbon loses ~1 electron, and nitrogen gains ~1 electron; Large resulting electric fields significantly polarize nearby H_2 molecule. *Center*: Comparison of H_2-substrate potential for g-C_3N_4 and carbon (coronene). In g-C_3N_4, the potential depth (~7 kJ/mol) exceeds that of carbon (~4 kJ/mol), resulting in binding energies of ~14 kJ/mol in narrow pores of g-C_3N_4. In addition, the location of the minimum moves closer to the substrate. This may favor additional H_2 storage enhancement as it reduces the "dead volume" around the substrate. Right: Hypothetical extrapolations based on these binding energies predict immense improvements in H_2 absolute adsorption for larger surface areas.

10.2 Synthesis of C_3N_4

Many synthetic routes to g-C_3N_4have been described. Of interest are routes involving polymerization of inexpensive bulk industrial precursors, such as cyanamide, dicyandiamide, or melamine. [E. Kroke and M. Schwarz, Coord. Chem. Rev. 248, 493 (2004)] Routes to laboratory-scale synthesis include both solvothermal reactions in high boiling organic solvents and solid-state metathesis reactions. In the present work, g-C_3N_4 is formed via the pyrolysis of melamine ($C_3H_6N_6$), a heterocyclic trimer of cyanamide (HN=C=NH) known to readily form assorted

crystalline structures. While nanoscale g-C_3N_4 materials have been described in literature, (J. Li et al., Nanotechnology 18, 115605 (2007)) adsorbent and crystallographic properties of these materials have been only cursorily studied. (D. Portehault et al., Adv. Funct. Mat. 20, 1827 (2010)).

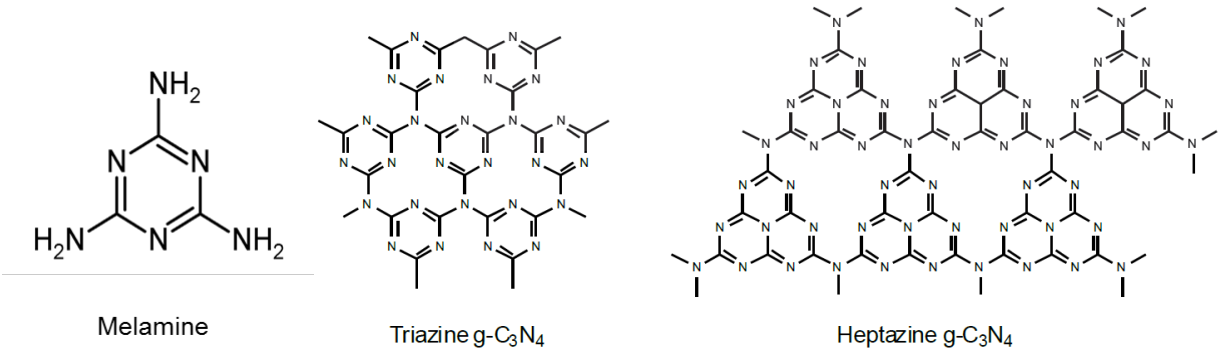

Figure 10.2.*Left*: Precursor compound of MU created g-C_3N_4. *Center*, *right*: Two possible structures formed upon pyrolysis of melamine include graphene-like sheets comprised of basis units s-triazine (C_3N_3, *center*) and heptazine (C_6N_7, *right*) joined by nitrogen linkers.

10.3 Physical and Chemical Characterization of C_3N_4

It is desired to confirm the formation of a graphite-like network from the aromatic precursor molecule, as well as to confirm a homogeneous distribution of carbon and nitrogen throughout. g-C_3N_4isn't especially sensitive to oxygen environments, and may thus be suspended in solution and centrifuged to obtain electron transparent particles within the supernatant suitable for characterization via TEM. EFTEM can be used to map the elemental distribution in real space, while EELS and XPS may be used for quantification.

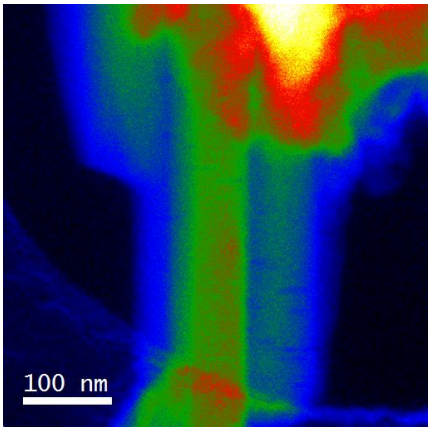

Figure 10.3. A thickness map from EFTEM confirming a selected region was suitable for EELS and EFTEM. All regions colored green and blue were lower than one mean free path, while the bright regions at the top are of greater thickness and excluded.

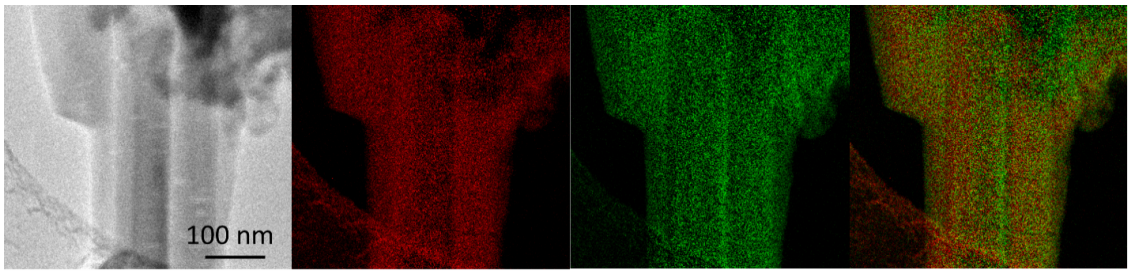

Figure 10.4. (*left to right*) Unfiltered EFTEM spectra (similar to bright-field mode) of a well-oriented particle, and carbon, nitrogen, and composite maps of the assigned mixed colors in RGB. The system is confirmed to be quite uniform as expected, resulting in the relatively homogeneous mix of the two maps. The object in the lower left of the carbon map is the edge of the carbon grid that the sample is suspended over.

Figure 10.5. EEL spectra from the particle pictured in Figure 10.4 with clear defined k-edges for both nitrogen and carbon. The resolution (~1 eV) of the spectrometer (U. Missouri) is not suitable to deconvolute the peak for finer chemical structure.

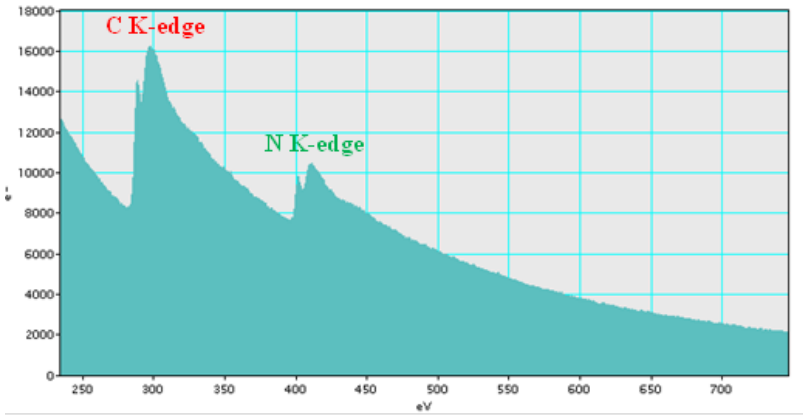

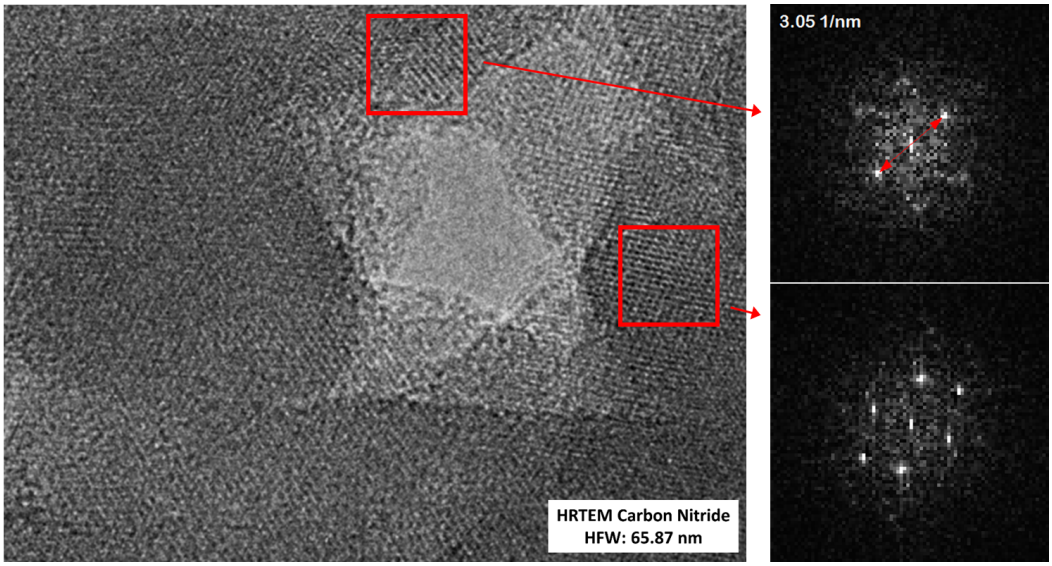

Figure 10.6. HRTEM confirming high crystallinity of MU produced graphitic carbon nitride. The distance between repeating units may be measured directly, or as is more useful for sections of overlapping groups (*bottom right*), through real-time FFT calculation. The distance observed here (3.28 Å) represents the space between layers and is consistent with the literature ($d_{g\text{-}CN}$ = 3.26 Å).

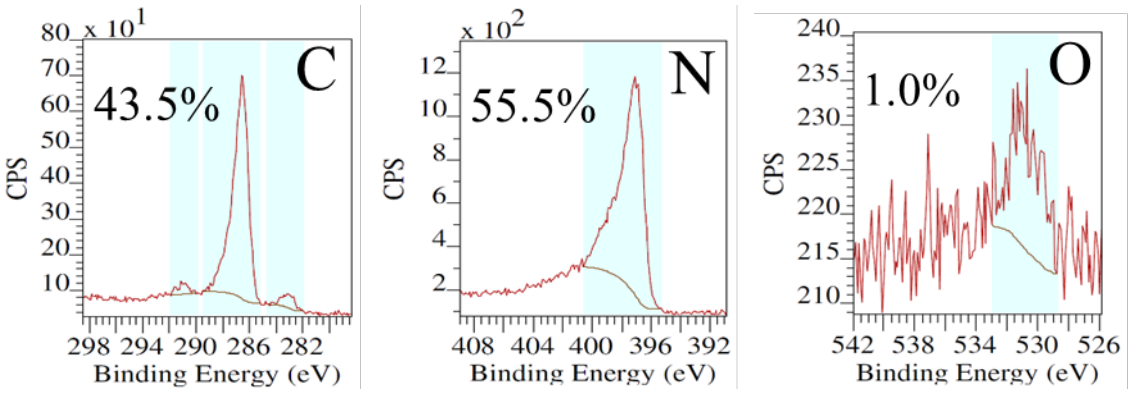

Figure 10.7. XPS quantification of MU-created graphitic carbon nitride yields an atomic ratio of $C_{3.14}N_4$, in good agreement with the ideal C_3N_4 structure. A small amount of oxygen is detected and attributed to surface contaminants absorbed during the scan.

To resolve in-plane features, supplemental techniques are required. The XRD spectrum of MU-created g-CN is dominated by a large peak at 27.3° (d = 3.26Å) and contains several smaller features at $2\theta < 25°$, similar to what is seen for graphite. The large peak corresponds to the interplanar spacing of the sheets and agrees well with the measurements from HRTEM, while those at smaller angles refer to the larger, in-plane features. These features are resolved well assuming a combination of two distinct structures (fig 10.6): s-triazine g-C_3N_4 (80%) and a polymeric chain of heptazine units (20%), commonly referred to as a melon.

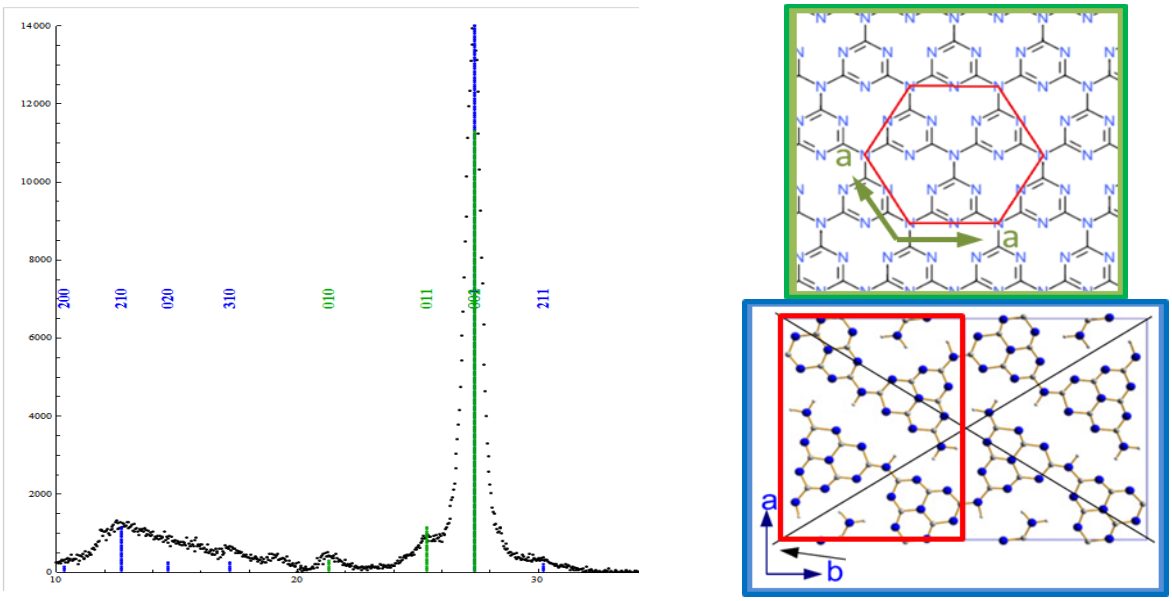

Figure 10.8. *Left*: XRD spectrum of MU-created g-C_3N_4, fitted to a combination of two structures. *Top right*: s-triazine based g-CN. *Bottom right*: heptazine based polymeric carbon nitride chains, figure and peak assignments from (Tyborski et al., *Journal of Physics: Condensed Matter*, **25**(2013), 395-402). Both models agree to an inter-planar distance of 3.26Å. Tyborski et al. explain that the broadening of the low-angle peaks is due to a temperature-induced shearing of the plane, driving the chains apart; this ultimately results in a split of previously superpositioned, symmetric reflections.

10.4 Hydrogen Adsorption on C_3N_4

Due to its extremely low surface area (Σ_{BET} = 13 m^2/g), MU-created g-C_3N_4 (GCN-1001) features an exceptionally low gravimetric excess of $G_{ex,max}$(77K) = 0.03 wt% in accordance with Chahine's rule. However, the calculated surface excess features a maximum similar to that of a typical activated carbon. In an effort to increase storage, GCN-1001 was exfoliated via bath sonication to improve the surface area. This sample (GCN-1003) was measured to have almost 3x the surface area but 5x the maximum gravimetric excess, giving a surface excess of almost double the activated carbon. This suggests the exfoliated g-C_3N_4 sample hosts binding energies significantly higher than 5 kJ/mol.

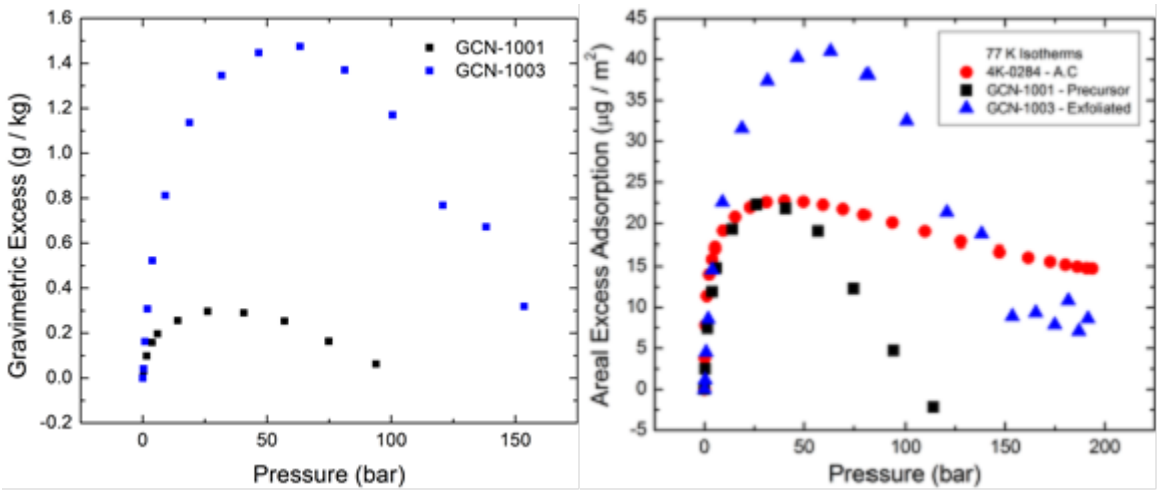

Figure 10.9.*Left*: Gravimetric excess adsorption isotherms for MU-created g-C_3N_4 at 77K and 297K. The poor performance (<0.03 wt%) is attributed to the sample's small surface area. *Right*: Surface excess of unexfoliated g-C_3N_4 is comparable to that of a typical activated carbon, and is greatly improved upon exfoliation.

Table 10.1.N_2 (BET surface areas, porosities, and pore volumes) and H_2 gravimetric excess of MU-created g-C_3N_4 before and after exfoliation.

Sample	Σ_{BET}	ϕ	V_{pore}	$G_{ex,max}$(77K)	$G_{ex,max}$(77K)/Σ_{BET}
GCN-1001	13 m^2/g	0.21	0.15 cm^3/g	0.3 g/kg	22 $\mu g/m^2$
GCN-1003	36 m^2/g	0.40	0.48 cm^3/g	1.5 g/kg	41 $\mu g/m^2$

Appendix A — Validation of H_2 Sorption Isotherms

A.1 Introduction: Statement of the Problem

Gravimetric Excess Adsorption

Adsorption is the process by which an adsorbate gas increases in density when in the vicinity of a material interface due to Van der Walls interactions. Strong Van der Walls forces are capable of condensing H_2 into a high density fluid at pressures and temperatures at which H_2, in the absence of an adsorbing surface, would be a low density gas. Among several variables, this effect is largely due to the extent of the interfacial area, which is generated by increasing the network of channels in the pore volume of the adsorbent material. Though adsorption instruments vary greatly in type and technique, they all measure the same quantity: excess adsorption. Excess adsorption is defined as follows.

> "*Consider two systems of equal volume. The first system is that of free gas at a temperature T_0, pressure p_0, and contains N_0 gas molecules. The second system contains an external potential $U(\vec{r})$ due to an adsorbing surface outside of the system and the gas has a temperature T, pressure p far from the adsorbing surface, and contains N gas molecules. If both systems have the same temperature and pressure (i.e. $T = T_0$ and $p = p_0$), then the excess adsorption is given by $N\text{-}N_0$*"
>
> T. Hill, An Introduction to Statistical Thermodynamics, 1960

For high surface area adsorbent materials, excess adsorption is one of the only directly measureable quantities without theoretical assumptions. Excess adsorption may be thought as the mass of the adsorbed film minus the mass of an equal volume of compressed gas.

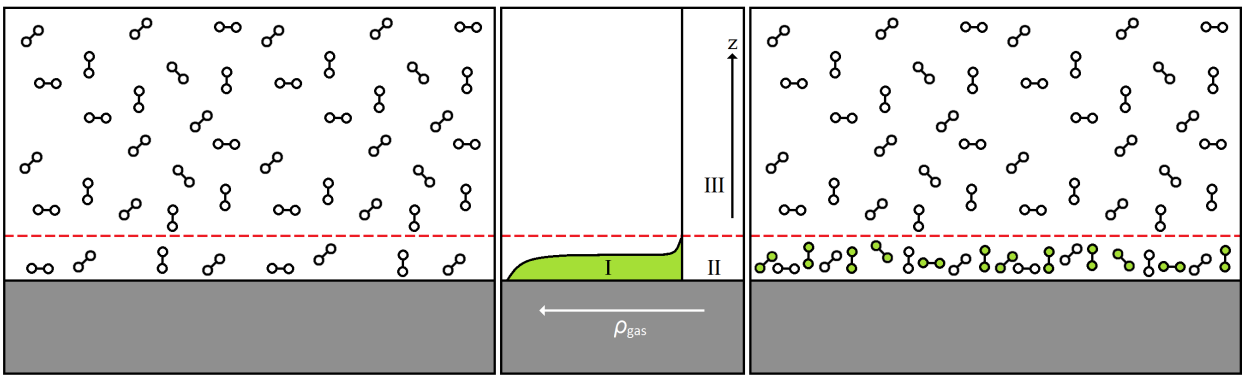

Figure A.1: *Left*: Volume of compressed gas at a constant density in the absence of an adsorbing potential. *Right:* Compressed gas in the presence of an adsorbing potential. The gas densifies near the adsorbing surface. Colored molecules have been adsorbed in excess of those that would be present in the absence of an adsorbing potential. Thus, they are defined as the excess adsorption. *Middle:* Graphical representation of gas density vs. distance from the adsorbent surface. The three regions indicated show excess adsorption (I), absolute adsorption (I + II), and total storage capacity (I + II + III).

As previously stated, excess adsorption is the only quantity that may be directly measured without theoretical assumptions. Storage capacities and absolute adsorption are derived from the excess adsorption measurement using assumptions about the pore volume, adsorbed film thickness, or surface geometry. Therefore, the only way to improve the accuracy of absolute adsorption or storage capacity is to improve the accuracy of excess adsorption measurements. In our laboratory, we employ both gravimetric methods and the volumetric method in determining gravimetric excess adsorption.

The simplest method of measuring excess adsorption may be performed using only a pressure cell and a mass balance. This method requires no knowledge of the sample volume. Derivation of excess adsorption from these quantities is quite simple, coming from simple force addition. However, gravimetric methods pose difficulties when measuring hydrogen sorption due to its relatively low uptake on reversible storage materials. For this reason, researchers tend toward manometry to determine excess adsorption of hydrogen.

Hydrogen gravimetric excess adsorption isotherms were measured using a modified HTP-1 Volumetric Analyser manufactured by Hiden Isochema. The HTP-1 is a manometric instrument capable of measuring hydrogen isotherms at pressures ranging from 0.001 mbar to 1 bar using a set of two low-pressure Baratron capacitance manometers and from 1 bar to 200 bar using a 200 bar Baratron manometer. The system consisted of a dosing volume and a reactor volume , which contained the sample, separated by a pneumatic valve whose diaphragm displaced a volume when closed. The dosing and pneumatic valve volumes were contained within a temperature controlled cabinet that was maintained at 30.0 ± 0.1 °C. The reactor volume was partially contained in this cabinet and the remainder was exposed to the lab environment. The sample temperature was controlled using cooling baths of ice water, liquid argon, or liquid nitrogen. This allowed for measurement of isotherms at 77 K, 87 K, 273 K, and 296 K. The cabinet or dosing volume temperature was measured using two platinum resistance thermometers (PRTs) surrounding the dosing volume.

Volumetric methods for determining excess adsorption have been used for almost 90 years. Most modern volumetric sorption instruments employ the Sieverts' method, monitoring changes in pressure and temperature in order to measure excess. Basic manometric instruments consist of two known volumes, referred to here as the dosing volume V_d, and the reactor volume V_r, separated by a valve. Let V_s, represent the skeletal volume of the sample.

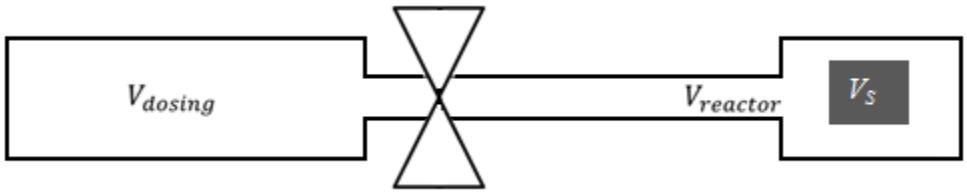

Figure A.2: Manometric instrument consisting of two known volumes, separated by a valve.

After V_d, V_r, and V_s are known (calibration), manometric instruments use mass balance to perform sorption measurements. Beginning with an evacuated system, the dosing volume is pressurized with the adsorbate gas. The temperature and pressure are measured and the mass

density ρ_1 is calculated using an appropriate equation of state. The mass of adsorbate gas contained in the system is now given by

$$m_{\mathrm{g}} = \rho_1 V_{\mathrm{d}} \tag{A.1}$$

After an adequate equilibration time, the valve separating the dosing volume and reactor volume is opened allowing the adsorbate gas to enter V_{r}. Again, equilibrium is reached and the gas density ρ_2 is calculated based on pressure and temperature measurements. In the presence of a non-adsorbing sample, the mass of the adsorbate gas may now be expressed as

$$m_{\mathrm{g}} = \rho_2(V_{\mathrm{d}} + V_{\mathrm{r}} - V_{\mathrm{s}}) \tag{A.2}$$

In the presence of an adsorbing sample, the mass of adsorbate gas in the system may be expressed as

$$m_{\mathrm{g}} = \rho_2(V_{\mathrm{d}} + V_{\mathrm{r}} - V_{\mathrm{s}}) + \mathrm{V}_{\mathrm{film}}(\rho_{\mathrm{film}} - \rho_2) \tag{A.3}$$

where V_{film} is the volume occupied by the adsorbed film of adsorbate gas, ρ_{film} is the density of gas in the adsorbed phase. The last term in this expression is the definition of excess adsorption. Thus, the mass of adsorbate gas contained in the system may be expressed as

$$m_{\mathrm{g}} = \rho_2(V_{\mathrm{d}} + V_{\mathrm{r}} - V_{\mathrm{s}}) + \mathrm{m}_{\mathrm{exc}} \tag{A.4}$$

Equating equations A.1 and A.4 yields

$$m_{\mathrm{exc}} = V_{\mathrm{d}}(\rho_1 - \rho_2) - \rho_2(V_{\mathrm{r}} - V_{\mathrm{s}}) \tag{A.5}$$

If two or more data points are to be measured, the valve is closed and a third density ρ_3 is determined. This third measurement is used to determine the amount of adsorbate gas that remains in each volume at the end of the measurement and is used to avoid double counting gas molecules. This dosing process is repeated for as many data points are desired. However, it is important to note that any uncertainties will compound with increasing successive measurements. The excess adsorption is calculated for any number of data points by determining the total amount of gas added to the system and subtracting from it the amount of gas that would be present in the system if there were no adsorption. The general expression for excess calculated for the k^{th} data point will be given by

$$m_{\mathrm{exc}} = \sum_{i=1}^{k}\left[\rho_{1i}V_{\mathrm{d}} - \rho_{2i}(V_{\mathrm{d}} + V_{\mathrm{r}} - V_{\mathrm{s}}) + \rho_{2(i-1)}(V_{\mathrm{d}} + V_{\mathrm{r}} - V_{\mathrm{s}}) - \rho_{3(i-1)}V_{\mathrm{d}}\right] \tag{A.6}$$

where the first digit in the subscripts represents the step in the measurement and the second digit represents the measurement iteration. Gravimetric excess adsorption is obtained by normalizing the above expression by the sample mass.

One consequence of this expression is that every successive measurement in an isotherm is dependent upon all previous data points. Though this does result in an accumulation of uncertainties, the uncertainties do not simply add from data point to data point because all of the

terms with rho2i cancel from the previous data point. Additionally, since these are the only terms accounting for sample temperature, thermal fluctuations in the sample do not propagate errors to later data points in the isotherm. To emphasize this point, I present a slightly more compact version of Eq. A.6.

$$m_{\text{exc}} = \sum_{i=1}^{k}\left[\rho_{1i} - \rho_{3(i-1)}\right] V_d - \rho_{2k}(V_{\text{d}} + V_{\text{r}} - V_{\text{s}}) \tag{A.7}$$

When the dosing volume is maintained at a different temperature than the sample, a volume fraction must be used in order to estimate the thermal gradient. Consider the case of using a liquid nitrogen cooling bath:

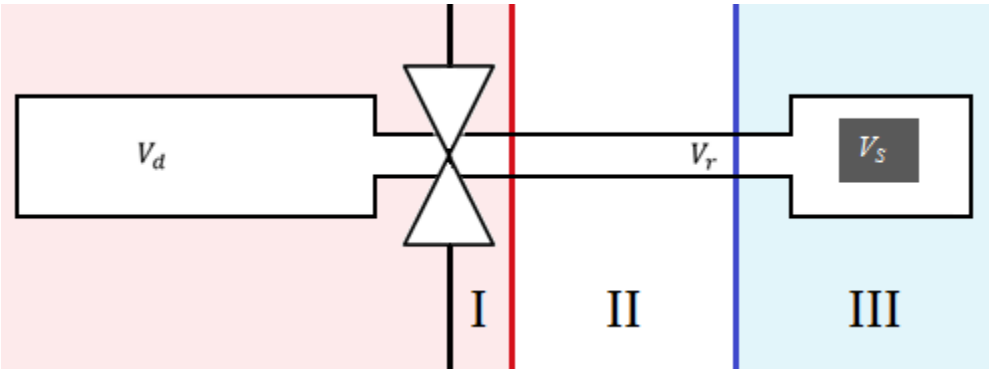

Figure A.3: Manometric instrument consisting of two known volumes, separated by a valve. The reactor volume is partially contained within a temperature controlled manifold, partially exposed to the laboratory environment, and partially submerged in the liquid nitrogen cooling bath.

$$V_{\text{r}} = \text{I} + \text{II} + \text{III} \tag{A.8}$$

The reactor volume is the comprised of the sum of regions I, II, and III. Let f_0 represent the fraction of the reactor volume not contained in the manifold ($0 \leq f_0 \leq 1$). Let $f_{77\,\text{K}}$ represent the fraction of the remaining reactor volume submerged in the cooling bath ($0 \leq f_{77\,\text{K}} \leq 1$).

$$\text{I} = V_{\text{r}}(1 - f_0) \tag{A.8a}$$
$$\text{II} = V_{\text{r}} f_0 (1 - f_{77\,\text{K}}) \tag{A.8b}$$
$$\text{III} = V_{\text{r}} f_0 f_{77\,\text{K}} \tag{A.8c}$$

Accounting for volume fractions in the excess equation requires the consideration of additional new gas densities. After substituting the new densities, the excess equation for the k^{th} data point becomes

$$m_{\text{exc}} = \left[\sum_{i=1}^{k} \rho_{1i} - \rho_{3(i-1)}\right] V_{\text{d}} - \left[\rho_{2k}\left(V_{\text{d}} + V_{\text{r}}(1 - f_0)\right) + \rho'_{2k} V_{\text{r}} f_0 (1 - f_{77\,\text{K}}) + \rho''_{2k}(V_{\text{r}} f_0 f_{77\,\text{K}} - V_{\text{s}})\right] \tag{9}$$

where ρ_{2k} is still the mass density of the adsorbate gas after opening the valve, $\rho_{2k}^{'}$ is the mass density of gas that is contained within region II and at the same temperature as the laboratory environment, and $\rho_{2k}^{''}$ is the mass density of gas that is contained within region III and maintained at the same temperature as the cooling bath. For the purpose of exhaustive validation of this equation, it is important to note two cases: 1) when the region III is maintained at the same temperature as region II such that $\rho_{2k}^{'}=\rho_{2k}^{''}$ and 2) when all three regions are maintained at the same temperature such that $\rho_{2k}=\rho_{2k}^{'}=\rho_{2k}^{''}$. Considering the first case, $\rho_{2k}^{'}=\rho_{2k}^{''}$, which necessitates that $f_{77\,\mathrm{K}} = 0$ such that there is no fraction of the reactor volume maintained at the same temperature as the cooling bath. The excess equation becomes

$$m_{\mathrm{exc}} = \left[\sum_{i=1}^{k} \rho_{1i} - \rho_{3(i-1)}\right] V_{\mathrm{d}} - \left[\rho_{2k}\left(V_{\mathrm{d}} + V_{\mathrm{r}}(1-f_0)\right) + \rho_{2k}^{'}(V_{\mathrm{r}}f_0 - V_{\mathrm{s}})\right] \tag{A.10}$$

Considering the second case, $\rho_{2k}=\rho_{2k}^{'}$, which necessitates that $f_0 = 1$ such that the entire reactor volume is maintained at the same temperature as the dosing volume. The excess equation becomes

$$m_{\mathrm{exc}} = \left[\sum_{i=1}^{k} \rho_{1i} - \rho_{3(i-1)}\right] V_{\mathrm{d}} - [\rho_{2k}(V_{\mathrm{d}} + V_{\mathrm{r}} - V_{\mathrm{s}})] \tag{A.11}$$

which is equivalent to Eq. (A.7).

Volume Determinations & Quality of Measurements

The formulation of the above excess equations was based on the assumption that all volumes were known. I will now outline the process used to calibrate the dosing volume, reactor volume, and fractional volumes. Assuming that neither the dosing nor reactor volumes are known, three sets of measurements are required:

1. 15 individual data points with no sample
2. 15 individual data points with a non-adsorbing sample of known volume (silicon beads; $\rho_{\mathrm{Si}} = 2.3290\ \mathrm{g/cm^3}$)
3. A blank isotherm at room temperature

For the fifteen individual data points with no sample, we may again use conservation of particle number to construct the equation

$$\rho_{i1}V_{\mathrm{d}} = \rho_{f1}\left(V_{\mathrm{d}} + V_{\mathrm{r}}(1-f_0)\right) + \rho_{f1}^{'}V_{\mathrm{r}}f_0 \tag{A.12}$$

where the additional subscript "1" has been added to indicate measurements taken with no sample. For the five individual data points with non-adsorbing sample of known volume, conservation of particle number gives

$$\rho_{i2}V_{\mathrm{d}} = \rho_{f2}\left(V_{\mathrm{d}} + V_{\mathrm{r}}(1-f_0)\right) + \rho_{f2}^{'}\left(V_{\mathrm{r}}f_0 - V_{\mathrm{disp}}\right) \tag{A.13}$$

where V_{disp} is the volume of the displacer. Solving the system of Eqs. (2) and (3) gives the dosing and reactor volumes

$$V_{\text{r}} = \frac{\rho'_{f2}(\rho_{f1}-\rho_{i1})V_{\text{disp}}}{\rho_{f1}\rho_{i2}-\rho_{f2}\rho_{i1}+f_0\left(\rho_{f1}\rho'_{f2}+\rho_{f2}\rho_{i1}-\rho_{f2}\rho_{i1}-\rho_{f1}\rho_{i2}+\rho'_{f1}(\rho_{i2}-\rho_{f2})\right)} \tag{A.14}$$

$$V_{\text{d}} = \frac{\rho'_{f2}(\rho_{f1}(f_0-1)-f_0\rho'_{f1})V_{\text{disp}}}{\rho_{f1}\rho_{i2}-\rho_{f2}\rho_{i1}+f_0\left(\rho_{f1}\rho'_{f2}+\rho_{f2}\rho_{i1}-\rho_{f2}\rho_{i1}-\rho_{f1}\rho_{i2}+\rho'_{f1}(\rho_{i2}-\rho_{f2})\right)} \tag{A.15}$$

We start with $f_0 = 1$, and we decrease f_0 until the room temperature blank isotherm is minimized.

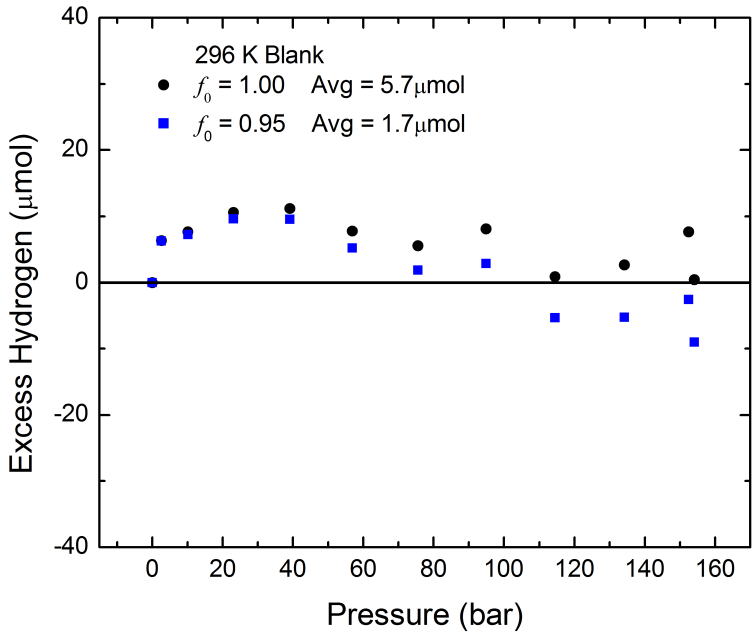

Figure A.4. Blank isotherm at 296 K with $f = 1$ and $f = 0.95$. The fractional volume is decreased until the average departure from zero in the blank isotherm is minimized.

This volume fraction corresponds to 95% of the rector volume maintained at the same temperature as the laboratory environment and only 5% maintained at the same temperature as the dosing volume. This set of calibration measurements yielded a dosing volume of $V_{\text{d}} \cong 5.08 \pm 0.02$ mL and a reactor volume of $V_{\text{r}} \cong 6.32 \pm 0.02$ mL. This blank has a maximum departure from zero excess of approximately 12 μmol, which is well below the tolerance of 40 μmol, proposed by the manufacturer.

The above calibrations allow one to take isothermal measurements at the same temperature as the laboratory environment. In order to measure isotherms at alternate temperatures, additional volume fractions must be determined. The following procedure is used to determine the volume fraction for a setup using an isothermal bath. Cooling baths of liquid nitrogen or liquid argon evaporate as a function of time and, therefore, the thermal gradient also changes as a function of time. In order to determine the fractional volume one must use the following procedure:

1. Measure the kinetics for a single data point for more than 100 min
2. Use this data to calculate the volume fraction

In general, the excess adsorption for the k^{th} data point in a non-room temperature measure is given by Eq. (A.9). For an empty sample cell ($m_{\text{exc}} = 0$) the first data point ($k = 1$) may be expressed as

$$m_{\text{exc}} = \rho_{11} V_{\text{d}} - \left[\rho_{21}\left(V_{\text{d}} + V_{\text{r}}(1 - f_0)\right) + \rho_{21}^{'} V_{\text{r}} f_0 (1 - f) + \rho_{21}^{''} V_{\text{r}} f_0 f\right] \tag{A.16}$$

For an empty sample cell $m_{\text{exc}} = 0$ and Eq. (16) can be solved for f.

$$f(t) = \frac{\rho_{21}^{'} f_0 V_{\text{r}} - \rho_{11} V_{\text{d}} + \rho_{21}(V_{\text{d}} + V_{\text{r}} - f_0 V_{\text{r}})}{\left(\rho_{21}^{'} - \rho_{21}^{''}\right) f_0 V_{\text{r}}} \tag{A.17}$$

where the all mass densities are a function of time. It may not be immediately apparent why the mass densities are time dependent. The temperatures of the manifold, cooling bath, and laboratory environment are maintained and constant in time, but the pressure will vary due to the evaporation of the liquid cooling bath, which changes the fraction of submerged reactor volume.

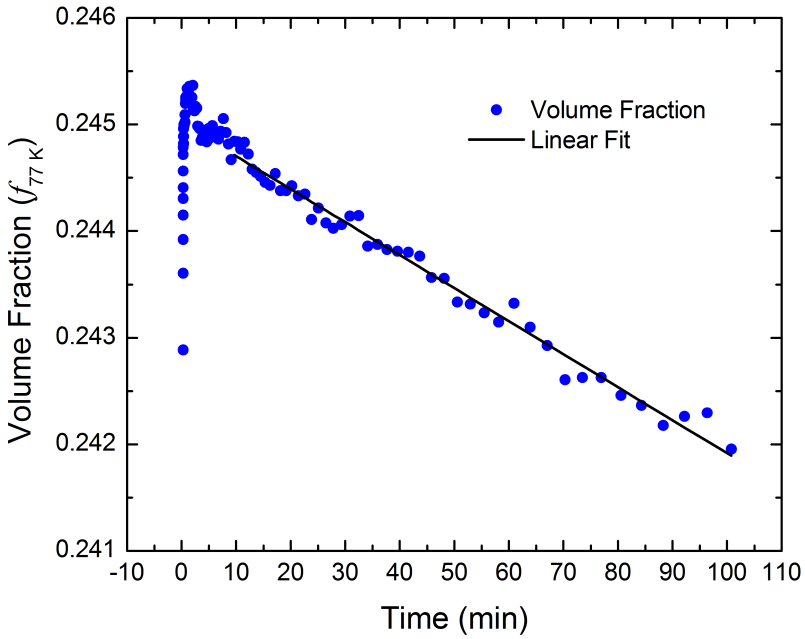

Figure A.5. Volume fraction describing the approximate percent of the reactor volume maintained at the same temperature as the cooling bath.

The initial rise is due to the adsorbate gas equilibrating as it expands from the dosing volume and temperature into the reactor volume. Applying a linear fit to applicable fractional volume data yields the following relationship for *f*(t)

$$f_{77\,K}(t) \cong -3.1 * 10^{-5} t + 0.245013 \tag{A.18}$$

where time is in minutes. By knowing the equilibration time allotted to each data point, one can

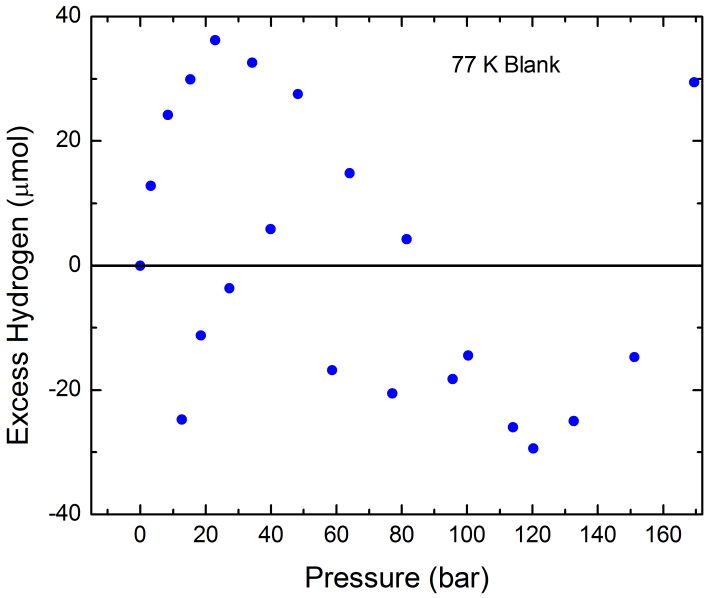

Figure A.6. Blank isotherm measured at 77 K using the experimental fractional volume from Eq(17) with the excess equation from Eq(9).

use the corresponding fractional volume in Eq. (A.9) to calculate excess adsorption. After all volumes and volume fractions have been determined, a blank isotherm should be measured to verify the quality of the calibration. The maximum departure from zero excess hydrogen is much larger at 77 K compared to the departure at 296 K. However, it is still well within the suggested tolerance of 40 μmol proposed by the manufacturer. It may serve as a figure of merit to display the difference between a gravimetric excess isotherm and the corresponding blank-subtracted isotherm for an arbitrary sample.

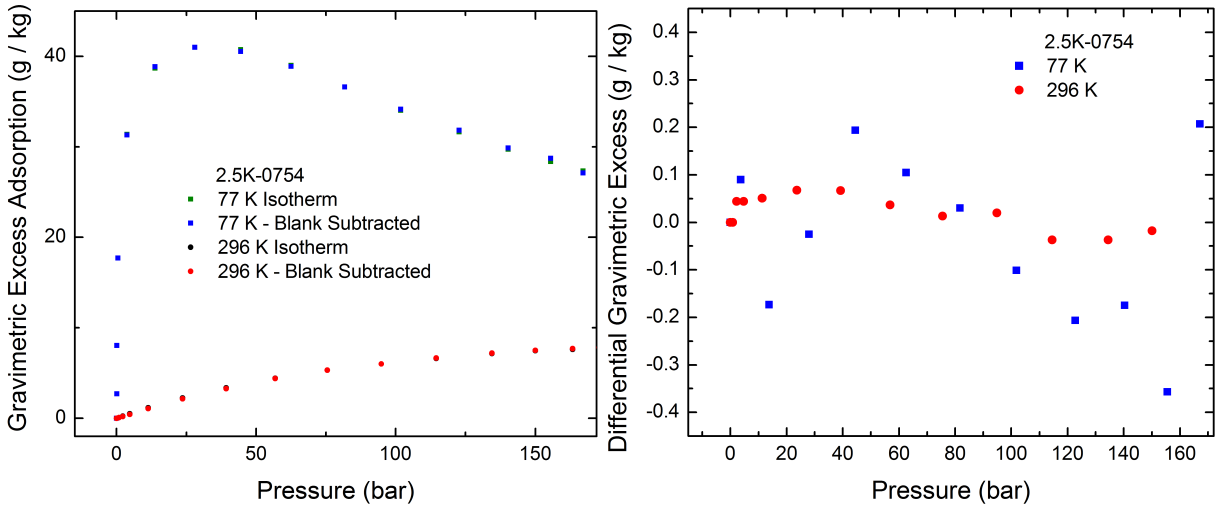

Figure A.7. The difference between isothermal gravimetric excess isotherms and blank-subtracted gravimetric excess isotherm for sample 2.5K-0754. *Left*: Isotherms and corresponding blank subtracted isotherms at 296K and 77 K. *Right*: Differential gravimetric adsorption between isotherms and their corresponding blank subtracted isotherms at 296 K and 77 K.

The gravimetric excess isotherm and corresponding blank-subtracted isotherms overlap one another. As long as the sample is adsorbs a large amount relative to the blank, subtracting the blank isotherm has little effect on the measured gravimetric excess. This holds true for all MU activated carbons.

A.2 H_2 sorption isotherms with and without determination of headspace volume

Pycnometry and Determining Sample Volume

The last volume that remains unexplained from Eq. (A.9) is the sample volume, V_s. This may be determined by taking headspace measurements or by prior knowledge of the skeletal density. It is common practice to measure headspace by through helium pycnometry. However, these measurements are highly sensitive to uncertainties in dosing and reactor volumes. For this reason, helium pycnometry should be performed in a well-calibrated, voluminous reactor and on a large amount of the adsorbent sample.

We will now outline the process used to determine headspace and thus sample volume. Once the system is fully calibrated such that V_d, V_r, and f_0 are known, one can begin measuring the sample volume using a non-adsorbent gas, such as helium. Only one set of measurements is required: 15 individual data points using a non-adsorbing gas with a sample of unknown volume.

We may again use conservation of particle number to construct the equation for sample volume

$$\rho_{1i}V_{\mathrm{d}} = \rho_{2k}\left(V_{\mathrm{d}} + V_{\mathrm{r}}(1-f_0)\right) + \rho_{2k}^{'}(V_{\mathrm{r}}f_0 - V_s) \tag{A.19}$$

Solving Eq (A.19) assuming zero excess yields

$$V_s = V_{\mathrm{r}}f_0 + \frac{1}{\rho_{2k}^{'}}\left[\rho_{2k}\left(V_{\mathrm{d}} + V_{\mathrm{r}}(1-f_0)\right) - \rho_{1i}V_{\mathrm{d}}\right] \tag{A.20}$$

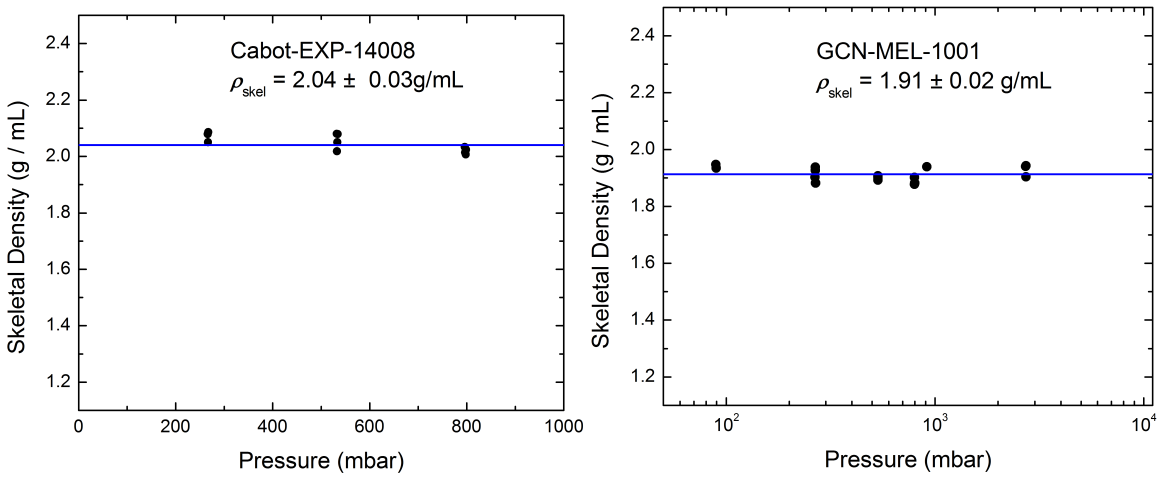

Figure A.8. Skeletal density measurements for sample Cabot-EXP-14008 and GCN-MEL-1001 by applying Eq. (A.20) in conjunction with the definition of skeletal density ($\rho_{\mathrm{skel}} = m_{\mathrm{s}}/V_{\mathrm{s}}$).

This analysis was performed on 0.363 g of sample Cabot-EXP-14008 and 0.550 g of sample GCN-MEL-1001 in a dosing volume $V_d = 51.75 \pm 0.02$mL and a reactor volume $V_r = 6.32 \pm$ mL. The exhaustive nature of accurate helium pycnometry measurements, the typically small sample size of experimental adsorbent material, and the high throughput of adsorption measurements make it impractical to determine skeletal densities for all samples. For these reasons, we find it reasonable to determine the skeletal density of representative materials and apply it to all carbonaceous materials being screened. The majority of materials screened at MU are carbonaceous materials with skeletal densities of $\rho_{skel} = 2.04 \pm 0.04$mL. Occasionally, alternate materials were screened, such as graphitic carbon nitride and various metal organic frameworks.

Other considerations

It has been suggested that helium may adsorb on the surface of select samples. Though we do not observe this phenomenon, one must take precautions to ensure that helium sorption is not occurring. The simplest method to check this is to perform an isothermal measurement at several pressures.

Consider a system *S* composed of *N* molecules in a volume *V* at pressure *p* and temperature *T* that includes the adsorbing solid. In the low pressure limit, the system obeys Henry's Law

$$N_{exc} = k_H p \tag{A.21}$$

where N_{exc} is the number of molecules contributing to excess adsorption. Now consider a subsystem of *S*, *S'*, composed of *N'* molecules in a volume *V'* at pressure *p* and temperature *T* in which gas molecules are allowed to freely move in and out of the subsystem. Inherently, $N > N'$ and $V > V'$. From the point of view of *S'*, adsorption is equivalent to a change in the number of gas molecules.

Let us take the largest possible volume of *S'* in which *V'* occupies the entire portion of *V* that is at constant gas density. Consider that there is no adsorption potential and at some time, the adsorption potential is simply switched on. In *S'*, the number of molecules decreases and the pressure decreases. A gas molecule in *S'* would infer that the total system volume *V* must be increasing and that the change in volume is directly proportional to the number of gas molecules that have left *S'* (assuming ideal gas applies to low pressures). If Henry's Law is valid, then the apparent change in system volume must also be a linear function of pressure such that

$$V_{observed} - V_0 = k_H p \tag{A.22}$$

where k_H is a constant with units of volume per pressure and V_0 is the observed volume of the system at zero pressure. Applying headspace measurements as outlined above would correspond to a direct measurement of $V_{observed}$.

By measuring adsorption isotherms at sufficiently low pressures and high temperatures, it should be possible to graph V_0 as a function of pressure. If Henry's Law is valid for experimental data, then the observed sample volume will be a linear with respect to pressure and may be extrapolated to zero pressure. The observed volume of the system at zero pressure will be equivalent to the true value of the sample volume, V_s.

Additional Figures of Merit – NREL Validation

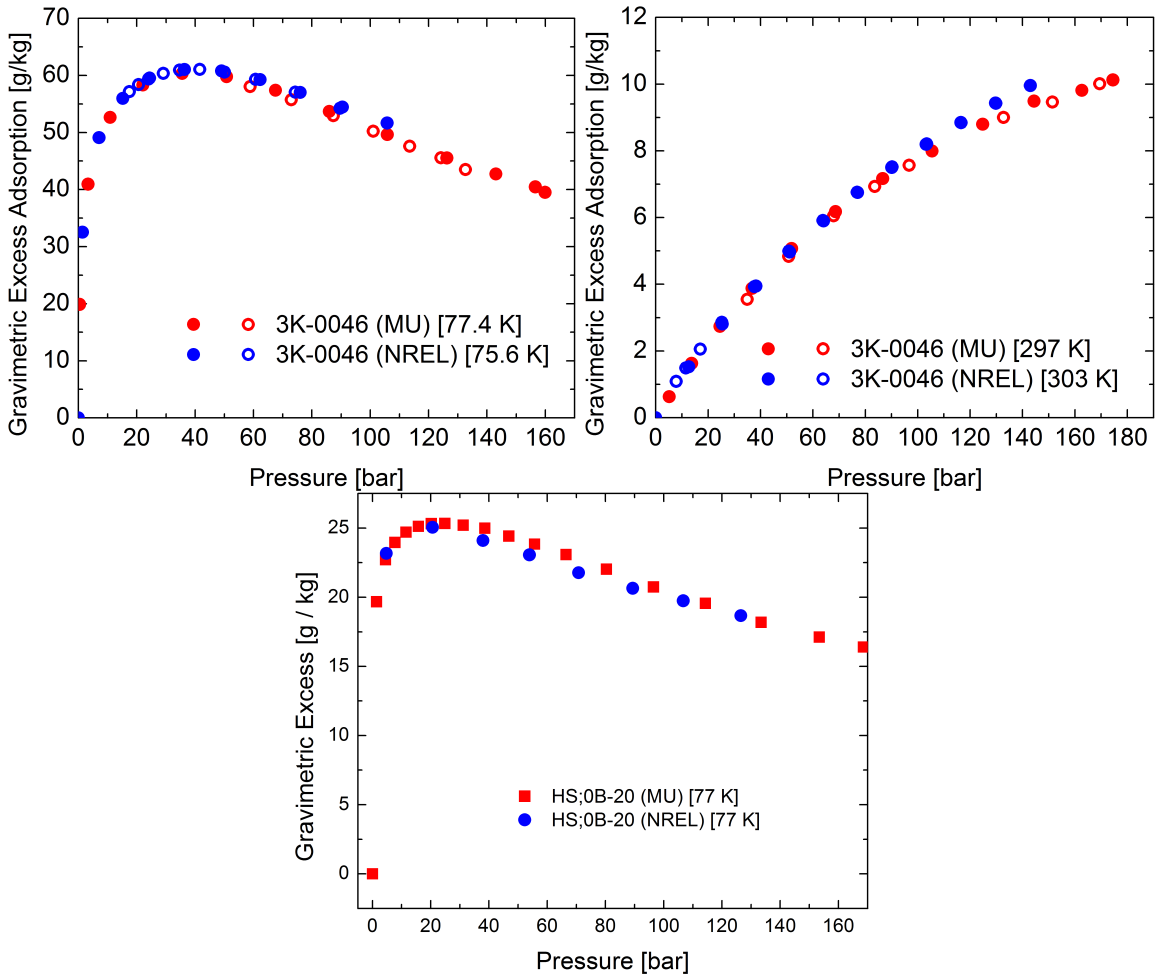

Figure A.9. Comparison of gravimetric excess measurements performed by MU and NREL *Top*: on sample 3K-0046 at 303 K and 77 K. *Bottom*: on sample HS;0B-20 at 77 K.

Isothermal adsorption measurements performed at NREL and MU agree with one another within the uncertainty of the equipment.

Appendix B — List of Publication

1. J. Romanos, M. Beckner, M. Kraus, J. Burress, P. Pfeifer. "Magnetic Properties of High-Surface-Area Carbons and Their Effect on Adsorbed Hydrogen." Bull. Am. Phys. Soc. 54, W27.00009 (2009)
2. M. Beckner, J. Burress, C. Wexler, Z. Yang, F. Hawthorne, P. Pfeifer. "Boron-Doped Carbon Nanospaces for High-Capacity Hydrogen Storage." Bull. Am. Phys. Soc. 54, W27.00010 (2009)
3. M. Kraus, J. Burress, M. Beckner, C. Wexler, P. Pfeifer. "Hierarchical Pore Structure of Engineered Carbon Nanospaces for Use in Hydrogen Storage." Bull. Am. Phys. Soc. 54, W27.00011 (2009)
4. J. Burress, M Beckner, N. Kullman, R. Cepel, C. Wexler, P. Pfeifer. "Analysis of Hydrogen Adsorption in Engineered Carbon Nanospaces." Bull. Am. Phys. Soc. 54, W27.00012 (2009)
5. R. Cepel, B. Kuchta, L. Firlej, P. Pfeifer, C. Wexler. "Quantum energy levels of hydrogen adsorbed on nanoporous carbons: an intrinsic probe for pore structure, and improving Monte Carlo simulations of adsorption." Bull. Am. Phys. Soc. 54, W27.00013 (2009)
6. B. Kuchta, L. Firlej, R. Cepel, P. Pfeifer, C. Wexler. "Structural and energetic factors in designing a perfect nano-porous sorbent for hydrogen storage." Bull. Am. Phys. Soc. 54, W27.00014 (2009)
7. L. Firlej, B. Kuchta, C. Wexler, and P. Pfeifer, "Boron-Substituted Graphene: Energy Landscape for Hydrogen Adsorption." Adsorption **15**, 312-317 (2009).
8. J. Burress, M. Kraus, M. Beckner, R. Cepel, G. Suppes, C. Wexler, and P. Pfeifer, "Hydrogen Storage in Engineered Carbon Nanospaces." Nanotechnology **20**, 204026 (2009). [Invited paper; Special Issue on Nanoscale Phenomena in Hydrogen Storage; selected as "Article of Particular Interest."]
9. B. Kuchta, L. Firlej, P. Pfeifer, and C. Wexler, "Numerical Estimation of Hydrogen Storage Limits in Carbon-Based Nanospaces." Carbon **48**, 223-231 (2009).
10. P. Pfeifer, C. Wexler, G. Suppes, F. Hawthorne, S. Jalisatgi, M. Lee, D. Robertson, P. Buckley, and J. Clement, "Multiply Surface-Functionalized Nanoporous Carbon for Vehicular Hydrogen Storage." In: *Proceedings of the 2009 DOE Hydrogen Program Annual Merit Review and Peer Evaluation, May 18-22, 2009, Arlington, VA, Hydrogen Storage—Hydrogen Storage Sorption Center of Excellence*. http://www.hydrogen.energy.gov/annual_review09_storage.html#scehttp://www.hydrogen.energy.gov/pdfs/review09/st_31_pfeifer.pdf
11. P. Pfeifer, C. Wexler, G. Suppes, F. Hawthorne, S. Jalisatgi, M. Lee, and D. Robertson, "Multiply Surface-Functionalized Nanoporous Carbon for Vehicular Hydrogen Storage." In: *DOE Hydrogen Program, 2009 Annual Progress Report*, ed. S. Satyapal (U.S. Department of Energy, Washington, DC, 2009; DOE/GO-102009-2950), p. 646-651. http://www.hydrogen.energy.gov/annual_progress09.html http://www.hydrogen.energy.gov/pdfs/progress09/iv_c_1p_pfeifer.pdf
12. B. Kuchta, L. Firlej, S. Roszak, P. Pfeifer, and C. Wexler, "Influence of Structural Heterogeneity of Nanoporous Sorbent Walls on Hydrogen Storage." Appl. Surf. Sci. **256**, 5270-5274 (2010). doi:10.1016/j.apsusc.2009.12.116
13. E. Leimkuehler, A. Tekeei, M. Gordon, J. Burress, B. Sawyer, J. Romanos, P. Pfeifer, and G. J. Suppes, "Highly Nanoporous Activated Carbon Process Characterization." Ind. Eng.

Chem. Res., submitted (2009)
14. C. Wexler, M. Beckner, J. Romanos, J. Burress, M. Kraus, R. Olsen, E. Dohnke, S. Carter, G. Casteel, B. Kuchta, L. Firlej, E. Leimkuehler, A Tekeei, G. Suppes. "Record Hydrogen Storage Capacities in Advanced Carbon Storage Materials." Bull. Am. Phys. Soc. 55, T30.00007 (2010)
15. J. Romanos, D. Robertson, M. Beckner, M. Kraus, B. Kuchta, L. Firlej, P. Pfeifer. "Ultrananopores in Carbons by Boron-neutron Capture and Their Effect on Hydrogen Storage." Bull. Am. Phys. Soc. 55, T30.00008 (2010)
16. L. Firlej, B. Kuchta, S. Roszak, P. Pfeifer, C. Wexler. "Adsorption of hydrogen in boron-substituted nanoporous carbons." Bull. Am. Phys. Soc. 55, T30.00009 (2010)
17. M. Beckner, R. Olsen, J. Romanos, J. Burress, E. Dohnke, S. Carter, G. Casteel, C. Wexler, P. Pfeifer. "Isosteric heats of adsorption for activated carbons made from corn cob." Bull. Am. Phys. Soc. 55, T30.00010 (2010)
18. R. Olsen, L. Firlej, B. Kuchta, P. Pfeifer, H. Taub, C. Wexler. "Quantization of Adsorbed Hydrogen for Inhomogeneous Materials Characterization using Inelastic Neutron Scattering." Bull. Am. Phys. Soc. 55, T11.00011 (2010)
19. M. Kraus, M. Beckner, D. Stalla, C. Wexler, P. Pfeifer, J. Ilavsky. "Nanopore structure from USAXS/SAXS in advanced carbon materials for hydrogen storage." Bull. Am. Phys. Soc. 55, T30.00012 (2010)
20. P. Pfeifer, M. Kraus. "Fractal Structure in Hydrogen and Methane Storage Materials." Bull. Am. Phys. Soc. 55, T30.00013 (2010)
21. B. Kuchta, L. Firlej, R. Cepel, P. Pfeifer, and C. Wexler, "Structural and Energetic Fac-tors in Designing a Nanoporous Sorbent for Hydrogen Storage." Colloids Surf. A **357**, 61-66 (2010). doi:10.1016/j.colsurfa.2010.01.020
22. C. Wexler, R. Olsen, P. Pfeifer, B. Kuchta, L. Firlej, and S. Roszak, "Numerical Analysis of Hydrogen Storage in Carbon Nanopores." Int. J. Mod. Phys. B **24**, 5152-5162 (2010)
23. B. Kuchta, L. Firlej, Sz. Roszak, P. Pfeifer, "A Review of Boron Enhanced Nanoporous Carbons for Hydrogen Adsorption: Numerical Perspective." Adsorption **16**, 413-421 (2010). doi:10.1007/s10450-010-9235-0
24. P. Pfeifer, C. Wexler, G. Suppes, F. Hawthorne, S. Jalisatgi, M. Lee, D. Robertson, P. Buckley, and J. Clement, "Multiply Surface-Functionalized Nanoporous Carbon for Vehicular Hydrogen Storage." In: *Proceedings of the 2010 DOE Hydrogen Program Annual Merit Review and Peer Evaluation, June 7-11, 2010, Washington, DC, Hydrogen Storage—Hydrogen Storage Sorption Center of Excellence*.
http://www.hydrogen.energy.gov/annual_review10_storage.html#sce
http://www.hydrogen.energy.gov/pdfs/review10/st019_pfeifer_2010_o_web.pdf
25. P. Pfeifer, C. Wexler, G. Suppes, F. Hawthorne, S. Jalisatgi, M. Lee, and D. Robertson, "Multiply Surface-Functionalized Nanoporous Carbon for Vehicular Hydrogen Storage." In: *DOE Hydrogen Program, 2010 Annual Progress Report*, ed. S. Satyapal (U.S. Department of Energy, Washington, DC, 2011; DOE/GO-102011-3178), p. 474-480.
http://www.hydrogen.energy.gov/annual_progress10.html
http://www.hydrogen.energy.gov/pdfs/progress10/iv_c_1c_pfeifer.pdf
26. C. Wexler, M. Beckner, J. Romanos, T. Rash, P. Pfeifer, R. Olsen. "Anomalous Characteristics of a PVDC Carbon Adsorbant." Bull. Am. Phys. Soc. 56, H20.00009 (2011)
27. E. Dohnke, M. Beckner, J. Romanos, R Olsen, C. Wexler, P. Pfeifer. "Evaluation of the isosteric heat of adsorption at zero coverage for hydrogen on activated carbons." Bull. Am. Phys. Soc. 56, H20.00010 (2011)
28. R. Olsen, M. Beckner, H. Taub, P. Pfeifer, C. Wexler. "Inelastic Neutron Scattering from

Hydrogen Adsorbed in Carbon." Bull. Am. Phys. Soc. 56, H20.00011 (2011)
29. M. Beckner, J. Romanos, D. Stalla, E. Dohnke, A Singh, M. Lee, G. Suppes, M.F. Hawthorne, P. Yu, C. Wexler, P. Pfeifer. "Analysis of hydrogen sorption characteristics of boron-doped activated carbons." Bull. Am. Phys. Soc. 56, H20.00012 (2011)
30. T. Rash, M. Beckner, J. Romanos, E. Leimkuehler, A. Takeei, G. Suppes, C. Wexler, P. Pfeifer. "The effect of KOH:C and activation temperature on hydrogen storage capacities of activated carbons." Bull. Am. Phys. Soc. 56, H20.00013 (2011)
31. Y. Soo, M. Beckner, J. Romanos, C. Wexler, P. Pfeifer, P Buckley, J. Clement. "A high volume, high throughput volumetric sorption analyzer." Bull. Am. Phys. Soc. 56, V20.00003 (2011)
32. R.J. Olsen, L. Firlej, B. Kuchta, H. Taub, P. Pfeifer, and C. Wexler, "Sub-nanometer characterization of activated carbon by inelastic neutron scattering." Carbon **49**, 1663-1671 (2011). doi:10.1016/j.carbon.2010.12.051
33. P. Pfeifer, C. Wexler, G. Suppes, F. Hawthorne, S. Jalisatgi, M. Lee, D. Robertson, P. Buckley, and J. Clement, "Multiply Surface-Functionalized Nanoporous Carbon for Vehicular Hydrogen Storage." In: *Proceedings of the 2011 DOE Hydrogen and Fuel Cells Program Annual Merit Review and Peer Evaluation, May 9-13, 2011, Washington, DC, Hydrogen Storage—Hydrogen Storage, Sorption Independent*.
http://www.hydrogen.energy.gov/annual_review11_storage.html
http://www.hydrogen.energy.gov/pdfs/review11/st019_pfeifer_2011_o.pdf
34. P. Pfeifer, C. Wexler, P. Yu, G. Suppes, F. Hawthorne, S. Jalisatgi, M. Lee, and D. Robertson, "Multiply Surface-Functionalized Nanoporous Carbon for Vehicular Hydrogen Storage." In: *DOE Hydrogen and Fuel Cells Program, 2011 Annual Progress Report*, ed. S. Satyapal (U.S. Department of Energy, Washington, DC, 2011; DOE/GO-102011-3422), p. 444-449.
http://www.hydrogen.energy.gov/annual_progress11.html
http://www.hydrogen.energy.gov/pdfs/progress11/iv_c_3_pfeifer_2011.pdf
35. J. Romanos, M. Beckner, T. Rash, L. Firlej, B. Kuchta, P. Yu, G. Suppes, C. Wexler, and P. Pfeifer, "Nanospace Engineering of KOH Activated Carbon." Nanotechnology **23**, 015401 (2012).
36. J. Romanos and P. Pfeifer, "Nano-engineered carbons promise better gas storage mater-ials for advanced transportation." *Nanotechweb.org*, January 11, 2012.
http://nanotechweb.org/cws/article/lab/48268
37. C. Wexler, M. Connolly, M. Beckner, P. Pfeifer. "Boron Doping Carbon Structures Using Decaborane? A Theoretical Study." Bull. Am. Phys. Soc. 57, W33.00001 (2012)
38. T. Rash, D. Stalla, M. Beckner, J. Romanos, G. Suppes, A. Tekeei, P. Buckley, P. Doynov, P. Pfeifer. "Industrial Scale Measurements of Hydrogen Uptake and Delivery in KOH Activated Carbons." Bull. Am. Phys. Soc. 57, W33.00004 (2012)
39. J. Romanos, M. Beckner, T. Rash, P. Yu, G. Suppes, P. Pfeifer. "Reversible Storage of Hydrogen and Natural Gas in Nanospace-Engineered Activated Carbons." Bull. Am. Phys. Soc. 57, W33.00005 (2012)
40. R. Olsen, H. Taub, C. Wexler. "The Stationary States of Adsorbed Hydrogen." Bull. Am. Phys. Soc. 57, W33.00006 (2012)
41. M. Beckner, J. Romanos, E. Dohnke, A. Singh, J. Schaeperkoetter, D. Stalla, J. Burress, S. Jalisatgi, G. Suppes, M.F. Hawthorne, P. Yu, C. Wexler, P. Pfeifer. "Measured Enthalpies of Adsorption of Boron-Doped Activated Carbons." Bull. Am. Phys. Soc. 57, W33.00007 (2012)
42. E. Dohnke, J. Romanos, M. Beckner, J. Burress, P. Yu, P. Pfeifer. "Performance of Carbon Hydrogen Storage Materials as a Function of Post-Production Thermal Treatment." Bull.

Am. Phys. Soc. 57, W33.00008 (2012)
43. M. Connolly, C. Wexler. "Adsorption-induced Pore Expansion and Contraction in Activated Carbon." Bull. Am. Phys. Soc. 57, X11.00011 (2012)
44. P. Pfeifer, C. Wexler, P. Yu, G. Suppes, F. Hawthorne, S. Jalisatgi, M. Lee, D. Robert-son, and S. Chakraborti, "Multiply Surface-Functionalized Nanoporous Carbon for Vehi-cular Hydrogen Storage." In: *Proceedings of the 2012 DOE Hydrogen and Fuel Cells Program Annual Merit Review and Peer Evaluation, May 14-18, 2012, Washington, DC, Hydrogen Storage—Hydrogen Storage, Sorption.*
http://www.hydrogen.energy.gov/annual_review12_storage.html#sorption
http://www.hydrogen.energy.gov/pdfs/review12/st019_pfeifer_2012_o.pdf
45. B. Kuchta, L. Firlej, A. Mohammadhosseini, P. Boulet, M.W. Beckner, J. Romanos, and P. Pfeifer, "Hypothetical High-Surface-Area Carbons with Exceptional Hydrogen Storage Capacities: Open Carbon Frameworks." J. Am. Chem. Soc. **134**, 15130-15137 (2012). doi:10.1021/ja306726u
46. P. Pfeifer, C. Wexler, P. Yu, G. Suppes, F. Hawthorne, S. Jalisatgi, M. Lee, and D. Robertson, "Multiply Surface-Functionalized Nanoporous Carbon for Vehicular Hydrogen Storage." In: *DOE Hydrogen and Fuel Cells Program, 2012 Annual Progress Report*, ed. S. Satyapal (U.S. Department of Energy, Washington, DC, 2012; DOE/GO-102012-3767), p. IV-(72-77).
http://www.hydrogen.energy.gov/annual_progress12.html
http://www.hydrogen.energy.gov/pdfs/progress12/iv_c_3_pfeifer_2012.pdf
47. P. Pfeifer, C. Wexler, M.F. Hawthorne, M.W. Lee, and S. Jalisatgi, "New Pathways and Metrics for Enhanced, Reversible Hydrogen Storage in Boron–Doped Carbon Nano-spaces." In: *DOE Hydrogen and Fuel Cells Program, 2012 Annual Progress Report*, ed. S. Satyapal (U.S. Department of Energy, Washington, DC, 2012; DOE/GO-102012-3767), p. IV-(233-235).
http://www.hydrogen.energy.gov/annual_progress12.html
http://www.hydrogen.energy.gov/pdfs/progress12/iv_h_7_pfeifer_2012.pdf
48. J. Burress, E. Dohnke, M. Beckner, M. Lee, C. Wexler, P. Pfeifer. "Adsorbed Hydrogen Film Densities and Thicknesses Determined from Low-Temperature Hydrogen Sorption Experiments." Bull. Am. Phys. Soc. 58, M38.00008 (2013)
49. A. Gillespie, M. Beckner, N. Chada, J. Schaeperkoetter, A. Singh, M. Lee, C. Wexler, J. Burress, P. Pfeifer. "Measurements of Increased Enthalpies of Adsorption for Boron-Doped Activated Carbons." Bull. Am. Phys. Soc. 58, M38.00010 (2013)
50. L. Firlej, B. Kuchta, A. Lazarewicz, and P. Pfeifer, "Increased H_2 Gravimetric Storage Capacity in Truncated Slit Pores Modeled by Grand Canonical Monte Carlo Simula-tions." Carbon **53**, 208-215 (2013). http://dx.doi.org/10.1016/j.carbon.2012.10.049
51. J. Romanos, M. Beckner, D. Stalla, A. Tekeei, G. Suppes, S. Jalisatgi, M.W. Lee, M.F. Hawthorne, J.D. Robertson, L. Firlej, B. Kuchta, C. Wexler, P. Yu, and P. Pfeifer, "Infrared Study of Boron-Carbon Chemical Bonds in Boron-Doped Activated Carbon." Carbon **54**, 208-214 (2013). http://dx.doi.org/10.1016/j.carbon.2012.11.031
52. B. Kuchta, L. Firlej, A. Mohammadhosseini, M. Beckner, J. Romanos, and P. Pfeifer, "Open Carbon Frameworks—a Search for Optimal Geometry for Hydrogen Storage." J. Mol. Mod. **19**, 4079-4087 (2013). doi:10.1007/s00894-012-1700-0
53. R.J. Olsen, M. Beckner, J. Romanos, M. Stone, P. Pfeifer, C. Wexler, and H. Taub, "Quantum excitation spectrum of hydrogen adsorbed in nanoporous carbons observed by inelastic neutron scattering." Carbon **58**, 46-58 (2013).
54. R. Olsen, M. Beckner, R. Romanos, P. Lewellyn, B. Kuchta, P. Pfeifer, and C. Wexler, "Experimental determination of adsorbed film volumes." Adsorption (under review, 2013).

55. J. Romanos, D. Stalla, M. Beckner, A. Tekeei, G. Suppes, S. Jalisatgi, M. Lee, F. Hawthorne, D. Robertson, L. Firlej, B. Kuchta, C. Wexler, P. Yu, P. Pfeifer, "Functional B-C bonds in nanoporous boron carbide and boron-doped carbon materials." Carbon (under review, 2013).
56. P. Pfeifer, C. Wexler, P. Yu, J. Burress, G. Suppes, F. Hawthorne, S. Jalisatgi, M. Lee, D. Robertson, and S. Chakraborti, "Multiply Surface-Functionalized Nanoporous Carbon for Vehicular Hydrogen Storage." In: *Proceedings of the 2013 DOE Hydrogen and Fuel Cells Program Annual Merit Review and Peer Evaluation, May 13-17, 2013, Washington, DC, Hydrogen Storage—Hydrogen Storage, Sorption.*
http://www.hydrogen.energy.gov/annual_review13_storage.html#sorption
http://www.hydrogen.energy.gov/pdfs/review13/st019_pfeifer_2013_o.pdf
57. L. Firlej, P. Pfeifer, and B. Kuchta, "Understanding universal adsorption limits for hydrogen storage in nanoporous systems." Adv. Mater. **25**, 5971-5974 (2013).
58. L. Firlej, M. Beckner, J. Romanos, P. Pfeifer, and B. Kuchta, "Different Approach to Estimation of Hydrogen-Binding Energy in Nanospace-Engineered Activated Carbons." J. Phys. Chem. C **118**, 955-961 (2014).
59. P. Pfeifer, A. Gillespie, E. Dohnke, and Y. Soo, "Hydrogen densities greater than liquid hydrogen at 77 K in engineered carbon nanospaces." In: *Materials Challenges in Alternative & Renewable Energy, Conference Program* (American Ceramic Society, Columbus, OH, 2014), MCARE-166-2014, p. 36
60. E. Dohnke, A. Gillespie, P. Pfeifer. "Liquid-like hydrogen densities in engineered carbon nanospaces." Bull. Am. Phys. Soc. 59, M22.00003 (2014)
61. A. Gillespie, E. Dohnke, J. Schaeperkoetter, D. Stalla, P. Pfeifer. "Adsorption Enthalpies of Hydrogen on Chemically Enhanced Carbon Nanospaces." Bull. Am. Phys. Soc. 59, M22.00005 (2014)
62. C. Wexler, A. St John, M. Connolly. "Energetics of Boron Doping of Carbon Pores." Bull. Am. Phys. Soc. 59, Z37.00007 (2014)
63. P. Pfeifer, C. Wexler, P. Yu, M. Lee, D. Robertson, L. Firlej, and B. Kuchta, "Multiply Surface-Functionalized Nanoporous Carbon for Vehicular Hydrogen Storage." In: *Proceedings of the 2014 DOE Hydrogen and Fuel Cells Program Annual Merit Review and Peer Evaluation, June 16-20, 2014, Washington, DC, Hydrogen Storage—Hydrogen Storage, Sorption.*
http://www.hydrogen.energy.gov/annual_review14_storage.html#sorption
http://www.hydrogen.energy.gov/pdfs/review14/st019_pfeifer_2014_o.pdf
64. P. Pfeifer, L. Firlej, B. Kuchta, M. Lee, C. Wexler, P. Yu, and D. Robertson, "Multiply Surface-Functionalized Nanoporous Carbon for Vehicular Hydrogen Storage." In: *DOE Hydrogen and Fuel Cells Program, 2014 Annual Progress Report*, ed. S. Satyapal (U.S. Department of Energy, Washington, DC, 2014; DOE/GO-102014-4504), p. IV-(86-91).
http://www.hydrogen.energy.gov/annual_progress14_storage.html
hhttp://www.hydrogen.energy.gov/pdfs/progress14/iv_c_4_pfeifer_2014.pdf
65. J. Schaeperkoetter, A. Gillespie, C. Wexler, P. Pfeifer. "Boron Substitution in Disordered Graphene-like Carbon." Bull. Am. Phys. Soc. 60, B1.00002 (2015)
66. E. Dohnke, A. Gillespie, P. Pfeifer. "Properties of adsorbed hydrogen films in nanospaces." Bull. Am. Phys. Soc. 60, T34.00011 (2015)
67. A. Gillespie, E. Dohnke, D. Stalla, M. Sweany, P. Pfeifer. "Application of Henry's Law for Binding Energies of Adsorbed Hydrogen." Bull. Am. Phys. Soc. 60, T34.00013 (2015)